

# Imaging Stray Magnetic Fields Using 3D Scanning Techniques

*by*

*Robert Malcolm Gibbs MSci., MSc., PGCE*

A thesis submitted to Cardiff University in candidature for the degree of  
Doctor of Philosophy



*Cardiff School of Engineering, Cardiff University*

*December, 2019*



*for*  
*Mother and Father*



## Summary

A new versatile magnetic field scanning system has been developed; based on a *Micromagnetics*<sup>®</sup> STJ-020 tunnelling magneto-resistance (TMR) sensor and a 3-axis positioning arm, with a 3D-printed sensor enclosure, precision goniometer and integrated microscopic sight. Calibration of the hardware, quantifying the slack/backlash of the three axes, and the capabilities of the system and its sensors are recounted. The system is capable of; scanning precisely and repeatably at 1  $\mu\text{m}/\text{step}$  with a 4 x 2  $\mu\text{m}^2$  sensing area; scanning smooth continuously dynamic magnetic field changes at a sampling frequency up to 1 MHz; producing scans of three-dimensional volumes; and resolving the field components along multiple axes. The Scanner Control software (available as open access<sup>†</sup>) has been developed to be modular, powerful and adaptable, permitting large datasets from multiple sensors to be analysed. Studies are made of the domain structure in 3% Grain-Oriented Electrical Steel, Amorphous Alloy materials, *Cubex* doubly oriented Si-Fe Alloy and manufactured Planar coils, both statically and when reacting dynamically to externally applied alternating fields. Interpretation of the resulting field maps and comparison of the advantages and disadvantages of the Scanner system over other domain observation methods is given. The ability to scan a three-dimensional volume above the surface of the sample and to derive the  $H_z$  and  $H_x$  components from only a single axis sensor is developed and demonstrated, both statically and dynamically. The principles are tested against the known geometries of constructed planar coils, the expected fields from which are determined using Finite Element Modelling. The novel developments of the project, and the advantages of the developed Scanner System, culminate in, and are ultimately demonstrated by, the final dynamic three-dimensional, component-resolved stray-field scan of a volume above the surface of an unprepared sample of coated 3% grain-oriented electrical steel under alternating applied magnetic field.

<sup>†</sup> Open Access through the Cardiff Portal Arxive (<http://doi.org/10.17035/d.2019.0079831572>) and on the accompanying DVD.









## ***Acknowledgements***

I gratefully acknowledge the Engineering and Physical Science Research Council, UK (EPSRC) for supporting this research through a studentship and Doctoral Training Grant (Ref EP/M507842/1). The LabView code, 3D printing files and data underpinning each of the figures, tables and analysis produced in this thesis can be found in the Cardiff Portal Arxiv at <http://doi.org/10.17035/d.2019.0079831572> and through the included DVD-ROM.

I acknowledge my Supervisors Dr Turgut Meydan and Dr Paul Williams for all their advise and support during this research.

I wish to thank my Parents for their moral and financial support, and my daughter Amy for her patience and acceptance of her father's undertaking.

I acknowledge my colleagues in the School of Engineering and Cardiff University for their encouragement, friendship and amusement during this research.

I acknowledge all the staff of Cardiff University, the Doctoral Academy and the School of Engineering for their help in facilitating this research.

I acknowledge the external examiner Prof. Anthony Peyton of Manchester University, internal examiner Dr Stephen Robson and *viva voca* chair Dr Johannes Benedikt for their time and suggestions.





## ***Table of Contents***

<i>Summary</i>	<i>v</i>
<i>Declaration</i>	<i>vii</i>
<i>Acknowledgements</i>	<i>ix</i>
<i>Table of Contents</i>	<i>xi</i>
<i>Collected Chapter Summaries</i>	<i>xvii</i>
<i>List of Figures and Tables</i>	<i>xxi</i>
<b>1. Introduction</b>	<b>1</b>
1.1 The Research Specification	1
1.2 Aims of the Research	1
1.2.1 Initial Aims based on the Specification	1
1.2.2 Enhanced Aims following the Review of Prior Literature	2
<b>2. Background</b>	<b>5</b>
2.1 Foundations of Electromagnetism and Magnetization	5
2.1.1 Physical Origins of the Magnetic Flux Density $\underline{B}$	5
2.1.2 Physical Origins of Applied Magnetic Field $\underline{H}$	16
2.1.3 Physical Origins of Material Magnetization $\underline{M}$	21
2.1.4 The relationship between $\underline{B}$ , $\underline{H}$ and $\underline{M}$	23
2.2 Magnetic Materials, Magnetic Domains and Stray Fields at the Surface	25
2.2.1 Magnetic Materials	25
2.2.2 Physical Origins of Magnetic Domains	28
2.2.3 Dynamics of Magnetic Domains	31
2.2.4 Stray Fields at the Surface	32
<b>3. Review of Literature</b>	<b>35</b>
3.1 Methods of Detecting Magnetic Fields and Observing Domains	35
3.1.1 The Bitter technique	36
3.1.2 The Faraday and Kerr Magneto-optical Effect	38
3.1.3 Magneto-Optical Indicator Films	41
3.1.4 Magnetic Field Sensors	43

3.2 Existing Procedural Scanner Systems	45
3.2.1 Systems Using Hall-Effect Magnetic Field Sensors	45
3.2.2 Systems Using Tunnelling Magneto-resistance Sensors	48
3.3 Existing studies of Domain Dynamics	51
3.3.1 Using Magneto-optical Techniques	51
3.3.2 Using Procedural Scanner Systems	53
<b>4. Development of the Scanner Hardware</b>	<b>55</b>
4.1 System Overview	55
4.1.1 System Requirements	58
4.1.2 Hardware Architecture	58
4.2 Scanner Base	60
4.2.1 3-axis Framework	60
4.2.2 Slack/Backlash Calibration	61
4.3 Parker Automation Hardware	64
4.3.1 Control Modules	64
4.3.2 Power	67
4.4 Analogue Data Acquisition	68
4.4.1 NI USB-6356 Multifunction Data Acquisition	68
4.4.2 Low Pass Filters	68
4.5 Controlling PC System	69
4.5.1 32-bit Drivers for VISA serial control and RS232 connections	69
4.6 Philtec Displacement Sensors	70
4.6.1 D6 Displacement Sensor	70
4.6.2 RC20 Displacement Sensor	70
4.6.3 Continued Application of the Displacement Sensors	71
4.7 Micromagnetics STJ-020 TMR Magnetic Field Sensor	72
4.7.1 Physical principles of the sensor	72
4.7.2 Calibration of the STJ-020 TMR Sensor	74
4.8 Lakeshore Hall-Effect Magnetic Field Sensor	77
4.9 Sensor Head Development	78
4.9.1 Sensor Head Version 1 - Fixed Block	78
4.9.2 Sensor Head Version 2 - 3D printed Sensor Pivot	78
4.9.3 Sensor Head Version 3 - Micrometer Rotation Stage Sensor Pivot	80
4.10 Sample Stage Development	81
4.10.1 Integrated Microscopic Sight	81
4.10.2 Micrometer Controlled Levelling Platform	81
4.10.3 Energising Yoke and Coils	81
4.10.4 Energising the Samples for Dynamic Studies	82

<b>5. Development of the Scanner Control Software</b>	<b>85</b>
5.1 System Overview	85
5.1.1 System Requirements	86
5.1.2 National Instruments LabView 15 Programming Language	86
5.2 Scanner Control System 1 – Basic 2D Scanning	87
5.2.1 SC1 User Interface	87
5.2.2 SC1 LabVIEW Code	88
5.3 Scanner Control System 2 – 3D Volume Scanning	90
5.3.1 SC2 User Interface	90
5.3.2 SC2 LabVIEW Code	92
5.4 Scanner Control System 3 – Dynamic 3D Volume Scanning	94
5.4.1 SC3 User Interface	95
5.4.2 SC3 LabVIEW Code	96
5.4.2.1 <i>Axis Limits, a critical error during development</i>	97
5.4.2.2 <i>The mouse-based interaction on the bitmap display</i>	98
5.4.2.3 <i>(Motion).vi - communication with the Scanner Hardware</i>	106
5.4.2.4 <i>[DATA_stream].vi - storing the scan data</i>	108
5.4.2.5 <i>Bitmap.vi - creating the greyscale Bitmap display</i>	112
5.4.2.6 <i>SAVE.vi - saving the scans to file</i>	116
5.4.2.7 <i>PNG.vi - exporting PNG and Histograms of the Scans</i>	118
5.4.2.8 <i>Synchronise.vi - processing time-series scans</i>	122
5.5 Practical Considerations when Using the Software	123
5.5.1 Initial User Interface	123
5.5.2 Defining a Scan	124
5.5.3 Scanning	126
5.5.4 Saving and Loading a Scan	128
5.5.5 Processing and Analysis of Data	129
<b>6. Two Dimensional Investigation of Stray Fields</b>	<b>133</b>
6.1 Domain Observation of 3% Si Grain-Oriented Electrical Steel	133
6.1.1 Comparative Scans with Different Sensors	133
6.1.2 Comparison Between Domain Observations Using the Scanner and MOKE	136
6.1.3 Domains in Coated 3% Si Grain-Oriented Electrical Steel After Laser Etching the Surface	140
6.2 Observation of Stray Fields from Amorphous Alloy Materials	142
6.2.1 Mapping Stray Fields from As-cast Amorphous Ribbon	142
6.2.2 Mapping Stray Fields from AF10 Amorphous Wire and Comparison with the Bitter Technique	144

6.3 Comparison Between the Modelled and Measured $H_z$ Fields from Different Topologies of Planar Coils	146
6.3.1 Finite Element Modelling of Stray Fields from Planar Coils	146
6.3.2 Scanning of Stray Fields from Planar Coils	147
6.4 Observation of Stray Fields from <i>Cubex</i> Doubly Oriented Si-Fe Alloy	152
<b>7. Investigation of Three Dimensional Stray Field Structure</b>	<b>155</b>
7.1 Scans of $H_z$ Stray Fields within a Volume above a Sample Surface	155
7.1.1 $H_z$ Stray Fields Volume Scans of <i>Cubex</i> Doubly Oriented Si-Fe Alloy	156
7.1.2 $H_z$ Stray Field Volume Scans of <i>Metglas</i> Amorphous Ribbon	157
7.2 Resolving $H_z$ and $H_x$ Components with a Single-axis Sensor	158
7.2.1 Tilted Sensor Scanning with Sensor Head 2	160
7.2.2 Variable Angle Scans with Sensor Head 3	162
7.3 Comparison between the Modelled and Measured $H_z$ and $H_x$ Components of the Fields from Planar Coils	163
7.4 Resolved Stray Field $\underline{H}$ Vectors from Coated 3% Si Grain-Oriented Electrical Steel	167
7.4.1 Resolved Stray Field $\underline{H}$ Vectors from Laser Etched Coated 3% Si Grain-Oriented Electrical Steel Before and After Etching	167
7.4.2 Resolved Stray field $\underline{H}$ Vector in a Volume Above Coated 3% Si Grain-Oriented Electrical Steel	169
<b>8. Investigation of Alternating Domain Dynamics</b>	<b>171</b>
8.1 Investigating Dynamics with the Scanner System	171
8.1.1 The Process of Frame Synchronisation	171
8.1.2 Dynamics Oscillation of the Fields from the Square Planar coil	172
8.2 Investigating Stray Field and Domain Dynamics	175
8.2.1 Laser Etched Coated 3% Si Grain-Oriented Steel subjected to alternating applied field from a Yoke	175
8.2.2 As-cast 2605 Co IPF895 <i>Metglas</i> Alloy Amorphous Ribbon subjected to alternating applied field from a Yoke	178
8.2.3 Uncoated 3% Si Grain-Oriented Steel subjected to alternating applied field from 20 + 20 Coils	181
8.2.4 Coated 3% Si Grain-Oriented Steel subjected to alternating applied field from 50 + 50 Coils	185
8.3 Investigating Three Dimensional Stray Field Dynamics	194

<b>9. Conclusions</b>	<b>197</b>
9.1 Review of the Original Scanner Specifications and Enhancements	197
9.1.1 Review of Scanner Hardware Specifications	197
9.1.2 Review of Scanner Software Specifications	199
9.2 General Conclusions of the Domain Observation Studies	201
9.3 Future Enhancements to the Scanner System	205
9.4 Final Remarks	206

<i>References</i>	<i>ccxli</i>
-------------------	--------------

## **Appendix**

The Appendices are made available electronically through the Cardiff Portal Arxive at <http://doi.org/10.17035/d.2019.0079831572> and through the included DVD-ROM.

<i>Summary</i>	<i>Aiii</i>
<i>Table of Contents</i>	<i>Av</i>
<i>Collected Appendix Summaries</i>	<i>Avii</i>

<b>Appendix 1 - Scanner Control 1 LabView VI Code</b>	<b>A1</b>
---	-----------

<b>Appendix 2 - Scanner Control 2 LabView VI Code</b>	<b>A73</b>
---	------------

<b>Appendix 3 - Scanner Control 3 LabView VI Code</b>	<b>A239</b>
---	-------------

<b>Appendix 4 - Scanner Hardware Specifications</b>	<b>A469</b>
---	-------------

<b>Appendix 5 - Catalogue of Data</b>	<b>A563</b>
---------------------------------------	-------------

<b>Appendix 6 - Publications</b>	<b>A599</b>
----------------------------------	-------------

Table of Contents



## ***Collected Chapter Summaries***

A collection of the Chapter Summaries of each of the Chapters in the Thesis and Appendix.

### **Chapter 1 - Introduction**

The design and project overview for this research are presented. The motivation for its undertaking and the constraints within which the design was facilitated.

### **Chapter 2 - Background**

The physical origins of the magnetism and material magnetisation are discussed. A full understanding of the Magnetic Flux Density vector-field  $\mathbf{B}$  is derived from the Lorentz transformation of the Coulomb force between two moving charges, developed further to the origin of the Applied Field  $\mathbf{H}$  around a current carrying wire. Consequently, material magnetisation  $\mathbf{M}$  and the magnetic characteristics of paramagnetic and ferrimagnetic elements are discussed, leading to an understanding of magnetic domain formation within crystalline and amorphous ferromagnetic alloys. Throughout, vector quantities are indicated by a bold underlined symbol eg.  $\underline{\mathbf{u}}$ . The scalar magnitude of  $\underline{\mathbf{u}}$  is then  $u$  whilst  $u_x$  is the magnitude of the x component of  $\underline{\mathbf{u}}$ .

### **Chapter 3 - Review of Literature**

A review of the Literature relevant to the detection of magnetic fields and observation of domains and domain dynamics is provided along with existing procedural scanner systems making use of the magnetic field detection techniques available.

### **Chapter 4 - Development of the Scanner Hardware**

The Scanner Hardware is built around a 3-axis positioning arm, controlled by Parker Automation drivers with a 3D-printed sensor enclosure, precision goniometer and integrated microscopic sight. Here the system requirements and architecture are discussed. Calibration of the hardware, particularly quantifying the slack/backlash of the three axis, and progressive improvement in the capabilities of the system and its sensors

is recounted. The technical drawings for the developed 3D-printed sensor heads are provided. Detailed description and data-sheets for both the manufactured and purchased components of the Scanner Hardware are provided in Appendix 4.

## **Chapter 5 - Development of the Scanner Software**

As the requirements of the Scanner and the understanding of LabVIEW architecture increased three distinct main versions of the Scanner Control Software were developed. The complete structure and functional logic of each Scanner Control system is described in detail in Appendix 1, Appendix 2 and Appendix 3. The pertinent points of the development of the software and its functions are recounted here along with detailed guidance on the practical operation of the final Scanner Control 3 system.

## **Chapter 6 - Two Dimensional Investigation of Stray Fields**

The study of the domain structure in Grain Oriented Electrical Steel, Amorphous Alloy materials, *Cubex* doubly oriented Si-Fe Alloy and manufactured Planar coils by the scanning of stray fields from the sample surface has been made. Interpretation of the resulting field maps and comparison of the advantages and disadvantages of the Scanning System over other domain observation methods is given.

## **Chapter 7 - Investigation of Three Dimensional Stray Field Structure**

The ability to scan in a three dimensional volume above the surface of the sample and to derive the  $H_z$  and  $H_x$  components from only a single axis sensor is developed and demonstrated. The principles are tested against the known geometries of constructed planar coils, the expected fields from which can be determined using FEM.

## **Chapter 8 - Investigation of Alternating Domain Dynamics**

The Scanner Control 3 software was specifically developed with the aim of investigating the dynamics of domains as they change under the influence of an alternating external applied field. Dynamic scans of samples are presented in a filmstrip fashion within the thesis, with fully animated versions of each figure available as animated GIFs in *Chapter 8.7z* of the Cardiff Portal Arxive ([page ix](#)) and on the accompanying DVD.

## Chapter 9 - Conclusions

Overall conclusions of the Thesis, review of the aims achieved and the advantages and disadvantages of the Scanner System are presented. Future work is proposed including improvements to the Hardware and Software and discussion of alternative sensors and applications.

## Appendix 1 - Scanner Control 1 LabView VI Code

The final version of the first Scanner Control software, in use from 19/02/16 to 16/06/16. The software is structured as a main Virtual Instrument (VI), 19 sub-VIs and 10 Global Variables. The individual Elements of the VI are identified by sub-VI (v), Global Variable (g), While Loop (w), Case (c), Stacked Sequence (s) and Diagram Disable (d) structure. The functionality of each element is explained. Pertinent aspects of the development of this code are discussed in Chapter 5. The LabView code itself is available in the *Chapter 5.7z* archive in the Cardiff Portal Archive and through the included DVD-ROM. Appendix 5 presents a Catalogue of the files available.

## Appendix 2 - Scanner Control 2 LabView VI Code

The final version of the second Scanner Control software, in use from 09/06/16 to 23/05/18. The core differences between the second and first versions of the Scanner Control software were an entirely innovative implementation of Mouse based interaction with the data display, and the ability to scan in three dimensions, rather than just the xy-plane. The core differences in LabView VI architecture was greater modularity, adoption of event based rather than continuous-polling architecture, the use of shift registers rather than global variables and the beginnings of the use of single iteration while loops. The software is structured as a main Virtual Instrument (VI), 14 sub-VIs and 1 scratch file. The individual Elements of the VI are identified by sub-VI (v), scratch file (f), While Loop (w), Event(e), Case (c), Stacked Sequence (s) and Diagram Disable (d) structures. The functionality of each element is explained. Pertinent aspects of the development of this code are discussed in Chapter 5. The LabView code itself is available in the *Chapter 5.7z* archive in the Cardiff Portal Archive and through the included DVD-ROM. Appendix 5 presents a Catalogue of the files available.

## Appendix 3 - Scanner Control 3 LabView VI Code

The third and final version of the Scanner Control software, in use from 22/06/18 onwards. The software is structured as a main Virtual Instrument (VI), 22 sub-VIs and one 7z archive containing scratch files. The individual Elements of the VI are identified by sub-VI (v), 7z archive (f), While Loop (w), Event(e), Case (c), Stacked Sequence (s) and Diagram Disable (d) structures. The functionality of each element is explained. Pertinent aspects of the development of this code are discussed in Chapter 5. The LabView code itself is available in the *Chapter 5.7z* archive in the Cardiff Portal Archive and through the included DVD-ROM. Appendix 5 presents a Catalogue of the files available.

## Appendix 4 - Scanner Hardware Specifications

The Scanner Hardware is built around a 3-axis positioning arm, controlled by Parker Automation drivers, a 3D-printed sensor enclosure, precision goniometer and incorporated microscopic sight. The Scanner Hardware is formed of four electronically communicating groups of components; the Scanner Base components, the Parker Automation modules, the Analogue Data Acquisition components, and the PC Control components with an additional optical Microscope and Power Oscillators. The technical drawings for the developed 3D-printed sensor heads are provided. For purchased components the manufacturer specifications and user guides are provided. Detailed description of the development of the Scanner Hardware is provided in Chapter 4.

## Appendix 5 - Catalogue of Data

The Data which supports this thesis can be found on the included DVD and through the Cardiff Portal Archive at <http://doi.org/10.17035/d.2019.0079831572>. A catalogue of the data available in the Data Archive is presented, organised by Chapter. The Data from each Chapter are compressed in a 7zip archive (.7z). The 7zip unarchiver is available at <https://www.7-zip.org/>.

## Appendix 6 - Publications

During this research three posters have been presented at conference, one conference proceedings paper, one short journal paper and one long journal paper have been published, each demonstrating novel peer reviewed research. The publications are available in *Publications.7z* on the included DVD and through the Cardiff Portal Archive at <http://doi.org/10.17035/d.2019.0079831572>.

## List of Figures

A list of the Figures used throughout the Thesis.

### Chapter 2 Background

**Figure 2.1:** An illustration of the situation of two charges  $q_1$  and  $q_2$  travelling parallel to each other at different speeds. (b) is (a) transformed into the rest frame,  $S'$ , of  $q_1$ . [Page 7](#)

**Figure 2.2:** An illustration of the situation of two charges  $q_1$  and  $q_2$  travelling perpendicular to each other at different speeds. (b) is (a) transformed into the rest frame,  $S'$ , of  $q_1$ . [Page 9](#)

**Figure 2.3:** An illustration of the forces experienced by a test electron  $q_t$  from the electrons and protons in a current carrying wire. The direct Coulomb acceleration from the electrons ( $\mathbf{a}$ ) is exactly balanced by that from the protons ( $\mathbf{a}_+$ ), the wire being electrostatically neutral. The only remaining acceleration is the cumulative magnetic effect from each moving source electron ( $\mathbf{a}_B$ ), in each case perpendicular to the velocity of the test charge. [Page 16](#)

**Figure 2.4:** (a) The test charge  $q_t$  experiences an acceleration  $\mathbf{a}_B$  radially away from a current carrying wire it is travelling parallel to. The constructed vector-field  $\mathbf{B}$  is perpendicular to both  $\mathbf{u}$  and  $\mathbf{a}_B$ . The acceleration  $\mathbf{a}_B$  is said to be a response to the local magnetic flux density  $\mathbf{B}$ . (b) The acceleration of the test particle travelling parallel to the wire at distance  $r$  is always radial from the wire, thus the constructed magnetic flux density at any point radial to the wire is always tangential to a circle of radius  $r$ . That circle can be considered the vector-field of the magnetic effect produced by the current carrying wire and is termed the Applied Magnetic Field  $\mathbf{H}$ . [Page 17](#)

**Figure 2.5:** (a) Two parallel wires with electrons travelling in the same direction experience a repulsive acceleration. (b) Two parallel wires with electrons travelling in opposite directions experience an attractive acceleration. In both cases the acceleration is solely the result of the magnetic effect of the two sets of moving electrons. Both wires are electro-statically neutral. [Page 18](#)

**Figure 2.6:** (a) Two parallel wires with parallel current experience a repulsive acceleration. (b) Two parallel wires with anti-parallel current experience an attractive acceleration. In both cases the acceleration is solely the result of the magnetic effect. Both wires are electro-statically neutral. [Page 19](#)

**Figure 2.7:** (a) The Magnetic Moment  $\underline{m}$  is defined as the vector perpendicular to the current loop, the result of the culmination of the Applied Magnetic Field  $\underline{H}$  within the loop, thus proportional to the current and radius of the loop. (b) A test loop whose Magnetic Moment  $\underline{m}_2$  is misaligned with  $\underline{m}_1$  will feel the acceleration  $\underline{a}_b$  necessary to rotate and translate until  $\underline{m}_1$  and  $\underline{m}_2$  are coincident. [Page 20](#)

**Figure 2.8:** Illustration of the differences in atomic magnetic moment alignment,  $\underline{M}$  with representations of (a) magnetic moments in a disordered state; (b) diamagnetism; (c) paramagnetism; (d) ferromagnetism; (e) anti-ferromagnetism and (f) ferrimagnetism. [Page 25](#)

**Figure 2.9:** The Periodic Table of elements illustrating which elements are Diamagnetic, Paramagnetic, Ferromagnetic and Anti-ferromagnetic, including the Néel and Curie temperatures. Derived from information available in [19]. [Page 27](#)

**Figure 2.10:** The metallic crystalline structures; body centred cubic (bcc) and face centred cubic (fcc) and hexagonal close-packed (hcp). [Page 28](#)

**Figure 2.11:** The rotation of the magnetization vector from one domain through a  $180^\circ$  wall to another domain. The two alternative modes of rotation are; (a) *Bloch* wall, the optimal mode and (b) a *Néel* wall, which is less favourable. Reproduced from [31]. [Page 30](#)

**Figure 2.12:** Single-domain particle diameter size ( $D_{sd}$ ) and super-paramagnetic transition diameter size ( $D_{sp}$ ) of selected ferromagnetic materials. Reproduced from [27]. [Page 30](#)

**Figure 2.13:** Barhausen noise; discontinuous changes in the flux density  $\underline{B}$  as the applied field  $\underline{H}$  is changed. Reproduced from [27]. [Page 31](#)

## Chapter 4 Development of the Scanner Hardware

**Figure 4.1:** Photograph of the Scanner System showing; (a) the 3-axis positioning arm, (b) scanner base, (c) sample platform with energising Yoke, (d) microscopic sight, (e) Sensor Head version 3 with STJ-020 TMR sensor and (f) Scanner Control 3 PC display. [Page 55](#)

**Figure 4.2:** The Block Schematic of the connections between the different components of the Scanner Hardware, illustrating the physical relationships and the electrical connections. The blue wires indicate direct analogue electrical connection, the green

wires indicate USB or RS232 serial communications and the black bars indicate a physical connection between components not already enclosed in groups. [Page 56](#)

**Figure 4.3:** The four electronically communicating groups of components; the Scanner Base components, the Parker Automation modules, the Analogue Data Acquisition components, and the PC Control components. [Page 59](#)

**Figure 4.4:** The individual components of the Scanner Base group of components, all physically attached but independently wired. Three separate versions of Sensor Head were developed. [Page 59](#)

**Figure 4.5:** Photograph of the 3-axis framework showing; (a) the stepper motors, thread drives, carriages and arms. Also visible in the photograph are; (b) the *Thorlabs* MB3045\_M Aluminium Breadboard, (c) the *National Instruments* 6351 USB mDAQ and (d) Sensor Head version 1 with the *Micromagnetics* STJ-020 TMR sensor and *Philtex* D6 sensor. [Page 60](#)

**Figure 4.6:** Fine single-step voltage changes are plotted as the displacement sensor passes back and forth over the same location repeatedly. The displacement between the forward and reverse paths represents the backlash in the thread of the (a) X, (b) Y and (c) Z axis when the motors change direction. The finely tuned  $X_s(38)$ ,  $Y_s(130)$  and  $Z_s(195)$  constants reduce this displacement in the Scanner Control software. [Page 62](#)

**Figure 4.7:** Scan with the D6 displacement sensor of a 1p coin (a) at 1mm/pixel resolution with the backlash compensation disabled, illustrating the distortion from circular due to “scanner drift”; (b) at 0.25 mm/pixel with the backlash compensation engaged illustrating the lack of “scanner drift”; and (c) at 0.025 mm/pixel with 608000 pixels illustrating the effectiveness of the backlash compensation in preventing any drift. [Page 63](#)

**Figure 4.8:** Illustration of the Parker Automation components; (a)P25L DOL, (b)L25i Drive, (c) D1i DOL, (d) D2i with (e) Motor and (f) RS232 wiring details. The parts are reproduced from [113]. Further detailed description of each component are given in Appendix 4. [Page 65](#)

**Figure 4.9:** Table of ASCII commands which can be sent to the L25i Parker Automation Motion Control Module via RS232, and the internal system variables, elements reproduced from [113]. [Page 66](#)

**Figure 4.10:** (a) Photograph of Philtec D6 displacement sensor reproduced from [115], (b) Photograph of Philtec RC20 displacement sensor reproduced from [116], (c) calibration curves of Philtec RC20 reflection compensated displacement sensor, determined as Voltage output against the vertical displacement from a mirrored surface obtained using the Scanner systems z-axis control. The “M” crosses represent displacements achieved manually using the sample stage micrometer adjustment, the S lines represent continuous single stepping displacements achieved with the z-axis stepper motor. Both the sensor voltage (RC20) and a signal-to-noise (SNR) levels are presented. [Page 71](#)

**Figure 4.11:** (a) Illustration of the TMR-020 sensor, (b) Photograph of microscopic view of the first and second STJ-020 sensor, illustrating the original and corner lapped dies, (c) Schematic of the STJ-020 active sensor area, (d) Photograph of the AL-05 pre-amplifier and power adapter, reproduced from [2]. [Page 73](#)

**Figure 4.12:** (a) The Long solenoid used to produce a varying magnetic field for both the STJ-020 TMR and Lakeshore 475 DSP sensors. (b) and (c) the two sensors mounted alongside on the carrier to be positioned in the centre of the coil. The Calibration of the STJ-020 voltage the Field Strength as measured by the Lakeshore 475 DSP as connected with the Potential Divider (d) and Low Pass Filter (e). For (d), blue crosses are the mean of 10 surrounding samples. Error bands indicated with dotted lines. [Page 75](#)

**Figure 4.13:** (a) Schematic of Lakeshore 475 DSP Axial probe, with an active area diameter (D) of 0.51mm, reproduced from [117]. (b) Photograph of the axial probe attached to Sensor Head 3. (c) Photograph of the Gaussmeter unit itself. [Page 77](#)

**Figure 4.14:** (a) Sensor Head Version 1 illustration and photograph, (b) Sensor Head Version 2 illustration and photograph, (c) Sensor Head Version 3 illustration and photograph. Dimensions in mm. [Page 79](#)

**Figure 4.15:** (a) Photograph of Microscopic Sight with view through it. (b) Set of 50 + 50 coils in use on a sample of coated Electrical Steel. (c) *Thorlabs* AMA027/M levelling platform, illustration reproduced from [119]. (d) Photograph of Smaller Yoke. (e) Photograph of both the Larger Yoke and 20 + 20 coils on a polished Electrical Steel Sample. [Page 82](#)

**Figure 4.16:** Schematic illustration of the sample scanning area featuring the (a) MB3045\_M Aluminium Breadboard and the (b) AMA027/M levelling platform from *Thorlabs* with the (c) Small Yoke and a (d) coated Electrical Steel Sample with 50 x 50 coils attached ([Section 4.10.3](#)). The (e) *Micromagnetics* TMR-020 sensor is encased in the (f) 3<sup>rd</sup> 3D printed sensor head, attached to (g) two MS1S/M translations stages and (h) the CR1/M precision goniometer from *Thorlabs* ([Section 4.9.3](#)). [Page 83](#)



**Figure 4.17:** Calibration of the field strength of the second set of Coils, two parallel 50 turn windings on sleeves which fit wither end of any sample. The coils have a total resistance of  $1\Omega$ . When energised by a power oscillator the combined field strength amplitude of the two coils has been measured as  $2.164 \text{ Am}^{-1}/\text{V}$  with the Lakeshore 475 DSP gaussmeter. [Page 84](#)

## Chapter 5 Development of the Scanner Software

**Figure 5.1:** The Front Panel interface of Scanner Control 1, separated into distinct functional groups, a merger of Hardware Control and Scanning and Data Display. [Page 87](#)

**Figure 5.2:** The Block Diagram of Scanner Control 1. The main block diagram is divided into 6 parallel While loops. [Page 89](#)

**Figure 5.3:** The Front Panel interface of Scanner Control 2 with Tab elements separating distinct functional groups. [Page 91](#)

**Figure 5.4:** The Block Diagram of Scanner Control 2. The main block diagram is divided into 3 parallel While loops. [Page 92](#)

**Figure 5.5:** The Front Panel interface of Scanner Control 3 [Page 95](#)

**Figure 5.6:** The Block Diagram of Scanner Control 3 divided into an initialisation sequence and 2 parallel while loops which manage the user interface and data acquisition. [Page 96](#)

**Figure 5.7:** Case 2 of the 12<sup>th</sup> Event of the 1<sup>st</sup> While loop of Scanner Control 3 (*SC3w1e12c2* in Appendix 3) enables the *User Interface Manager* to handle an “Axis Limit Change” to the “Axis Limits” group. Failure of a wire of True to the first boolean terminal of (*Motion*).vi was a critical error during development. Case 1 in this event (*SC3w1e12c1*), setting “AL\_Defaults”, contained the same error. [Page 98](#)

**Figure 5.8:** The 8<sup>th</sup> Event of the 1<sup>st</sup> While loop of Scanner Control 3 (*SC3w1e8* in Appendix 3). Mouse Down on the “Bitmap Display”. [Page 99](#)

**Figure 5.9:** Case 0 of the 9<sup>th</sup> Event of the 1<sup>st</sup> While loop of Scanner Control 3 (*SC3w1e9c0* in Appendix 3). Mouse Move over the “Bitmap Display” with no button pressed. A red rectangle outlines the cell currently hovered over. [Page 100](#)

**Figure 5.10:** Case 1 and 2 of the 9<sup>th</sup> Event of the 1<sup>st</sup> While loop of Scanner Control 3 (*SC3w1e9c1* and *SC3w1e9c2* in Appendix 3). Mouse Move over the “Bitmap Display” with left or right button pressed. Dragging the greyscale image of the data or drawing a green selection rectangle. [Page 101](#)

**Figure 5.11:** Case 1 and 2 of the 10<sup>th</sup> Event of the 1<sup>st</sup> While loop of Scanner Control 3 (*SC3w1e10c1* and *SC3w1e10c2* in Appendix 3). Mouse Up on the “Bitmap Display” of the left or right button. End of dragging the greyscale image of the data or drawing a green selection rectangle. [Page 103](#)

**Figure 5.12:** The 22 subVIs (labelled *SC3v*) which handle the storage of front panel controls, the storage and display of the data and communication with the Parker Automation hardware. Detail of the functioning of each of these VIs is provided in Appendix 3. [Page 105](#)

**Figure 5.13:** The Block Diagram of (*Motion*).vi which works with *{Motion\_Control}.vi* and the ...\*Parker Automation*\ subVIs to communicate the desired position of the Sensor head to the Scanner Hardware. [Page 107](#)

**Figure 5.14:** The Block Diagram of [*DATA\_stream*].vi, which manages the storage of the scan data in the system. [Page 109](#)

**Figure 5.15:** The “Read” and “Write” Cases of [*DATA\_stream*].vi (*SC3v4c2* and *SC3v4c3* in Appendix 3), which manage the scan data in the system. [Page 110](#)

**Figure 5.16:** The Block Diagram of *Bitmap.vi* showing the “Initialise” case. [Page 113](#)

**Figure 5.17:** The “File” case (*SC3v11c3* in Appendix 3) and “Register” case, sequence frames 0 - 1 (*SC3v11c4s0* and *SC3v11c4s1* in Appendix 3), of *Bitmap.vi*. [Page 114](#)

**Figure 5.18:** The “Register” case, sequence frames 2 - 5 (*SC3v11c4s2* to *SC3v11c4s5* in Appendix 3), of *Bitmap.vi*. [Page 115](#)

**Figure 5.19:** The Block Diagram of *SAVE.vi* showing the “Dynamic” and “Static” cases (*SC3v17c1* and *SC3v17c2* in Appendix 3). [Page 117](#)

**Figure 5.20:** The Block Diagram of *PNG.vi* showing the “Initialise” case (*SC3v15c1* in Appendix 3). [Page 119](#)

**Figure 5.21:** The “Current Frame” case (*SC3v15c4* in Appendix 3) of *PNG.vi* showing the 2nd frame of the “Register” state sequence (*SC3v15c4c(3)2s2* in Appendix 3) and the “Source 1” case of the “Write to PNG” case structure (*SC3v15c4c(4)1* in Appendix 3). [Page 120](#)

**Figure 5.22:** The “PNG stack” case (*SC3v15c5* in Appendix 3) of *PNG.vi* showing the 2nd frame of the “Register” state sequence (*SC3v15c5c(4)2s2* in Appendix 3) and the “All Sources” case of the “Write to PNG” case structure (*SC3v15c5c(5)15* in Appendix 3). [Page 121](#)

**Figure 5.23:** The Block Diagram of *Synchronise.vi* illustrating the initialisation sequence, event-controlled while loop and final processing For loop. [Page 122](#)

**Figure 5.24:** The *Motion Control* (a), *Axis Limits* (b) and *Scan Region* (c) groups of the front panel of *Scanner Control 3* (presented in Figure 5.5). [Page 124](#)

**Figure 5.25:** The progress bars displayed during the initialisation of the *[DATA\_#xyz].vi*, *[DATA\_stream].vi* (a) and *Bitmap.vi* (b) arrays. [Page 125](#)

**Figure 5.26:** The *SCAN* group; (a) in preparation for a scan showing system time and estimated scan time, (b) when requesting a single sample, (c) when scanning showing elapsed and estimated time, (d) paused during a scan, (e) scanning continuing, (f) scanning complete showing system time and total scan time. [Page 126](#)

**Figure 5.27:** The Data Display groups (a) and the Data Display tab; the Graphical Display (b) showing a plot of Amplitude (Voltage) against Time for each of the four Sources and the Bitmap Display (c) showing a greyscale map of the scan data. [Page 127](#)

**Figure 5.28:** (a) The User interface *File* group, (b) the “Save as a Static or Dynamic File?” dialogue box, (c) and (d) the “Saving File...” progress display, (e) the “Which type of DataFile is being loaded?” dialogue box and (f) the “Loading File...” progress display. [Page 129](#)

**Figure 5.29:** (a) The “Process DATA” menu and selection, (b) the “Process DATA” *Synchronise.vi* User Interface and (c) the “Process DATA” *zxCombine.vi* User Interface. [Page 131](#)

**Figure 5.30:** The “Exporting Bitmap as PNG” *PNG.vi* User Interface. [Page 132](#)

## Chapter 6 Two Dimensional Investigation of Stray Fields

**Figure 6.1:** Scans of 25 x 25 mm<sup>2</sup> of polished 3% Si Grain Oriented Electrical Steel with; (a) *Philtec RC20* displacement sensor and (b) *Micromagnetics STJ-020* TMR sensor at 0.05mm/cell resolution. A higher resolution scan of the green highlighted region and indicated domains is presented in [Figure 6.2](#). Scans of 10 x 10 mm<sup>2</sup> of coated 3% Si Grain Oriented Electrical Steel with; (c) *Lakeshore 475* DSP Gaussmeter Hall-effect sensor and (d) *Micromagnetics STJ-020* TMR sensor at 0.05mm/cell resolution. The corresponding region of the sample is indicated. The H<sub>z</sub> stray field strength (A/m) is indicated by a greyscale with positive field out of the page. [Page 134](#)

**Figure 6.2:** Domain observation of the 7.5 x 7.5 mm<sup>2</sup> region of polished 3% Si Grain Oriented Electrical Steel from [Figure 6.1\(b\)](#) produced by; (a) Scan with STJ-020 and (b) MOKE imaging of the same area of sample. The pinhole used to identify the common area and corresponding magnetic domain features are indicated with blue dotted lines. The regions of the scans of [Figure 6.4](#) and [Figure 7.5](#) are highlighted in green. [Page 137](#)

**Figure 6.3:** Raw Images from the MOKE system; (a) uncleaned sample, (b) cleaned sample, indicating the very narrow depth of field. The indicated narrow bands of in-focus image need to be manually combined to produce a coherent image of a large area (c), which retains perspective distortion. [Page 138](#)

**Figure 6.4:** Domain observation of the 3.5 x 2.14 mm<sup>2</sup> region of polished 3% Si Grain Oriented Electrical Steel from [Figure 6.2\(a\)](#) produced by a scan with the STJ-020 sensor at 0.005 mm/cell. The Stray field strength ranges over  $\pm 220$  A/m. The location of the zx Transect presented in [Figure 7.5](#) is illustrated. [Page 138](#)

**Figure 6.5:** Domain observation of (a) 23 x 18 mm<sup>2</sup> region of Laser Etched Coated 3% Si Grain Oriented Electrical Steel produced by a scan with the STJ-020 sensor at 0.1 mm/cell with the 19.5 x 5 mm<sup>2</sup> region (b) indicated, scanned at 0.01 mm/cell. The Stray field strength ranges over  $\pm 350$  A/m. The coating is etched with a 10.6  $\mu\text{m}$  wide CO<sub>2</sub> laser at 14% of 50 W power along the lines indicated. (c) Photograph of the scanning through the incorporated microscopic sight. [Page 141](#)

**Figure 6.6:** Scan of of (a) 19 x 12 mm<sup>2</sup> region of as-cast 2605 Co IPF895 *Metglas* Alloy Amorphous Ribbon produced with the STJ-020 sensor at 0.05 mm/cell, the indicated (b) 6.85 x 6.4 mm<sup>2</sup> at 0.01 mm/cell and (c) 0.5 x 0.5 mm<sup>2</sup> at 0.005 mm/cell. The Stray field strength ranges over  $\pm 88$  A/m. [Page 143](#)

**Figure 6.7:** Progressively higher resolution scans of the top of AF-10 Amorphous wire (running left to right); (a) at 0.005 mm/cell, (b) at 0.002 mm/cell and (c) at 0.001 mm/cell. The Stray field strength in the final 0.001 mm/cell scan ranges over  $\pm 80$  A/m, with distinct features 30  $\mu\text{m}$  apart. [Page 145](#)

**Figure 6.8:** Domain structure of a 50 mm length AF-10 Amorphous wire with an applied perpendicular magnetic field of 1.1 kA/m and twist angles of (a) zero, (b)  $1/2\pi$ , (c)  $\pi$  and (d)  $2\pi$  rad. Reproduced from [6]. A red scale line indicates a distance of  $30\mu\text{m}$  between domain lines. [Page 145](#)

**Figure 6.9:** Comparison of ANSYS FEM and Scans of Planar Coils. (a) Circular, (b) Mesh, (c) Meander, (d) and Square planar coils. (i) Photographs of the manufactured coils, (ii) ANSYS models, (iii)  $H_z$  stray field scans with the TMR-020 sensor at  $0.1\text{ mm/pxl}$ , (iv) FEM of the  $H_z$  fields above the coils. (iii') and (iv') are scans of the Circular coil at a closer scan height. The transect marked by red single-chevrons indicates the path of  $H_z$  amplitude plots ([Figure 6.10](#)). The blue double-chevrons indicate the path of the  $z_x$  Transect presented in ([Figure 7.7\(ii\)](#)). [Page 148](#)

**Figure 6.10:**  $H_z$  amplitude plots of the (a) and (b) Circular and (c) Square planar coils along the paths indicated by red single-chevrons in [Figure 6.9](#) at a scan height of (a)  $0.50\text{ mm} \pm 0.01\text{ mm}$ , (b) and (c)  $0.15\text{ mm} \pm 0.01\text{ mm}$ . The  $\pm$  errors are indicated by dashed lines above and below for both the Scan and ANSYS plots. [Page 151](#)

**Figure 6.11:** Scan of (a)  $20 \times 20\text{ mm}^2$  region of *Cubex* doubly oriented Silicon-iron alloy produced with the STJ-020 sensor at  $0.05\text{ mm/cell}$ , with an indicated (b)  $7 \times 7\text{ mm}^2$  region at  $0.01\text{ mm/cell}$ . The Stray field strength ranges from  $-135$  to  $216\text{ A/m}$ . The indicated further  $2 \times 2\text{ mm}^2$  region is presented in [Figure 7.1](#). [Page 153](#)

## Chapter 7 Investigation of Three Dimensional Stray Field Structure

**Figure 7.1:** Scan of  $H_z$  stray fields within a volume of  $2 \times 2 \times 0.2\text{ mm}^3$  above the sample of *Cubex* doubly oriented Silicon-iron alloy produced with the STJ-020 sensor at  $0.02 \times 0.02 \times 0.002\text{ mm/cell}$  resolution. The area scanned is highlighted in [Figure 6.11](#). The lowest  $xy$  Plane is presented along with ten different  $z_x$  Slices at the indicated locations along the  $y$ -axis. Animated sweeps through each  $xy$  Plane and each  $z_x$  Slice are available in the [Chapter 7.7z arxive \(page ix\)](#). The  $H_z$  Stray field strength ranges over  $\pm 200\text{ A/m}$ . [Page 156](#)

**Figure 7.2:** Scan of  $H_z$  stray fields within a volume of  $0.5 \times 0.5 \times 0.1\text{ mm}^3$  above the sample of as-cast 2605 Co IPF895 *Metglas* Alloy Amorphous Ribbon produced with the STJ-020 sensor at  $0.01 \times 0.01 \times 0.002\text{ mm/cell}$  resolution. The area scanned is highlighted in [Figure 6.6](#). The lowest  $xy$  Plane is presented along with five different  $z_x$  Slices at the indicated locations along the  $y$ -axis. Animated sweeps through each  $xy$  Plane and each  $z_x$  Slice are available in the [Chapter 7.7z arxive \(page ix\)](#). The  $H_z$  Stray field strength ranges over  $\pm 88\text{ A/m}$ . [Page 157](#)

**Figure 7.3:** The geometry of the *Micromagnetics* STJ-020 TMR sensor die; (a) When perpendicular the minimum height of the sensor's active area  $z_0 = 12 \mu\text{m} \pm 3 \mu\text{m}$ . Two simple cases exist where; (b) the clockwise rotation and counterclockwise rotation are equal, or (c) the counterclockwise rotation is  $45^\circ$ , where the z-axis and x-axis components of the stray field can be easily resolved (d). [Page 158](#)

**Figure 7.4:** A scan of a volume of  $2 \times 2 \times 0.5 \text{ mm}^3$  above the sample of polished 3% Si Grain Oriented Electrical Steel produced with the STJ-020 sensor at  $0.1^3 \text{ mm/cell}$  resolution mounted in Sensor Head 2. Two consecutive scans with a sensor tilt of  $5^\circ$  (a) counterclockwise and (b) clockwise are combined to produce a (c) colour representation of the stray field  $\underline{H}$  vector. Only one zx Slice is presented at the indicated location on the lowest xy Plane. (d) The colour representation of the  $\underline{H}$  stray field vector. The  $H_z$  stray field strength ranges over  $\pm 139 \text{ A/m}$  and the  $H_x$  stray field strength ranges over  $\pm 38 \text{ A/m}$ . Some indication of the rotation of the  $\underline{H}$  vector is illustrated in (c). Animated sweeps through each xy Plane and each zx Slice are available in the *Chapter 7.7z* archive ([page ix](#)). [Page 161](#)

**Figure 7.5:** (a) Illustration of the three-dimensional relationship between zx Transect scans of polished 3% Si Grain Oriented Electrical Steel above the surface of the sample at the location indicated in [Figure 6.4](#). (b) Scans of the stray field strength at  $0^\circ, 5^\circ, 10^\circ, 15^\circ, 20^\circ$  counterclockwise to perpendicular above the sample forming  $2.35 \times 0.1 \text{ mm}$  zx Transects at  $0.005 \times 0.005 \times 0.002 \text{ mm/cell}$  resolution. The  $H_y$  Stray field strength ranges from  $-116$  to  $270 \text{ A/m}$ . An animated sweep through each angle is available in the *Chapter 7.7z* archive ([page ix](#)). [Page 162](#)

**Figure 7.6:** Photographs of the system scanning the square planar coil; (a,b) with the STJ-020 sensor perpendicular and (c,d) with the STJ-020 sensor at  $45^\circ$  supported by the precision goniometer of Sensor Head 3. The centre of rotation is precisely aligned to the centre of the sensor's active area. [Page 163](#)

**Figure 7.7:** Comparison of scans of the Square planar coil with the STJ-020 sensor compared with ANSYS FEM of the corresponding topology. (i) xy Scans of the Square planar coil (ii) FEM of the fields from xy plane, (iii) zx Transect scan of the Square planar coil (iv) FEM of the fields from the zx plane; (a)  $H_z$ , (b)  $H_{45}$ , (c)  $H_x$ . Colour representation of the stray field  $\underline{H}$  vector are presented as scanned (a.v) and (b.v) and from FEM (a.vi) and (b.vi). (c.v) The colour representation of the  $\underline{H}$  stray field vector. [Page 165](#)

**Figure 7.8:** (a) Etching lines in Coated 3% Si Grain Oriented Electrical Steel with a  $10.6 \mu\text{m}$  wide  $\text{CO}_2$  laser at 14% of 50 W. (b) the indicated Etched lines are present in the coating made diagonally through the central scanned region. (c) the sample is scanned perpendicularly and at  $45^\circ$  counterclockwise. [Page 167](#)

**Figure 7.9:** A stray field scan of 24 x 20 mm Coated 3% Si Grain Oriented Electrical Steel produced by a scan with the STJ-020 sensor at 0.1<sup>3</sup> mm/cell (i) Before and (ii) After etching the coating with a 10.6  $\mu\text{m}$  wide CO<sub>2</sub> laser at 14% of 50 W (Figure 7.8). Measured (a) H<sub>z</sub> and (b) H<sub>45</sub> fields along with calculated (c) H<sub>x</sub> fields are presented. Colour representation of the stray field **H** vector is presented before (a.iii) and after (b.iii) etching. The colour representation of the **H** stray field vector is presented in (c.iii).  
[Page 168](#)

**Figure 7.10:** A stray field scan of fields within a volume of 10 x 10 x 0.5 mm above a sample of Coated 3% Si Grain Oriented Electrical Steel produced by a scan with the STJ-020 sensor at 0.5 x 0.5 x 0.05 mm/cell. Measured (a) H<sub>z</sub> and (b) H<sub>45</sub> fields along with calculated (c) H<sub>x</sub> fields are presented (i). Colour representation of the stray field **H** vector is presented (ii) with 10 different zx Slices at the indicated locations along the y-axis. The colour representation of the **H** stray field vector is presented in (c.ii). Animated sweeps through each xy Plane and each zx Slice are available in the *Chapter 7.7z* archive ([page ix](#)).  
[Page 169](#)

## Chapter 8 Investigation of Alternating Domain Dynamics

**Figure 8.1(a):** Filmstrip representation of a dynamic scan of the Square Planar coil (Figure 6.9(d.i)) energised at 3kHz with  $\pm 0.2$  V. Scan made with the Lakeshore 476 DSP Gaussmeter at 1kHz sampling rate. 336 frames represent 1 cycle. The full animated GIF is provided in *Chapter 8.7z* of the Cardiff Portal Archive ([page ix](#)) and on the accompanying DVD. The stray field strength (H<sub>z</sub>) is represented in greyscale from -300 to 300 A/m.  
[Page 173](#)

**Figure 8.1(b):** (i) The Mean field strength across the entire surface scanned for each of 336 frames (in black) and the voltage applied to the Square Planar Coil (in red). (ii) The percentage area coverage of each greyscale level across the entire scan for each of 336 frames. The stray field (H<sub>z</sub>) strength is represented in greyscale from -300 to 300 A/m.  
[Page 174](#)

**Figure 8.2(a):** Filmstrip representation of a dynamic scan of Laser Etched Coated 3% Si Grain-Oriented Steel energised at 3kHz with the Large Yoke. The full animated GIF is provided in *Chapter 8.7z* of the Cardiff Portal Archive ([page ix](#)). The stray field strength (H<sub>z</sub>) is represented in greyscale from -500 to 500 A/m. The border 20 pixels of each frame presents the oscillating voltage driving the C-Yoke ( $\pm 0.15$  V). [Page 176](#)

**Figure 8.2(b):** (i) The Mean field strength across the entire surface scanned for each of 336 frames (in black) and the voltage applied to the Large Yoke (in red). (ii) The percentage area coverage of each greyscale level across the entire scan for each of 336 frames. The stray field (H<sub>z</sub>) strength is represented in greyscale from -500 to 500 A/m.  
[Page 177](#)

**Figure 8.3(a):** Filmstrip representation of a dynamic scan of As-cast 2605 Co IPF895 Metglas Alloy Amorphous Ribbon energised at 3kHz with the Large Yoke. The full animated GIF is provided in *Chapter 8.7z* of the Cardiff Portal Arxive ([page ix](#)). The stray field strength ( $H_z$ ) is represented in greyscale from -500 to 500 A/m. The border 20 pixels of each frame presents the oscillating voltage driving the C-Yoke ( $\pm 0.2$  V). [Page 179](#)

**Figure 8.3(b):** (i) The Mean field strength across the entire surface scanned for each of 336 frames (in black) and the voltage applied to the Large Yoke (in red). (ii) The percentage area coverage of each greyscale level across the entire scan for each of 336 frames. The stray field ( $H_z$ ) strength is represented in greyscale from -500 to 500 A/m. [Page 180](#)

**Figure 8.4(a):** Filmstrip representation of a dynamic scan of Uncoated 3% Si Grain-Oriented Steel subjected to a 3kHz oscillating x-axis field of  $\pm 1$  kA/m from the 20 + 20 coils. The full animated GIF is provided in *Chapter 8.7z* ([page ix](#)). The border 20 pixels of each frame presents the oscillating Applied field (inverted greyscale). [Page 182](#)

**Figure 8.4(b):** (i) The Mean stray field strength across the entire surface for each of 336 frames (in black) and the Applied x-axis field strength (in red). (ii) The percentage area coverage of each greyscale level across the entire scan for each of 336 frames. (iii) The Mean Stray field strength plotted against the Applied x-axis field strength. [Page 183](#)

**Figure 8.5(a):** Filmstrip representation of a  $10 \times 10$  mm<sup>2</sup> (@0.05mm/pixel) dynamic scan of Coated 3% Si Grain-Oriented Steel subjected to a 3kHz oscillating x-axis field of  $\pm 1.95$  kA/m from the 50 + 50 coils. The stray field strength ( $H_z$ ) is represented in greyscale  $\pm 300$  A/m. The full animated GIF is provided in *Chapter 8.7z* ([page ix](#)). The border 20 pixels of each frame presents the oscillating Applied field (inverted greyscale). [Page 186](#)

**Figure 8.5(b):** (i) The Mean stray field strength across the entire surface for each of 336 frames (in black) and the Applied x-axis field strength (in red). (ii) The percentage area coverage of each greyscale level across the entire scan for each of 336 frames. (iii) The Mean Stray field strength plotted against the Applied x-axis field strength. [Page 187](#)

**Figure 8.6(a):** Filmstrip representation of a  $2 \times 2$  mm<sup>2</sup> (@0.01mm/pixel) dynamic scan of Coated 3% Si Grain-Oriented Steel, a subregion of [Figure 8.5\(a\)](#) as indicated in the top left frame. The stray field strength ( $H_z$ ) is represented in greyscale  $\pm 300$  A/m. The full animated GIF is provided in *Chapter 8.7z* ([page ix](#)). The border 20 pixels of each frame presents the oscillating Applied field (inverted greyscale). [Page 190](#)

**Figure 8.6(b):** (i) The Mean stray field strength across the entire surface for each of 336 frames (in black) and the Applied x-axis field strength (in red). (ii) The percentage area



coverage of each greyscale level across the entire scan for each of 336 frames. (iii) The Mean Stray field strength plotted against the Applied x-axis field strength. [Page 191](#)

**Figure 8.7(a):** Filmstrip representation of a  $2 \times 2 \text{ mm}^2$  (@0.01mm/pixel) dynamic scan of Coated 3% Si Grain-Oriented Steel, a subregion of [Figure 8.5\(a\)](#) as indicated in the top left frame. The stray field strength ( $H_z$ ) is represented in greyscale  $\pm 300 \text{ A/m}$ . The full animated GIF is provided in *Chapter 8.7z* ([page ix](#)). The border 20 pixels of each frame presents the oscillating Applied field (inverted greyscale). [Page 192](#)

**Figure 8.7(b):** (i) The Mean stray field strength across the entire surface for each of 336 frames (in black) and the Applied x-axis field strength (in red). (ii) The percentage area coverage of each greyscale level across the entire scan for each of 336 frames. (iii) The Mean Stray field strength plotted against the Applied x-axis field strength. [Page 193](#)

**Figure 8.8:** Filmstrip representation of the  $10 \times 10 \times 0.1 \text{ mm}^3$  dynamic scan of Coated 3% Si Grain-Oriented Steel subjected to a 3kHz oscillating x-axis field(@  $0.1 \times 0.1 \times 0.05 \text{ mm}^3/\text{pixel}$ ). The full animation is provided in *Chapter 8.7z* ([page ix](#)). The colour representation of the  $\underline{H}$  stray field vector is provided. The  $H_z$  component ranges in magnitude  $\pm 350 \text{ A/m}$ . The  $H_x$  component ranges in magnitude  $\pm 530 \text{ A/m}$ . The background of each frame represents the Applied field ( $\pm 1.95 \text{ kA/m}$ , inverted greyscale). [Page 195](#)

List of Figures

## Chapter 1

# Introduction

The design and project overview for this research are presented. The motivation for its undertaking and the constraints within which the design was facilitated.

## 1.1 The Research Specification

*“Mapping the magnetic field intensity at the surface provides information about a material’s magnetic character as well as data relating to its physical state. This work will incorporate a state-of-the-art 3D scanning system to map out magnetic surface fields. The data will be used to construct detailed magnetic domain images on various magnetic samples. The work will involve developing LabView software to operate the scanner and produce quantitative surface measurements and magnetic domain images. This will provide a useful technique for studying magnetic domain processes in magnetic materials.”* – Dr. Turgut Meydan; Dr. Paul Williams

## 1.2 Aims of the Research

### 1.2.1 Initial Aims based on the Specification

The interest and motivation for undertaking this Engineering PhD, stemming from an MSc background in developing scanning techniques, has been in the hardware/software co-development of a scanning system, with the application of mapping, in three dimensions, the otherwise invisible stray magnetic fields known to emanate from the surface of magnetic materials. This aim is coupled with the opportunity to gain a thorough understanding of the origins of magnetism and the magnetic effect, and the opportunity to map and elucidate aspects of the stray fields, the three-dimensional shape and even the dynamics, which have not been previously observed.

Various magnetic samples have been studied with the scanner such as grain-oriented electrical steel and constructed planar coils and amorphous materials and those studies have aided the progressive development of the system over the course of the work.

The initial basic design specification for the Scanner system, based on the Research Specification, were to;

- a. Make use of the existing hardware that has been provided.
- b. Be controlled manually and automatically by an external NI LabView system.
- c. Correctly position the scanner head along three independent axis.
- d. Permit the user to confidently position a sensor in a chosen location.
- e. Guard against the scanner hardware exceeding its physical limits.
- f. Control the actions of the scanner in a systematic automated scan.
- g. Enable the user to define the automated scan in a simple way.
- h. Be adaptable, to allow any desired sensor to be physically attached.
- i. Position any attached sensor with a repeatable precision greater than the footprint of the provided sensor ( $2\ \mu\text{m} \times 4\ \mu\text{m}$ ).
- j. Acquire voltages inputs from sensors attached to the scanner head (in the range  $\pm 10.000\ \text{V}$ ) and store those values alongside the corresponding sensor position.
- k. Display and permit interrogation of those data in both raw form and in the form of a greyscale map, displaying the stored values into adjustable 8-bit levels.
- l. Enable the saving and loading of previous scans and the resulting data including the export of data in a form which can be understood and analysed externally.
- m. Operate for periods of days at a time without fault.

As the capabilities of the system developed, and the nature of the resulting data were better defined, these basic requirements were greatly augmented.

### **1.2.2 Enhanced Aims following the Review of Prior Literature**

After the review of prior literature, discussed in [Chapter 3](#), it was clear from the outset that there are plentiful readily available commercial systems for the basic observation of surface domains in materials, utilising magneto-optical techniques [1] and that the company which manufacture the provided magnetics sensor, *Micromagnetics*, produce themselves a commercial scanning system with the TMR-020 sensor, the CS1000, for which the TMR-020 sensor was itself developed [2]. Other academic scanner systems

also already make use of the resolution available with the sensor [4] for basic two dimensional domain observation.

If the aim of this work was simply to produce the best basic domain observation possible, then that aim would be better served by these and other existing systems. But these systems are not available in the department, and are prohibitively expensive, and so it became a fundamental part of the design specification of this project to produce a useful and simple to use scanner within the boundaries of the existing equipment available in the department, including motion control hardware which is not servo-motor based.

The major part of this work has focused on how to solve the engineering issues imposed by the limitations of the available equipment (discussed in [Chapter 4](#)), and how to solve the software issues imposed by the increasing size and complexity of data as the capabilities of the system developed (discussed in [Chapter 5](#)). The software development of the Scanner Control software follows the evolution of the capabilities of the scanner.

The basic scanning functionality was achieved with Scanner Control 1 and results of this basic functionality are presented in [Chapter 6](#) and compared against other existing methods of basic domain observation.

As mentioned, in general, obtaining these basic domain observations are better served by existing commercial systems if available. However, these commercial systems do not allow for investigation of the three-dimensional shape of the stray fields as they emerge from a sample surface and close on other domains, or interact with external factors.

Developing a 3D scanning system is the titular design criteria of the project. The study of the three-dimensional shape of domain based stray fields, is an important active area of research which has not been previously investigated using high-resolution

scanner based systems. In addition to the gaining of new knowledge about the extent and shape of stray fields, new sensors are being developed in the department [5, 6] which make use of the interaction between domains in magnetic materials and external control elements, which would benefit from observation of the structure of these stray fields.

Three-dimensional magnetic field structure above a sample cannot be studied with magneto-optical methods. Three-axis magnetic sensors are common but are generally of mm-scale resolution [7].  $\mu\text{m}$ -scale three-axis magnetic sensors do exist [8] but are developmental or prohibitively expensive. Again, with the defining design principle being making use of the equipment available, a novel tilting single-axis sensor technique has been developed to resolve the z and x axis components of stray fields; utilizing the STJ-020 TMR sensor provided. The results of this work required the development of the Scanner Control 2 system and are discussed in [Chapter 7](#).

The study of how domains change dynamically within a material exposed to an alternating external magnetic field is an active field of research with applications in power electronics and domain theory [9, 10]. Some attempts to produce dynamic domain observations with automated scanning systems exist [11]. The success of these attempts is limited and debatable, as discussed in [Chapter 3](#). The development of a scanning system to study the three-dimensional dynamics of the surface stray fields has not been previously undertaken within the available literature.

The development of Scanner Control 3 software was specifically to provide the novel capacity of scanning and observing the three dimensional shape of dynamic stray fields above a sample surface. First, positive observation of dynamic domain movement with the scanner system has been made and presented in [Chapter 8](#).

The thesis and work of the previous development stages culminates in the novel observation and analysis of dynamic three-dimension stray fields above a sample surface, presented in [Chapter 8](#).

## Chapter 2

**Background**

The physical origins of the magnetism and material magnetisation are discussed. A full understanding of the Magnetic Flux Density vector-field  $\underline{\mathbf{B}}$  is derived from the Lorentz transformation of the Coulomb force between two moving charges, developed further to the origin of the Applied Field  $\underline{\mathbf{H}}$  around a current carrying wire. Consequently, material magnetisation  $\underline{\mathbf{M}}$  and the magnetic characteristics of paramagnetic and ferrimagnetic elements are discussed, leading to an understanding of magnetic domain formation within crystalline and amorphous ferromagnetic alloys. Throughout, vector quantities are indicated by a bold underlined symbol eg.  $\underline{\mathbf{u}}$ . The scalar magnitude of  $\underline{\mathbf{u}}$  is then  $u$  whilst  $u_x$  is the magnitude of the x component of  $\underline{\mathbf{u}}$ .

**2.1 Foundations of Electromagnetism and Magnetization****2.1.1 Physical Origins of Magnetic Flux Density  $\underline{\mathbf{B}}$** 

Electromagnetism is one of the four fundamental forces of nature against which energy can be stored; the others being Gravitation and the Strong and Weak nuclear Forces. Electromagnetism and consequently magnetisation are both derived consequences of the relativistic transformation of the electrostatic (Coulomb) force [12] between electrical charges (most commonly electrons) when both are in motion.

The Coulomb force between two static point charges  $q_1$  and  $q_2$  with separation  $\underline{\mathbf{r}}$  is;

$$\underline{\mathbf{F}} = k \frac{q_1 q_2}{r^2} \hat{\underline{\mathbf{r}}} \quad \text{Equation 2.1}$$

where  $k = \frac{1}{4\pi\epsilon_0}$

and  $\epsilon_0$  is the *permittivity of free space*, equal to  $8.854 \times 10^{-12}$  F/m (to 4sf), discussed later (Section 2.1.4, page 23).

The unit vector  $\hat{\underline{\mathbf{r}}}$  becomes the radial vector  $\frac{\underline{\mathbf{r}}}{r}$  ( $r$  being the magnitude of  $\underline{\mathbf{r}}$ ) giving;

$$\underline{\mathbf{F}} = \frac{k q_1 q_2}{r^3} \underline{\mathbf{r}} \quad \text{Equation 2.2}$$

With a stationary source charge  $q_1$ , this law holds true for both a stationary and a moving test charge  $q_2$ , even if  $q_2$  approaches the speed of light.

In the case of a moving test charge Coulomb's law becomes;

$$\mathbf{F} = \frac{\gamma k q_1 q_2}{r^3} \mathbf{r} \quad \text{Equation 2.3}$$

with the Lorentz factor  $\gamma = \frac{1}{\sqrt{1 - v^2/c^2}}$  and represents the instantaneous force felt by the test charge as it moves past the stationary source. It is at first incongruous that the test charge  $q_2$  should instantaneously react to the source in a manner that recognises both direction and distance ( $\mathbf{r}$ ) without a light-travel-time delay. However the full treatment of the case given by A. P. French [13] demonstrates how this does not violate Special Relativity, and is in fact a consequence of it.

The case relevant to magnetism is where both the source ( $q_1$ ) and test ( $q_2$ ) charges are in motion. “The Coulomb force law is a complete statement of the force exerted on a charged particle, moving or stationary, by *stationary* charges. The magnetic force is associated with *moving source charges*... What appears as a magnetic field in one coördinate system is nothing else but an electric field when viewed in some other coördinate system.” [13]



This can be demonstrated with the following two cases.

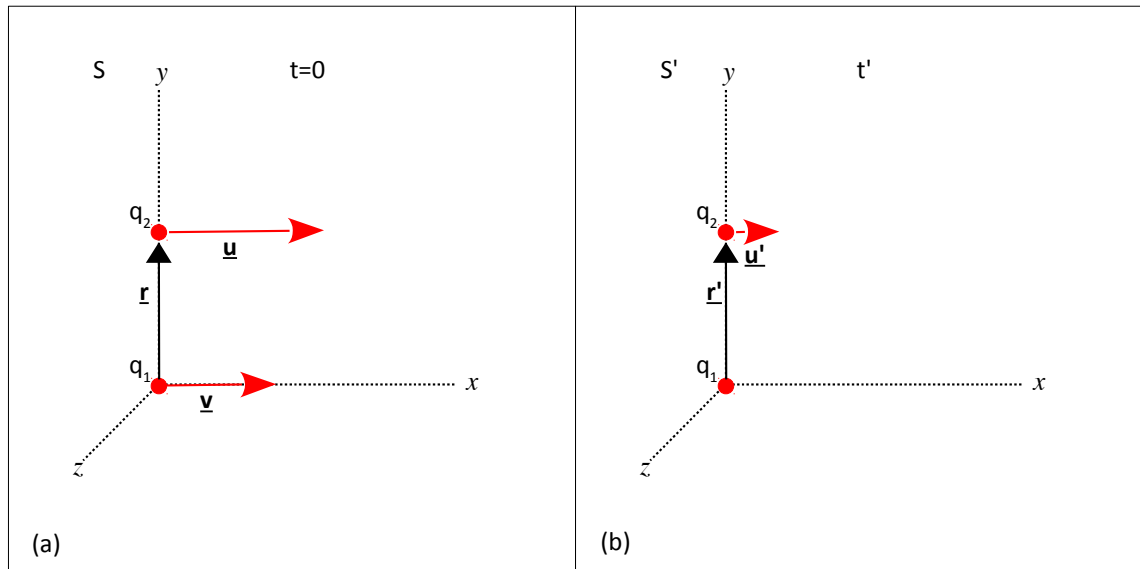


Figure 2.1: An illustration of the situation of two charges  $q_1$  and  $q_2$  travelling parallel to each other at different speeds. (b) is (a) transformed into the rest frame,  $S'$ , of  $q_1$ .

In [Figure 2.1\(a\)](#) frame  $S$  is chosen for the velocity of  $q_1$  ( $\underline{v}$ ) to travel along the  $x$ -axis, at time  $t=0$  when  $q_1$  and  $q_2$  are aligned on the  $y$ -axis. Thus,

$$\underline{r}=[0, y, 0] \quad , \quad \underline{v}=[v_x, 0, 0] \quad \text{and} \quad \underline{u}=[u_x, 0, 0]$$

Transforming into the rest frame of  $q_1$ ,  $S'$  ([Figure 2.1\(b\)](#)), permits the Coulomb force ([Equation 2.2](#)) on  $q_2$  by the now stationary  $q_1$  to be expressed as;

$$\underline{F}' = \frac{\gamma k q_1 q_2}{r'^3} \underline{r}' \quad \text{Equation 2.4}$$

where  $\underline{r}'=[0, y', 0]$  and  $r'=\sqrt{y'^2}$  meaning

$$F_x' = 0 \quad F_y' = \frac{k q_1 q_2}{y'^2} \quad F_z' = 0$$

To transform the Coulomb force back into  $S$  the Lorentz transformations needed are;

$$\underline{F} = \frac{1}{1 + v u_x' c^{-2}} \begin{bmatrix} F_x' + (v c^{-2})(\underline{F}' \cdot \underline{u}') \\ F_y' \gamma^{-1} \\ F_z' \gamma^{-1} \end{bmatrix} \quad \text{Equation 2.5}$$

where  $v$  is the magnitude of  $\underline{v}$  and  $\underline{u}'=[u_x', 0, 0]$  with  $u_x' = \frac{u_x - v}{1 - v u_x c^{-2}}$

These transformations are well established and a derivation is provided in [\[13\]](#).

The transformation of the coulomb force from  $\underline{F}'$  back to  $\underline{F}$  proceeds as;

$$\text{with } (\underline{F}' \cdot \underline{u}') = F'_x u'_x + F'_y u'_y + F'_z u'_z ; \\ = 0$$

$$F_x = \frac{1}{1 + v u'_x c^{-2}} [0 + 0]$$

$$= 0$$

whilst,

$$F_y = F'_y \gamma^{-1} (1 + v u'_x c^{-2})^{-1} \\ = k q_1 q_2 y'^{-2} \gamma^{-1} (1 + v u'_x c^{-2})^{-1}$$

then with  $y' = y$  and the transformations from [Equation 2.5](#);

$$F_y = k q_1 q_2 y'^{-2} \gamma^{-1} \left( 1 + v c^{-2} \frac{u'_x - v}{1 - v u'_x c^{-2}} \right)^{-1} \\ = k q_1 q_2 y'^{-2} \gamma^{-1} \left( \frac{1 - v u'_x c^{-2} + v u'_x c^{-2} - v^2 c^{-2}}{1 - v u'_x c^{-2}} \right)^{-1} \\ = k q_1 q_2 y'^{-2} \gamma^{-1} \left( \frac{1 - v^2 c^{-2}}{1 - v u'_x c^{-2}} \right)^{-1} \\ = k q_1 q_2 y'^{-2} \gamma^{-1} \left( \frac{1 - v u'_x c^{-2}}{1 - v^2 c^{-2}} \right)$$

and remembering  $\gamma = \frac{1}{(1 - v^2/c^2)^{1/2}}$  then  $\gamma^{-1} = (1 - v^2 c^{-2})^{1/2}$  so;

$$F_y = k q_1 q_2 y'^{-2} \frac{(1 - v^2 c^{-2})^{1/2} (1 - v u'_x c^{-2})}{(1 - v^2 c^{-2})} \\ = k q_1 q_2 y'^{-2} \frac{1}{(1 - v^2 c^{-2})^{1/2}} (1 - v u'_x c^{-2}) \\ = k q_1 q_2 y'^{-2} \gamma (1 - v u'_x c^{-2})$$

with the result;

$$F_y = \frac{\gamma k q_1 q_2}{y^2} \left( 1 - \frac{v u_x}{c^2} \right)$$

and

$$F_z = 0$$

Equations 2.6

It can be seen that after the transformation,  $F_y$  (Equations 2.6) comprises two components;

the normal Coulomb force,

$$F_{y_1} = \frac{\gamma k q_1 q_2}{y^2}$$

and what becomes the magnetic effect,

$$F_{y_2} = \frac{v u_x}{c^2} \frac{\gamma k q_1 q_2}{y^2}$$

which can be seen to be proportional to the speed of both  $q_1$  and  $q_2$ .

Significantly in this case, this additional force derived purely from the transformation of the coulomb force between frames, acts parallel to the  $y$ -axis; perpendicular to the velocity of the test charge  $\underline{u}$ .

In the second case the velocity of  $q_2$  is set perpendicular to  $q_1$ , as illustrated in Figure 2.2. Frame  $S$  is chosen for the velocity of  $q_1$  ( $\underline{v}$ ) to travel along the  $x$ -axis with the test charge  $q_2$  some displacement  $\underline{r}$  from the source travelling parallel to the  $y$ -axis with velocity  $\underline{u}$ .

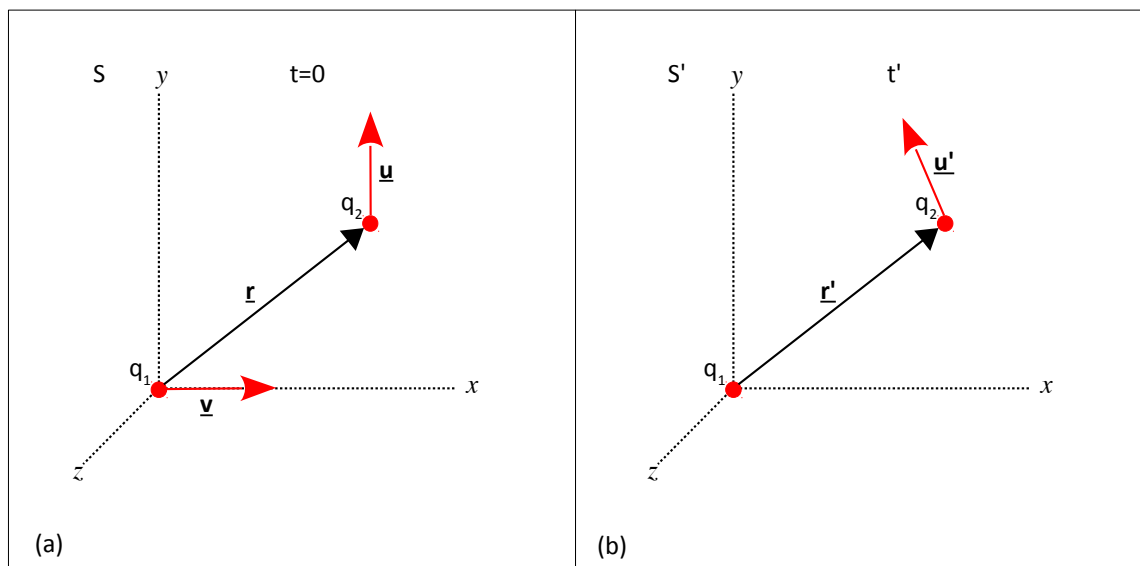


Figure 2.2: An illustration of the situation of two charges  $q_1$  and  $q_2$  travelling perpendicular to each other at different speeds. (b) is (a) transformed into the rest frame,  $S'$ , of  $q_1$ .

In this case,

$$\mathbf{r}=[x, y, 0] \quad , \quad \mathbf{v}=[v_x, 0, 0] \quad \text{and} \quad \mathbf{u}=[0, u_y, 0]$$

Again transforming into the rest frame of  $q_1$ ,  $S'$  (Figure 2.2(b)), permits the coulomb force on  $q_2$  by the now stationary  $q_1$  (Equation 2.2) to be expressed, with

$$\mathbf{r}'=[x', y', 0] \quad \text{and} \quad r'=\sqrt{x'^2+y'^2} \quad , \quad \text{to give;}$$

$$F_x'=\frac{kq_1q_2x'}{r'^3} \quad F_y'=\frac{kq_1q_2y'}{r'^3} \quad F_z'=0$$

Using the previous Lorentz transformation for the Coulomb force (Equation 2.5) and the additional transformations [13];

$$u_x'=\frac{u_x-v}{1-vu_x/c^2} \quad , \quad u_y'=\frac{u_y\gamma^{-1}}{1-vu_x/c^2} \quad \text{and} \quad u_z'=\frac{u_z\gamma^{-1}}{1-vu_x/c^2}$$

$$x'=y(x-vt) \quad , \quad y'=y \quad \text{and} \quad z'=z$$

then at  $t=0$  and with  $u_x=0$  ,

$$x'=yx \quad , \quad y'=y \quad r'=\sqrt{y^2x^2+y^2}$$

$$u_x'=-v \quad , \quad u_y'=u_y\gamma^{-1} \quad \text{and} \quad u_z'=0$$

and the transformation from  $\mathbf{F}'$  back to  $\mathbf{F}$  proceeds as;

$$\text{with} \quad (\mathbf{F}' \cdot \mathbf{u}')=F_x'u_x'+F_y'u_y'+F_z'u_z'$$

$$=\frac{kq_1q_2x'}{r'^3} \cdot -v + \frac{kq_1q_2y'}{r'^3} u_y\gamma^{-1} + 0$$

$$=\frac{kq_1q_2x'}{r'^3} (yu_y\gamma^{-1}-yxv)$$

then;

$$F_x=(1+vu_x'c^{-2})^{-1} [F_x'+(vc^{-2})(\mathbf{F}' \cdot \mathbf{u}')] ]$$

$$=(1+vu_x'c^{-2})^{-1} \left[ \frac{kq_1q_2yx}{r'^3} + \frac{kq_1q_2}{r'^3} (yu_y\gamma^{-1}-yxv)(vc^{-2}) \right]$$

and remembering  $\gamma=(1-v^2c^{-2})^{-1/2}$

$$=y^2 \frac{kq_1q_2}{r'^3} [\gamma x + yu_y\gamma^{-1}vc^{-2} - \gamma xv^2c^{-2}]$$

$$=y^2 \frac{kq_1q_2}{r'^3} [\gamma x(1-v^2c^{-2}) + yu_y\gamma^{-1}vc^{-2}]$$

$$\begin{aligned}
&= \gamma^2 \frac{k q_1 q_2}{r'^3} [\gamma x \gamma^{-2} + \gamma^{-1} y u_y v c^{-2}] \\
&= \gamma^2 \frac{k q_1 q_2}{r'^3} \gamma^{-1} (x + y u_y v c^{-2})
\end{aligned}$$

with the result;

$$F_x = \gamma \frac{k q_1 q_2}{r'^3} \left( x + \frac{v u_y}{c^2} y \right)$$

$$\begin{aligned}
F_y &= (1 + v u_x' c^{-2})^{-1} F_y' \gamma^{-1} \\
&= (1 - v^2 c^{-2})^{-1} \frac{k q_1 q_2 y'}{r'^3} \gamma^{-1} \\
&= \gamma^2 \frac{k q_1 q_2}{r'^3} y \gamma^{-1} \\
&= \frac{\gamma k q_1 q_2}{r'^3} y
\end{aligned}$$

and

$$F_z = 0$$

Equations 2.7

Once again an additional term, this time in  $F_x$  (Equations 2.7), has formed due to the transformation between frames. Remembering that  $r' = \sqrt{\gamma^2 x^2 + y^2}$ , then  $F_x$  contains the expected Coulomb force;

$$F_{x_1} = \frac{\gamma k q_1 q_2}{(\gamma^2 x^2 + y^2)^{3/2}} x$$

and

$$F_{x_2} = \frac{\gamma k q_1 q_2}{(\gamma^2 x^2 + y^2)^{3/2}} \frac{v u_y}{c^2} y \quad \text{Equation 2.8}$$

This time the magnetic effect acts along the x-axis. It is again perpendicular to the velocity of  $q_2$  and proportional to the speed of both the source and test charges. These two cases have been chosen as examples with solvable algebra but it is asserted [13] and demonstrated by experiment [14, 15] that the conclusions found hold true for all velocity and displacement vectors.

The additional force created by the magnetic effect, the transformation of the static Coulomb force into the frame in which both source and test charge are in motion, is *always*;

1. proportional to the product of the charges,  $q_1q_2$ .
2. proportional to the product of the speeds,  $uv$ .
3. perpendicular to the velocity of the test charge,  $\mathbf{u}$ .

To ensure that the force is always perpendicular to  $\mathbf{u}$ , in a more generalised expression, a mathematical construct can be used where the force can be expressed as the cross-product of  $\mathbf{u}$  with some other vector quantity. The cross product,  $\mathbf{a} \times \mathbf{b}$ , produces a vector that is perpendicular to both  $\mathbf{a}$  and  $\mathbf{b}$  with a direction given by the *right-hand-grip-rule* and a magnitude equal to the area of the parallelogram that the vectors span. If the vector  $\mathbf{b}$  is *chosen* to also be perpendicular to  $\mathbf{a}$ , such that the vectors span a rectangle, then the magnitude of the cross-product becomes simply the product of the magnitudes  $a$  and  $b$ .

Re-arranging Equation 2.8 as;

$$F_{x_2} = q_2 u_y \frac{\gamma k q_1}{r'^3} \frac{v y}{c^2}$$

the force from the magnetic effect when generalised becomes;

$$F_{x_2} = q_2 \mathbf{u} \times \mathbf{B} \quad \text{Equation 2.9}$$

where the constructed vector  $\mathbf{B}$  has the magnitude;

$$B = \frac{\gamma k q_1}{r'^3} \frac{v y}{c^2} \quad \text{Equation 2.10}$$

and is *defined* as perpendicular to  $\mathbf{u}$ .

The vector quantity  $\mathbf{B}$  is part of an orthogonal mathematical construction which ensures  $F_{x_2}$  is perpendicular to  $\mathbf{u}$ . However, it is useful in itself and can be used to generalise for the behaviour of a test charge where the response is due to the cumulative effects of many sources.

To do this it is necessary to define  $\underline{\mathbf{B}}$  independently of  $F_{x_2}$  and  $\underline{\mathbf{u}}$ . To describe  $\underline{\mathbf{B}}$  as a quantity from which an unknown  $F_{x_2}$  can be determined, rather than as a value chosen to match what  $F_{x_2}$  is known to be.

The solution is again suggested by the orthogonality of the simple cases chosen in [Figures 2.1](#) and [2.2](#) and is asserted [[13](#)] and proven experimentally [[14](#), [15](#)] to be true generally. The product  $v y$  in the rearranged [Equation 2.8](#) has exactly the magnitude of the cross-product  $\underline{\mathbf{v}} \times \underline{\mathbf{r}}$ . Thus, by developing a second set of orthogonal vectors based on the velocity of the source charge,  $\underline{\mathbf{v}}$ , and the displacement from it,  $\underline{\mathbf{r}}$ , a correct description of  $\underline{\mathbf{B}}$  in both magnitude and direction is;

$$\underline{\mathbf{B}} = \frac{1}{c^2} \underline{\mathbf{v}} \times \left( \frac{\gamma k q_1}{r^3} \underline{\mathbf{r}} \right) \quad \text{Equation 2.11}$$

Combining the components of [Equations 2.7](#) and [Equation 2.9](#) the total force on a moving test charge from a moving source charge can be written as;

$$\underline{\mathbf{F}} = \frac{\gamma k q_1 q_2}{r^3} \underline{\mathbf{r}} + q_2 \underline{\mathbf{u}} \times \underline{\mathbf{B}} \quad \text{Equation 2.12}$$

with  $\underline{\mathbf{B}}$  as just described ([Equation 2.11](#)).

In physics, a force-field is a construct that allows discussion of the force felt by a test particle (which accelerates under action of the force) at a particular point in space. Fields are used as an intermediary culmination when it is impractical to determine the individual contributions from many sources and a generalised description of the overall effect on the test particle is preferable.

For the electrostatic force the force between two charges can be generalised to the force on a test charge  $q_2$ ,

$$\underline{F} = q_2 \underline{\epsilon} \quad \text{where} \quad \underline{\epsilon} = \sum_{\text{all } n} \frac{\gamma k q_n \underline{r}_n}{r_n^3} \quad \text{Equation 2.13}$$

and is referred to as the electric field.  $\underline{\epsilon}$  is a genuine force-field in that the vector  $\underline{\epsilon}$  represents the direction and magnitude of the acceleration of the test particle. Both [Equations 2.11](#) and [2.12](#) contain expressions which can be substituted by the electric field  $\underline{\epsilon}$ .

[Equation 2.11](#) can be rewritten as,

$$\underline{B} = \frac{1}{c^2} \underline{v} \times \underline{\epsilon} \quad \text{Equation 2.14}$$

and consequently [Equation 2.12](#) as,

$$\underline{F} = q_2 \underline{\epsilon} + q_2 \underline{u} \times \underline{B} \quad \text{Equation 2.15}$$

[Equation 2.15](#) is known as the Lorentz force. The force on a test charge  $q_2$  moving in an electric field  $\underline{\epsilon}$  and “magnetic field”  $\underline{B}$ . Because  $\underline{B}$  also has the effect of causing an acceleration of the test charge, it is often considered as a force-field itself, as in the above definition of the Lorentz force. However, remembering that  $\underline{B}$  is only a vector-field representing the result of the frame-transformation and does not directly originate from a physical force,  $\underline{B}$  is more correctly called the Magnetic Flux Density. The term Magnetic Flux is introduced to describe and illustrate the constructed vector-field. Unfortunately, historically the terms Magnetic Flux Density, Magnetic Flux and Magnetic Field are often confused and used interchangeably.



It has already been seen (Equation 2.11) that  $\mathbf{B}$  has the magnitude,

$$\mathbf{B} = \frac{\gamma k q_1 v y \hat{\mathbf{i}}}{r^3 c^2}$$

Given  $\gamma$  is a unit-less factor and the permittivity of free space  $\epsilon_0$  is equal to  $8.854 \times 10^{-12}$  F/m (to 3dp.) with a Farad (F) defined as Coulomb per Volt (  $C/V = C^2/J = C^2/Nm$  ) then the units of  $\mathbf{B}$  can be seen to be;

$$\text{units} = \frac{NmC}{C^2 m^3} \frac{m s^{-1} m}{m^2 s^{-2}} m$$

which simplify to,

$$T = \frac{N \cdot s}{C \cdot m}$$

The units Newton.second per Coulomb.metre are collectively called a Tesla (T). A particle carrying a charge of one Coulomb, and moving perpendicularly through a magnetic field of one Tesla, at a speed of one metre per second, experiences a force from the Lorentz force (Equation 2.15) with magnitude of one Newton.

### 2.1.2 Physical Origins of Applied Magnetic Field $\underline{H}$

If the source electrons are confined to move in one direction along a current carrying wire then the effect on a negative test charge  $q_t$  is illustrated in [Figure 2.3](#).

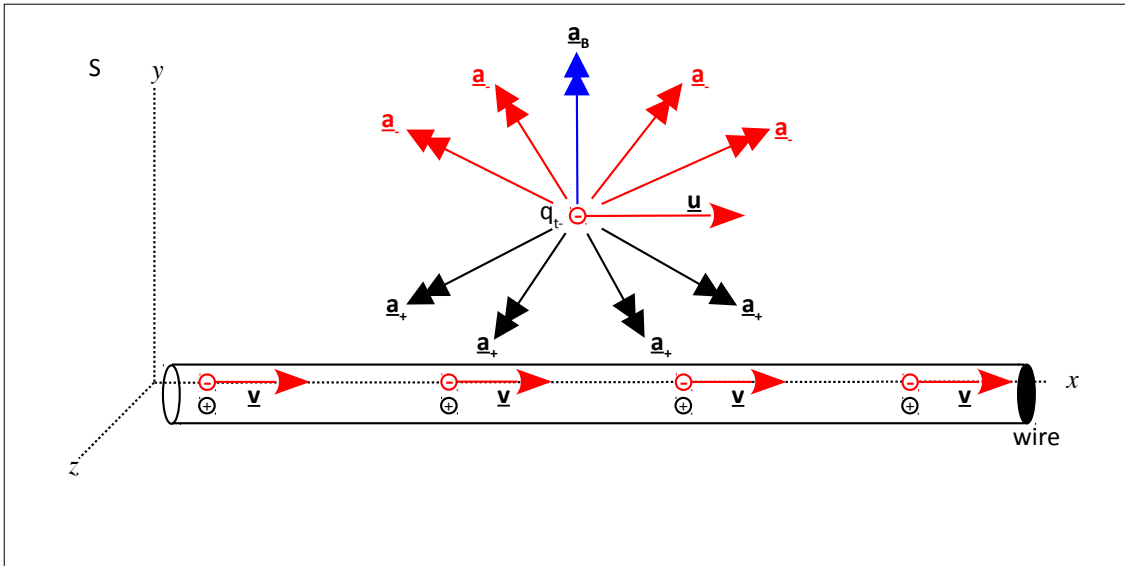


Figure 2.3: An illustration of the forces experienced by a test electron  $q_t$  from the electrons and protons in a current carrying wire. The direct Coulomb acceleration from the electrons ( $\underline{a}_e$ ) is exactly balanced by that from the protons ( $\underline{a}_p$ ), the wire being electrostatically neutral. The only remaining acceleration is the cumulative magnetic effect from each moving source electron ( $\underline{a}_B$ ), in each case perpendicular to the velocity of the test charge.

A conducting wire, even a current carrying wire, is to a very great approximation electro-statically neutral. The negative test charge  $q_t$  is repulsed by all the moving and static electrons in the wire and attracted by all the positive protons in the atoms of the wire. To a very fine approximation the Coulomb force from each source electron is equally balanced by the Coulomb force from each source proton. Though exaggerated in [Figure 2.3](#), the distance of the test charge  $q_t$  from the wire is very much greater than the difference in relative position of the charges in the wire. The positional differences are negligible. The Coulomb force between the test charge and the moving source electrons is equal in magnitude to the Coulomb force between the test charge and the stationary atomic protons, but opposite in sign. However, as the electrons in the wire are a moving source they also produce a magnetic effect which causes an additional acceleration to the test charge. Because the protons in the wire are stationary they

produce no such magnetic effect to counter it. Whilst the magnetic effect on the test charge from only one electron travelling through the wire at the electron drift velocity is tiny, each of the multitude of electrons in the wire produce this effect. Crucially, the effect from each electron, irrespective of its relative position, is *always perpendicular to the direction of the test charge velocity*. Thus, the acceleration on the test charge caused by the magnetic effect from each and every moving source electron (all moving in the same direction along the wire) accumulate to an appreciable and measurable force which is not cancelled out by anything from the stationary protons.

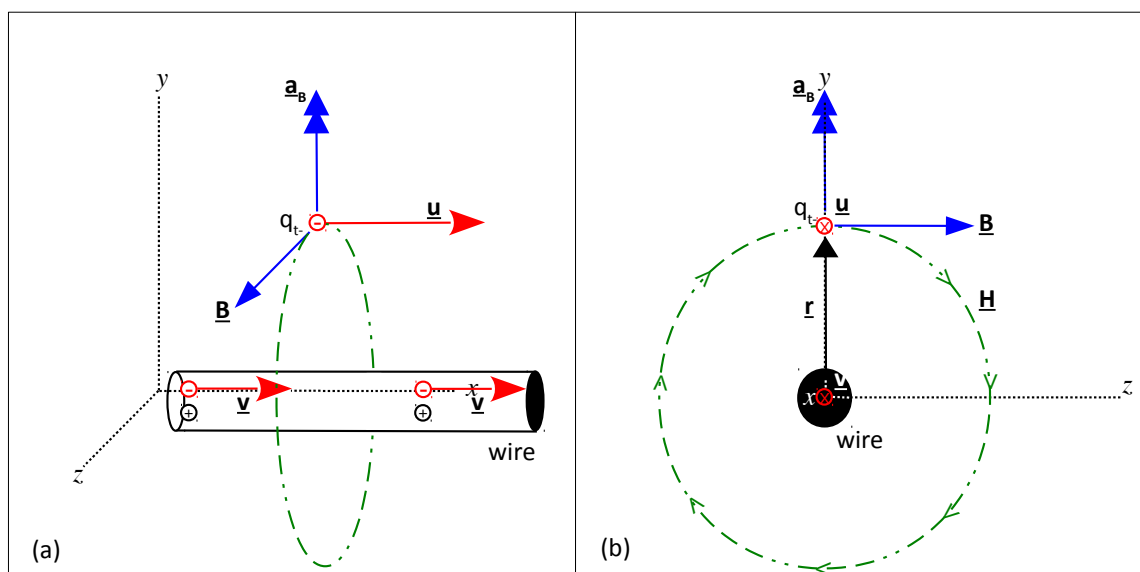


Figure 2.4: (a) The test charge  $q_t$  experiences an acceleration  $\mathbf{a}_B$  radially away from a current carrying wire it is travelling parallel to. The constructed vector-field  $\mathbf{B}$  is perpendicular to both  $\mathbf{u}$  and  $\mathbf{a}_B$ . The acceleration  $\mathbf{a}_B$  is said to be a response to the local magnetic flux density  $\mathbf{B}$ . (b) The acceleration of the test particle travelling parallel to the wire at distance  $r$  is always radial from the wire, thus the constructed magnetic flux density at any point radial to the wire is always tangential to a circle of radius  $r$ . That circle can be considered the vector-field of the magnetic effect produced by the current carrying wire and is termed the Applied Magnetic Field  $\mathbf{H}$ .

As [Figure 2.4\(a\)](#) illustrates, the test charge experiences an acceleration radially away from a current carrying wire it is travelling parallel to. The constructed  $\mathbf{B}$ -field is perpendicular to both  $\mathbf{u}$  and  $\mathbf{a}_B$ . The acceleration  $\mathbf{a}_B$  is said to be a response of a moving test charge to the local magnetic flux density  $\mathbf{B}$ . The acceleration of the test particle travelling parallel to the wire at distance  $r$  is always radial from the wire, thus the constructed magnetic flux density at any point radial to the wire is always tangential to

the circle of radius  $r$  (Figure 2.4(b)). That circle can be considered the vector-field of the magnetic effect produced by the current carrying wire and is termed the Applied Magnetic Field  $\underline{H}$ . The magnitude of the Applied Magnetic Field is defined by the velocity of the source electrons (related to the current passing through the wire) and the distance  $r$  from the wire, and is thus defined in the units of Amps per meter. An Applied Magnetic Field  $\underline{H}$  of  $1/2\pi \text{ Am}^{-1}$  is produced at a radial distance of 1 metre from a wire carrying a current of 1 Amp. The direction of the field is tangential to the 1 metre radius circle in the direction given by the *right-hand-grip-rule*.

If the single test electron in Figure 2.4(a) is replaced by an ensemble of electrons travelling parallel to the source wire and each other, in another current carrying wire, then the cumulative acceleration on each electron produces a combined acceleration on the wire (Figure 2.5).

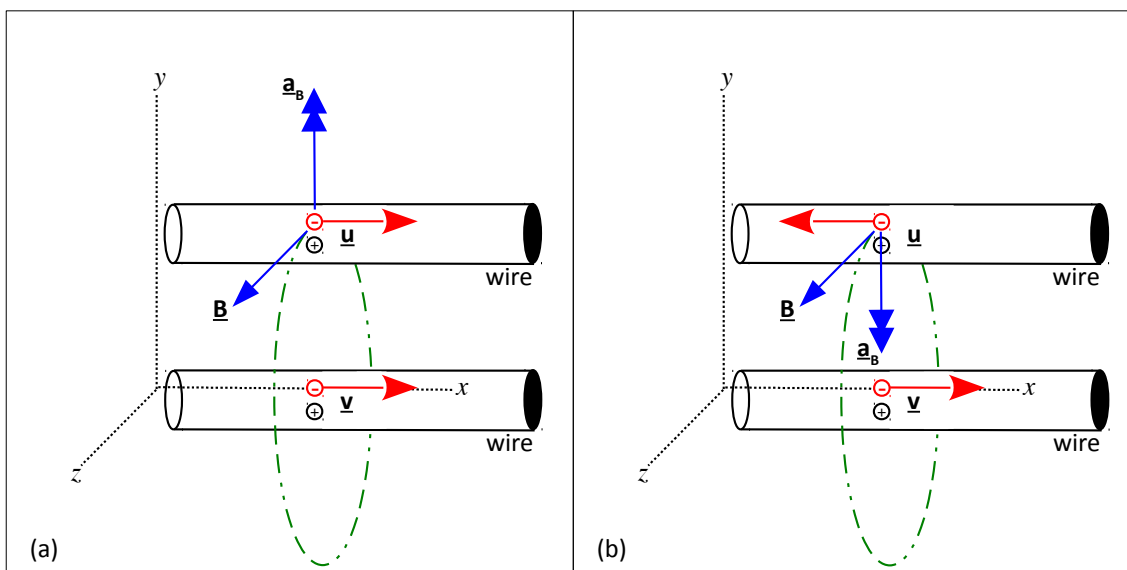


Figure 2.5: (a) Two parallel wires with electrons travelling in the same direction experience a repulsive acceleration. (b) Two parallel wires with electrons travelling in opposite directions experience an attractive acceleration. In both cases the acceleration is solely the result of the magnetic effect of the two sets of moving electrons. Both wires are electro-statically neutral.

The discussion until now has concerned the actions and effects of negative source charges on negative test charges (the electrons). It is an historic artefact that *conventional* current, defined for the direction of positively charged ions in

electrochemical solution before the discovery of electron, is by definition opposite in direction to the true motion of the electrons in a current carrying wire. Henceforth and by convention, the direction of the Applied Magnetic field  $\underline{H}$  and the Magnetic Flux density are reversed to correspond to the direction of *conventional* current and the action of a positive charge in a  $\underline{B}$ -field. Figure 2.5 becomes Figure 2.6.

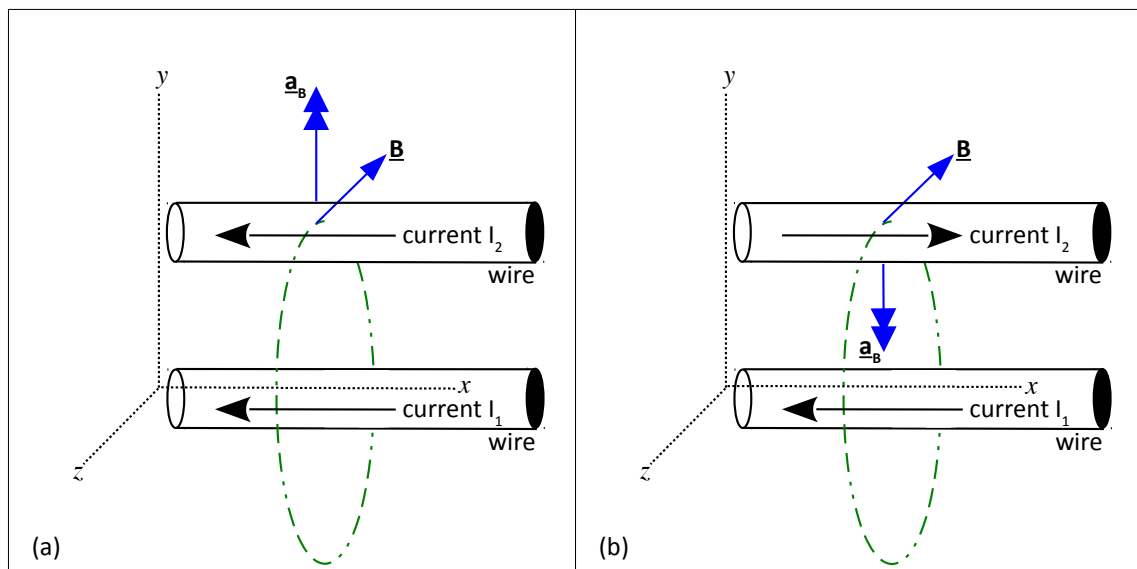


Figure 2.6: (a) Two parallel wires with parallel current experience a repulsive acceleration. (b) Two parallel wires with anti-parallel current experience an attractive acceleration. In both cases the acceleration is solely the result of the magnetic effect. Both wires are electro-statically neutral.

If the electrons are forced to travel in a loop (by producing loops of wire, or repeatedly stacking loops to form a coil) then the resultant magnetic force from each electron's path will sum to produce a combined force perpendicular to the plane of the loop and parallel to the axis of the loop or coil, as illustrated in Figure 2.7. The applied field at any point within the loop is a culmination of applied fields from every point on the loop, in proportion to the distance from the wire (as in Figure 2.4(b)). The centre of the loop receives equal contribution from all parts of the loop. As a test charge is moved away from the centre the increase in field from the edge it approaches is exactly matched by the decrease in field contribution from the diametrically opposed edge. Thus the applied field within a loop is uniform. The Magnetic Moment  $\underline{m}$  is defined as the vector perpendicular to the loop, as illustrated in Figure 2.7(a).

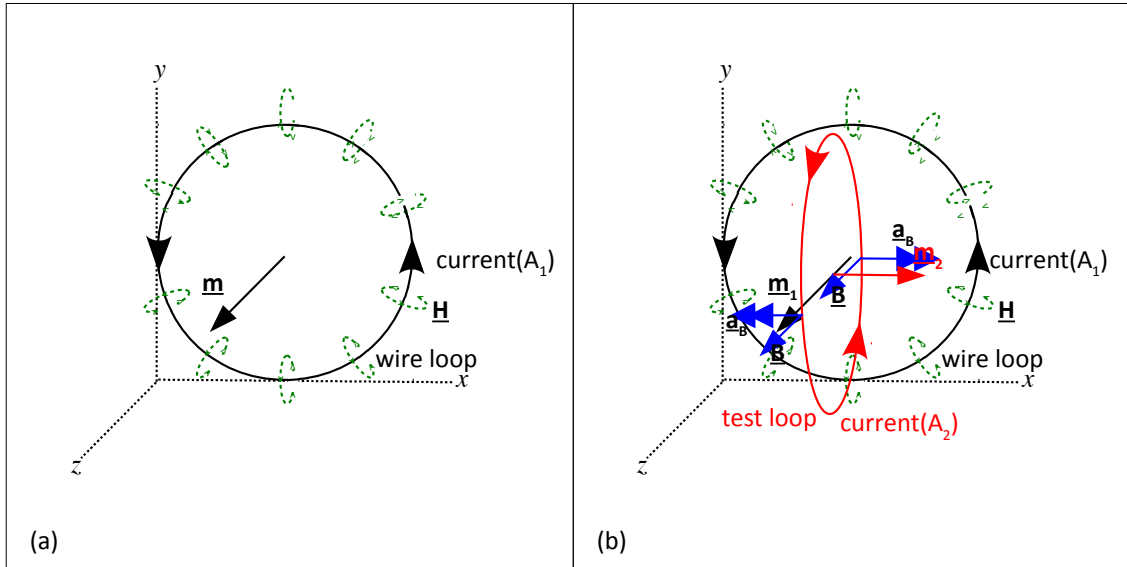


Figure 2.7: (a) The Magnetic Moment  $\underline{m}$  is defined as the vector perpendicular to the current loop, the result of the culmination of the Applied Magnetic Field  $\underline{H}$  within the loop, thus proportional to the current and radius of the loop. (b) A test loop whose Magnetic Moment  $\underline{m}_2$  is misaligned with  $\underline{m}_1$  will feel the acceleration  $\underline{a}_B$  necessary to rotate and translate until  $\underline{m}_1$  and  $\underline{m}_2$  are coincident.

If a second, “test loop” is placed with a Magnetic Moment ( $\underline{m}_2$ ) in a different direction to the magnetic moment of the original loop ( $\underline{m}_1$ ) (as illustrated in Figure 2.7(b)) then the edges of the test loop feel an acceleration  $\underline{a}_B$  from the local resultant  $\underline{B}$ -field, a consequence of the Applied Field  $\underline{H}$ , in a combination of directions that rotate the test loop until  $\underline{m}_2$  is coincident with  $\underline{m}_1$ . If neither loop is fixed then both will rotate and translate until  $\underline{m}_1$  and  $\underline{m}_2$  are coincident. If some physical restriction prevents coincidence then the loops will rotate and translate until they are as close to coincidence as possible, which is an energy minimizing phenomenon. As the applied field  $\underline{H}$  is uniform everywhere within the loop then the radius of the loop has no effect on the magnitude of  $\underline{H}$  within the loop, and hence the magnitude of the Magnetic Moment  $\underline{m}$  is dependent only on the current in the loop, the velocity of the electrons around the loop, or crucially; the *Angular Momentum* of the electrons as they are forced around the loop by the electrostatic boundaries formed by the stationary protons in the wire. The Magnetic Moment  $\underline{m}$  has a magnitude dependent on the Angular Momentum of the electrons in the current loop and a direction perpendicular to the plane of that Angular Momentum.

### 2.1.3 Physical Origins of Material Magnetization **M**

The magnetic moment is inextricably linked to the angular momentum of the electrons. The vector is perpendicular to the plane of angular rotation and is of a magnitude proportional to the magnitude of the momentum. This angular momentum can be macroscopic, as with many electrons travelling through a loop of wire. However, the electrons also have angular momentum on the atomic (atomic orbital momentum) and subatomic (electron spin) scales. At the atomic and subatomic quantum mechanical scales the two electron momenta are discrete harmonic quantities of the bound electron wave, related by a spin-orbit coupling factor [16]. It is the interplay of these two angular momenta which result in the atomic magnetic moment of the electrons, the protons and thus ultimately the atoms in a material.

The challenges involved in describing the ensemble effects of the complex interplay of electron spin and orbit coupling, coupling to the other atomic electrons, and coupling to the protons in the nucleus (which themselves have a spin) are extensive. The formal discussion of the quantum mechanics involved are summarised in van Vleck's Nobel lecture article "Quantum Mechanics: The Key to Understanding Magnetism" [17] quoting his seminal work [16] and the work of Tyablikov [18]. From this strict quantum mechanical treatment the smallest discrete quanta of atomic magnetic moment, the Bohr Magneton  $\beta$ , is defined;

$$\beta = \frac{eh}{4\pi m_e c} = 9.274009994(57) \times 10^{-24} J/T \quad \text{Equation 2.16}$$

where,  $e$  is the charge on an electron,  $h$  is the Plank constant,  $m_e$  is the electron rest mass and  $c$  is the speed of light.

By the nature of subatomic physics, the magnitude of the magnetic moment of an atom will be an integer multiple of  $\beta$ . The cumulative vector-field produced by the ensemble of atomic magnetic moment magnitudes and directions in a material is termed the material's Magnetisation **M**.

The collective Magnetization field  $\mathbf{M}$  of a material is the cumulative effect of the ensemble of atomic magnetic moments coupled with the molecular (crystalline) structure of the material, a complex multi-body problem. Materials made of atoms with filled electron shells have a total moment of zero, because the electrons all exist in pairs with opposite mutually cancelling spins. Only atoms with partially filled shells (unpaired spins) can have a net magnetic moment. When two nearby atoms have unpaired electrons, the parallel or antiparallel states of the electron spins affects whether the electrons can share the same orbit, as a result of the Pauli exclusion principle. When the orbitals of unpaired outer valence electrons from adjacent atoms overlap, the magnetic interaction due to magnetic moment orientation will tend to align the moments antiparallel. However, the distributions of the electron's electric charge in space is farther apart when the electrons have parallel spins than when they have opposite spins, a difference called the *exchange energy*, so the parallel-spin state is more stable [19]. In some materials this energy difference can be orders of magnitude larger than the energy differences associated with the magnetic moment interaction and these are the materials which exhibit the greatest magnetic properties (*magnetic materials*). For example, in iron the exchange force is about one thousand times stronger than the magnetic moment interaction [19].

With recent advances in computing power, efforts at fundamental “micromagnetic” modelling have been made [20, 21, 22, 23, 24] but more commonly the observable collective magnetic behaviour of a material has been the subject of empirical investigation and experimental measurement (discussed in the review of literature, Chapter 3) which can be described and tabulated as a set of material properties, discussed further in Section 2.2.1, page 25.

The degree of material Magnetisation  $\mathbf{M}$  occurring for a given applied field  $\mathbf{H}$  is represented by the dimensionless ratio  $\chi_m$  - the *magnetic susceptibility*.

$$\mathbf{M} = \chi_m \mathbf{H}$$

Equation 2.17



If, due to the material properties, the atomic magnetic moments align parallel with the applied field and amplify it then  $\chi_m > 0$  and the material is called *Paramagnetic*. If, due to the material properties, the atomic magnetic moments align in opposition to the applied field (anti-parallel) then the applied field through the material is suppressed,  $\chi_m < 0$  and the material is called *Diamagnetic*.

#### 2.1.4 The relationship between **B**, **H** and **M**

The Magnetic Flux density **B** is a constructed vector-field with magnitude measured in Tesla (Newton.second per Coulomb.metre) to which a moving test charge (or ensemble of test charges) is said to react, in a direction perpendicular to its velocity. The Applied Magnetic Field **H** has a magnitude measured in Amps per metre which is said to form a vector-field tangential to a circle of chosen radius around a current carrying wire. **B** is framed in the form of its effect on the test charges, whilst **H** is framed in the form of what is being produced by the source charges. They are not identical but are related.

In a vacuum they are related by a scaling factor  $\mu_0$  called the *permeability of free space*, thus;

$$\mathbf{B} = \mu_0 \mathbf{H} \quad \text{Equation 2.18}$$

$$\text{where } \mu_0 = 4\pi \times 10^{-7} \text{ N/A}^2 \times 1.00000000082(20)$$

As of 20<sup>th</sup> May 2019 [25] this has been determined by measurement, with units that relate the units of **B** to **H**. The units Newton per square Amp relate how the force on the test charge increases as the speed of the source charges increases.

The previously mentioned *permittivity of free space*,  $\epsilon_0$ , which relates the Coulomb force between two charges (Equation 2.1) is related to  $\mu_0$  by the universally constant speed of light,

$$c^2 = \epsilon_0 \mu_0 \quad \text{Equation 2.19}$$

c is defined equal to 299,792,458 m/s [25].

The overall magnetic flux density  $\underline{\mathbf{B}}$  within a material is a combination of the applied magnetic field  $\underline{\mathbf{H}}$  and the material magnetization  $\underline{\mathbf{M}}$ ,

$$\underline{\mathbf{B}} = \mu_0 (\underline{\mathbf{H}} + \underline{\mathbf{M}}) \quad \text{Equation 2.20}$$

and from Equation 2.17 this can be written as,

$$\begin{aligned} \underline{\mathbf{B}} &= \mu_0 (\underline{\mathbf{H}} + \chi_m \underline{\mathbf{H}}) \\ \underline{\mathbf{B}} &= \mu_0 (1 + \chi_m) \underline{\mathbf{H}} \\ \underline{\mathbf{B}} &= \mu_0 \mu_r \underline{\mathbf{H}} \end{aligned} \quad \text{Equation 2.21}$$

with  $\mu_r = (1 + \chi_m)$  termed the *relative permeability* of the material compared with vacuum, which is sometimes more usefully tabulated than just the *magnetic susceptibility*.

The magnetic flux density  $\underline{\mathbf{B}}$  within the bulk of a material can be measured with a vibrating-sample magnetometer [26] and local assumptions can be made about the bulk behaviour based on measurement of field at the surface [27], but computer modelling of the magnetic flux within a material using Finite Element Analysis proceeds using the relationship in Equation 2.21. The relationship between the time-varying magnetic flux density  $\underline{\mathbf{B}}$  within a material and an alternating external field applied to it  $\underline{\mathbf{H}}$ , provides one of the principle magnetic characteristics of a material, illustrated by the material's B-H curve (Figure 2.13).

Methods of applying a magnetic field  $\underline{\mathbf{H}}$  include the use of electromagnets [28], c-core [29] or a close approximation to an idealized long solenoid of length  $l$  with  $N$  turns. The applied magnetic field within the solenoid is along its axis and proportional to the number of turns per unit length of solenoid and the current  $I$  in each turn.

$$H = \frac{N}{l} I \quad \text{Equation 2.22}$$

## 2.2 Magnetic Materials, Magnetic Domains and Stray Fields at the Surface

### 2.2.1 Magnetic Materials

Magnetic materials are those elements, or alloys of elements, which have a magnetic susceptibility  $\chi_m > 0$ , and are said to be paramagnetic, having atoms with partially filled shells, with atomic moments which readily align parallel to an externally applied field.

All materials exhibit a diamagnetic effect, which opposes an applied magnetic field, but the paramagnetic effect in magnetic materials is so much greater than the diamagnetic effect that it is hidden. Materials which do not show a paramagnetic effect are considered non-magnetic, purely diamagnetic ( $\chi_m < 0$ ).

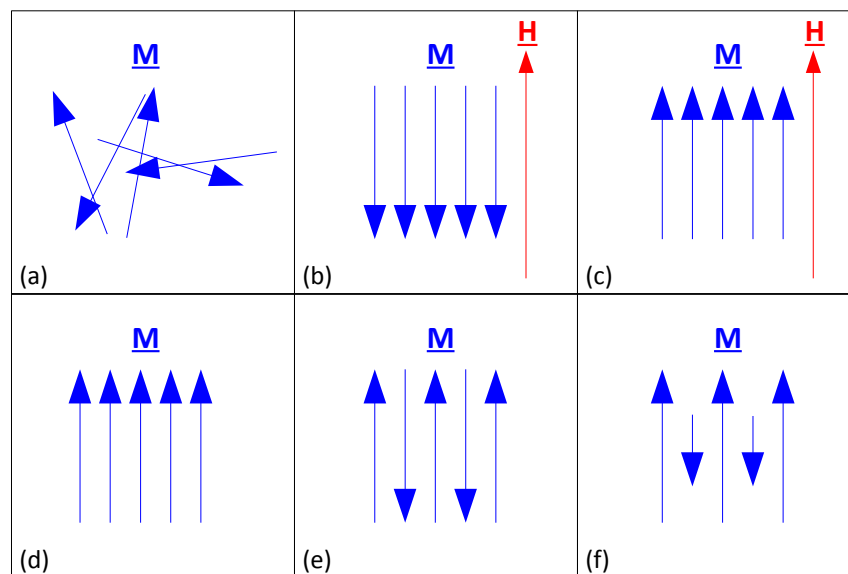


Figure 2.8: Illustration of the differences in atomic magnetic moment alignment, **M** with representations of (a) magnetic moments in a disordered state; (b) diamagnetism; (c) paramagnetism; (d) ferromagnetism; (e) anti-ferromagnetism and (f) ferrimagnetism.

Figure 2.8(b) is a representation of diamagnetism where the atomic magnetic moments align in opposition to the applied field **H**. Figure 2.8(c) is a representation of paramagnetism where the atomic magnetic moments align in support of the applied field **H**.

A periodic table of the elements, indicating which are diamagnetic and which are paramagnetic is presented in [Figure 2.9](#).

Of the paramagnetic elements some also exhibit properties of *ferromagnetism*, *ferrimagnetism* and *anti-ferromagnetism*, which are all manifestations of ordered magnetism within the material. Materials with these properties maintain their ordered magnetic state even in the absence of an applied field, and exhibit spontaneous magnetic ordering.

The atoms of Iron, Cobalt, Nickel and Gadolinium are *ferromagnetic* at 290 K (17 °C). [Figure 2.8\(d\)](#) illustrates the alignment of atomic magnetic moment, which in ferromagnetic atoms is maintained even in the absence of an externally applied field. The magnetic moments align spontaneously below their Curie temperature [19]. Above the Curie temperature the thermal excitation disorders the atomic moments (as illustrated in [Figure 2.8\(a\)](#)) and the elements lose their magnetism. Other elements in the Lanthanides series are also ferromagnetic if cooled below their Curie temperatures.

[Figure 2.8\(e\)](#) illustrates the alignment of atomic magnetic moments in an *anti-ferromagnetic* material. The atomic moments spontaneously align in an alternating anti-parallel state resulting in net zero magnetization. Above the element's Néel temperature [27] the thermal excitation breaks the spontaneous alignment and the material behaves as a paramagnetic material, free to align to an externally applied field. Chromium is the only element which is anti-ferromagnetic at room temperature but Manganese and some of the Lanthanide series are anti-ferromagnetic if sufficiently cooled. *Ferrimagnetic* compounds were originally classified by Néel, but many naturally occurring magnetic materials, including the original magnetite ( $\text{Fe}_3\text{O}_4$ ) of antiquity, are actually ferrimagnetic rather than pure ferromagnetic [19]. Ferrimagnetic materials have anti-ferromagnetic alignment with an imbalance in strength of atomic moments resulting in a net positive magnetization, as illustrated in [Figure 2.8\(f\)](#).

1		2		3		4		5		6		7		8		9		10	
1.01		4.00		10.80		12.00		14.00		16.00		19.00		20.20		23.00		23.00	
H		He		B		C		N		O		F		Ne		Na		Ar	
Hydrogen		Helium		Boron		Carbon		Nitrogen		Oxygen		Fluorine		Neon		Sodium		Argon	
6.94		9.01		10.81		12.01		14.01		16.00		18.99		20.18		22.99		39.95	
Li		Be		Al		Si		P		S		Cl		Ar		K		Ca	
Lithium		Beryllium		Aluminum		Silicon		Phosphorus		Sulfur		Chlorine		Argon		Potassium		Calcium	
7.00		9.01		26.98		28.09		30.97		32.06		35.45		39.95		39.09		40.08	
11		12		13		14		15		16		17		18		19		20	
Na		Mg		Al		Si		P		S		Cl		Ar		K		Ca	
Sodium		Magnesium		Aluminum		Silicon		Phosphorus		Sulfur		Chlorine		Argon		Potassium		Calcium	
22.99		24.31		26.98		28.09		30.97		32.06		35.45		39.95		39.09		40.08	
19		20		21		22		23		24		25		26		27		28	
K		Ca		Sc		Ti		V		Cr		Mn		Fe		Co		Ni	
Potassium		Calcium		Scandium		Titanium		Vanadium		Chromium		Manganese		Iron		Cobalt		Nickel	
39.09		40.08		44.96		47.88		50.94		51.99		54.94		55.85		58.93		58.71	
37		38		39		40		41		42		43		44		45		46	
Rb		Sr		Y		Zr		Nb		Mo		Tc		Ru		Rh		Pd	
Rubidium		Strontium		Yttrium		Zirconium		Niobium		Molybdenum		Technetium		Ruthenium		Rodium		Palladium	
85.47		87.62		88.91		91.22		92.91		95.94		98.00		101.07		102.91		106.42	
55		56		57		58		59		60		61		62		63		64	
Cs		Ba		La		Ce		Pr		Nd		Pm		Sm		Eu		Gd	
Cesium		Barium		Lanthanum		Cerium		Praseodymium		Neodymium		Promethium		Samarium		Europium		Gadolinium	
132.91		137.33		138.90		140.12		140.91		144.24		144.91		145.00		151.96		157.25	
87		88		89		90		91		92		93		94		95		96	
Fr		Ra		Ac		Th		Pa		U		Np		Pu		Am		Cm	
Francium		Radium		Actinium		Thorium		Protactinium		Uranium		Neptunium		Plutonium		Americium		Curium	
[223]		[226]		[227]		[232]		[231]		[238]		[237]		[244]		[243]		[247]	
53		54		55		56		57		58		59		60		61		62	
I		Xe		Ba		La		Ce		Pr		Nd		Pm		Sm		Eu	
Iodine		Xenon		Barium		Lanthanum		Cerium		Praseodymium		Neodymium		Promethium		Samarium		Europium	
126.90		131.29		137.33		138.90		140.12		140.91		144.24		144.91		145.00		151.96	
85		86		87		88		89		90		91		92		93		94	
At		Rn		Fr		Ra		Ac		Th		Pa		U		Np		Pu	
Astatine		Radon		Francium		Radium		Actinium		Thorium		Protactinium		Uranium		Neptunium		Plutonium	
210.00		222.00		[223]		[226]		[227]		[232]		[231]		[238]		[237]		[244]	
117		118		119		120		121		122		123		124		125		126	
Uuh		Uuo		Uut		Uuq		Uuq		Uup		Uuh		Uus		Uuo		Uuu	
Ununhexium*		Ununseptium*		Ununquadium*		Ununquadium*		Ununquadium*		Ununpentium*		Ununhexium*		Ununseptium*		Ununseptium*		Ununseptium*	
[292]		[292]		[292]		[292]		[292]		[292]		[292]		[292]		[292]		[292]	
71		72		73		74		75		76		77		78		79		80	
Lu		Hf		Ta		W		Re		Os		Ir		Pt		Au		Hg	
Lutetium		Hafnium		Tantalum		Tungsten		Rhenium		Osmium		Iridium		Platinum		Gold		Mercury	
175.00		178.49		180.95		183.85		186.21		192.22		195.08		200.59		200.59		200.59	
103		104		105		106		107		108		109		110		111		112	
Lr		Rf		Db		Sg		Bh		Hs		Mt		Ds		Rg		Uub	
Lawrencium		Rutherfordium		Dubnium		Seaborgium		Bohrium		Hassium		Meitnerium		Darmstadtium		Roentgenium		Ununbium*	
[260]		[261]		[262]		[263]		[264]		[265]		[266]		[267]		[268]		[269]	
101		102		103		104		105		106		107		108		109		110	
Md		No		Lr		Lu		Hf		Ta		W		Re		Os		Ir	
Mendelevium		Nobelium		Lawrencium		Lutetium		Hafnium		Tantalum		Tungsten		Rhenium		Osmium		Iridium	
[288]		[289]		[290]		[291]		[292]		[293]		[294]		[295]		[296]		[297]	
69		70		71		72		73		74		75		76		77		78	
Tm		Yb		Lu		Hf		Ta		W		Re		Os		Ir		Pt	
Thulium		Ytterbium		Lutetium		Hafnium		Tantalum		Tungsten		Rhenium		Osmium		Iridium		Platinum	
168.93		173.05		175.00		178.49		180.95		183.85		186.21		192.22		195.08		200.59	

Figure 2.9: The Periodic Table of elements illustrating which elements are Diamagnetic, Paramagnetic, Ferromagnetic and Anti-ferromagnetic, including the Néel and Curie temperatures. Derived from information available in [19].

### 2.2.2 Physical Origins of Magnetic Domains

In most ferromagnetic materials there are physical boundaries and restrictions to the propagation and permitted orientation of spontaneous magnetic ordering. Most ferromagnetic and ferrimagnetic elements, compounds and alloys form a crystalline lattice when solid. An exception to this are the amorphous metal alloys, forced to form non-crystalline by rapid cooling and random atomic radii.

The interaction between the atoms in the crystal lattice physically restricts the preferred magnetic orientations to only particular directions, called the *easy axis* of the lattice. [Figure 2.10](#) illustrates the three common metallic crystalline structures; *hexagonal close-packed (hcp)*, *body centred cubic (bcc)* and *face centred cubic (fcc)*.

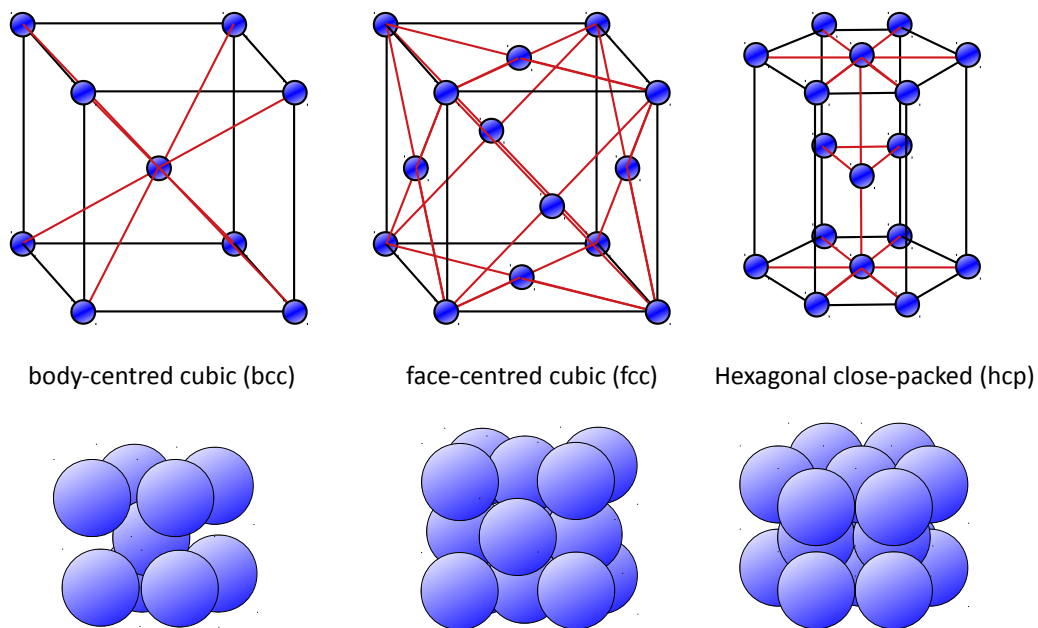


Figure 2.10: The metallic crystalline structures; body centred cubic (bcc) and face centred cubic (fcc) and hexagonal close-packed (hcp).

The easy axis of a material (element, compound or alloy) can be in any direction within the lattice and is a particular property of the material. The easy axis is normally perpendicular to one of the repeatable planes permitted by the lattice structure. Both the easy axis direction and the planes within the lattice are described using Millar Indices [30].

Natural imperfections in the crystal lattice lead to *grain boundaries* which provide physical dislocations and discontinuities in the orientation of the crystal lattice. This in turn provides edges and discontinuities in the orientation of the materials magnetic ordering. The atomic magnetic orientations self adjust to these large scale crystalline imperfections; towards a minimal energy configuration for the bulk material, with the net orientation within one grain differing to its neighbours resulting in a net magnetisation.

For a non-magnetised sample the net magnetisation is by definition zero, though individual grains may have magnetisation in a particular direction, others have magnetisation in an opposing direction. A ferromagnetic sample can become magnetised by application of an external magnetic field, in which case the net magnetisation of each grain aligns to the external field resulting in net magnetisation for the bulk material.

For materials with large grains it requires energy input from an externally applied field to maintain the atomic moments in the same orientation throughout the entire grain (saturation). Without the external field supporting this energy state, the atomic moments within a grain will spontaneously break into regions which orient alternately within the grain, to minimise the net magnetisation towards zero (or towards the current level of external field).

These separate regions within an otherwise continuous crystal grain are called Magnetic Domains and are a topic of extensive study. For the atomic moments to be able to change orientation within a physically continuous crystal grain, regions of reorientation, called domain walls, form. Two types of domain walls are common *Block* and *Néel*, as illustrated in [Figure 2.11](#), reproduced from [31]. Formation of a domain wall requires energy, and so the number of domain walls which spontaneously form in a material, and hence the size of individual magnetic domains, depend on the properties and internal energies (including temperature) of the material. If a grain or particle is small enough that the energy needed to create a domain boundary between

two domains is greater than the energy of the single-domain particle, the particle will remain a single domain. There is a single-domain size for each material ( $D_{sd}$ ), below which size it will be a single domain and above which it will be a multi-domain. The single-domain sizes for various ferromagnetic materials are illustrated in Figure 2.12, reproduced from [27]. If the particle size gets much smaller, the internal coupling energy between the atomic magnetic moments can no longer be sufficient to counter thermal energy. This critical size is known as the *super-paramagnetic limit* ( $D_{sp}$ ) [27].

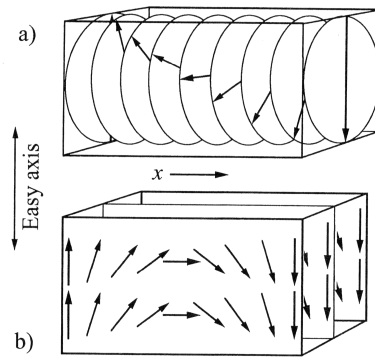


Figure 2.11: The rotation of the magnetization vector from one domain through a 180° wall to another domain. The two alternative modes of rotation are; (a) *Bloch* wall, the optimal mode and (b) a *Néel* wall, which is less favourable. Reproduced from [31].

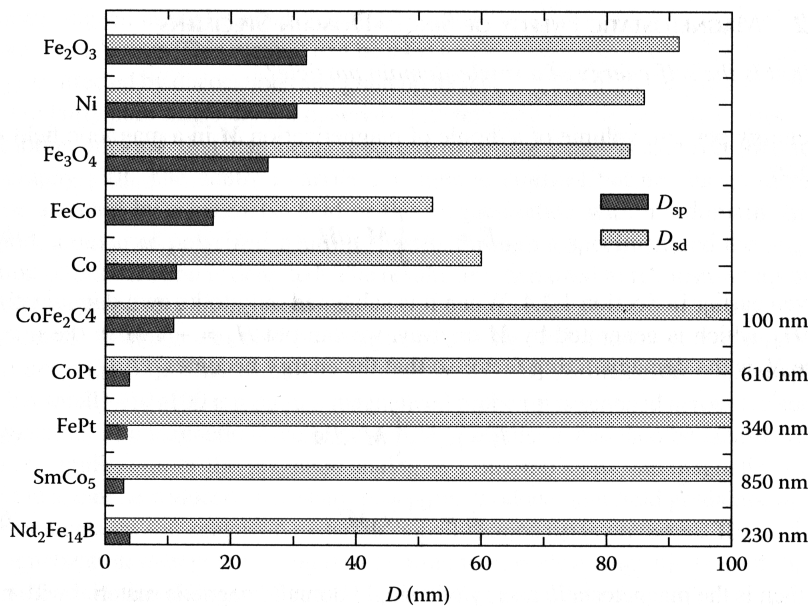


Figure 2.12: Single-domain particle diameter size ( $D_{sd}$ ) and super-paramagnetic transition diameter size ( $D_{sp}$ ) of selected ferromagnetic materials. Reproduced from [27].



### 2.2.3 Dynamics of Magnetic Domains

As an applied field  $\underline{H}$  on a material changes, the orientation of individual magnetic moments will react not only to the external field, but also to the internal material Magnetization  $\underline{M}$  caused by the orientation of the moments in the atom's neighbours. Observation of the magnetic domains as a changing externally applied field magnetizes a sample demonstrates how the domain pattern re-arranges to maintain a minimal energy configuration that equals the new net magnetisation of the material. *Barkhausen noise* [32, 33, 27, 34], which was first heard as a crackling signal from a pickup coil connected to a speaker, is seen as evidence of discrete jumps in the atomic magnetic moments as they align to the required direction. In the study of the bulk magnetic properties of a material by the plot of the magnetic flux density  $\underline{B}$  (as detected with a pickup coil) against the applied field  $\underline{H}$ , applied using a Yoke or Helmholtz coil [35, 36, 37, 38] the *Barkhausen* effect can be observed directly in the discrete jumps present at small scale on the resulting B-H curve, as illustrated in [Figure 2.13](#), reproduced from [27].

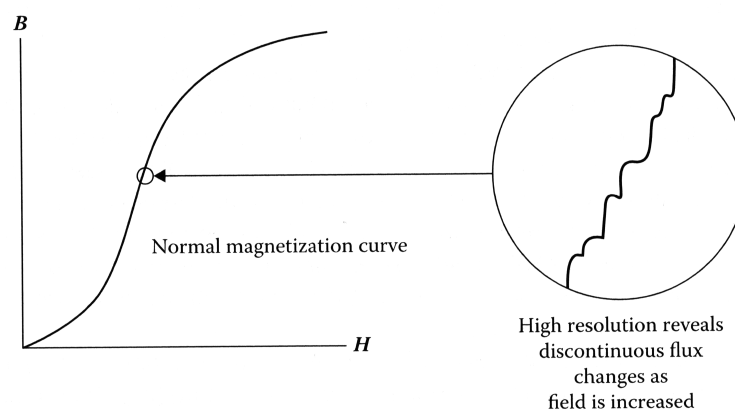


Figure 2.13: Barkhausen noise; discontinuous changes in the flux density  $\underline{B}$  as the applied field  $\underline{H}$  is changed. Reproduced from [27].

It is stated [27] that the magnetic *Barkhausen* effect is “caused mostly by sudden irreversible motion of magnetic domain walls when they break away from pinning sites”. This is investigated further and discussed as part of the domain dynamics work presented in [Chapter 8](#).

### 2.2.4 Stray Fields at the Surface

Study of the effect of a material's bulk domain structure on its average material magnetisation can be made through B-H curve and *Barkhausen* noise studies [39, 32, 33, 40]. Investigation of the specific domain structure within the bulk of a material must be approximated by the study of those domains which are observable at the material's surface [41, 42, 43, 31].

Study of the domain structure at the surface of a material is possible because imperfect orientation of the domains at the surface leads to a leakage of magnetic flux beyond the boundary of the material, particularly at domain walls and grain boundaries. This flux leakage manifests as measurable "Stray Fields" at the surface of a sample. Alex Hubert and Rudolf Schäfer [31] provide an extensive account of the different ways that the complex domain structures within samples can manifest as patterns of stray field above the surface.

Because the magnetic flux and magnetic flux density cannot be sharply discontinuous [19], the assumption that the magnetic flux above the surface boundary corresponds to the flux just below the surface is valid. Consequently, by measuring or observing the stray fields emanating from the surface of a sample it is possible to determine the structure of the domains just below the surface.

By studying the structure and dynamics of domains at the surface of a magnetic material it is possible to gain a better understanding of the behaviour of the domains within the bulk of the material, which are beyond direct observation, and consequently a better understanding of the mechanisms behind the bulk magnetic behaviour and properties of a material. Those properties can then be better engineered to fit particular requirements in power electronics [44, 45], actuator [46, 47, 48] and sensor [49, 50, 51, 52] applications.

Numerous techniques in the discipline of domain observation, the study of the structure and dynamics of surface magnetic domains, of which this work forms part, have been developed and are discussed at length in the following review of prior literature, [Chapter 3](#).

Most of the previous domain observation techniques discussed in [Chapter 3](#) provide only a planar (top down) view of domains just below the surface of the sample. It is an open topic of research, which is investigated in [Chapter 7](#), as to how the stray fields behave in the volume of space above the surface of the sample, how far they extend beyond the surface of the sample and over what range the magnetic flux lines might loop back into the surface.

How the stray fields vary in shape dynamically above a sample in an alternating applied magnetic field is also an open topic of research, which is investigated in [Chapter 8](#). Being able to observe and measure these empirically for the first time will help either confirm or improve upon the models of bulk domain formation and movement [[27](#)], [[31](#)] currently assumed from the planar observations.



*Chapter 3***Review of Literature**

A review of the Literature relevant to the detection of magnetic fields and observation of domains and domain dynamics is provided along with existing procedural scanner systems making use of the magnetic field detection techniques available.

**3.1 Methods of Detecting Magnetic Fields and Observing Domains**

The topic of domain observation is extensive and spans a century of research. For the purposes of this chapter it is necessary to focus on those areas of the topic most pertinent to the techniques directly employed in this work.

The techniques for observing domains are discussed extensively in the review work and authoritative publications of Hubert and Schäfer [31]. This older work provides extensive review and explanation of domain observation using the Bitter technique and Magneto-Optical techniques but is naturally limited in the discussion of Magnetic Field Sensor Scanning, mentioning only older Hall and vibrating-pickup-coil sensors. They discuss the practical limitations in spatial and sensitivity resolution which the current project addresses.

Hubert and Schäfer [31] also give a summary of the principle motivations for the field of domain observation; why they are studied. “The role of magnetic microstructures varies strongly between different applications of magnetic materials. In some fields, such as in the cores of electrical machinery, domains and domain walls are essential. Electrical machines would not work without the easily displaceable domain walls providing the necessary permeability. The same is true for most inductive devices at medium and high frequencies. Irregularities in the magnetic microstructure are also the origin of losses and noise (electrical and acoustical) in these devices.”

“In some applications of magnetic materials domains play no role at all, such as microwave components, nucleation-type permanent magnets, and particulate recording media. Other devices would ideally work without any non-uniform magnetic microstructures, but domains are the origin of irregular behaviour if they cannot be

suppressed. In these cases, mostly in the field of small sensor and memory elements, domain studies are necessary to understand the conditions of their occurrence and their control. Finally there are applications in which domain propagation is directly put to technical use; magnetic memories, domain shift register devices and magneto-optical display and sensor devices” [31].

There are three main techniques for detecting magnetic fields and consequently observing magnetic domains in materials; methods related to the Bitter technique, methods employing magneto-optical effects and methods using electronic means of detecting magnetic fields (magnetic field sensors).

### 3.1.1 The Bitter Technique

As mentioned in Chapter 2, magnetic flux is a constructed vector-field which describes the direction that a single unconstrained magnetic moment will align itself to (Chapter 2, Figure 2.7). Iron is an easily magnetised material and a small elongated particle of iron (an iron filing or the microscopic particles in a “ferrofluid” ethyl acetate suspension), that is free to move, will act like an unconstrained magnetic moment and align its long axis to the direction of the magnetic flux. Many aligned particles will cluster head-to-tail along a line of flux. Particles following adjacent lines of flux will cluster laterally, forming thicker lines. The thickness and number of the lines is a balance between the density of the magnetic flux and the physical restriction-to-movement on the particles, the friction of the surface or viscosity of the “ferrofluid”. The number and thickness of the lines formed thus becomes, against a known or standard viscosity of “ferrofluid”, an indication of the Magnetic Flux Density  $\mathbf{B}$ . The work of Bitter in 1931 on the inhomogeneities in the magnetization of ferromagnetic materials [53], involved observations on crystals of iron and iron-silicon, having large grains. The samples had been ground and annealed but the traces from the ferrofluid did not show any relationship to the grain structure. “For [small] magnetizations... various systems of evenly spaced straight parallel lines appear[ed], but varying slightly in direction and spacing from grain to grain.” This led to his work on the nature of

ferromagnetism [54] using a “ferrofluid” of magnetic  $\text{Fe}_2\text{O}_3$  particles about  $1\ \mu\text{m}$  in diameter suspended in ethyl acetate. This is the technique which bears his name. He studied the patterns on iron crystals, nickel crystals and cobalt crystals. The patterns obtained ranged from straight lines on some crystals, and spotty patterns on others. “The spots arrange themselves in rows when the crystals are magnetized”. At the time “an explanation of these effects [was] not known”, though these are now known to be the result of domain formation and magnetic structure and dynamics within the samples.

In 1949 Williams, Bozorth and Shockley [55] were using the Bitter technique to outline the domains in single crystals of silicon iron and derive understanding of the domains in the bulk of the material, including energising the sample in alternate directions to determine the direction of the domains observed and provide verification of the theory of Bloch walls [31] between the domains (Chapter 2, Figure 2.11). They also noticed that “if a scratch [in the surface] crosses a domain in which the magnetization is not parallel to the scratch, magnetic poles are formed when the flux emerges into the air where it crosses the scratch.” A stray-field phenomenon discussed in Chapter 7.

Narita [56] also employed the bitter technique to study the annihilation of domain walls under magnetization of a sample of silicon-iron in varying directions, making use of the result that the colloidal particles in the ferrofluid, once the ethyl acetate has evaporated, collect around the stray fields presumed to emanate from the Bloch walls at the edges of the domains at the surface of the sample.

The Bitter technique highlights the locations of the edges of the domains in a sample, in the theory [31], collecting around the points of strongest z-component stray fields emanating from the surface of the sample. A common method for enhancing the z-component stray fields from the Bloch walls is using a coil to supply an emphasising z-field (perpendicular to the sample surface), called a bias field. Grechishkin *et al.* [57] use a bias field of 40 mT to study the domain structures in polycrystalline Ni-Mn-Ga shape memory alloys. Xu *et al.* [43] provide an illustration of such a “domain viewer”

setup and compare the magnetic domain patterns observed in Grain-Oriented Electrical Steel using this technique with those obtained using the Magneto-Optical Kerr effect (Section 3.1.2).

One advantage of the Bitter technique is that “the resolution of the Bitter technique reaches easily 100 nm and is in principle limited only by the colloid particle size to some 10 nm” [31]. Alimohammadi *et al.* [6] use such a method to highlight the < 100 nm wide zig-zag field patterns on AF10 amorphous wire, a result reproduced with permission in Chapter 6. Hubert and Schäfer [31] mention development of the Bitter method using magnetotactic bacteria for decorating stray fields.

Bitter patterns do not always require surface preparation and even coated samples can be investigated, but resolution and sensitivity are higher for well polished samples [31]. However, because of the settling time of the colloid particles, the technique is largely a static domain observation technique. To respond to any altered external field, the settled particles must be re-suspended, or reapplied [56].

### 3.1.2 The Faraday and Kerr Magneto-optical Effect

In 1846 Faraday discovered that the plane of plane-polarised light, being a polarised electromagnetic wave, is rotated when passing through a region of magnetic field. If light polarised on a single plane passes through a magnetic field then the orientation of that plane is rotated in relation to the strength and relative direction of the magnetic field [58]. If a magnetic material is transparent then the plane of the light passing through it will be rotated in relation to the internal magnetization fields of the material. The rotation of the polarisation is investigated using a pair of crossed polarisers.

Unfortunately most magnetic materials are not transparent to visible light, however, in 1877 Kerr recognised that the same rotational result occurred for reflected polarised light [59]. If the surface of a sample is sufficiently smooth and reflective as to faithfully return the plane of the polarised light, rather than scatter it, then that plane is again



rotated by interaction with the magnetic fields in the material. It is important to recognise that the effect occurs due to interaction with the fields in the material itself (in the surface layer) rather than the stray fields emanating above the surface of the sample. The effects are small so digital contrast enhancement and image difference techniques are often employed to enhance the signal.

“The observation of magnetic domains by magneto-optical microscopy, based on the Kerr and the Faraday effect, is one of the most prominent techniques for the visualization of distributions of magnetization within magnetic materials. The method has gained increased attention due to the possibility to visualize field and current induced phenomena in nano-structured magnetic materials on fast time-scales” [60].

The Magneto-Optical Kerr Effect (MOKE) method differs in relation to the relative orientation of the expected fields. Polar MOKE is when the magnetization vector is perpendicular to the reflective surface and parallel to the plane of incidence, in longitudinal MOKE the magnetization vector is parallel to both the reflective surface and the plane of incidence, while in transverse MOKE the magnetization vector is perpendicular to the plane of incidence and parallel to the surface. Fowler and Fryer [61] contrast between the longitudinal and transverse effect and in this way some impression as to the three-dimensional shape of the fields within the sample can be obtained. Schäfer and Schinnerling [62] use such comparison to validate “three-dimensional echelon models” for domain refinement close to strongly mis-oriented iron surfaces. Meguro *et al.* [63] recognise that the rotation of longitudinal MOKE is reversed when the illumination direction is reversed whilst the rotation of Polar MOKE remains the same. This can be used to eliminate the polar component of the magnetisation field in NiFe thin films and, together with sample rotation, determine the three dimensional direction of the local magnetisation field. It is again important to recognise that these previous studies look at the three-dimensional structure of the magnetisation fields within the material, and not the three-dimension structure of the stray fields above the sample, which this work addresses.

The high optical-resolution of light microscopy, the relative ease of setting up a cross-polariser system compared to the Bitter technique, and the image enhancement and temporal resolution possible with modern digital photography, has made MOKE methods common in domain observation studies where the nature of the samples permit it, and the limited available field of view is nevertheless sufficient.

Takezawa *et al.* [64] built a MOKE system for domain observation of Fe-Si-B-Nb amorphous wires with large diameters for micro-sensor applications, indicating that domain size in the inner core of the wire is important for high sensor output and [65] use the same system to observe Nd-Fe-B sintered magnets at elevated temperatures up to 320 °C. At these temperatures oxidation would normally prevent the surface from remaining mirrored, but a 5 nm surface coating of Tantalum (Ta) was found to prevent the oxidation without affecting the MOKE results.

Životský *et al.* [66] used longitudinal MOKE to investigate the surface magnetic anisotropy and the domain behaviour in as-quenched and strain-annealed Fe-Nb-B amorphous ribbons.

MOKE is commonly used to analyse the effects on the magnetic properties of electrical (Si-Fe) steels of mechanical operations necessary during manufacture in the power transformer industry, including bending [67], punching [68] and cutting [44].

The disadvantage of the magneto-optical Kerr effect is the need for a sample with a clean smooth reflective surface which does not introduce its own scattering or optical artefacts to the data. This necessitates sometimes difficult sample preparation, which, even if successfully done, may introduce stresses or alteration to the material properties which may render the resulting domain observations irrelevant to the study of the raw unaltered material.

Even where sample preparation is not an issue, and the surface of the sample can be appropriately prepared to a perfectly clean mirrored surface, there is an issue of

limited depth of field imposed by the necessary 60° incident angle of the light and camera, common in longitudinal and transverse MOKE. The area of in-focus data available is a great limit for domain observation over large areas, which is discussed further in the comparison of the Scanner System with MOKE results in [Chapter 6](#).

One solution to the issue of sample preparation is by the use of magneto-optical indicator films as an intermediary.

### 3.1.3 Magneto-optical Indicator Films

Magneto-optical Indicator Films (MOIFs) are optically transparent thin films of bismuth-substituted yttrium iron garnet ( $\text{Bi}_1\text{Y}_2\text{Fe}_5\text{O}_{12}$ ) [42] which exhibit the Faraday effect on polarised light which passes through them. By mirroring the lower edge of the film, incident plane-polarised light will pass through the body of the film twice, the angle of the plane being rotated as it does so in relation to the film's internal magnetisation. As the film has a low coercivity [69], if the film is placed next to a magnetic sample with strong stray fields emanating from the surface then the internal magnetisation of the film will alter in relation to the stray fields passing through it, and communicate that by the induced Faraday-rotation. Lee *et al.* [42] produced a thickness of film of approximately 47 nm for a single coating, with Faraday-rotation angles estimated as  $-2.47^\circ/\mu\text{m}$ . Bennett *et al.* [70] were among the first to employ the technique in 1995 for nondestructive characterization of the defect structure of electrochemically produced CoNiCu/Cu magnetic multilayers.

Grechishkin *et al.* [71] use magneto-optical imaging films to study the magnetic stray field distributions above artificially patterned permanent magnet films and other miniature elements that could be used in magnetic micro-systems. Richert *et al.* [10] use MOIF techniques as a versatile method to characterize magnetic field distributions in grain-oriented electrical steel without removing the isolation layer. The combination of MOIF with digital high-speed camera technology enabled temporally resolved

investigations of the magnetization processes with optical resolution of 25  $\mu\text{m}$  and a temporal resolution of 1 ms (in single-shot mode).

*Matesy* have produced the *CMOS-MagView* commercial system [72] which uses an integrated magneto-optical indicator film to detect stray fields in the range 0.01 to 160 kA/m placed in direct contact with its 50 x 60 mm sample region. The CMOS sensor permits a spatial resolution of 25  $\mu\text{m}$ . This device is useful for observation of manufactured magnetic features and even hairline-crack detection in magnetised samples but lacks the spatial resolution for detailed domain observation.

As these studies highlight, MOIF techniques *do* investigate the stray fields above a magnetic sample rather than the internal magnetisation probed by direct MOKE. They can provide high-resolution observation of unprepared samples, although in some cases the films require deposition. They can also respond quickly in dynamic studies.

However, MOIF is only able to probe the stray field in the 50 nm layer above the surface and thus not able to elucidate the three-dimension shape of the stray fields as they extend above the surface, which is an aim of this work. As an optical technique again dependent on the 60° incident angle common with MOKE setups, they still exhibit the issue of limited depth of field as discussed in the comparison of the Scanner System with MOKE results in [Chapter 6](#).

### 3.1.4 Magnetic Field Sensors

As an alternative to the mechanical, and optical methods discussed previously it is possible to detect magnetic fields purely electronically, using magnetic field sensors. As a fundamentally electro-magnetic effect ([Chapter 2](#)) a magnetic field, *by definition*, has a direct effect on the electrons present in a system. The exact manifestation of that effect is dependent on the nature of the electronic sensor employed, and is itself again a very extensive topic of research.

As stated in Pipka and Janošek's 2010 review of advances in magnetic field sensors [[73](#)] “the most important milestone in the field of magnetic sensors was when [anisotropic magnetoresistance] sensors started to replace Hall sensors in many applications where the greater sensitivity...was an advantage and [giant magnetoresistance]..sensors finally found applications”.

Magnetic field sensors either; produce their own induced potential difference or current in relation to the strength of an applied magnetic field (Hall-effect [[74](#)] , VSM [[26](#)] or flux-gate sensors [[50](#)]) or vary their resistance to the flow of current in relation to the strength of an applied magnetic field (magneto-resistance sensors) [[75](#), [76](#)].

Tumanski provides a thorough review of the modern magnetic field sensors in [[77](#)] and [[78](#)] with description of their principles of operation.

The sensor provided for this work is the STJ-020 Tunnelling Magneto-Resistance sensor from *Micromagnetics* [[79](#)] . The *Micromagnetics* STJ-020 TMR sensor is a Tunnelling Magneto-resistance Sensor with a  $2\ \mu\text{m} \times 4\ \mu\text{m}$  active area. The sensor die is mounted on a long-armed probe. The physical principles of the sensor are presented in Chapter 4 ([Section 4.7.1](#)).

Magnetic field sensors detect the field in one location. In order to observe stray fields over a surface area it is necessary to scan the sensor over the surface and collect multiple measurements across the surface at known positions, to build a picture digitally. Some efforts have been made to produce fixed arrays of sensors [80]. The MagCam MiniCube 3D [81] contains 16,384 3D Hall sensors in a 128 x 128 2D array with a spatial resolution of  $0.1 \times 0.1 \text{ mm}^2$  per pixel. This has the advantage of being a solid state device with rapid ( $< 1$  second) sampling times but has a fixed resolution and only covers an area of  $12.7 \times 12.7 \text{ mm}^2$  per image. Tumanski and Baranowski [80] investigate various magnetic sensor arrays using Hall-effect and Magneto-resistance sensors and an array is used to sample either a fixed number of points across a steel strip as it passes beneath the sensor, or as an amplification and averaging method, or as a way of increasing the speed of a scanner system.

For economic reasons it is more common to use just a single sensor and scan the sensor over the area mechanically. This is slower but permits a higher (variable) spatial resolution (limited by the size of the sensor) and large (variable) scan area. The STJ-020 TMR sensor provided for this work was created by *Micromagnetics* as part of the development effort on their *Circuit Scan 1000* system [3], which uses magnetic fields to perform diagnostics on semiconductor die and packages, specifically because the *CS1000* required high spatial resolution to be able to see the tiny current paths which exist in integrated circuits. The *CS1000* is one of several already available, but expensive, commercial systems.

## 3.2 Existing Procedural Scanner Systems

Scanning systems are required to build up an image from a collection of single point magnetic field sensor measurements. The method is not unique to magnetic field sensors; Halahovets *et al.* [82] developed a scanning magneto-optical Kerr microscope with a light detection scheme based on a differential photodetector. The spatial resolution of the Kerr microscope was demonstrated by mapping an isolated  $5 \times 5 \mu\text{m}$  spin-valve pillar. Though the STJ-020 TMR sensor has been provided for use in this project, it is part of the development to make the system adaptable to any analogue sensor for future work, including the possibility of such a Kerr effect photo-detector sensor.

Although many different magnetic field sensors are used in scanning systems [77, 78], the subsequent review will focus on only those systems which employ Hall-effect or Magneto-resistive sensors as these are the most economically viable types of sensor for use in the current system.

### 3.2.1 Systems Using Hall-effect Magnetic Field Sensors

Kustov *et al.* [83] use a scanning hall probe microscope to quantify the out-of-plane component of the stray magnetic fields produced by NdFeB hard magnetic films patterned using both topographic and thermo-magnetic methods. The Hall sensor used had three offset active areas of size,  $40 \times 40 \mu\text{m}^2$ ,  $10 \times 10 \mu\text{m}^2$  and  $4 \times 4 \mu\text{m}^2$  and was mounted at  $5^\circ$  angle on a quartz tuning fork to enable air-pressure resonance to be used as a z-displacement measurement technique. The sensor itself was fixed, with a piezo-actuator controlled sample stage being used to control z-displacement and perform the scan. The magnetic field resolution of the sensor accuracy is stated as  $\pm 100 \mu\text{T}$  ( $\pm 80 \text{ A/m}$ ).

Shaw *et al.* [84] also use the tuning-fork technique (adapted from Atomic Force Microscopy scanners) to govern the distance of the sensor above the sample, this time with the piezo-actuator attached to the sensor rather than the sample stage. They

produce their own bespoke Hall-effect sensors with active areas between 1 and 5  $\mu\text{m}^2$  and magnetic field resolution of again  $\pm 80$  A/m. This is excellent spatial resolution, but with a bespoke non-commercially available sensor.

Though the spatial resolution of the above Hall-effect sensors are comparable with the *Micromagnetics* STJ-020 sensor provided for this project [85] the magnetic field sensitivity of the hall sensors (at  $\pm 80$  A/m) is an order of magnitude lower than the  $\pm 1.6$  A/m stated for the *Micromagnetics* STJ-020 sensor. For the study of the intrinsic stray fields from, for example amorphous magnetics materials, where field strength range is less than  $\pm 80$  A/m (Chapter 6), the Hall-effect sensors would not be sufficient.

Both the systems of Kustov *et al.* and Shaw *et al.* are sensible systems, but do not have sufficient field sensitivity for this work and measure only the z-component of the field without capacity to derive the three dimensional components of the stray field.

Huber *et al.* [7] use a commercially available deposition 3D printer to both produce and then 3D-scan poly-lactic acid (PLA) structures with embedded hard magnetic filler particles (ferrites or rare-earth materials). After printing the structures they attach an *Infineon* TLV493D-A186 3-axis hall sensor to the head of the printer to map the fields emanating from the geometry of the structures. These commercial sensors are commonly used as angle encoders for consumer electronics products like joysticks and compasses in mobile phones. The spatial resolution of the sensor is only 0.1 mm for the x and y-axis, and 0.05 mm for the z-axis. The low and asymmetric spatial resolution of commercial 3-axis Hall sensors are one of the difficulties in using such sensors for high resolution scanning, the field sensitivity is again only in the  $\pm 80$  A/m range.

In an effort to improve the issue of 3-axis spatial resolution Dede *et al.* [8] have produced a 3D scanning Hall probe microscope with 700 nm resolution. They demonstrate a non-standard mode of operation of a Hall-cross region where, rather than having to employ three orthogonal sensing regions, as per the commercial three-axis sensors, a single Hall-cross region can be forced to respond to non-perpendicular



fields in an interpretable manner. Three consecutive scans, with rotation of the sample, are required to calculate all three components of the field, but this method does increase the possible maximum resolution to the active volume of the Hall-cross. They demonstrate the method by scanning the surface of a magnetically encoded hard-disc drive. Again the field sensitivity is limited and an order of magnitude greater than that available from the STJ-020 TMR sensor.

Thus, in general, the use of Hall-effect sensors are limited to applications with strong sources of magnetic fields; permanent magnet materials, strongly magnetised surfaces like magnetic recording media, or tracks carrying electric current. Two-dimensional scanning is commercially possible with a resolution of  $4 \times 4 \mu\text{m}^2$  but three-axis scanning is commercially limited to the order of  $100 \times 100 \mu\text{m}^2$ .

Ignatiev, Orlov and Stankevich [86] use a 3-axis Hall magnetometer with active area of  $250 \times 400 \mu\text{m}^2$ , on a motorised positioning system with a positional accuracy of  $5 \mu\text{m}$  to measure current distribution on manufactured copper tracks. Their work demonstrates the difficulties encountered when the sensor active area is orders of magnitude greater than the precision of the positioning system. By working with specific reference geometry it is possible to demonstrate convolution of the sensor response to derive finer resolution than the raw active area provides, but it is much simpler to work toward good correspondence between the spatial resolution of the positioning system and the spatial resolution of the sensor (Chapter 4).

Okolo and Meydan [87] use a basic single-axis *Allegro Microsystems* A1302KUA-T Hall-effect sensor mounted to servo-motor controlled three-axis scanner to analyse the perpendicular stray field emitted from hairline cracks in samples of pulse magnetised steel pipes as part of the non-destructive testing (NDT) of pipework in the oil and gas industry, at a resolution of 0.1 mm per step and a sample-distance of 0.5 mm.

Araujo *et al.* [88] have developed a recent "Scanning Hall Effect Microscope" to characterise complex mineral structures in geological samples. The samples need

strong applied magnetization in the out-of-plane z-axis to help emphasise the stray fields under observation, which is achieved by a Yoke of strong electromagnets. Importantly the system incorporates two aligned Hall-sensors; one at a distance of 142  $\mu\text{m}$  from the sample surface, and the other beneath the sample to measure, and permit the subtraction of, the applied field. The system scans at a spatial resolution of 200  $\mu\text{m}$  over an area of 40 mm diameter.

### 3.2.2 Systems Using Magneto-resistance Sensors

Gontarza, Szulima and Leib [89] use an array of 63 Honeywell HMC5983 AMR magnetic sensors coupled with the optical sensor from a computer mouse to produce a handheld non-destructive testing instrument for the same purpose as Okolo and Meydan [87]. Though the millimetre scale spatial resolution and the stated field sensitivity of  $\pm 0.8$  mT ( $\pm 636$  A/m) is not sufficient for domain observation, the handheld nature of the equipment is a useful advantage in NDT. Whilst cheaper, low sensitivity, AMR sensors were used in development, the use of AMR sensors from the onset, rather than Hall-effect sensors, allows for replacement with greater sensitivity AMR sensors in the future. As previously stated, Pipka and Janošek [73] consider it “the most important milestone in the field of magnetic sensors was when [anisotropic magnetoresistance] sensors started to replace Hall sensors in many applications where the greater sensitivity...[is] an advantage”.

The papers and thesis of P.I. Nicholson [41, 90] present the development of a magnetic domain imaging system for electrical steel using a magnetoresistive sensor based stray field scanning technique. The system developed was capable of 2D scanning at 50  $\mu\text{m}$  per step resolution and has an associated US patent [91]. The system is driven by a 68000 microprocessor board with data collected by an ADM 7000 DAS ADC card, connected to a Windows 95 PC with control software written in Visual Basic. The current work is seen as a development, modernisation and improvement of the Nicholson scanner. Replicating the capabilities of Nicholson's system with a modern control system represented the first stage of the current project, with results presented

in [Chapter 6](#). The current work enhances the capabilities of the Nicholson system by scanning at 1  $\mu\text{m}$  per step resolution, with a 2 x 4  $\mu\text{m}^2$  TMR sensor and enabling the resolving of the field in 3-dimensions. Nicholson investigated the effect of static applied fields on the sample, the current work allows study of samples under dynamic applied fields.

Schrag *et al.* [92] use an unnamed scanning magnetoresistive imaging system to isolate and analyse faults in integrated circuits by detecting the stray magnetic fields at the surface of the IC, resolving features to a scale of 100 nm. In Liu *et al.* [93] the same authors investigate the magnetization reversal mechanism of narrow sub-micrometer Co rings with and without thermal annealing. Both publications reference the use of a magneto-resistive scanning system “detailed previously in” [94], but this reference does not actually provide any details as to the system which was used. This confusion is not an atypical occurrence in the literature. From the author Schrag's affiliation with the company *Micromagnetics* [95] it is reasonable to assume that the system being used is the *Micromagnetics* Circuit Scan 1000 (CS1000) [3, 96] making use of the STJ-020 TMR sensor which was developed for that system. In [95] Schrag *et al.* use the CS1000 to study the current flow in magnetic tunnel junctions themselves. The thinner the insulation layer between the two magnetic layers the more sensitive the junction is to small applied magnetic fields, but the greater the likelihood of pinhole breakdowns in the insulation layer and the less reliable the sensor becomes. A diagram of the structure of the magnetic tunnel junction in the STJ-020 sensor itself is provided in Chapter 4, [Figure 4.10\(c\)](#). In [97] Schrag *et al.* use the CS1000 system to study current flow in active integrated circuits.

Schen *et al.* [98] use the sensitivity of a custom built tunnelling magneto-resistance sensor with an active area of 2 x 6  $\mu\text{m}$  to detect single micron-sized magnetic beads as magnetic labels for biomolecules and in [99], rather than using a scanning technique, employ an array of 64 such sensors to detect target DNA labeled with 16 nm  $\text{Fe}_3\text{O}_4$  nanoparticles. Such fine resolution is suitable for molecular scale biomedical applications but would be an expensive solution for investigating larger scan areas.

Lei *et al.* [100] combine the high resolution scanning of magnetic nanoparticle-labelled biomolecules (antibodies) with a larger scanning area by passing a fluid suspension of the particles beneath the sensor at a controlled rate, in effect scanning along the length of the fluid.

Another system, also based on the *Micromagnetics* STJ-020 probe, has been developed at Pontifical University, Brazil by Lima *et al.* [4]. Their system differs in scanning approach, moving the sample stage rather than moving the probe. The area of sample scanned is restricted by a maximum travel distance of 5 mm along the x and y axis. They use a nonmagnetic sampling stage without any means of magnetizing a sample for dynamic studies. Additionally, they employ continuous movement along the x-axis rather than single cell stepping, relying on the DAQ sampling frequency to derive the size of the x-axis cells. This further prevents study of the dynamics within each scanner cell. The system scans only the two dimensional surface, without the capacity to scan a volume or tilt the sensor. The system has been used to study two polished thin (30  $\mu\text{m}$ ) sections of representative geological samples along with a synthetic sample containing magnetic micro-particles. The instrument has a range of applications in paleomagnetism and rock magnetism, nondestructive evaluation of materials, and biological assays but has not been used to study the 3-D structure of stray fields from domains.

### 3.3 Existing Studies of Domain Dynamics

Coey [19] discusses the theory of magnetic domains and domain dynamics but does not go into detail on how to observe the phenomenon he describes theoretically.

Whilst some efforts have been made to study dynamic domain movement using advanced techniques, a notable example being the use of high-frame-rate neutron dark-field imaging [101], most investigation of dynamic domain motion has been undertaken with MOKE techniques, either stroboscopically or using high-frame rate digital photography.

#### 3.2.1 Using Magneto-optical techniques

Initial attempts to study time-resolved movement of magnetic domains were made by Freeman *et al.* [102] and Yang *et al.* [103] using single point electronic optical sensors, enhanced by use of an optical fibre, with some element of scanning to study different points on a sample surface.

Once high-frame-rate CMOS based electronic cameras, with digital image capture and processing became available much more extensive study of domain movement over entire regions of sample surface could be made [104]. The advantages of real-time domain observation over stroboscopic magneto-optic studies, or studies where there is gradual stepped change in an otherwise static applied field [105] are that non-repeating dynamics can be observed, which are shown to be important in power loss issues for transformers [104].

In his topical review on “Progress in magnetic domain observation by advanced magneto-optical microscopy” [60] McCord outlines and reviews the progress in the use of MOKE microscopy to study magnetic domains in samples, including the change of domain spacing with varying applied magnetic fields and current induced domain wall motion (section 7.8 of the paper).

Magini [106] uses a stroboscopic illumination technique to investigate domain wall motion at frequencies from 20 kHz to 2 MHz. This method permits observation at frequencies much higher than the frame-rate of the camera and avoids issues with low levels of illumination by effectively integrating over several exposures. The method is very dependent on observing regularly repeatable domain motion.

Holländer *et al.* [107] have developed a MOKE setup which isolates the x and y components of the samples magnetisation. The resolving of the two components mean the “details of [the dynamic] magnetization response in the central domains, the gusset of the central domains, and the closure domains [become] directly visible in one set of images [with none] of these features...apparent in the regular non-selective component images.” They demonstrate the clear advantage in observing the component resolved dynamics of magnetisation. As stated; “the out-of-plane  $\Delta m_z$  component, however, cannot be calibrated from pure MOKE imaging”. This being the case it becomes necessary to use a magnetic field sensor to calibrate the component of the stray-field emanating from the surface.

Wells *et al.* [108] have developed an experimental setup which combines a high-frame-rate MOKE camera with a one-dimensional scanning hall probe to provide scanned measurement of the stray-field strength at single points on the two-dimensional MOKE image. This should permit them to obtain a time-dependent profile of the change in stray-field strength at a number of single points on their MOKE image but the technique is not well applied, rather they prefer to use a few scanned points to calibrate the intensity scale of the MOKE data, on which they more heavily rely.

With the need to use a magnetic field sensor to calibrate the MOKE observations of stray-field strength, together with the limitations of MOKE with regards sample preparation and limited depth of field and sample area, it is worthwhile investigating and developing the use of only a magnetic field sensor, in a procedural scanner system, to achieve the entire quantitative observation.

### 3.3.2 Using Procedural Scanner Systems

The study of domain dynamics using procedural scanning systems is much less common and an open area of research in which the current project finds novel application.

The study of dynamics with a slow scanning method necessitates a “stroboscopic” [11], “lock-in” [109] or otherwise synchronised approach to the observation of regularly repeating patterns. Some attempt has been made to develop this technique using the Hall-sensor based system of Abdul, Moses and Williams [11, 110]. Whilst their work demonstrates some movement of major bar domains within electrical steel, it does not have the resolution or field sensitivity that is available with the STJ-020 sensor. More importantly, their results exhibit some significant ambiguity in interpretation believed to be the artefacts of a Yoke based energising method that are an issue that is discussed in detail in [Chapter 8](#).

Kögel *et al.* [109] use the STJ-020 sensor in the *Micromagnetics* CS1000 system to study not only the static current distribution (as in Schrag *et al.* [92]) but also the dynamic changes in current due to possible defects within a Power MOSFET. They employ a “lock-in” method of triggering the externally applied power at the start of each sample point. Such pulse energising works well for observing current flow in fixed component geometries with expected repeatable dynamics.

Pulse magnetisation is also effective for investigating fixed surface topology features and defects such as hairline fractures [111], where the use of pulse magnetisation not only saves on power consumption but, the dynamic behaviour of stray-fields also reveals more details on the nature of the defect than just a static scan.

However, where the dynamics under investigation are those of the domains themselves, and not some topographically fixed feature, it is thought that pulsing the magnetisation, with inconsistent relaxation time between peaks, may itself cause

unwanted artefacts and non-repeatability in the results. It is considered better to attempt a smooth continuous sinusoidal magnetisation and consequently this work seeks to develop a novel synchronous scanning method for dynamic observation of domain movement with a continuous sinusoidal magnetisation of the sample.

The combination of this novel dynamic observation approach with the novel resolving of both the z and x axis components of stray field using only a single-axis sensor (presented in [Chapter 7](#) and published in [112]), culminates in the results presented in [Chapter 8](#). Together with the unique user interface design (discussed in [Chapter 5](#)), these elements are where this thesis provides novelty and new understanding for this area of engineering.



## Chapter 4

# Development of the Scanner Hardware

The Scanner Hardware is built around a 3-axis positioning arm, controlled by Parker Automation drivers with a 3D-printed sensor enclosure, precision goniometer and integrated microscopic sight. Here the system requirements and architecture are discussed. Calibration of the hardware, particularly quantifying the slack/backlash of the three axis, and progressive improvement in the capabilities of the system and its sensors is recounted. The technical drawings for the developed 3D-printed sensor heads are provided. Detailed description and data-sheets for both the manufactured and purchased components of the Scanner Hardware are provided in Appendix 4.

## 4.1 System Overview

The Scanner Hardware is built around a 3-axis positioning arm controlled by *Parker Automation* [113] drivers, originally inherited from a system developed by [11, 110] discussed in [Chapter 3 \(Section 3.3.2\)](#). A 3D-printed sensor head, precision goniometer and integrated microscopic sight have been added. A photograph of the completed system is presented in [Figure 4.1](#) and a schematic block diagram illustrating the connections between components is presented in [Figure 4.2](#). Detailed photographs of the sample scanning area ([Figure 4.1\(c\)](#) and [\(e\)](#)) are presented in [Figure 4.15](#) and a technical schematic illustration is presented in [Figure 4.16](#).

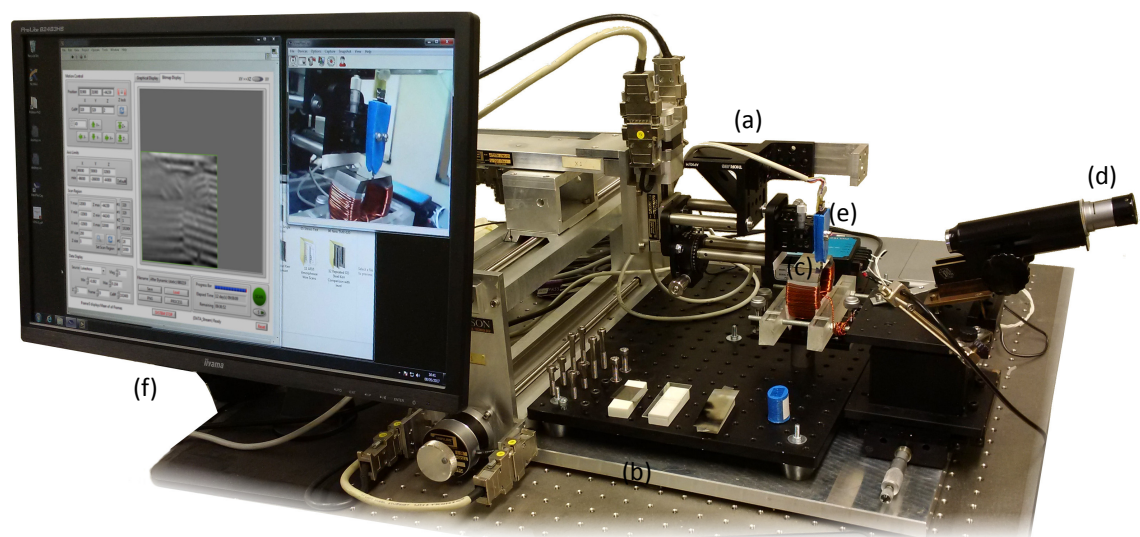


Figure 4.1: Photograph of the Scanner System showing; (a) the 3-axis positioning arm, (b) scanner base, (c) sample platform with energising Yoke, (d) microscopic sight, (e) Sensor Head version 3 with STJ-020 TMR sensor and (f) Scanner Control 3 PC display.

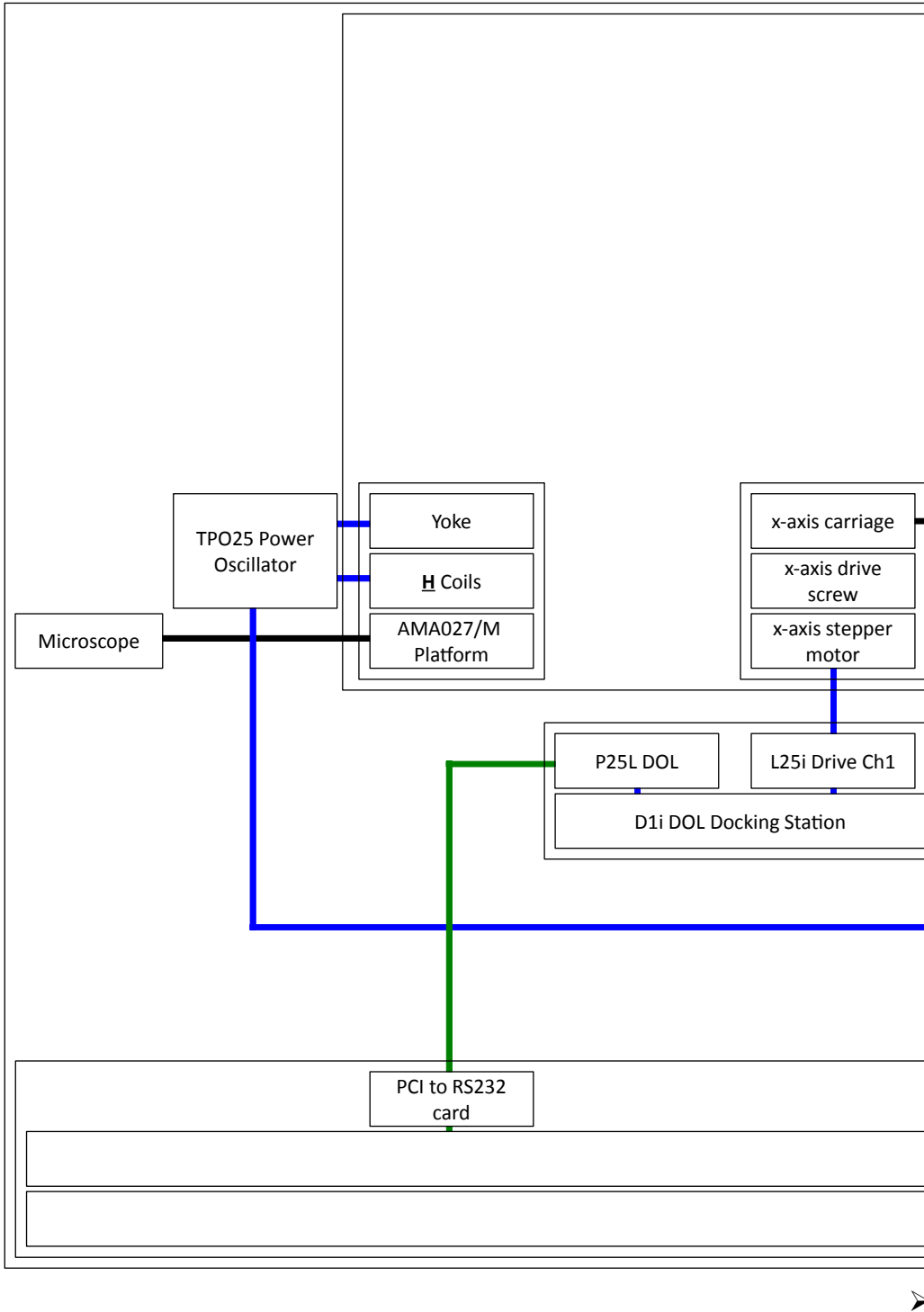
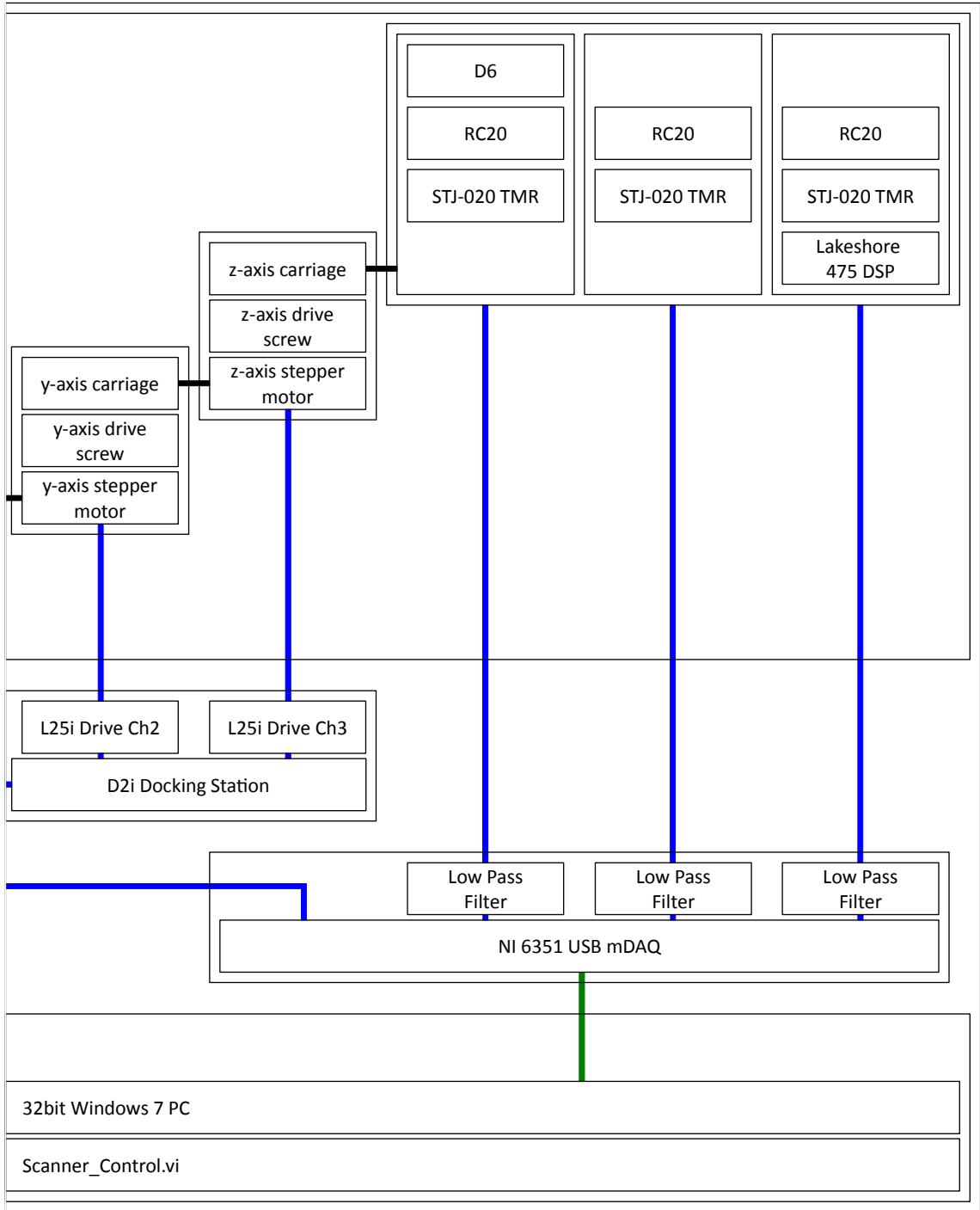


Figure 4.2: The Block Schematic of the connections between the different components of the Scanner Hardware, illustrating the physical relationships and the electrical connections.



The blue wires indicate direct analogue electrical connection, the green wires indicate USB or RS232 serial communications and the black bars indicate a physical connection between components not already enclosed in groups.

### 4.1.1 System Requirements

At its most basic the hardware must be able to;

- a. Make use of the existing hardware that has been provided.
- b. Be controlled manually and automatically by an external NI LabView system.
- c. Correctly position the scanner head along three independent axes (to a precision of  $\pm 1 \mu\text{m}$ ).
- d. Permit the user to confidently position a sensor in a chosen location (to a precision of  $\pm 1 \mu\text{m}$ ).
- e. Be adaptable, to allow any desired sensor to be physically attached.
- f. Sensor positioning with a repeatable precision greater than the footprint of the sensor (the provided sensor has a footprint of  $2 \times 4 \mu\text{m}$ ).
- g. Operate unsupervised for periods of days at a time without fault.

As the capabilities of the system developed and the nature of the resulting data were better defined, these basic requirements also evolved. In particular, the Sensor Head which attaches the Sensors to the end of the scanner arms has progressed through three separate developments (Section 4.9, [page 78](#)).

### 4.1.2 Hardware Architecture

The Scanner Hardware is formed of four electronically communicating groups of components; the Scanner Base components (Section 4.2, [page 60](#)), the Parker Automation modules (Section 4.3, [page 64](#)), the Analogue Data Acquisition components (Section 4.4, [page 68](#)), and the PC Control components (Section 4.5, [page 69](#)) which are illustrated in [Figure 4.3](#), with an additional optical Microscope and Power Oscillator (Section 4.10, [page 81](#)). The individual components of the Scanner Base group of components are illustrated in [Figure 4.4](#). These are physically attached to one another, but are communicated with independently. The x-axis, y-axis and z-axis hardware, collectively the 3-axis framework, are discussed in Section 4.2.1 ([page 60](#)), the sample Platform is discussed in Section 4.10 ([page 81](#)) and the three versions of the Sensor Head are discussed in Section 4.9 ([page 78](#)).

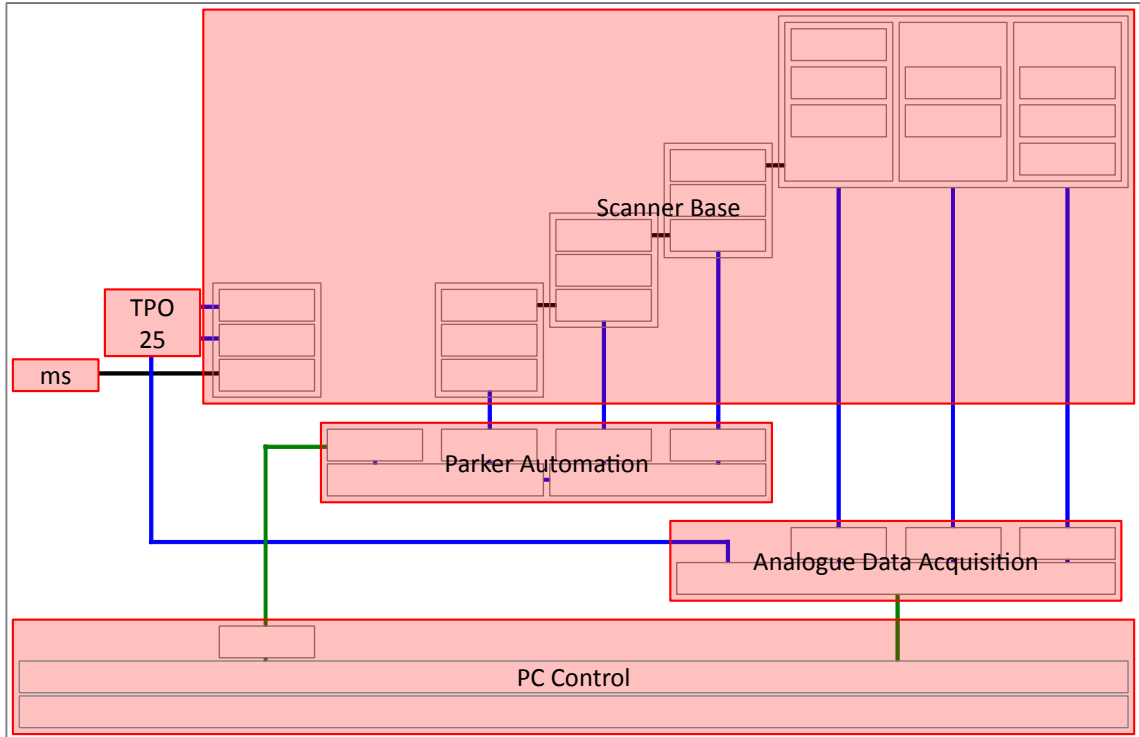


Figure 4.3: The four electronically communicating groups of components; the Scanner Base components, the Parker Automation modules, the Analogue Data Acquisition components, and the PC Control components.

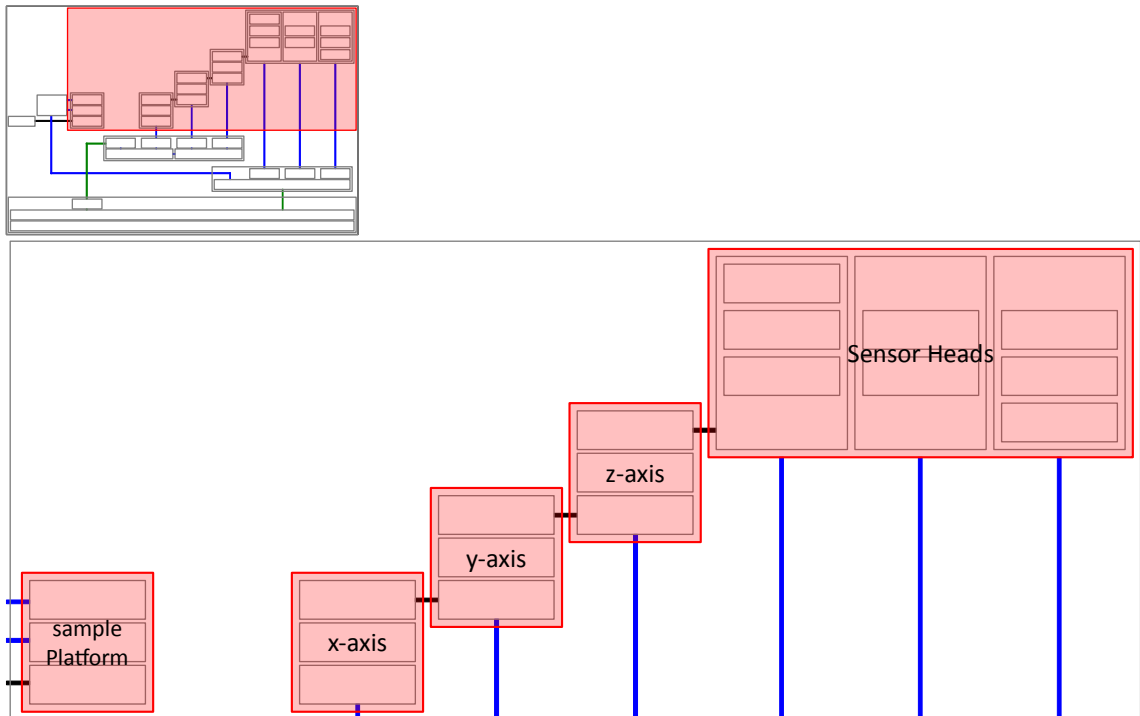


Figure 4.4: The individual components of the Scanner Base group of components, all physically attached but independently wired. Three separate versions of Sensor Head were developed.

## 4.2 Scanner Base

### 4.2.1 3-axis Framework

The Scanner Base and 3-axis framework hardware had been inherited from a system developed by [11, 110]. The 3-axis framework, presented in Figure 4.5, was manufactured by *Time and Precision Industries Ltd.* (Basingstoke, Hants, England) based on Parker SY873 stepper motors controlled using *Parker Automation* [113] L25i Drives, discussed in Section 4.3 (page 64). The stepper motors are 1.8° per step hybrid motors and in combination with the axis drive threads result in a step to distance ratio of 4000 steps to 1 mm of travel. Further details of the individual components of the 3-axis framework are provided in Appendix 4.

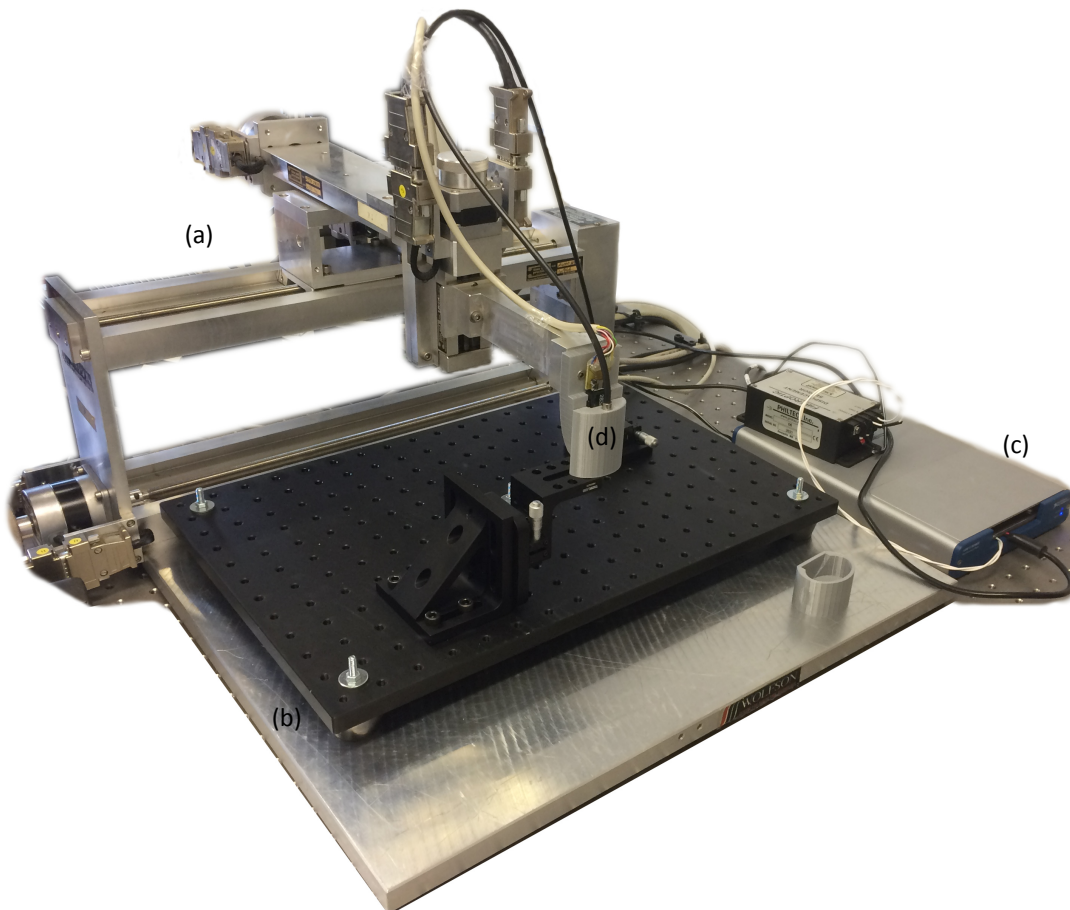


Figure 4.5: Photograph of the 3-axis framework showing; (a) the stepper motors, thread drives, carriages and arms. Also visible in the photograph are; (b) the *Thorlabs* MB3045\_M Aluminium Breadboard, (c) the *National Instruments* 6351 USB mDAQ and (d) Sensor Head version 1 with the *Micromagnetics* STJ-020 TMR sensor and *Philtec* D6 sensor

It was a requirement of the original PhD specification to make use of the existing available hardware. For this reason the system has been developed with the existing stepper motor based control system architecture, without position encoders that would be present in a more modern servo based system [87]. As such it was necessary to compensate for backlash in the threads by calibration rather than using positional feedback control. Nevertheless the backlash compensation developed, described in Section 4.2.2, provides for 1 $\mu$ m repeatable precision, which is better than the 2 x 4  $\mu$ m footprint of the smallest sensor (the *Micromagnetics* STJ-020).

#### 4.2.2 Slack/Backlash Calibration

When a thread based drive shaft changes direction there is a small portion of the rotation where no physical contact between the thread and the “nut” that travels along it is made. This is because there must be some slack to the nut, even if only slight, to avoid too much friction preventing the movement. This results in a lag between when the rotation of the thread begins and the movement of the carriage that is attached to the nut which is called the “Slack” or “Backlash” of the system [114]. As there is no physical compensation for the backlash in the provided 3-axis framework, once the existence of the backlash was identified a software solution was developed to compensate for it.

Making use of the D6 displacement sensor discussed in (Section 4.6, page 70) mounted on Version 1 of the Sensor Head (Section 4.9, page 78) with Scanner Control 2 software (Section 5.3), the slack constants for each axis  $X_s(38)$ ,  $Y_s(130)$  and  $Z_s(195)$  were determined. The fine 0.01 mm graduated scale and reflective surface of a *Graticule* L4079 Stage Micrometer slide were scanned and used as a distinct reference over which the sensor could repeatedly pass. The offset in apparent position of the Graticule scale caused by the backlash as the scanner passed back and forth over it, or as the scanner raised and lowered above the fixed surface, directly represented the amount of backlash present on each axis. The number of steps compensation for each axis, written as the slack constants into the (*Motion*).vi motion control subVI (Section 5.4.2.3), were fine tuned until the scan in one direction matched that in the other direction. The fine tuning of each axis is presented in Figure 4.6.

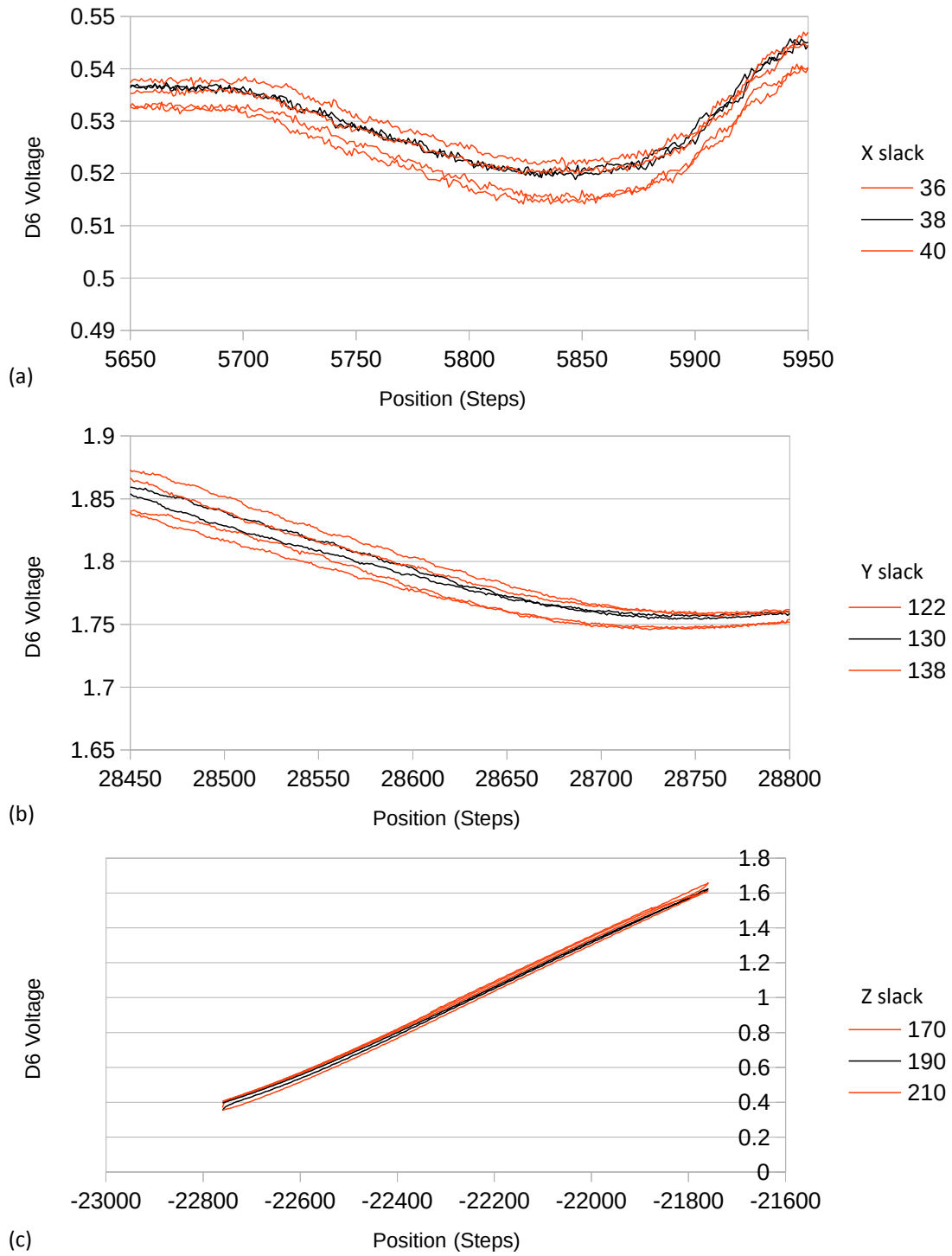


Figure 4.6: Fine single-step voltage changes are plotted as the displacement sensor passes back and forth over the same location repeatedly. The displacement between the forward and reverse paths represents the backlash in the thread of the (a) X, (b) Y and (c) Z axis when the motors change direction. The finely tuned  $X_s(38)$ ,  $Y_s(130)$  and  $Z_s(195)$  constants reduce this displacement in the Scanner Control software.



The constants could be determined to an accuracy of  $\pm 2$  steps ( $\pm 0.5 \mu\text{m}$ ) which results in the stated  $1 \mu\text{m}$  repeatable precision of the scanner. The data which supports this calibration is available in *Chapter 4.7z* of the Cardiff Portal Arxive ([page ix](#)) and on the accompanying DVD. The effectiveness of this backlash compensation mechanism is also demonstrated by the fact that there is no “scanner drift” ([Figure 4.7](#)) over the sampling of hundreds of lines of cells and changes of direction for any of the scans presented in this thesis.

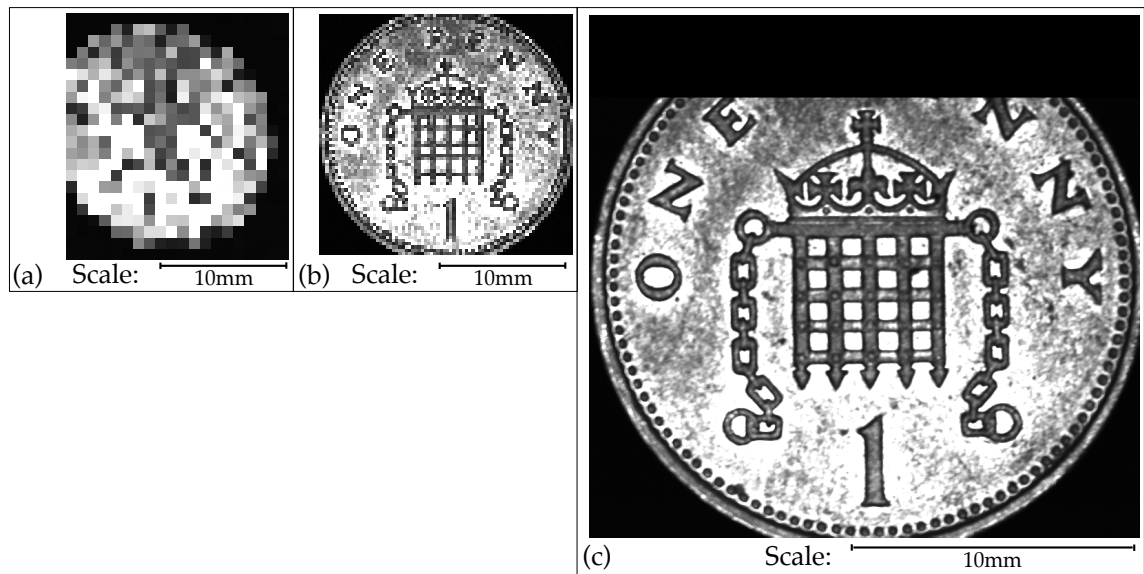


Figure 4.7: Scan with the D6 displacement sensor of a 1p coin (a) at 1mm/pixel resolution with the backlash compensation disabled, illustrating the distortion from circular due to “scanner drift”; (b) at 0.25 mm/pixel with the backlash compensation engaged illustrating the lack of “scanner drift”; and (c) at 0.025 mm/pixel with 608000 pixels illustrating the effectiveness of the backlash compensation in preventing any drift.

The slack/backlash compensation calibration has remained constant over the period of this research. Over time, however, wear on the mechanisms may lead to a need to recalibrate. This need would be seen in the occurrence of scanner drift in the resulting scans ([Figure 4.7\(a\)](#)). At that time the system can be recalibrated and the new values input into the  $X_s$ ,  $Y_s$  and  $Z_s$  constants in the (*Motion*).vi subVI ([Chapter 5, Section 5.4.2.3](#)).

## 4.3 Parker Automation Hardware

### 4.3.1 Control Modules

The stepper motors driving each axis are controlled by Parker Automation L25i Drive industrial motion control modules (Figure 4.8(b)). These modules are industrial rack mounted motion control units with an internal microprocessor and memory giving them the capacity to be programmed with a sequence of logic controlled actions and variables in their own right. The three L25i modules are programmed and communicated with via character strings sent over an RS232 interface through the LabView VISA subVIs. The full range of commands and internal variables available to the module are presented in Figure 4.9, reproduced from [113]. The Scanner Control software uses principally only the D (Distance), G (Go), R (Report), and M (Mode) commands to specify the distance and direction of movement on each axis, trigger the motion and check on the status of the MV (Moving?) system variable. Each axis is identified by its individual L25i Drive, which is in turn identified by a channel number (Figure 5.13). Other internal parameters, such as the acceleration and deceleration profiles were experimented with during the development of the Scanner Control 1 software but not subsequently altered. The internal settings are retained after power-loss on internal non-volatile memory. Most importantly the flag to state whether the instruction to move to a specified position as an “Incremental Move” (relative to the previous position) or an “Absolute Move” (relative to the controllers internal origin point) were set as Incremental during the development of Scanner Control 1. It was decided that the LabView system should store the absolute position of the scanner, with the Parker Automation hardware acting purely as a single command motor control system. Thus, no programming exists in the control units and they are setup to respond immediately to a single instruction from the LabView system and report once the motors have finished that instruction. The scan origin is set to the current position of the hardware whenever the system is restart. More details about the L25i Drive modules, and the wiring of the D2i Docking Station for the motors and RS232 (Figure 4.8(d-f)) can be found in Appendix 1 and Appendix 4.

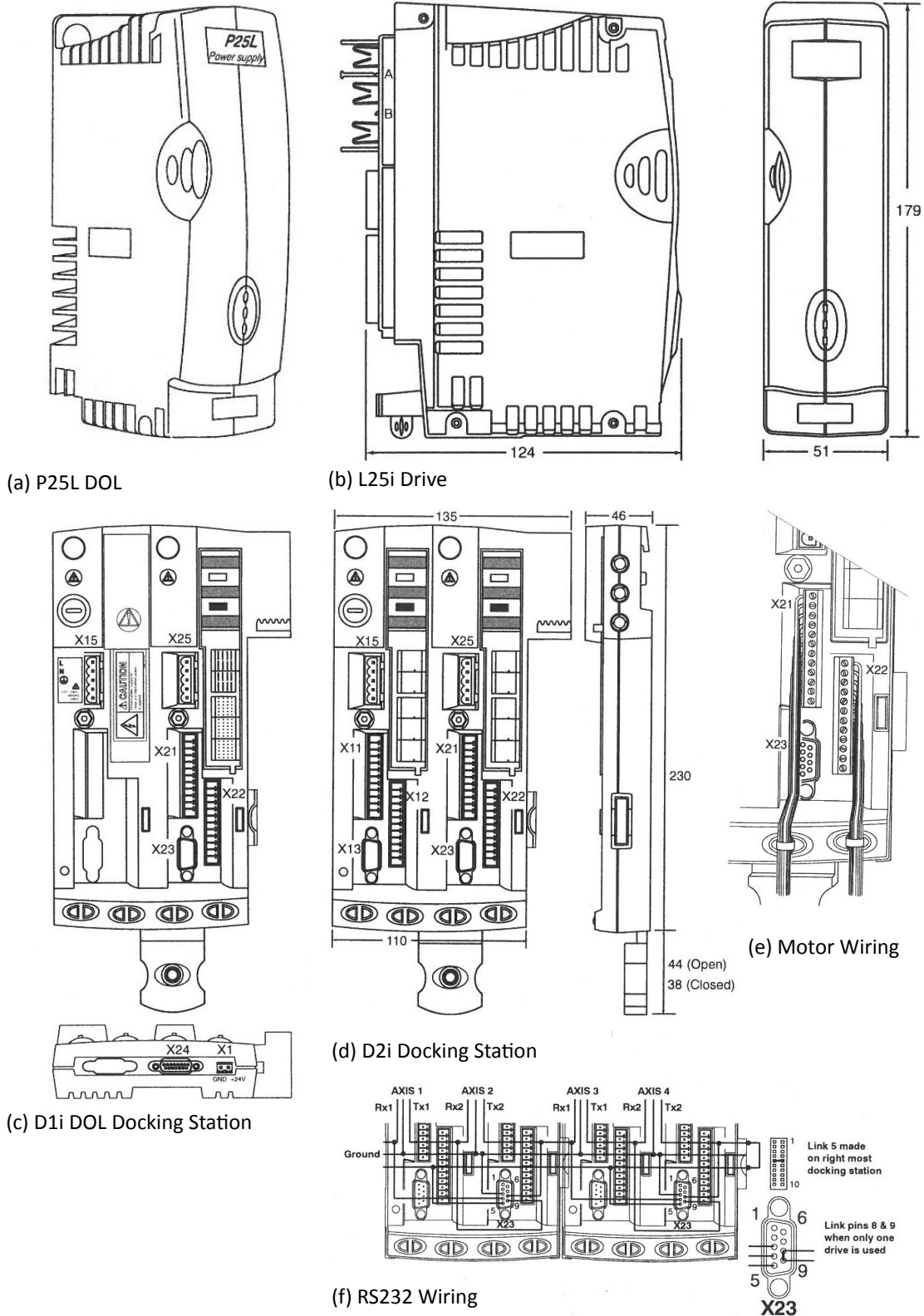


Figure 4.8: Illustration of the Parker Automation components; (a)P25L DOL, (b)L25i Drive, (c) D1i DOL, (d) D2i with (e) Motor and (f) RS232 wiring details. The parts are reproduced from [113]. Further detailed description of each component are given in Appendix 4.

Command	Description	Command	Description	Var	Name	R	W	Range/default value
A	Acceleration/Deceleration	POSMAIN	Position maintenance	AO	Analogue offset	Y	Y	-512 to 511, default=0 (10V = 512 counts)
AA	Acceleration	PROFILE	Define move profile	BU	Buffer usage	Y	N	% of program buffer used 0-100
AD	Deceleration	PS	Pause	CQ	Command queuing	Y	Y	1= Pauses until move complete (default) 0= continuous execution
ARM	Enable event triggered code	R	Report system parameter	DF	Drive Fault status	Y	N	See following section
BOOST	Apply motor boost	REG	Registration move	DJ	Distance Units	Y	Y	0= Motor steps or 1= Encoder steps, default=0
C	Continue	RFS	Return to factory settings	EI	Encoder input	Y	Y	0=step/dir, 1=cw/ccw, 2=quad ABZ, default=2
CLEAR	Clear user code	S	Stop	EO	Encoder signal output	Y	Y	0=step/dir, 1=cw/ccw, 2=quad ABZ, default=0
DECLARE	Declare	SN	Scan command	EP	Encoder Position	Y	Y	-2,147,483,648 to 2,147,483,647 counts
D	Distance	STALL	Stall detect	EQ	Echo Queuing	Y	Y	0=normal, 1=wait for <CR>, 2=cmd response only
E	Enable/disable communications	SV	Save configuration	ER	Feedback encoder resolution	Y	Y	1-65,535
EXIT	Exit from loop	T	Time delay	EX	Comms. Response Style & echo control	Y	Y	0= speak when spoken to, echo off, RS485, multi axis 1= speak whenever, echo off, RS485, single axis 2= speak when spoken to, echo on, RS232, multi axis 3= speak whenever, echo on, RS232, single axis
FRATE	Feed rate override	TR	Wait for trigger	IN	Inputs	N	N	Same format as IS command
G	Go	USE	Use	IP	In Position flag	Y	N	1= In position or 0= not yet in position
GH	Go home	V	Velocity	IT	In Position Time	Y	Y	1-500mS, default=10mS
GOSUB	Go to subroutine	VS	Start stop velocity threshold	MC	Motor current	Y	Y	50, 60, 70, 80, 90, 100 (in percent), default see RFS
GOTO	Go to routine	W	Write system variable	MR	Motor resolution	Y	Y	400, 800, 2000, 4000, default see RFS
H	Change direction	Z	Reset	MS	Motor standby current	Y	Y	50, 70 (in percent) , default see RFS
HOME	Configure homing	#	Set comms address remotely	MV	Moving	Y	N	Flag 1= moving or 0 = not moving
IF	Test condition	" "	Quote command	PA	Position Absolute	Y	Y	-2,147,483,648 to 2,147,483,647 steps/counts, default 0
IS	Input status			PE	Position Error	Y	N	Encoder count or motor steps, depending on DU
K	Kill			PI	Position Incremental	Y	Y	-2,147,483,648 to 2,147,483,647 steps/counts, default 0
LIMITS	Configure limit inputs			RB	Ready/Busy flag	Y	N	Flag 0= ready or 1= busy
LIST	List user program			RM	Registration Move	Y	N	Flag 1= reg move in progress, 0 = not doing reg move
LOOP	Repeat user code			RV	ReVision of software	Y	N	x.yy major.minor
LSEL	Label select			SN	Serial number	Y	N	Drive serial number
M	Mode			ST	Status of indexing	Y	N	See Reporting the Status of Variables
O	Output			UF	User program Fault status	Y	N	See Reporting the Status of Variables
OFF	Shutdown motor power							
ON	Turn on motor power							

Figure 4.9: Table of ASCII commands which can be sent to the L25i Parker Automation Motion Control Module via RS232, and the internal system variables, elements reproduced from [113].

### 4.3.2 Power

The L25i Drive modules are powered, and subsequently supply power to the stepper motors, via a common power rail which is supplied by the P25L DOL power module (Figure 4.8(a)). The P25L DOL Power supply module provides +24 V DC without requiring an EMC filter from an AC input of 230 V AC RMS. Output power is 200W. The P25L must be fitted to the left hand side of the D1i Docking station (Figure 4.8(c)) with an L25i Drive Module being fitted to the right. The D1i docking station holds the P25L Power Supply module and one L25i Drive module. Mains AC power supply connections are made to the left hand side of the connection (the X15 port). Stepper motor connections are made to the right hand side of the dock (the X25 port). RS232 connection should also be made to this docking module. The RS232 does not need to be terminated on this module because a D2i extension dock is connected to the right.

The D2i Docking Station (Figure 4.8(d)) connects to the right of the D1i Docking station and provides two extra connections for L25i Drivers and Stepper Motor Connections (X25 port) (Figure 4.8(e)).

The RS232 connections must be terminated on the end of the D2i docking station. Only three L25i drive modules are used in total, one for each axis. The wiring and termination of the RS232 connections illustrated in Figure 4.8(f) are described in detail in Appendix 4.

## 4.4 Analogue Data Acquisition

The sensors in the system all produce an analogue DC Voltage signal which is passed through a 10 Hz low-pass filter circuit (to remove background 50 Hz electrical interference) before being read by a *National Instruments* 6351 USB mDAQ unit and consequently interpreted by the Scanner Control Software.

### 4.4.1 NI USB-6351 Multifunction Data Acquisition

The *National Instruments* 6351 USB mDAQ is part of a family of Analogue samplers which can sample numerous simultaneous analogue voltage inputs sampled at 16-bit at a maximum of 1 Mhz against an internal clock, with an internal buffer, and transfer the resulting values to the accompanying LabView mDAQ subVI's over a USB interface.

### 4.4.2 Low Pass Filters

Initially a simple ohmic potential divider was used to limit the range of the sensor inputs ( $\pm 12$  V) to the input range of the NI USB-6351 ( $\pm 10$  V). However, following analysis of the noise in the STJ-020 sensor in particular (Section 4.7, [page 72](#)), it was discovered that a strong mains 50 Hz signal was present, coming from the electronics and control lines surrounding the Scanner system, that are difficult to shield practically. Thus a 10 Hz low-pass filter circuit was used. The Low Pass Filter consists of a Resistor-Capacitor circuit with values of  $R = 160$  k $\Omega$  and  $C = 100$  nF, to filter out AC frequencies above 9.95 Hz as determined by;

$$f_c = \frac{1}{2\pi RC} \quad \text{Equation 4.1}$$

The use of analogue voltage inputs with simultaneous timing facilitates generality and adaptability in the sensors which can be used. Although code could be added to the Scanner Control system ([Chapter 5](#)) to make use of sensors with digital outputs (such as I<sup>2</sup>C) simultaneity may be broken between the different inputs.

The manufacturer specifications for the NI USB-6351 and circuit diagram of the Low Pass filter are both presented in Appendix 4.

## 4.5 Controlling PC System

The scanner hardware is controlled by a newly developed LabView Scanner Control system which is discussed in detail in [Chapter 5](#).

### 4.5.1 32-bit Drivers for VISA serial control and RS232 connections

It is important that the controlling PC be based on 32-bit Windows 7 and 32-bit LabView 15, rather than the 64-bit versions, as the *VISA* driver software does not function properly on the 64-bit system. Many days of frustrating and complex diagnostic work on the integrity of the hardware connections, because of sudden intermittent and irregular communication failures, were wasted due to installing the 64-bit system. The communication errors were solved by re-installing the 32-bit system. The resulting restriction to only 32-bit memory addressing does limit the amount of RAM available to the LabView system. This is one contribution to the out-of-memory issues encountered for large scans with Scanner Control 2 ([Section 5.3](#)) that necessitated that the development of Scanner Control 3 ([Section 5.4](#)) be based from the outset on temporary file storage.

## 4.6 Philtec Displacement Sensors

### 4.6.1 D6 Displacement Sensor

The *Philtec* D6 Displacement Sensor was the first optical displacement sensor provided for use in the system. The sensor was inherited from [11]. A photograph of the D6 sensor mounted in Sensor Head 1 is presented in [Figure 4.10\(a\)](#), reproduced from [114]. The D6 is designed to work by measuring the strength of reflection off a surface of known uniform reflectivity (a mirror for example), which is calibrated against known distance away from that surface. The sensor is consequently highly sensitive to the differing reflectivity of a sample which limits its use as a general displacement sensor. The manufacturers specifications are provided in Appendix 4.

### 4.6.2 RC20 Displacement Sensor

In contrast to the D6, the *Philtec* RC20 Displacement Sensor (presented in [Figure 4.10\(b\)](#), reproduced from [116]), is designed to optically measure displacement whilst compensating for the different reflectivity of a surface. The sensor works by having two optical fibre channels of different known intensity. The relation of reflected intensity to reflectivity of surface is linear for both channels whilst the relation of reflected intensity to distance from surface is an inverse-squared relationship. Thus, the measured intensity of each channel varies differently and that difference provides a reflection-compensated measurement of displacement. The manufacturers specifications are provided in Appendix 4. A plot of the sensor voltage output against the distance away from a mirrored surface is presented in [Figure 4.10\(c\)](#). Both the height determined by the automatic z-axis control of the scanner (S) and a manual adjustment of the vertical micrometer stage the mirror is mounted on (M) are presented. The *Philtec* RC20 Displacement sensor has an additional voltage output which is indicative of the Signal to Noise ratio (SNR) and, as instructed by the manufacturer, should remain beneath 3 V to ensure linearity. It can be seen in [Figure 4.10\(c\)](#) that the displacement to voltage response is linear in the range 0.2 mm to 0.6 mm. The data which supports this calibration is available in *Chapter 4.7z* of the Cardiff Portal Arxiv ([page ix](#)) and on the accompanying DVD.



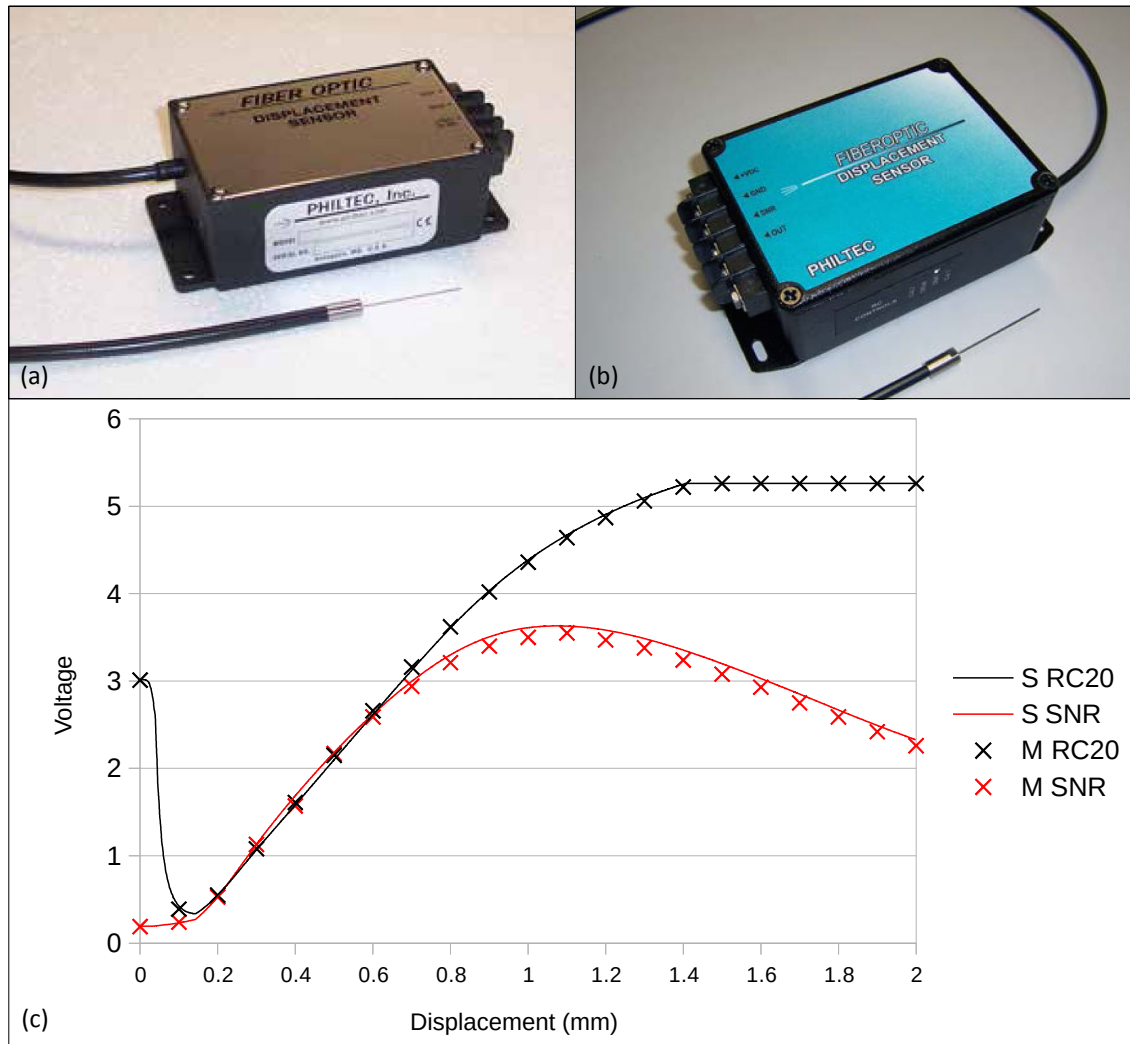


Figure 4.10: (a) Photograph of Philtec D6 displacement sensor reproduced from [115], (b) Photograph of Philtec RC20 displacement sensor reproduced from [116], (c) calibration curves of Philtec RC20 reflection compensated displacement sensor, determined as Voltage output against the vertical displacement from a mirrored surface obtained using the Scanner systems z-axis control. The “M” crosses represent displacements achieved manually using the sample stage micrometer adjustment, the S lines represent continuous single stepping displacements achieved with the z-axis stepper motor. Both the sensor voltage (RC20) and a signal-to-noise (SNR) levels are presented.

#### 4.6.3 Continued Application of the Displacement Sensors

Although the RC20 sensor has a beam diameter of 0.5 mm there was great difficulty in attempting to concurrently measure the same point of a sample surface as the STJ-020 magnetic sensor (Section 4.7, page 72), with a footprint of only  $2 \times 4 \mu\text{m}^2$ . The design of Sensor Head 2 attempted to achieve this proximity of sensors, but resulted in collision of the two sensors during development and damage to the first STJ-020 sensor.

## 4.7 Micromagnetics STJ-020 TMR Magnetic Field Sensor

The *Micromagnetics* STJ-020 TMR sensor is a Tunnelling Magneto-resistance Sensor with a  $2\ \mu\text{m} \times 4\ \mu\text{m}$  active area. The sensor die is mounted on a long armed probe, an illustration of the dimensions of the probe are presented in [Figure 4.11\(a\)](#). Over the course of this research three versions of the sensor have been used. The first sensor had a corner on the die which added approximately  $75\ \mu\text{m} \pm 0.5\ \mu\text{m}$  to the distance to the active area [79], the second and third versions of the sensor die have the corner lapped to be a distance of  $7.0\ \mu\text{m} \pm 0.5\ \mu\text{m}$  from the tip edge, a photograph of the two versions of sensor die are presented in [Figure 4.11\(b\)](#). The full manufacturers specifications are provided in Appendix 4.

### 4.7.1 Physical principles of the sensor

Magnetic tunnel junctions (MTJs) are a class of thin film device first successfully fabricated in the mid-1990s. In their simplest form MTJs are a tri-layer “sandwich” consisting of two layers of magnetic material separated by an ultra-thin insulating film, this sandwich is illustrated in [Figure 4.11\(c\)](#). If a voltage is applied to the top and bottom of the sandwich, classical physics does not permit a current to flow; however, if the insulating or “barrier layer” is sufficiently thin, electrons can flow by quantum mechanical tunnelling through the barrier layer. For tunnelling between two magnetized materials, the tunnelling current is maximum if the magnetization directions of the two electrodes are parallel, and minimum when they are aligned anti-parallel. The tunnelling current, and therefore the resistance of the device, will change as external magnetic fields alter the magnetic orientation of the two electrodes. The two electrodes are fabricated from CoFeB, while the insulating barrier is composed of  $\text{Al}_2\text{O}_3$ . The remaining layers in the structure are chosen to enhance the material and magnetic characteristics of the device. Typically, in order to achieve a linear, bipolar operation, one of the two magnetic electrodes has its magnetization fixed by an exchange energy biasing phenomenon with the adjacent IrMn layer, while the remaining electrode is left free to respond to external fields. The resulting structure has an electrical resistance which varies linearly as a function of the magnetic field strength

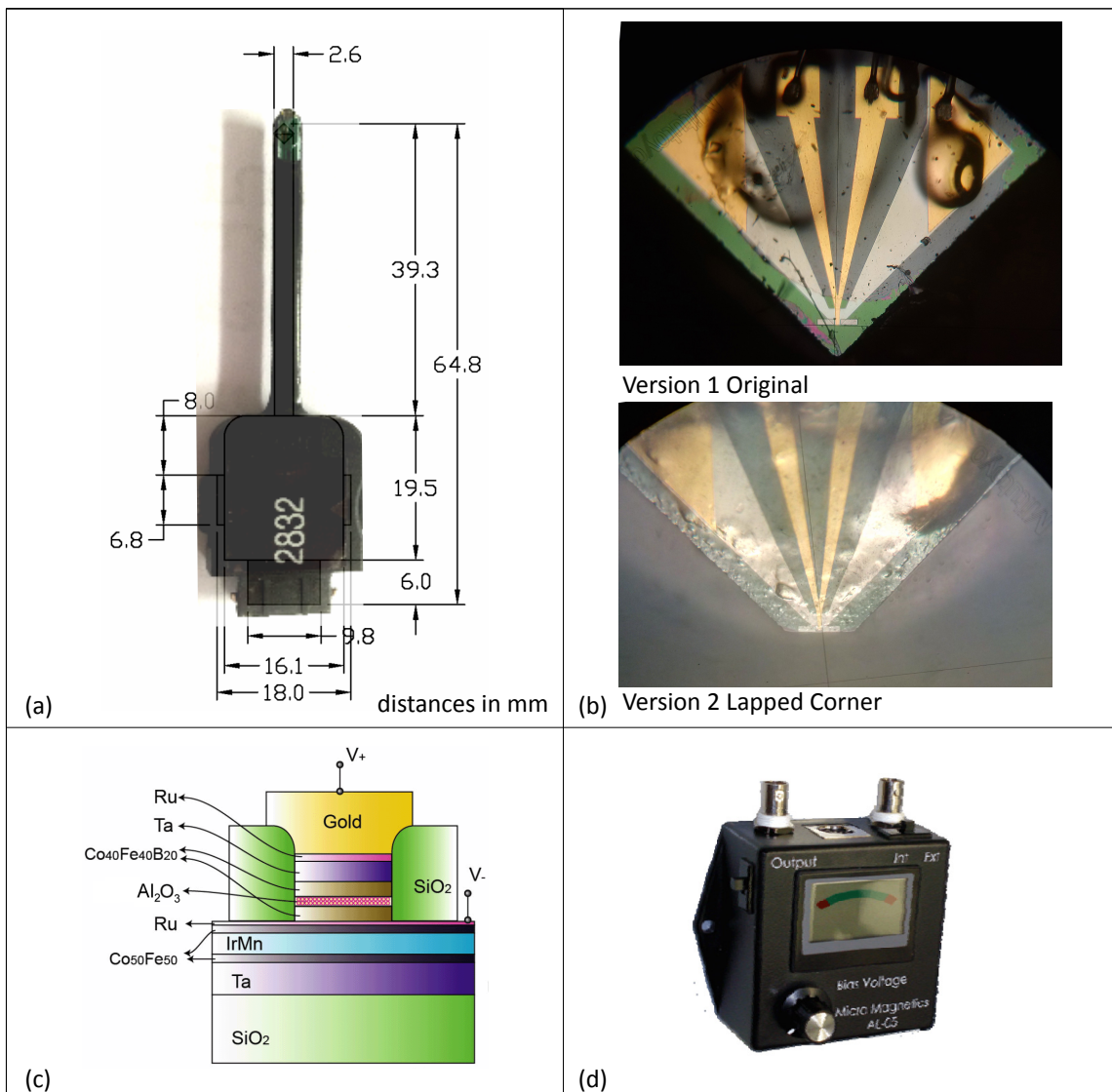


Figure 4.11: (a) Illustration of the TMR-020 sensor, (b) Photograph of microscopic view of the first and second STJ-020 sensor, illustrating the original and corner lapped dies, (c) Schematic of the STJ-020 active sensor area, (d) Photograph of the AL-05 pre-amplifier and power adapter, reproduced from [2].

over a substantial field range. Like the older anisotropic (AMR) and giant magnetoresistive (GMR) technologies, the magnetic tunnel junction is a magnetoresistive device. The SpinTJ product line was created by *Micromagnetics* as part of the development effort on their *Circuit Scan 1000* system [3], which uses magnetic fields to perform diagnostics on semiconductor die and packages because the *CS1000* required very high spatial resolution to be able to see the tiny current paths which exist in integrated circuits.

The STJ-020 sensor requires a power and pre-amplification unit, an AL-05 (Figure 4.11(d)). The pre-amplification circuitry amplifies and filters the voltage across the sensor and outputs an analog voltage proportional to the magnetic field. The design of the preamplifiers allow power supply noise and other common-mode noise across the sensor to be attenuated by over 100 dB. However, the *Micromagnetics* AL-05 power and preamplifier unit (Appendix 4) for the STJ-020 sensor remains electrically noisy which is a limitation discussed in [4]. The merits of this are discussed further in Chapter 6.3. The AL-05 unit permits the tuning of the DC offset voltage for the sensor which has the effect of adjusting the zero point of the sensor. This is done by tuning an adjustment dial, which is a light mechanical potentiometer that has a slight issue of drift evident in some of the results in Chapters 6 and 7.

#### 4.7.2 Calibration of the STJ-020 TMR Sensor

The STJ-020 TMR sensor output potential difference (Volts) has been calibrated to the stray field strength (A/m) by comparison with a factory calibrated Lakeshore 475 DSP Gaussmeter probe placed alongside within a long solenoid of varied energizing current. Photographs of this are presented in Figure 4.12(a-c) along with calibration plots. The coil was of Length 58.5 cm with 364 turns and a resistance of 0.5  $\Omega$ . Calibration was performed for both the basic ohmic potential divider connection to the NI USB 6351 mDAQ (Figure 4.12(d)) and the Low Pass filter connection (Figure 4.12(e)).

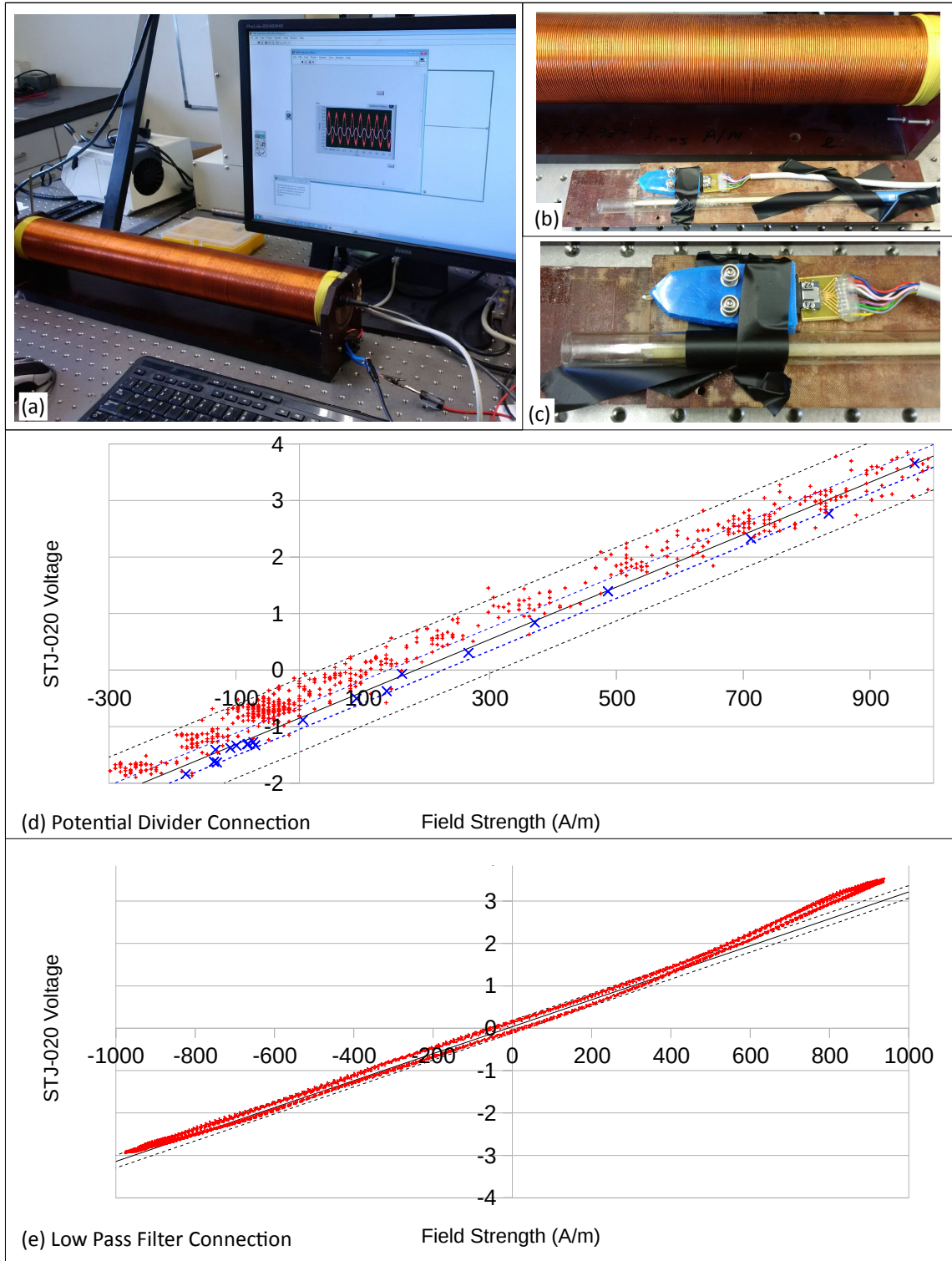


Figure 4.12: (a) The Long solenoid used to produce a varying magnetic field for both the STJ-020 TMR and Lakeshore 475 DSP sensors. (b) and (c) the two sensors mounted alongside on the carrier to be positioned in the centre of the coil. The Calibration of the STJ-020 voltage the Field Strength as measured by the Lakeshore 475 DSP as connected with the Potential Divider (d) and Low Pass Filter (e). For (d), blue crosses are the mean of 10 surrounding samples. Error bands indicated with dotted lines.

The Potential Divider (PD) linear calibration factor has been determined as  $4.63 \text{ mV/Am}^{-1} \pm 90 \text{ } \mu\text{V/Am}^{-1}$ . The sensor exhibits a good linear response in the range -300 to +600 A/m, with the zero-point offset being a result of the setting of the zero point of the DC bias voltage on the AL05. The noise present in the sensor is very evident in [Figure 4.12\(d\)](#), by taking the mean of 10 samples (the blue points) some of this noise can be improved to give a calibration factor of  $4.63 \text{ mV/Am}^{-1} \pm 20 \text{ } \mu\text{V/Am}^{-1}$ . This results in an inverted calibration factor of  $216.0 \pm 0.92 \text{ Am}^{-1}/\text{Volt}$ . FFT analysis of the noise indicated a strong peak of 50 Hz background electrical interference leading to the introduction of the 10 Hz Low Pass filter (Section 4.4.2, [page 68](#)).

The Low Pass filter (LP) linear calibration factor (illustrated in [Figure 4.12\(e\)](#)) has been determined as  $3.36 \text{ mV/Am}^{-1} \pm 10 \text{ } \mu\text{V/Am}^{-1}$ . The noise levels are greatly reduced. The resulting inverted calibration factor is  $296.7 \pm 0.89 \text{ Am}^{-1}/\text{Volt}$ . The broader  $\pm 1000 \text{ A/m}$  range of field presented to the sensor indicates its divergence from linearity at higher field strengths, but the sensor still provides a useful linear response in the  $\pm 500 \text{ A/m}$  range.

The manufacturers stated sensitivity of the STJ-020 [3] is “ $0.01 \pm 0.005 \text{ Oersteds}$ ” ( $0.80 \text{ Am}^{-1} \pm 0.40 \text{ Am}^{-1}$ ) which is in correspondence with the measured  $0.89 \text{ Am}^{-1}$  error. The measured calibration also incorporates the errors introduced by all the other elements of the system.

All the results presented in [Chapters 6, 7 and 8](#) have been presented in A/m using these calibrations.

## 4.8 Lakeshore Hall-Effect Magnetic Field Sensor

The *Lakeshore 475 DSP Gaussmeter* and probe is a Hall-effect based magnetic sensor that is factory calibrated to provide an accurate measure of absolute field strength. At 0.51 mm diameter the active area of the sensor is significantly bigger than the STJ-020 TMR sensor and thus has much lower spatial resolution as a scanning sensor. The Lakeshore was originally intended to be used just to calibrate the STJ-020 TMR sensor (Section 4.7.2, page 74) but after damage to the second sensor (recounted in Section 5.4.2.1) the sensor was used directly for initial investigation of dynamic fields (Chapter 8). Figure 4.13 presents both the sensor schematic and a photograph of the sensor in use during scanning. The Gaussmeter unit itself outputs a voltage on Pin 21 of the rear port which corresponds directly to the number displayed on the front (incorporating the scale and units selected). Whilst the front display is averaged and updated periodically, the rear voltage output is the unprocessed continuous response of the sensor. The full manufacturers specifications are provided in Appendix 4.

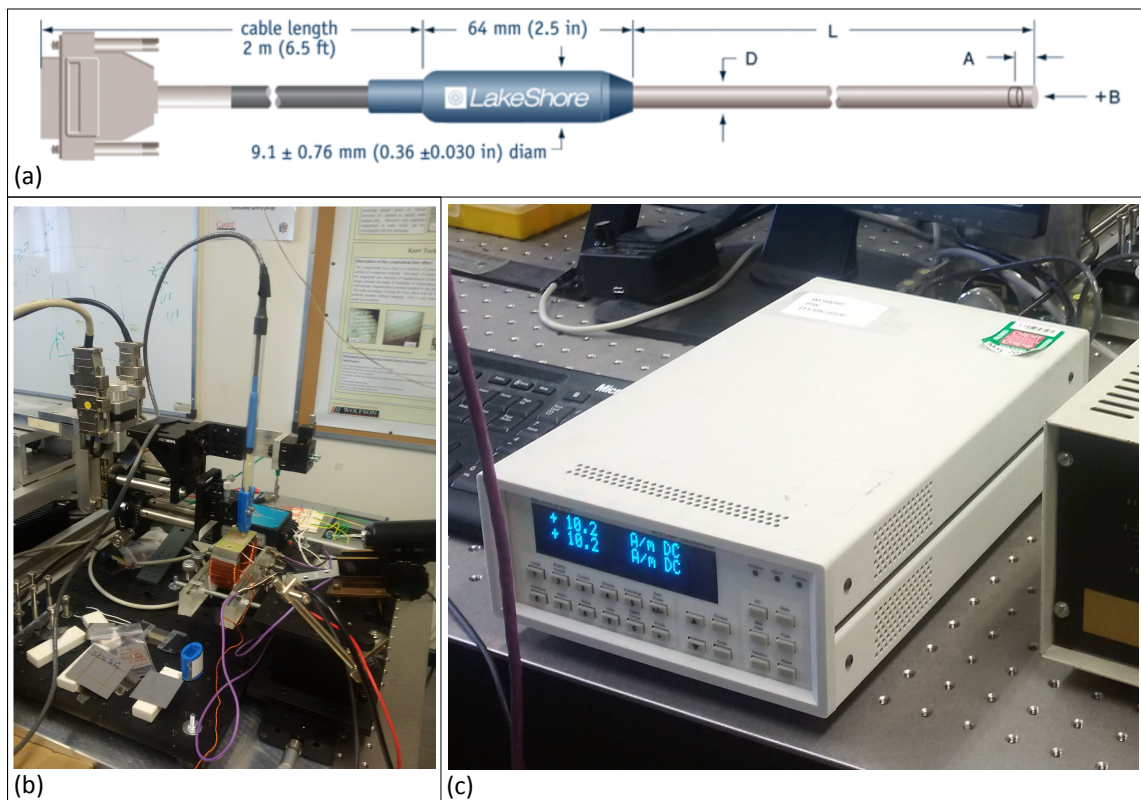


Figure 4.13: (a) Schematic of Lakeshore 475 DSP Axial probe, with an active area diameter (D) of 0.51mm, reproduced from [117]. (b) Photograph of the axial probe attached to Sensor Head 3. (c) Photograph of the Gaussmeter unit itself.

## 4.9 Sensor Head Development

The Sensor Head is mounted to the z-axis carriage, part of the 3-axis framework (Section 4.2.1, [page 60](#)). The Sensor Head holds the sensors correctly in position. Over the development of the system three distinct Sensor Heads have been developed, each with different functionality. Each Sensor Head was developed in *AutoDesk TinkerCAD* and exported as *.stl* files for 3D printing on an *Ultimaker<sup>2</sup>* Fused Deposition 3D printer with 0.4mm Polylactite Acid and a layer height of 100 $\mu$ m. The *.stl* files are available in *Chapter 4.7z* of the Cardiff Portal Arxive ([page ix](#)). The technical projections presented in [Figure 4.14](#) were produced with *AutoDesk Fusion 360* software.

### 4.9.1 Sensor Head Version 1 – Fixed Block

The first Sensor Head ([Figure 4.14\(a\)](#)) was developed for use with the D6 and RC20 displacement and STJ-020 TMR sensors. The simple design holds both the sensors in a suitable position in front of an extension bar attached to the z-carriage and approximately equal distance above the sample. The two part construction allows both installation of the delicate STJ-020 TMR sensor and simplified printing of the orthogonal holes for the screw bolts and the D6 sensor.

### 4.9.2 Sensor Head Version 2 – 3D printed Sensor Pivot

The second Sensor Head ([Figure 4.14\(b\)](#)) was developed for use with the RC20 displacement and STJ-020 TMR sensors, in addition to a pencil USB camera to observe the area being scanned. The complex design allows for tilting of the STJ-020 TMR sensor by 5° in either direction. The design intention was to also enable the RC20 and STJ-020 TMR sensors to sample a congruent area. Unfortunately this extreme proximity and difficulty in construction resulted in the damage to the original STJ-020 TMR sensor (Section 4.6.3, [page 71](#)). After initial investigation, published in [118], the limited tilt (which disproportionately measures  $H_z$  more than  $H_x$ ) and imprecision of the tilting mechanism (which reduced the confidence in sensor position to  $\pm 50 \mu\text{m}$ ) led to the development of Sensor Head 3, utilising a precision tilting mechanism.



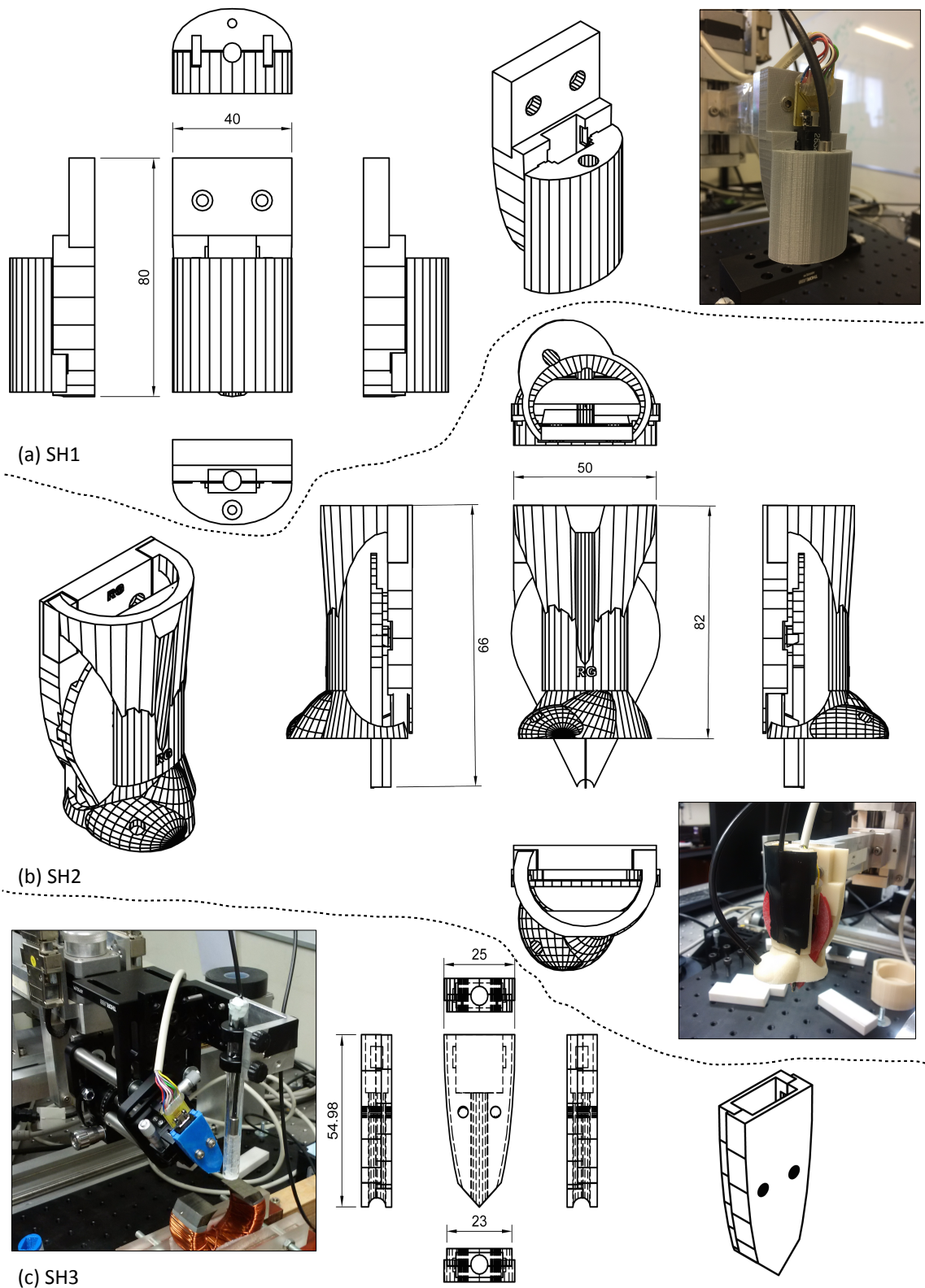


Figure 4.14: (a) Sensor Head Version 1 illustration and photograph, (b) Sensor Head Version 2 illustration and photograph, (c) Sensor Head Version 3 illustration and photograph. Dimensions in mm.

### 4.9.3 Sensor Head Version 3 – Micrometer Rotation Stage Sensor Pivot

The complete Sensor Head 3 assembly ([Figure 4.14\(c\)](#)) is constructed of purchased precision components and a minimal 3D printed STJ-020 TMR container. It was developed using a precision *Thorlabs* CR1/M 360° Continuous Rotator goniometer to tilt the STJ-020 TMR sensor at any angle. Other components purchased to construct the assembly are; a *Thorlabs* MS101 MS-series baseplate, a *Thorlabs* AP90/M metric angle plate, *Thorlabs* AB90E/M right angle bracket, 4x *Thorlabs* TR75/M 75mm Long Metric TR-series Post and importantly 2x *Thorlabs* MS1S/MS 6.5mm Travel, side-actuated translation stages which enable the centre of rotation of the sensor to be aligned precisely with the active area of the sensor. The manufacturers data-sheets for these components can be found in Appendix 4.

Using the integrated microscopic sight and the adjustable micrometers the tip of the sensor can be positioned at the exact centre of rotation. The basic TMR container, presented in [Figure 4.14\(c\)](#), is designed to hold the STJ-020 TMR sensor, but also mounts the *Lakeshore* 475 DSP Gaussmeter probe ([Figure 4.13\(b\)](#)). An additional bracket contains the RC20 displacement sensor independently of the tilting mechanism.

The ability to simply design and print suitable Sensor Heads to fit any new sensor to the scanner hardware makes the system very adaptable to the requirements of future projects.

## 4.10 Sample Stage Development

A *Thorlabs* MB3045\_M Aluminium Breadboard with rubber feet is added to permit various sample platforms to be attached (see Appendix 4).

### 4.10.1 Integrated Microscopic Sight

The incorporated microscopic sight ([Figure 4.15\(a\)](#)) is built from an existing microscope barrel mounted at an angle on a x-axis and z-axis micrometer stage. The microscopic sight allows for accurate calibration of the tip of the sensor at the centre of tilting rotation ([Figure 4.16](#)), accurate positioning of the sensor tip above the sample, and accurate levelling of the sample using the micrometer controlled levelling platform.

### 4.10.2 Micrometer Controlled Levelling Platform

The *Thorlabs* AMA027/M levelling platform ([Figure 4.15\(c\)](#)), in conjunction with the incorporated microscopic sight allows the sample to be levelled over the scan area. Given the impossibility in achieving coincident scanning of the magnetic and displacement sensors within the  $2 \times 4 \mu\text{m}^2$  footprint of the TMR sensor recounted in Section 4.6.3 ([page 71](#)) it was judged the simplest solution was to use manual levelling with a precision levelling platform. The corners of the scan region are registered to a chosen tip height using the micrometer adjustments and the incorporated microscopic sight prior to a scan.

### 4.10.3 Energising Yoke and Coils

The samples can be magnetically energised using either a Yoke or Coils wrapped around the sample. The smaller Yoke ([Figure 4.15\(d\)](#)) comprises a laminated C-core with 110 windings, resistance  $0.5 \Omega$ , the larger Yoke ([Figure 4.15\(e\)](#)) a laminated C-core with 240 windings, resistance  $3 \Omega$ . The first set of Coils ([Figure 4.15\(e\)](#)) comprise two parallel 20 turn windings wrapped directly on the sample, resistance  $0.3 \Omega$ . The second set of Coils ([Figure 4.15\(b\)](#)) comprise two parallel 50 turn windings on sleeves which fit either end of any sample, with a resistance of  $1 \Omega$ .

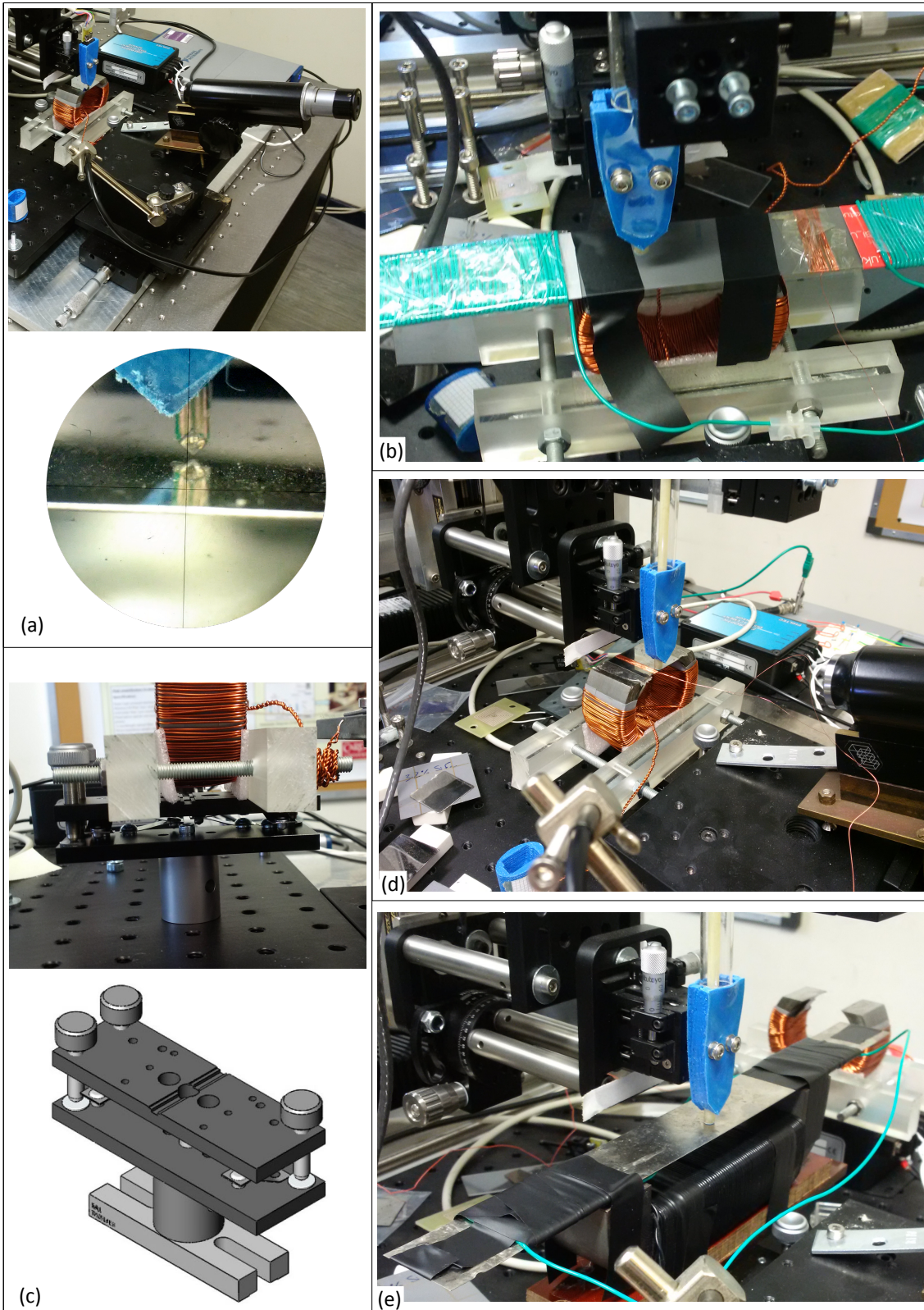


Figure 4.15: (a) Photograph of Microscopic Sight with view through it. (b) Set of 50 + 50 coils in use on a sample of coated Electrical Steel. (c) *Thorlabs* AMA027/M levelling platform, illustration reproduced from [119]. (d) Photograph of Smaller Yoke. (e) Photograph of both the Larger Yoke and 20 + 20 coils on a polished Electrical Steel Sample.

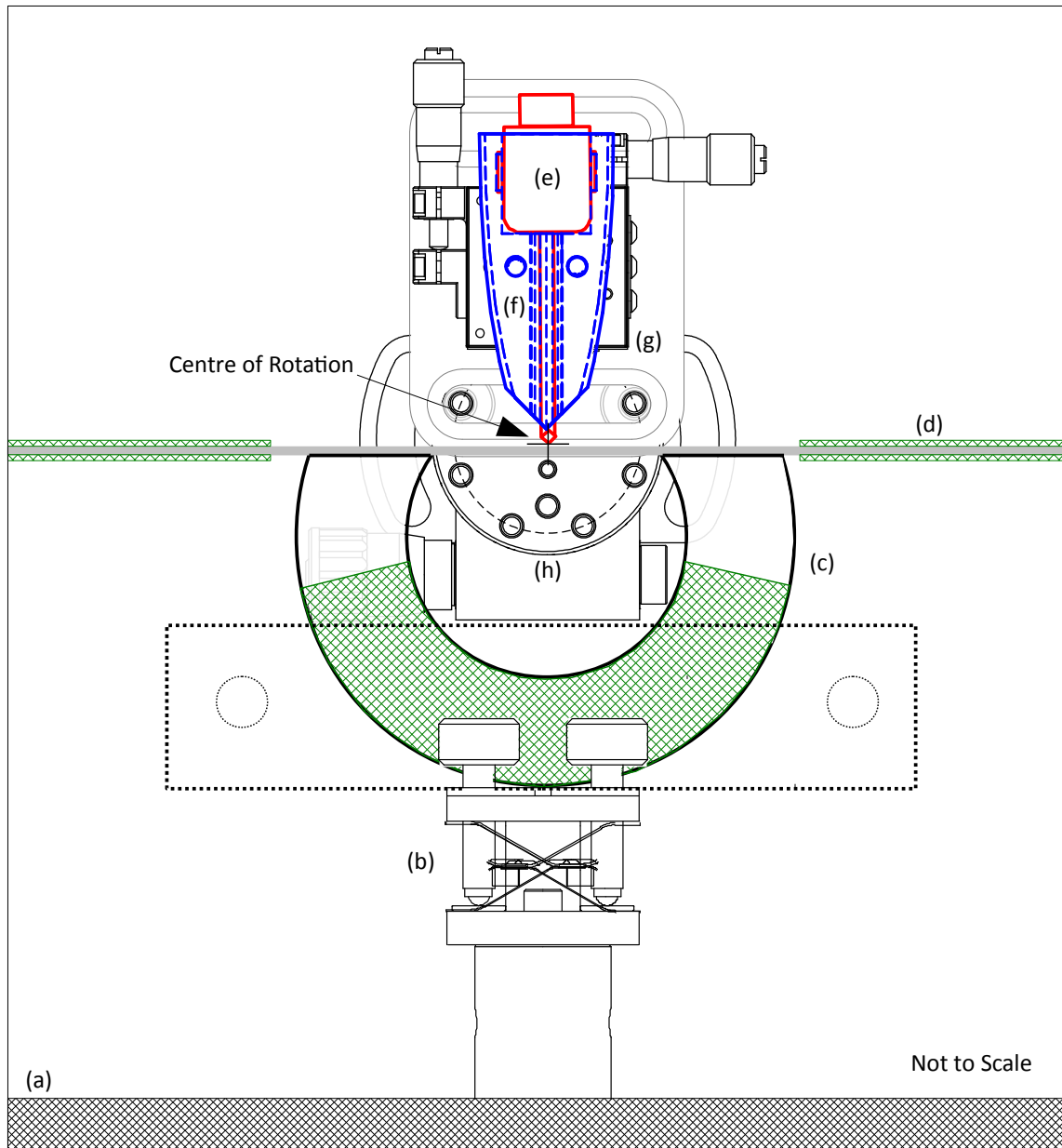


Figure 4.16: Schematic illustration of the sample scanning area featuring the (a) MB3045\_M Aluminium Breadboard and the (b) AMA027/M levelling platform from *Thorlabs* with the (c) Small Yoke and a (d) coated Electrical Steel Sample with 50 x 50 coils attached ([Section 4.10.3](#)). The (e) *Micromagnetics* TMR-020 sensor is encased in the (f) 3<sup>rd</sup> 3D printed sensor head, attached to (g) two MS1S/M translations stages and (h) the CR1/M precision goniometer from *Thorlabs* ([Section 4.9.3](#)).

#### 4.10.4 Energising the Samples for Dynamic Studies

Initially a *TPO 25 Power Oscillator* provided a sinusoidal voltage oscillation of frequency between 0.5 Hz and 25000 Hz and amplitude up to a maximum voltage of 2.5 volts for energising the Yokes or Coils. Due to the age of this unit an irreparable fault developed

after extended operation and it was replaced with a *BK Precision 4054* signal generator and *Amcron DC 300A* power amplifier. Further details of these units are provided in Appendix 4. [Figure 4.17](#) presents the calibration between the voltage provided to the 50 + 50 Coils ([Figure 4.15\(b\)](#)) and the field strength applied by the two coils. This was measured by doubling the result of the field measured inside one of the 50 turn coils by the Lakeshore 475 DSP gaussmeter. The combined coils apply a field of 2.164 kA/m for every volt energising them.

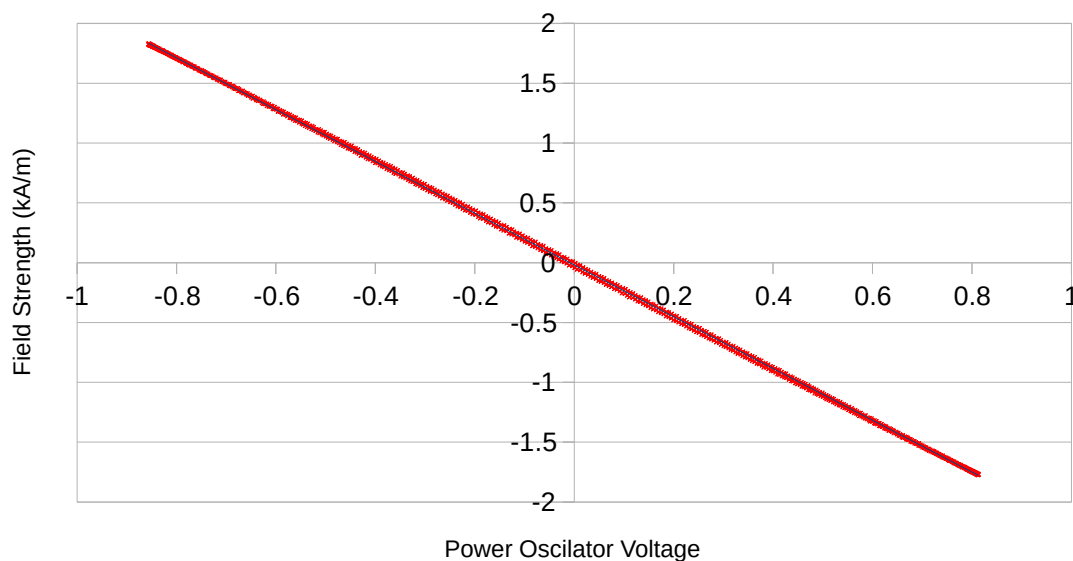


Figure 4.17: Calibration of the field strength of the second set of Coils, two parallel 50 turn windings on sleeves which fit with end of any sample. The coils have a total resistance of  $1\Omega$ . When energised by a power oscillator the combined field strength amplitude of the two coils has been measured as  $2.164 \text{ kAm}^{-1}/\text{V}$  with the Lakeshore 475 DSP gaussmeter.

Together with the Scanner Control Software described in detail in [Chapter 5](#) the hardware of this system successfully fulfils the system requirements described in [Section 4.1.1](#) and allows the study of not only the static domain patterns in magnetic materials, as presented in [Chapter 6](#), but also the novel study of the three dimensional structure of the stray fields presented in [Chapter 7](#) and the study domain wall movement in dynamically energised magnetic samples, the results of which are presented in [Chapter 8](#).

## Chapter 5

# Development of the Scanner Control Software

As the requirements of the Scanner and the understanding of LabVIEW architecture increased three distinct main versions of the Scanner Control Software were developed. The complete structure and functional logic of each Scanner Control system is described in detail in Appendix 1, Appendix 2 and Appendix 3. The pertinent points of the development of the software and its functions are recounted here along with detailed guidance on the practical operation of the final Scanner Control 3 system.

## 5.1 System Overview

From the original PhD specification the development of a novel, versatile operating system for the scanner, using the National Instruments LabVIEW programming language was specified. A capable system has been developed; which can scan and present time-varying data from up to four sensors, over three axis of movement using a user-friendly mouse-based interaction interface.

Three distinct main versions of the Scanner Control Software have been developed. The complete structure and functional logic of each Scanner Control system is described in detail in Appendix 1, Appendix 2 and Appendix 3. The pertinent points of the development of the software and its functions are recounted here along with detailed guidance on the practical operation of the final Scanner Control 3 system. The LabVIEW code for all three systems is provided in *Chapter 5.7z* of the Cardiff Portal Arxive and through the included DVD-ROM ([page ix](#)). Appendix 5 presents a Catalogue of the files available.

### 5.1.1 System Requirements

At its most basic the system must be able to;

- a. Correctly communicate with the Parker Automation hardware to accurately control the position of the scanner head.
- b. Guard against the scanner hardware exceeding its physical limits.
- c. Provide direct user control of the position of the scanner head to  $\pm 1 \mu\text{m}$  precision.
- d. Control the actions of the scanner in a systematic automated scan.

- e. Enable the user to define the automated scan in a simple way.
- f. Acquire voltages inputs from sensors attached to the scanner head and store those values to 3 d.p. alongside the corresponding sensor position.
- g. Display and permit interrogation of those data in both raw form and in the form of a greyscale map at 8-bit resolution whilst storing values at 16-bit.
- h. Enable the saving and loading of previous scans and the resulting data including the export of data in a form which can be understood and analysed externally.

As the capabilities of the system developed and the nature of the resulting data were better defined these basic requirements were greatly augmented. The two main drivers for the continual development of the system were the increase in quantity of data as the system capabilities improved from being able to scan only two axis, to three axis, then to three axis over time; and the increase in understanding [120, 121, 122] of the LabVIEW programming architecture, starting with a continuous-polling model, to an event-driven model, to a hybrid event-driven state-machine based model.

### **5.1.2 National Instruments LabVIEW 15 Programming Language**

The Scanner Control system has been developed in National Instruments LabVIEW 15 (32-bit) [123], a graphical data-flow programming language based on the original 1986 G language developed for the *Apple* Macintosh. The development of the system follows the evolution of both the expanding requirements of the scanner and the authors improving understanding of best programming practices in the LabVIEW language, from zero initial experience.



## 5.2 Scanner Control System 1 – Basic 2D scanning

The first version of the Scanner Control software was in development and use from the 19<sup>th</sup> February 2016 to the 16<sup>th</sup> June 2016. The LabVIEW code itself is available in *Chapter 5.7z* of the Cardiff Portal Arxive ([page ix](#)) and through the included DVD-ROM.

### 5.2.1 SC1 User Interface

The front panel of Scanner Control 1 ([Figure 5.1](#)) combines elements which were initially separated into Hardware Control (on the left) and Scanning and Data Display (on the right). LabVIEW provides no simple way of merging elements from different VIs developed in isolation, and so it is necessary to design the front panel outright from the start. This lack of built in modularity in LabVIEW is something which had to be overcome in future development.

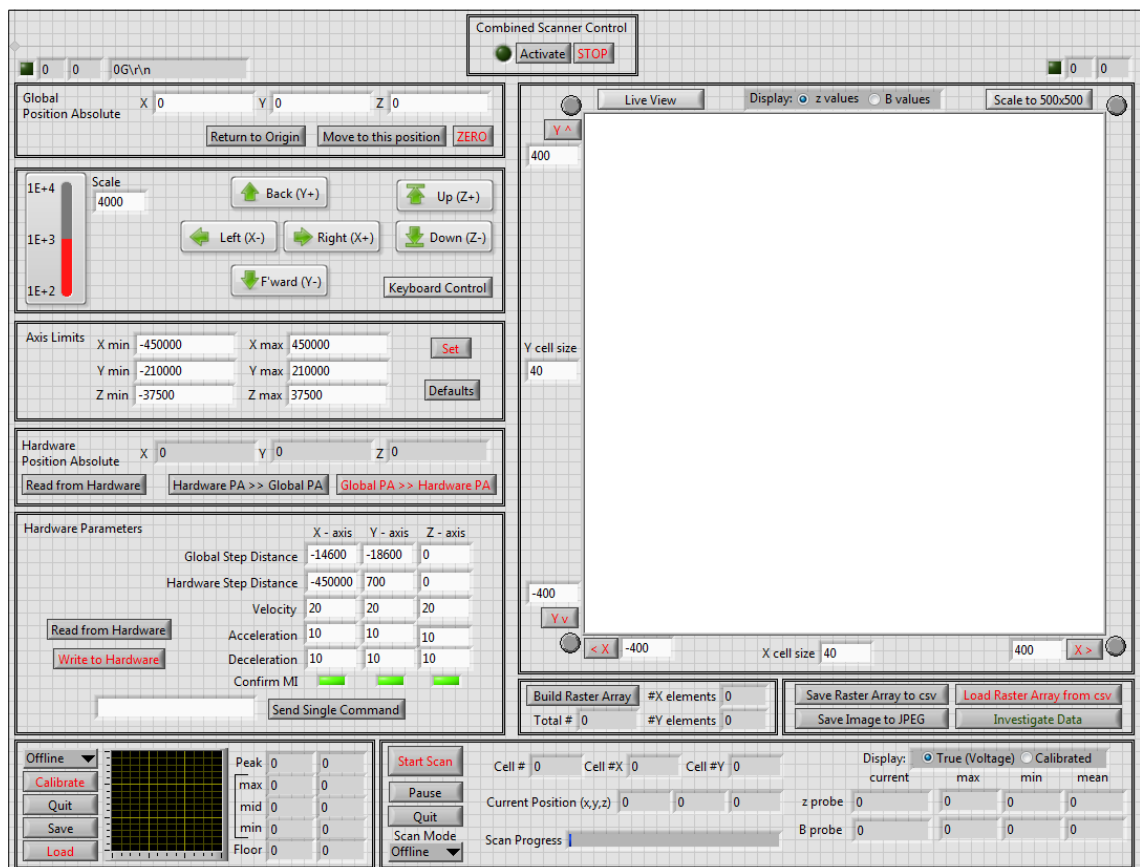


Figure 5.1: The Front Panel interface of Scanner Control 1, separated into distinct functional groups, a merger of Hardware Control and Scanning and Data Display.

The interface is separated into distinct functional groups and this version contains many of the low level hardware parameters, which were useful to understand how the hardware was behaving to begin with, but are not needed in later versions. The basic design elements of arrow based scanner movement controls (linked to the keyboard arrow keys), definition of a scan as a grid of cells of variable size, display of the data as a 500 x 500 pixel greyscale bitmap and control and monitoring of the scan as it occurs were all originated in this version. Scanner Control 1 also included calibration of the displacement probe as a separate activity, which is not something carried forward to the future versions.

### 5.2.2 SC1 LabVIEW Code

The software is structured as a main Virtual Instrument (VI), 19 subVIs and 10 Global Variables. The main Block Diagram is presented in [Figure 5.2](#), the functionality of each element of code is explained in detail in Appendix 1. The main VI employs a continuous polling structure for all of the controls on the front panel; before it was learnt that such a model is CPU resource intensive and how an Event based structure could be used instead. The main block diagram is divided into six parallel While loops. The first loop controls the termination of the system by polling the STOP button. The second updates and maintains the “Active” flag in order to disable direct user control of the scanner when an automated scan is occurring. The “Axis Control Front Panel” While loop handles motion control and hardware parameters. The “Raster Scan Front Panel” While loop handles the setting of the Scan Area, movement of the scanner to the corners of the scan area and file management for saving and loading the data. The “Update Live Front Panel Elements” while loop handles the constant updating of Front Panel elements including the Bitmap display (updated live during a scan), the “Scan Progress”, current position and the calibrated probe values display. Scanner Control 1 originates the use of boolean arrays throughout the system to enumerate which case is needed for different actions.

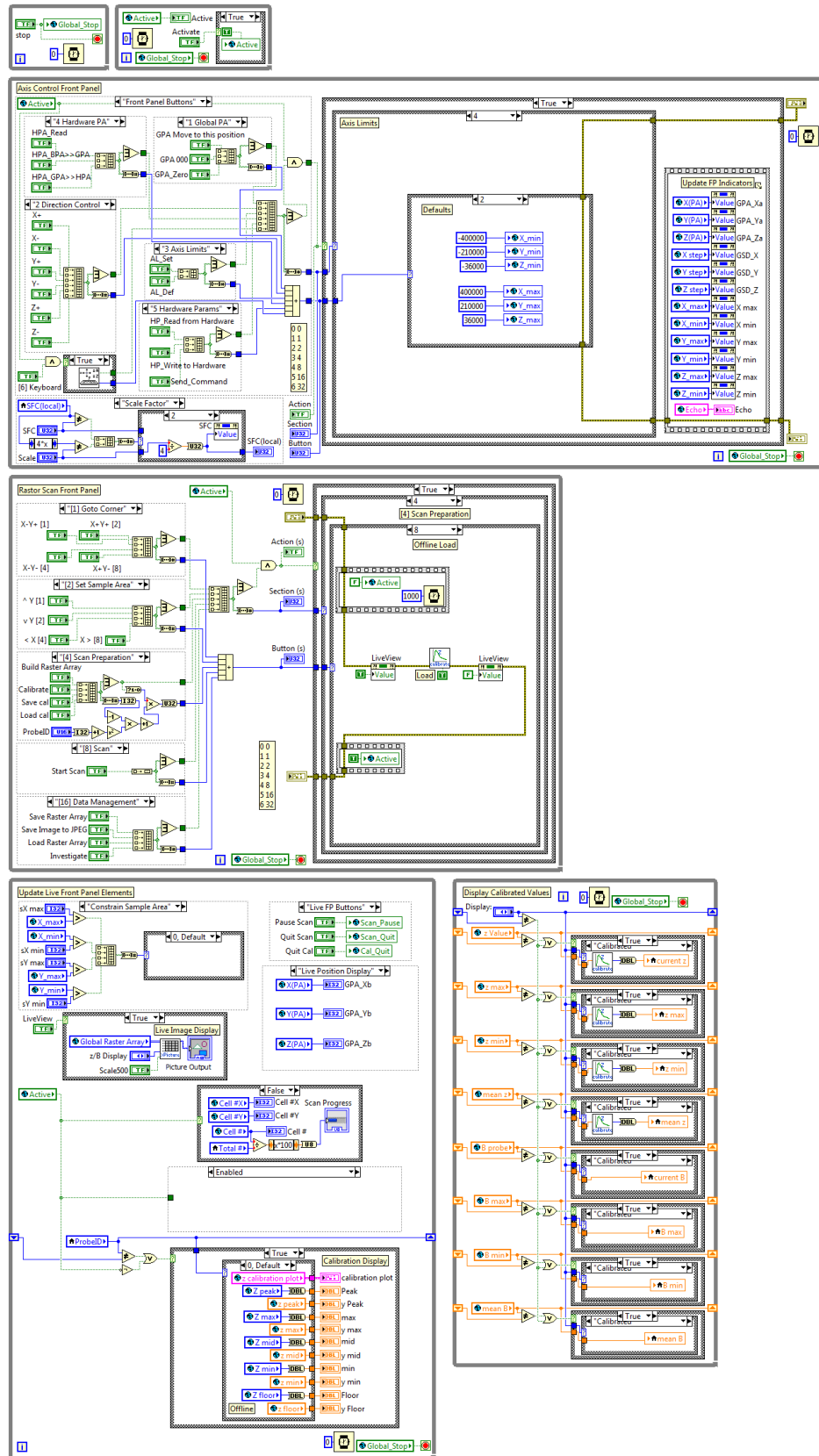


Figure 5.2: The Block Diagram of Scanner Control 1. The main block diagram is divided into 6 parallel While loops.

## 5.3 Scanner Control System 2 – 3D Volume scanning

The second version of the Scanner Control software was in development and use from the 9<sup>th</sup> June 2016 to the 23<sup>rd</sup> May 2018. The core user differences between the second and first versions of the Scanner Control software were an innovative implementation of mouse-based interaction with the data display, and the ability to scan in three dimensions, rather than just the *xy*-plane. The core differences in LabVIEW architecture were greater modularity, adoption of event-based rather than continuous-polling architecture, the use of shift-registers rather than global variables with the beginnings of the use of single iteration While loops. This version was the first to incorporate the slack/backlash compensation discussed in [Section 4.2.2](#) and [Section 5.4.2.3](#) ([page 106](#)). The LabVIEW code itself is available in *Chapter 5.7z* of the Cardiff Portal Arxiv.

### 5.3.1 SC2 User Interface

The main front panel ([Figure 5.3](#)) is divided into three tab groups. Each group manages a specific function of the system. The first tab group manages control of the motion, position and parameters of the hardware. The “Y+”, “X-”, “Y-” and “X+” buttons are used to move the scanner by the Step amount set and can also be controlled by the corresponding *keyboard arrow keys*, with *PgUp* and *PgDn* for the “Z+” and “Z-” buttons. The Z-lock button sets a floor value for the scanner. The second tab group manages display of the collected data and selection of the region to be scanned. The Bitmap Display tab is an innovative interface where, uncommon in LabVIEW, mouse-based interaction on a Bitmap display has been achieved. Along the left and bottom edges of the display are inputs defining the coordinates of the scan region and the Cell size (in steps), which when combined with the corresponding Max and Min z-axis values on the right hand side allow a volume to be defined and scanned. The two “Greyscale” sliders define which voltage levels represent Black and White on the 256 greyscale range, to permit different contrast levels to be set. “Magnify” indicates the magnification factor being applied to the display, which can also be changed using the Mouse Scroll-Wheel. Further Mouse-interaction with the display area includes: Left-click-and-drag to move the data around inside the window, Left-single-click to select a single cell for

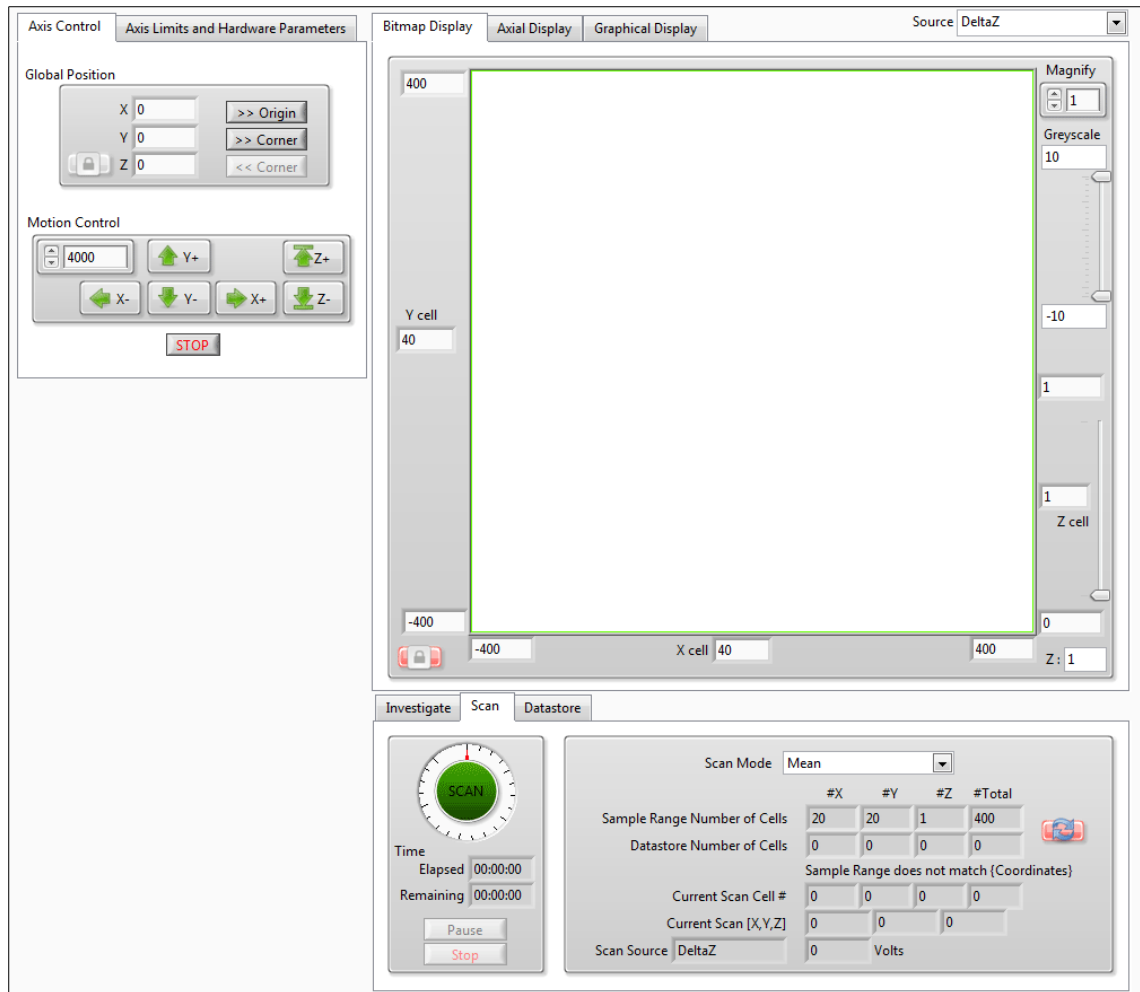


Figure 5.3: The Front Panel interface of Scanner Control 2 with Tab elements separating distinct functional groups.

investigation, Right-single-click to define the sample area and Middle click to move the scanner to that cell. The lower tab group manages investigation, acquisition and long term storage and retrieval of the data. The Investigate tab presents the numerical values for the Cells in the data, the current position of the scanner and the current cell over which the mouse pointer is hovering. The Scan tab permits initiation and control of a scan. The Scan Mode can be selected and is a modular element of the code so new methods of scanning could be developed. The current input/displayed source is selected in the menu on the top right corner. The Datastore tab permits the resulting data from a scan to be saved to a file and retrieved and redisplayed. Further details on the interface of Scanner Control 2 are provided in Appendix 2.

### 5.3.2 SC2 LabVIEW Code

The software block diagram for Scanner Control 2 (Figure 5.4) is structured as a main Virtual Instrument (VI), 14 subVIs and 1 scratch file. The functionality of each element of code is explained in detail in Appendix 2.

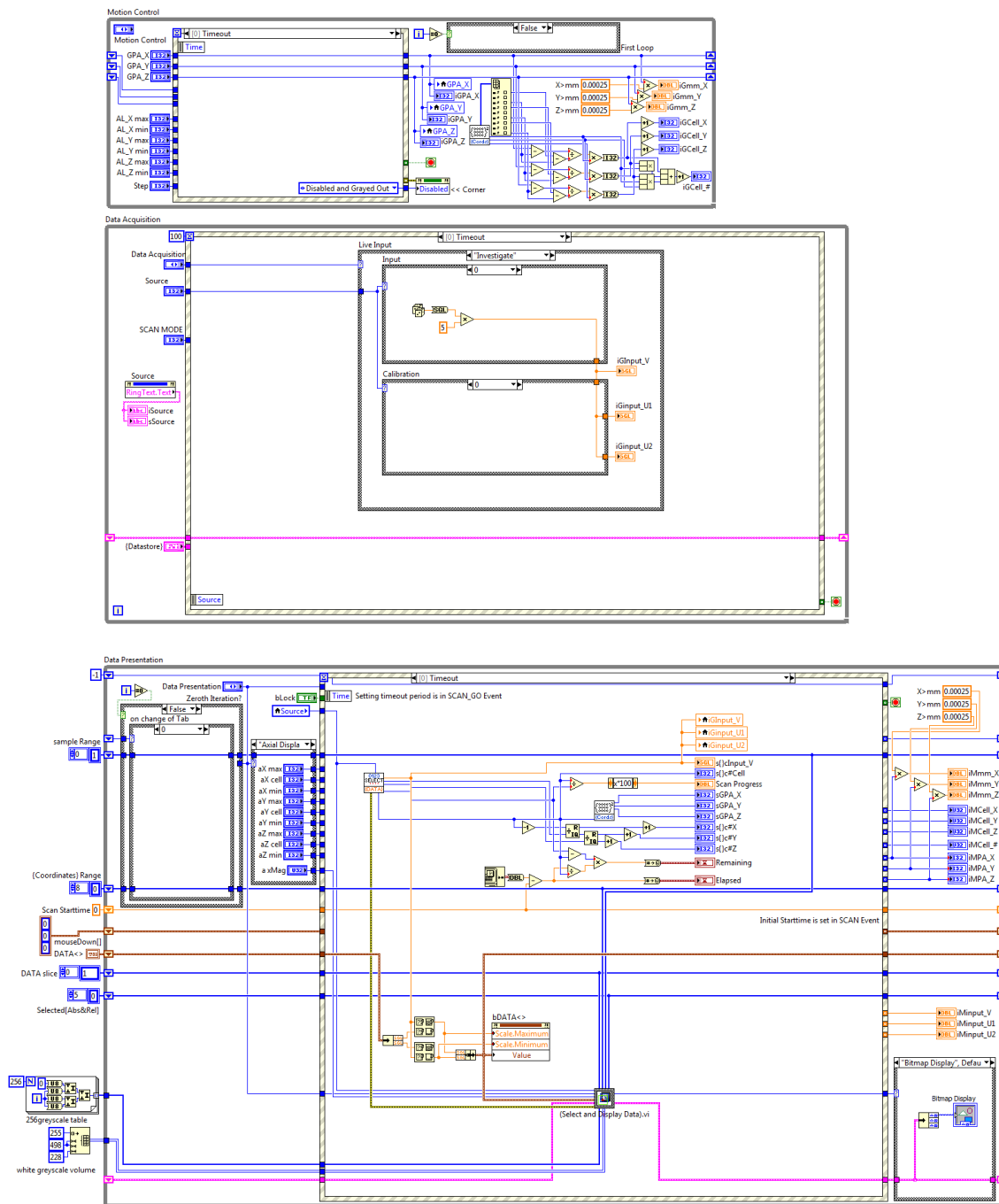


Figure 5.4: The Block Diagram of Scanner Control 2. The main block diagram is divided into 3 parallel While loops.

The main block diagram is divided into three parallel While loops which govern “Motion Control”, “Data Acquisition” and “Data Presentation”. The “Motion Control” loop handles the movement of the Scanner Hardware, input from the Axis Control and Axis Limits tabs, and communication with the scanner hardware. The current position of the Scanner is maintained in three shift registers. The Axis limits which prevent the scanner moving beyond the physical extent of the hardware are maintained by the Front Panel control values. An Event structure handles the control input. The “Data Acquisition” loop handles the acquisition of data during a scan. It is contained within its own parallel while loop to enable the operation of collecting data to be timed in isolation from the timings of user-interface interaction. This while loop also handles the saving and loading of data from a file. The third “Data Presentation” while loop contains an event structure of 24 events that handles the display of the data, defining the scan area and the innovative mouse-based interaction. Shift registers are used to store all the variables not represented by Front Panel controls and are initiated on first execution. “DATA<>”, “DATA slice”, “Selected[Abs&Rel]”, “256greyscale table” and “white greyscale volume” are collectively the inputs needed by the *(Select and Display Data).vi* subVI to produce a Bitmap of the data. Many of the repeated and complex data processing activities are undertaken by subVIs called by the main Virtual Instrument. In this way some modularity was introduced into the code. Different modes of performing a scan, from a basic single sample, to a mean of twenty samples, to the sampling of more than one source at a time could be independently developed and included in the ...*[Scan Modes]* directory for use during Scanner Control 2's period of operation. Each of the input sources could be given its own ...*{Data Arrays}* subVI for storing of the data. These subVIs were single-iteration while loops which used uninitiated shift-registers to store the data in RAM, rather than the disc storage used by the Global Variables of Scanner Control 1. This architecture is formally called a *Functional Global Variable* by National Instruments [124]. It has good speed benefits over accessing the disc, but issues were encountered when the number of cells being collected (for a large three-dimensional scan) exceeded the available RAM allocated to the shift-registers. Further details are given in Appendix 2.

## 5.4 Scanner Control System 3 – Dynamic 3D Volume Scanning

The third and final version of the Scanner Control software has been in development and use from 22<sup>nd</sup> June 2018. The LabVIEW code itself is available in *Chapter 5.7z* of the Cardiff Portal Arxive ([page ix](#)) and through the included DVD-ROM. The core user difference between the third and second versions of the Scanner Control software are the ability to acquire, store and present time-series data for each of the cells of a three-dimensional scan, to be able to study domain dynamics. The quantity of data collected for these types of scan prohibited the use of shift-register based storage in RAM. Instead a hybrid between shift-registers, where possible for speed, and .csv scratch files for quantity had to be developed from the outset. The use of LabVIEW “clusters” is more prevalent for the storage of the different front panel controls, those which are part of the same functional group ([Figure 5.5](#)). System variables and user front panel controls are stored in *Functional Global Variables* (subVIs with shift registers on single-iteration while loops) which are called as needed, rather than all being kept on the while loop of the main VI, to greatly simplify the wiring without the performance penalty of using disc based Global Variables. The use of Tabs on the main Front Panel is reduced, to clarify the display, but the use of Front Panels in subVIs, which appear in defined positions when called, enables extra features to be presented when needed. The mouse-based interaction on the bitmap display has been greatly refined and is explained here in detail alongside the process of producing the bitmaps and saving the data. Two file formats have been created for “Static” and “Dynamic” (time-series) scans with formats which can be readily interpreted externally to the system and are described here. Scanner Control 3 is also capable of reading the “Legacy” file format from Scanner Control 2. All the data which supports the results presented in this thesis, available in the Cardiff Portal Arxive ([page ix](#)) and through the included DVD-ROM, are saved in Scanner Control 3 format as a “Static” *[S].csv* or “Dynamic” *[D].zip* files. The system is designed for four independent sources to be sampled during scanning and these can be changed by simply redefining the list and DAQ Assistant parameters in the *(Input).vi* subVI, providing great versatility and modularity. Any additional processing of the data from scans, such as synchronising the frames of a “Dynamic” scan or the



combination of multiple scans into one output, can be added as extra modules to the ...\*subVis*\(Processing\) directory and the *PROCESS.vi* subVI shell – facilitating future expansion of the system.

### 5.4.1 SC3 User Interface

The Front Panel of Scanner Control 3 (Figure 5.5) presents all of the controls necessary to operate the scanner and visualise and process the resulting data. The controls are grouped into different functional groups using Clusters. A detailed description of the operation of the system is provided in Section 5.5 *Practical Considerations when Using the Software* (page 123). A Tab selection is used to switch between views of the data.

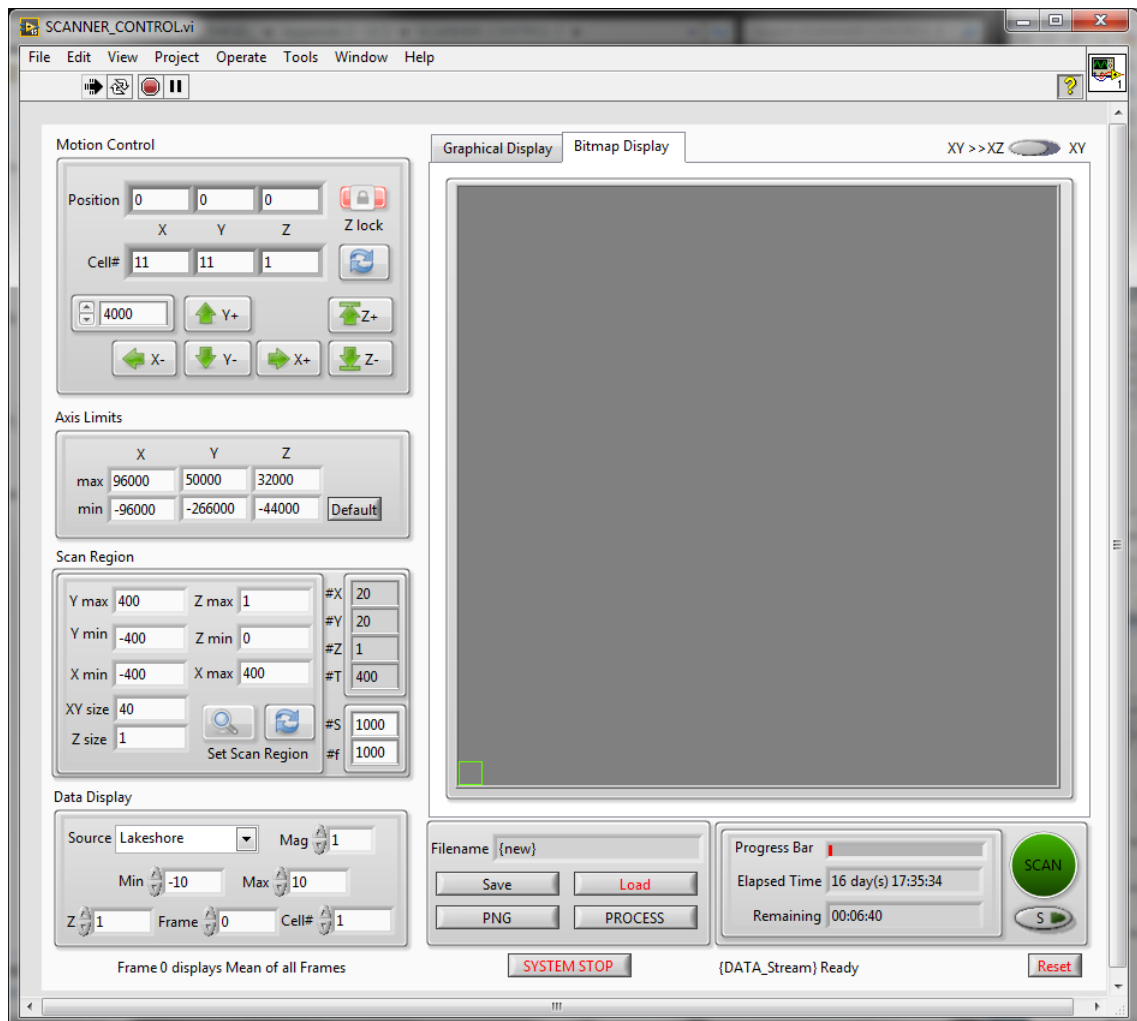


Figure 5.5: The Front Panel interface of Scanner Control 3

### 5.4.2 SC3 LabVIEW Code

The software is structured as a main Virtual Instrument (VI) with 22 subVIs and a number of scratch files stored in the *D:\scanner\_scratch\* directory. The functionality of each element of code is explained in detail in Appendix 3. The main block diagram (Figure 5.6) is divided into an *Initialisation* sequence and two parallel While loops which manage the *User Interface* and *Data Acquisition*. The hard-coded “Offline” flag should be set true if the code is run without being connected to the Scanner hardware and set false if the Scanner hardware is attached and active. Unlike Scanner Control 2, Scanner Control 3 makes extensive use of *Functional Global Variables* [124] rather than numerous shift-registers on the main user interface.

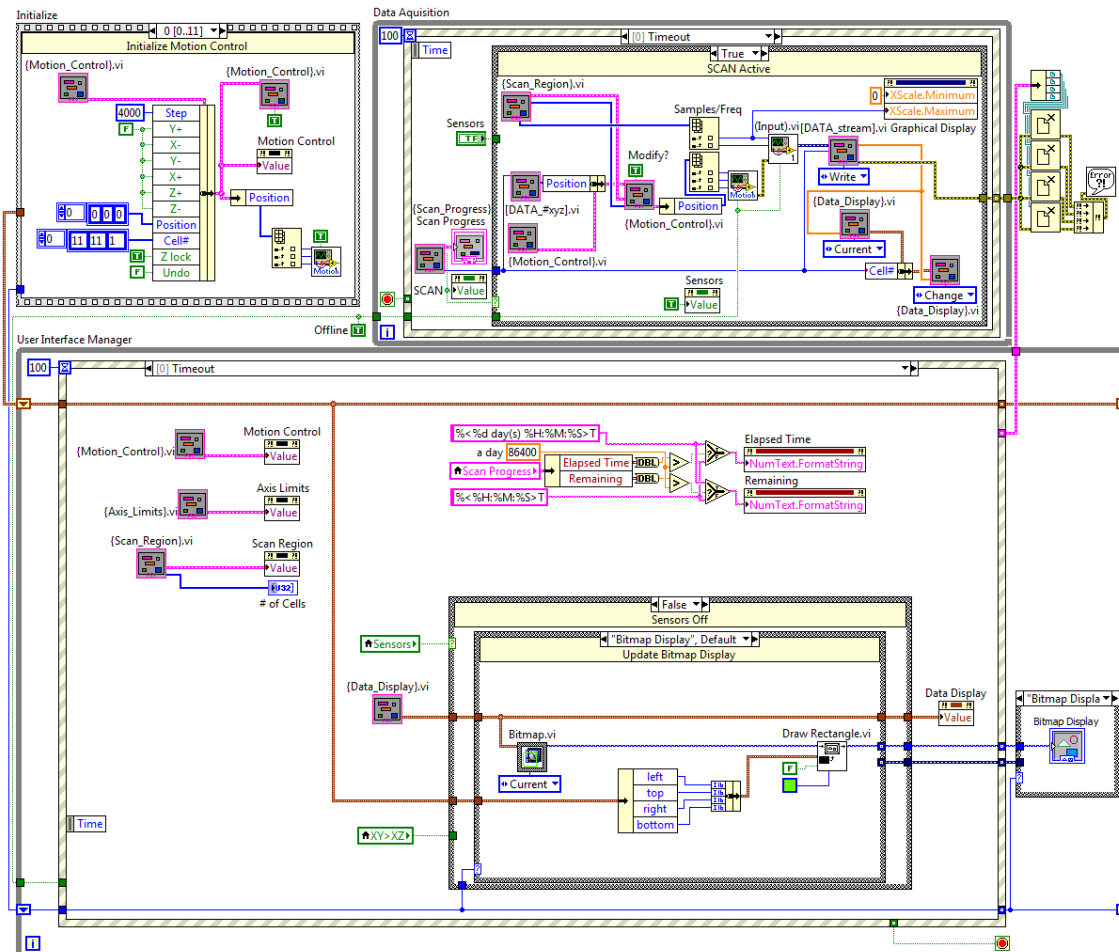


Figure 5.6: The Block Diagram of Scanner Control 3 divided into an initialisation sequence and 2 parallel while loops which manage the user interface and data acquisition.

Two shift-registers remain; the “Mousedown and Selection” cluster and the “Graphical Bitmap Tab” state. The Data Acquisition while loop executes immediately but does nothing unless “SCAN” is true. The remaining groups of controls are stored and managed by one of the 22 subVIs presented in [Figure 5.12](#).

The *Initialisation* sequence executes before the two While loops begin and initialises the front panel controls, internal registers and subVIs when the system is first run. The *User Interface Manager* is an Event structure controlled While loop with a timeout state of 100 ms. Termination of the while loop is Event controlled. The *Data Acquisition* while loop allows for parallel timing of the collection of data from the sensors during a scan.

#### **5.4.2.1 Axis Limits, a critical error during development**

Event 12 of the *User Interface Manager* ([Figure 5.7](#)) handles a change in the set values of the physical maximum extents of each axis, the *Axis Limits* group ([Figure 5.5](#)). These values are stored in the *(Motion).vi* subVI discussed in [Section 5.4.2.3 \(page 106\)](#) which is called by the event and passed the new values. When this call is made the two green boolean flags (*SC3v2*, [Figure 5.12](#)) “adjust Axis Limits” and “adjust PA without move” must be set to true, to enable the Axis limits to change and, critically, to prevent the scanner moving during this change. At some point during development an error was made which resulted in a missing wire to the “adjust PA without move” flag. During the first use of Scanner Control 3 a change to the minimum z-axis limit was made to allow the second of the STJ-020 sensors ([Section 4.7](#)) to approach the sample. Unfortunately the error in wiring meant that *(Motion).vi* responded by trying to position the sensor at that lower limit, crashing the sensor through the sample. The third of the STJ-020 sensors was acquired as a replacement, but an important lesson was learnt about the dangers of and care needed over apparently minor errors in code.

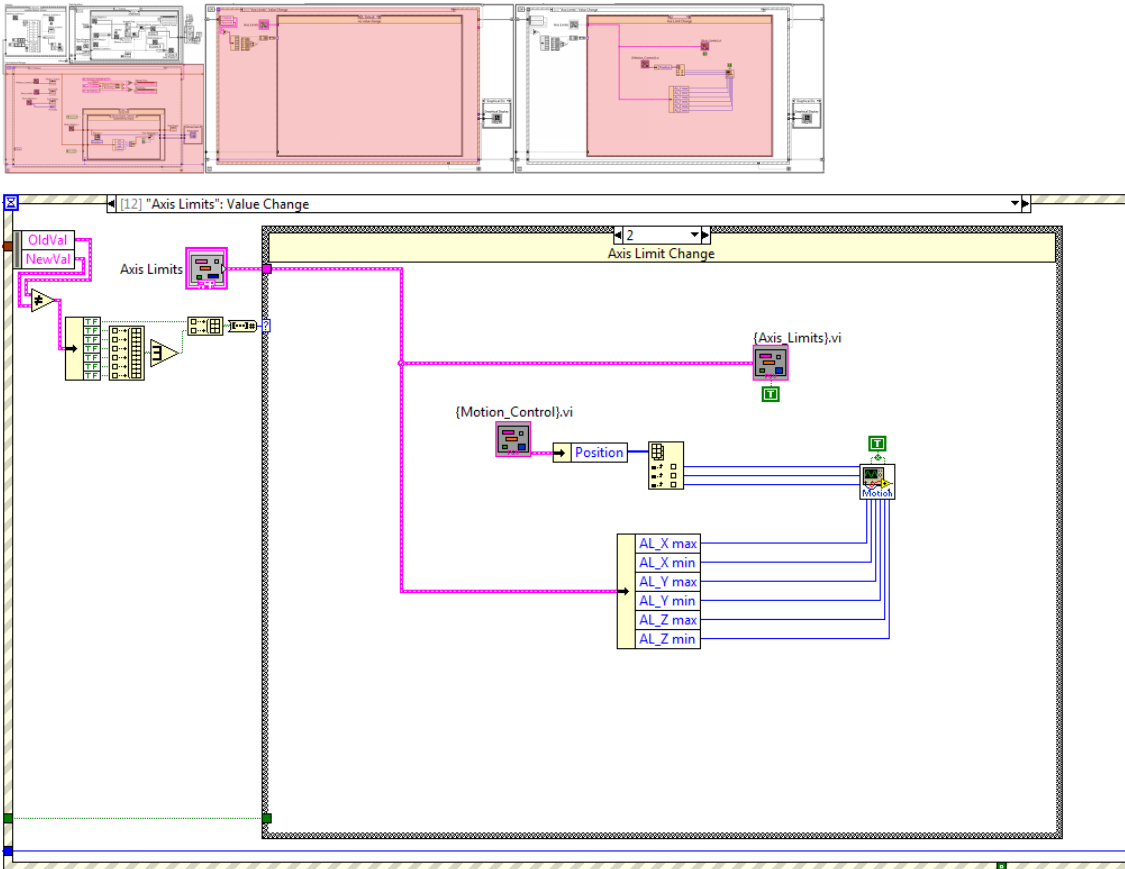


Figure 5.7: Case 2 of the 12<sup>th</sup> Event of the 1<sup>st</sup> While loop of Scanner Control 3 (SC3w1e12c2 in Appendix 3) enables the *User Interface Manager* to handle an “Axis Limit Change” to the “Axis Limits” group. Failure of a wire of True to the first boolean terminal of (Motion).vi was a critical error during development. Case 1 in this event (SC3w1e12c1), setting “AL\_Defaults”, contained the same error.

**5.4.2.2 The mouse-based interaction on the bitmap display**

The mouse-based interaction on the bitmap display is managed by Events 8 through 11 of the *User Interface Manager*. On clicking on the Bitmap display area a Mouse Down event occurs (Figure 5.8) and the coordinates of the click (relative to the top left corner) and the button pressed are provided by the operating system. The coördinates relative to the bottom left corner are calculated and stored in the “Mousedown and Selection” cluster register. A cluster is used rather than an array to ease with labelling and identifying the elements, and extracting only the required elements. The mouse button which was pressed is stored and the four coördinates which define the “Selection Rectangle” are set to zero.

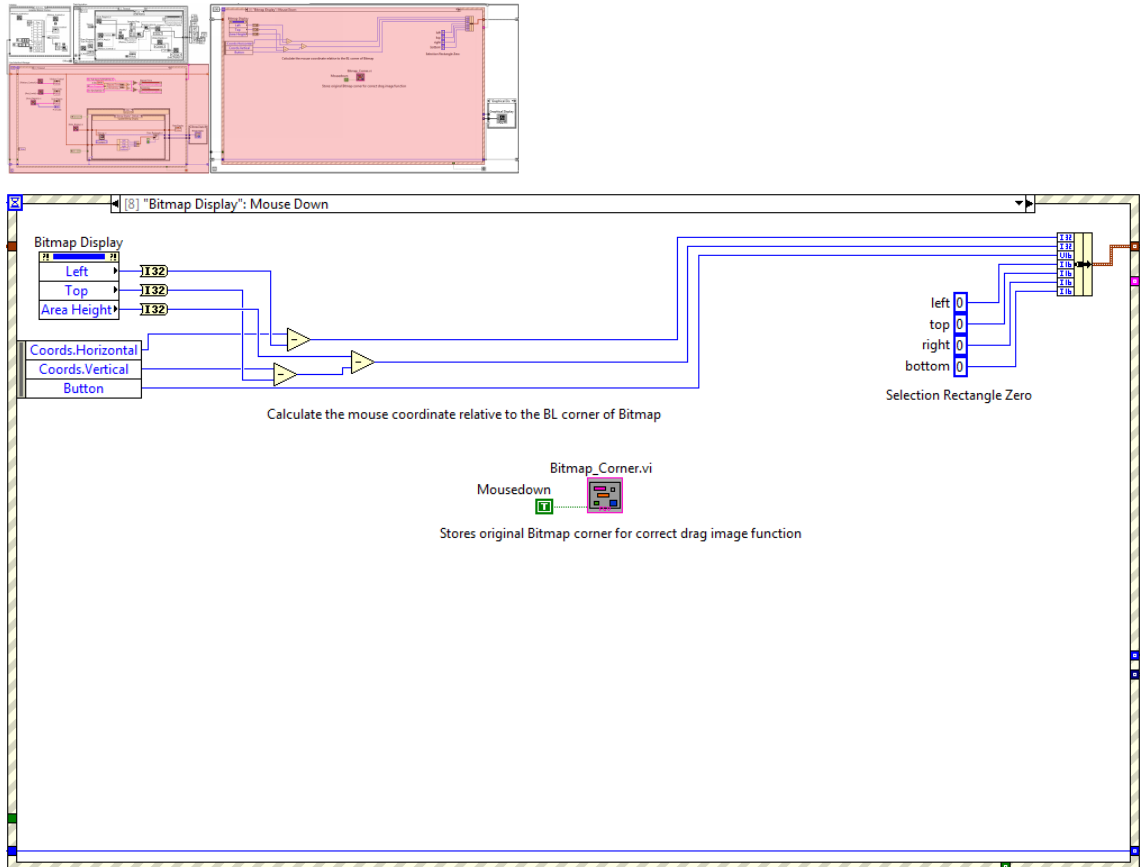


Figure 5.8: The 8<sup>th</sup> Event of the 1<sup>st</sup> While loop of Scanner Control 3 (SC3w1e8 in Appendix 3). Mouse Down on the “Bitmap Display”.

The “Mousedown” flag of *Bitmap\_Corner.vi* (SC3v12, Figure 5.12) is triggered to store the current Bitmap corner, which represents the location of the 500 x 500 pixel window over the data. Any movement of the mouse over the Bitmap display triggers a Mouse Move event (Figure 5.9) with different cases (Figure 5.10) to execute different actions depending on the button pressed. The “Mousedown and Selection” cluster provides the button that was pressed and the original click position relative to the bottom left corner. Each case is passed;

- the original click position
- the current difference in position ( $\Delta x, \Delta y$ ) relative to the original position with a boolean check as to if there is a difference
- calculation of the current mouse position relative to the bottom left corner
- the registers of *{Scan\_Region}.vi*, *{Data\_Display}.vi* and *Bitmap\_Corner.vi*

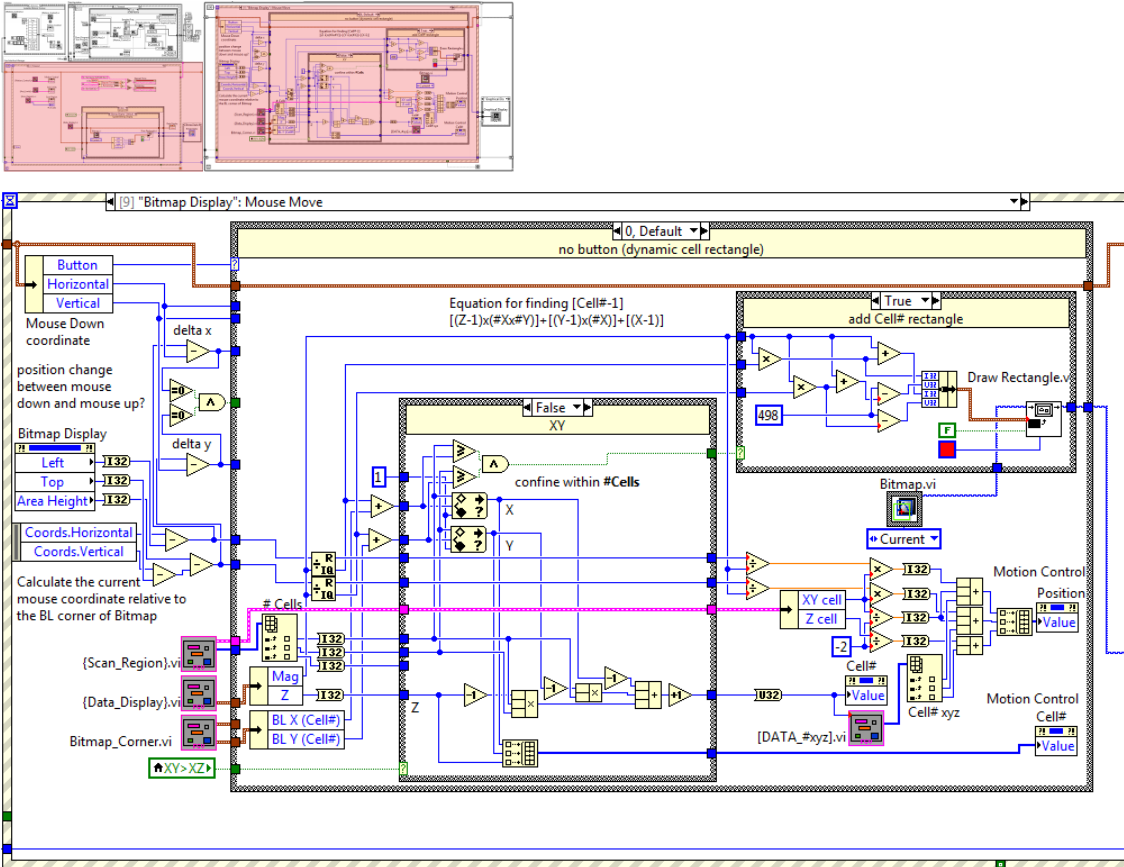


Figure 5.9: Case 0 of the 9<sup>th</sup> Event of the 1<sup>st</sup> While loop of Scanner Control 3 (SC3w1e9c0 in Appendix 3). Mouse Move over the “Bitmap Display” with no button pressed. A red rectangle outlines the cell currently hovered over.

If the mouse moves over the Bitmap display without a button being pressed (Figure 5.9) then a red bounding rectangle highlights the current cell over which the mouse is “hovering”. The current mouse position relative to the bottom left corner is used. The number of Cells on each axis (“# Cells”) and the Cell size (“XY cell”, “Z cell”) are provided by the registers of {Scan\_Region}.vi. The magnification factor and current Z layer are provided by the registers of {Data\_Display}.vi. The bottom-left-most cell of data within the display window is provided by Bitmap\_Corner.vi (Figure 5.12). These are used to calculate which relative cell the mouse is currently over, in terms of the number of cells along each axis of the Bitmap display. The absolute cell index (X#,Y#,Z#) and cell number (Cell#) of that cell are then determined, confined within the available data, performing a check to see if the mouse is currently hovering over an area outside of the available data. The X#,Y#,Z# cell index array is passed to the Motion

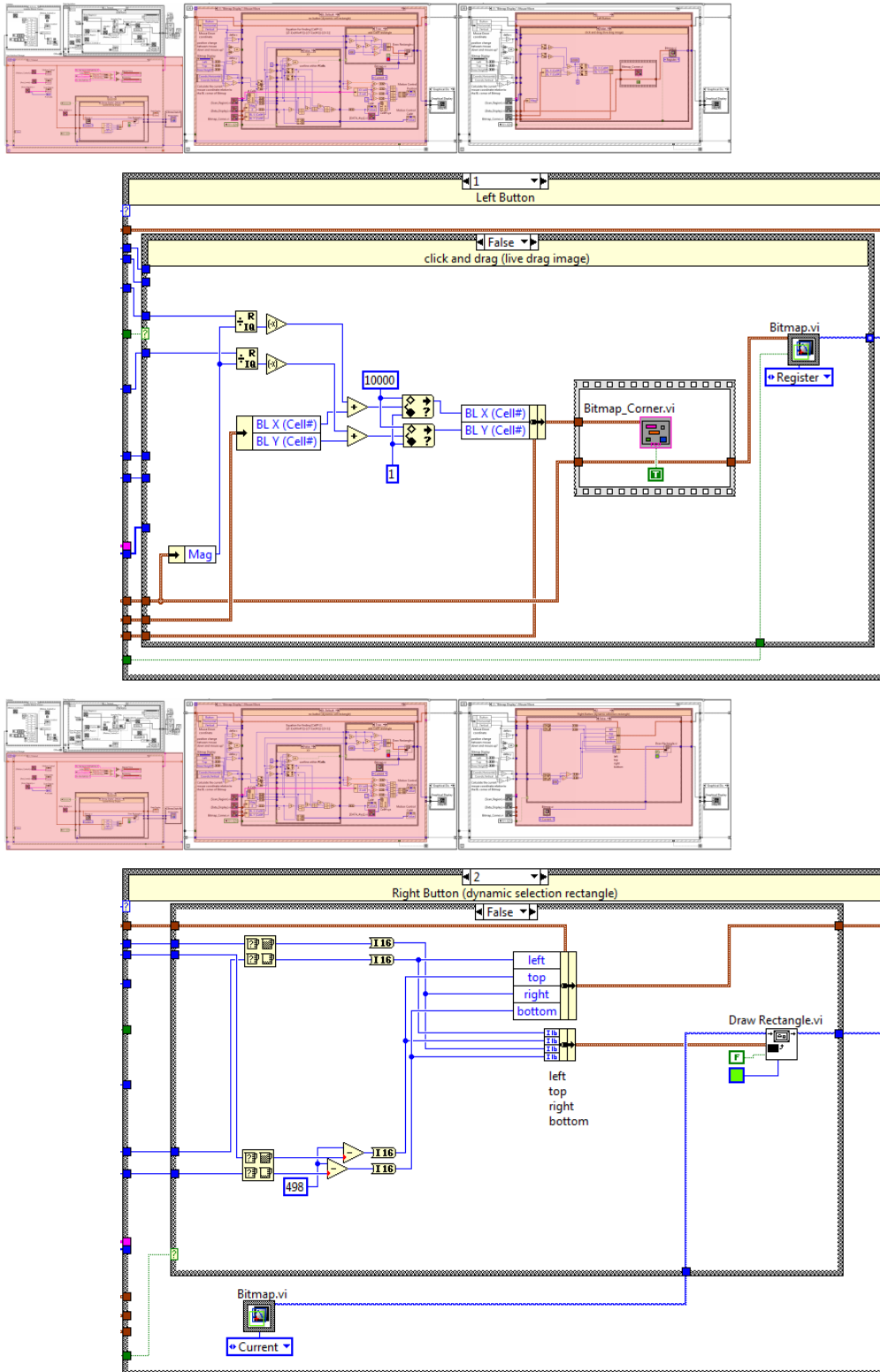


Figure 5.10: Case 1 and 2 of the 9<sup>th</sup> Event of the 1<sup>st</sup> While loop of Scanner Control 3 (SC3w1e9c1 and SC3w1e9c2 in Appendix 3). Mouse Move over the “Bitmap Display” with left or right button pressed. Dragging the greyscale image of the data or drawing a green selection rectangle.

Control “Cell#” indicator and Cell# is passed to *[DATA\_#xyz].vi* to retrieve the coördinates of the centre of that cell and display them in the Motion Control “Position” and Data Display “Cell#” indicators (Figure 5.5).

Moving over the “Bitmap Display” with a mouse button pressed is handled by Case 1 and 2 of Event 9 (Figure 5.10). Momentarily left-clicking on a cell in the Bitmap display selects that cell, placing a red rectangle around it and registering its number in the Cell# indicator in the Data Display group. Left-clicking and dragging the Bitmap display, moves the data window around permitting scans bigger than 500 x 500 cells (or smaller with magnification) to be viewed. If click and drag takes place then the image must be dragged live, changed on each iteration of the *User Interface Manager* While loop. The calculated  $\Delta x$  and  $\Delta y$  values are used, scaled by the magnification factor, to adjust the values of the *Bitmap\_Corner.vi* cluster which define which cell forms the bottom-left-most cell displayed. This change is then passed to the “Register” retrieval of *Bitmap.vi* (discussed in Section 5.4.2.5) to obtain the correct portion of the data to display. The update is real time because the display is being retrieved from the *Bitmap.vi* shift-register, which already contains all the data for the current Frame, Source and Layer, rather than from disc. Right clicking and moving on the bitmap display adds a green rectangle to the display, which updates in real time. The left, top, right and bottom coördinates of the LabVIEW *Draw Rectangle.vi* function are determined from the original click position and the current position and added to the “Mousedown and Selection” cluster. The rectangle is updated live, changed on each iteration of the *User Interface Manager* While loop as the mouse moves over the bitmap display. The Selection rectangle is not made permanent and added to *{Scan\_Region}.vi* until the Mouse Up event occurs (Figure 5.11). The Mouse Up event captures the end of the mouse interaction. The “Mousedown and Selection” cluster provides the button that was pressed and the original click position relative to the bottom left corner. The cases are passed the same inputs as during the Mouse Move event (page 99). If the Left mouse button was pressed then either; the Mouse has changed position between Mouse Down and Mouse Up and the data window has been dragged or the mouse is in the same position on Mouse Down and Mouse Up and a cell has been selected.



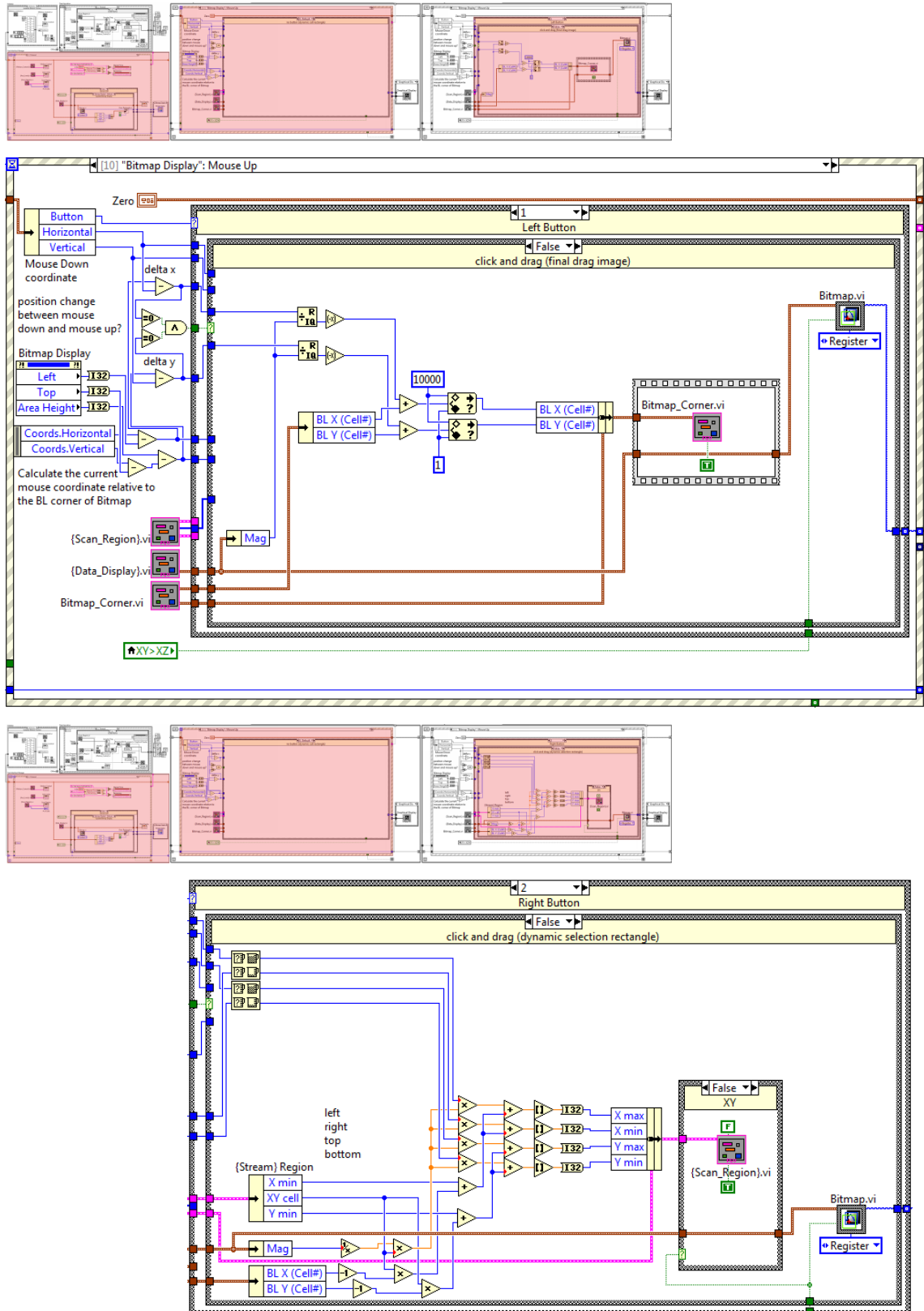


Figure 5.11: Case 1 and 2 of the 10<sup>th</sup> Event of the 1<sup>st</sup> While loop of Scanner Control 3 (SC3w1e10c1 and SC3w1e10c2 in Appendix 3). Mouse Up on the "Bitmap Display" of the left or right button. End of dragging the greyscale image of the data or drawing a green selection rectangle.

If click and drag has taken place then the calculated  $\Delta x$  and  $\Delta y$  values are used, scaled by the magnification factor, to adjust the values of the *Bitmap\_Corner.vi* cluster which define which cell forms the bottom-left-most cell displayed, as during the Mouse Move event (page 100). Right clicking and moving on the Bitmap display adds a green rectangle to the display, which updates in real time. On Mouse Up then either; the Mouse has changed position between Mouse Down and Mouse Up and the selection rectangle is permanent; or the mouse is in the same position on Mouse Down and Mouse Up, and the new selection is cancelled and undone to the previous values. The left, top, right and bottom coordinates of the LabVIEW *Draw Rectangle.vi* function are determined from the original click position and the current position. Consequently the selected Xmax, Xmin, Ymax, Ymin are determined using these values and the Xmin, XYcell and Ymin values in combination with the magnification factor and the bottom-left-most cell. If the Bitmap display is Right-clicked at a single point then the new selection is cancelled and the Front Panel “Undo” control in the Scan Region group is triggered to return the scan region back to its previous values. An additional Mouse Wheel event (Event 11) completes the mouse interaction of the Bitmap display by using the Delta value to alter the magnification factor of the display. Thus rolling the mouse wheel above the Bitmap display zooms in and out of the data. Further explanation of all the Events in the main Scanner Control 3 Virtual Instrument can be found in Appendix 3.

The 22 subVIs which support Scanner Control 3 are presented in Figure 5.12, and are discussed in detail in Appendix 3. *(Input).vi* manages the acquisition from and the names of the four sensors attached to the scanner and provides a single place to modify those details. *(Motion).vi* communicates with the Scanner Hardware and is discussed further in Section 5.4.2.3 (page 106). *[DATA\_#xyz].vi*, *[DATA\_stream].vi* and *[FrameSync].vi* store and manage the data from a scan. *[DATA\_stream].vi* is discussed in Section 5.4.2.4 (page 108). The subVIs with { }.vi names (*SC3v6* to *SC3v10*) are *Functional Global Variables* which store and manage the Front Panel groups (Figure 5.5). *Bitmap.vi* and *Graph.vi* manage the display of the scan data. *Bitmap.vi* is discussed in Section 5.4.2.5 (page 112).

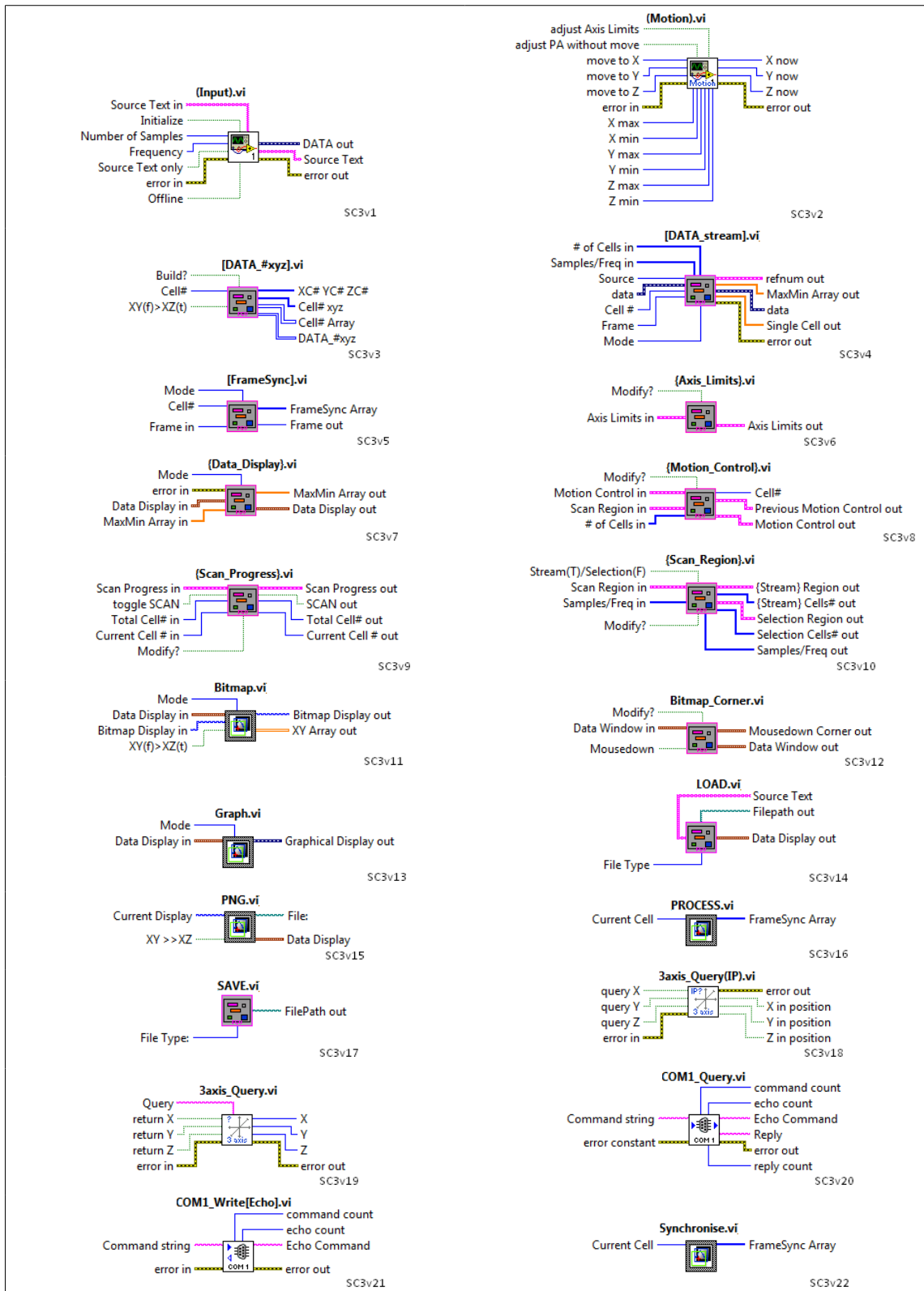


Figure 5.12: The 22 subVIs (labelled SC3v) which handle the storage of front panel controls, the storage and display of the data and communication with the Parker Automation hardware. Detail of the functioning of each of these VIs is provided in Appendix 3.

*LOAD.vi*, *PNG.vi*, *SAVE.vi* and *PROCESS.vi* manage the response to pressing their corresponding front panel buttons (Figure 5.5). *SAVE.vi* is discussed in Section 5.4.2.6 (page 116) The subVIs numbered *SC3v18* to *SC3v21* are stored in the ... \subVIs\Parker Automation\ directory and are inherited directly from Scanner Control 2. They send the low level VISA commands to the hardware (Figure 4.9). The final *Synchronise.vi* is a data processing subVI stored in the ... \subVIs\Processing\ directory that is called by the shell *PROCESS.vi* and is discussed in Section 5.4.2.7 (page 118).

### 5.4.2.3 (Motion).vi - communication with the Scanner Hardware

*(Motion).vi* works with *{Motion\_Control}.vi* and the ... \Parker Automation\ subVIs to communicate the desired position of the Sensor head to the Scanner Hardware and also guard against the scanner moving beyond the axis limits. *(Motion).vi* also manages the Slack/Backlash compensation to maintain positional accuracy during changes in direction (as discussed in Section 4.2.2). The Block Diagram of *(Motion).vi* is presented in Figure 5.13. If the “adjust Axis Limits” flag is set then the new Axis Limit inputs are passed into the shift registers storing those values rather than their existing values. The current Position Absolute (PA) of the scanner is stored in three shift registers of a single-iteration While loop. The “adjust PA without move” flag forces the passing of the new inputs into the registers without any action to move the scanner hardware. Otherwise, boolean enumerated Cases use *COM1\_Write[Echo].vi* (Figure 5.12) to communicate with the scanner hardware to move to the desired position. When a new position is requested the change is checked against the current position and only the required axis are instructed. Importantly, the subVI executes the absorption of the axis slack/backlash when the motion of each axis changes direction.

The inputs for each axis are;

- $m$ , the distance required to move (the difference between (PA) and move to)
- $s$ , step: the distance the motors are actually set to move
- $d$ , direction: 1 or -1, a register storing the previous direction of the axis
- $x_s$ , slack: the calibrated distance to absorb when direction changes.

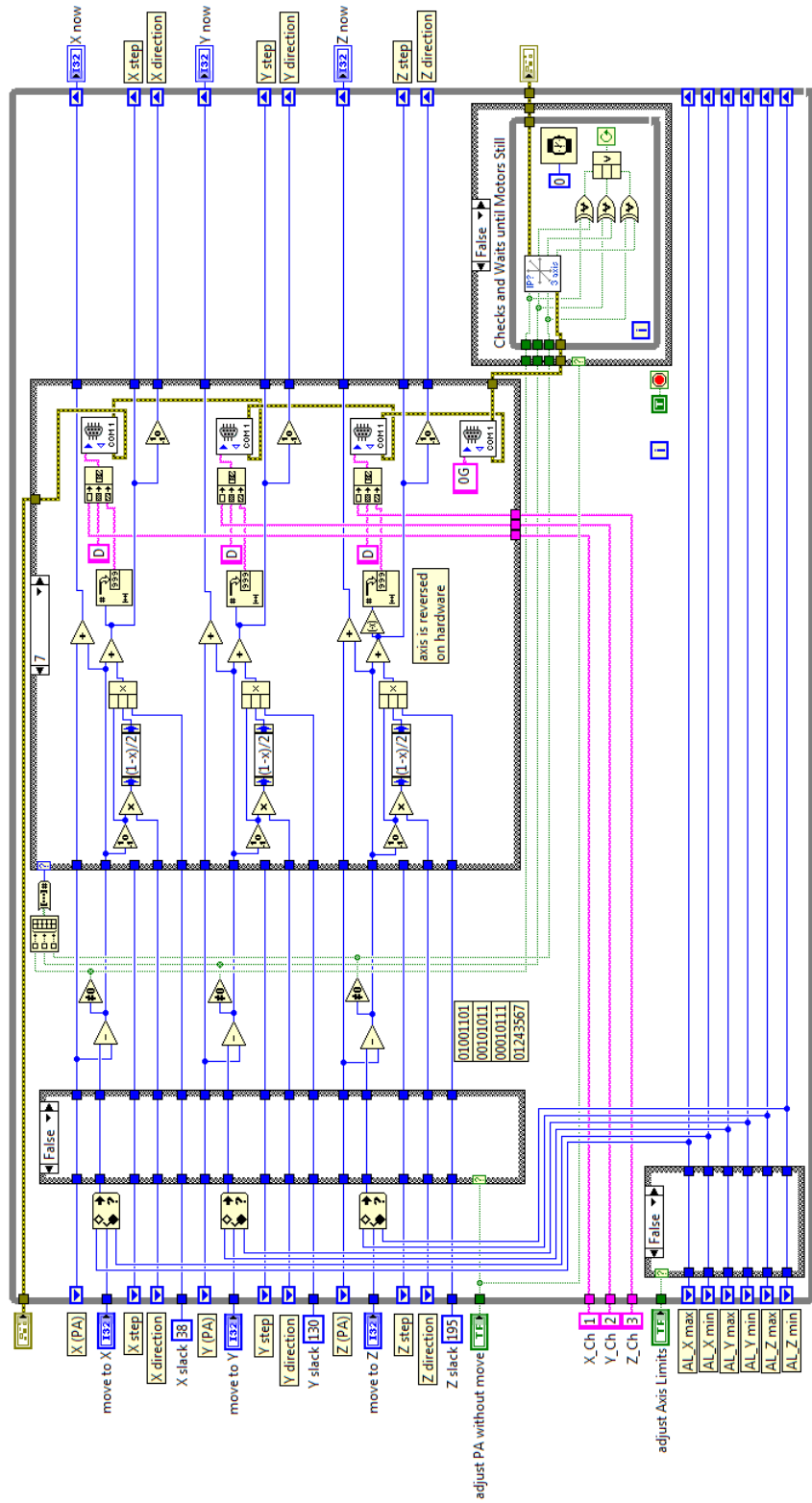


Figure 5.13: The Block Diagram of (Motion).vi which works with {Motion\_Control}.vi and the ...\Parker Automation\ subVIs to communicate the desired position of the Sensor head to the Scanner Hardware.

$$s = m + \left( x_s \times \frac{m}{|m|} \times \left( \frac{1}{2} \left( 1 - \left( d \times \frac{m}{|m|} \right) \right) \right) \right) \quad \text{Equation 5.1}$$

Equation 5.1 determines if the calibrated slack/backlash should be added to the distance to move. In essence, if the new position means the axis moves in the same direction as its immediately preceding movement then the slack does not need to be added. If the axis is asked to move in the opposite direction to its preceding movement then an additional calibrated distance must be included to absorb the slack/backlash. The constant values  $x_s(38)$ ,  $y_s(130)$  and  $z_s(195)$  were calibrated as part of Hardware Development (Section 4.2.2). The slack/backlash constant is added to the movement requested of the scanner, but is not added to the final value of “(PA)” stored in the shift-register, it is an *invisible* effect which accommodates the Hardware. The effectiveness of this system is demonstrated in Section 4.2.2 where the positional accuracy of the scanner under this system has been calibrated to  $\pm 1 \mu\text{m}$ .

#### 5.4.2.4 [DATA\_stream].vi - storing the scan data

[DATA\_stream].vi manages the storage of the data in four parallel .csv files in `D:\scanner_scratch\`, one for each Source. The raw data (the graph data for all four sources) for the current cell is stored in a shift-register on the single-iteration while loop along with an array storing the Minimum and Maximum values of each source and an output of the four values of the current cell of the current frame. Inputs into each case are; DATA in, # of Cells in, Cell #, Frame, Sample/Frequency in and Source. Shift-registers store the values of; a Zero array, MaxMin Array, Current DATA out, Number of Cells, Number of Samples, ref num for the four .csv files and the error cluster. The “Initialize” mode presented within Figure 5.14 “replace or create”[s] each of the .csv files for storing the sources and populates them with the correct number of lines for the number of cells needed. The length of each line is four times the number of samples and each four byte hexadecimal string represents the real data value of zero (2710).

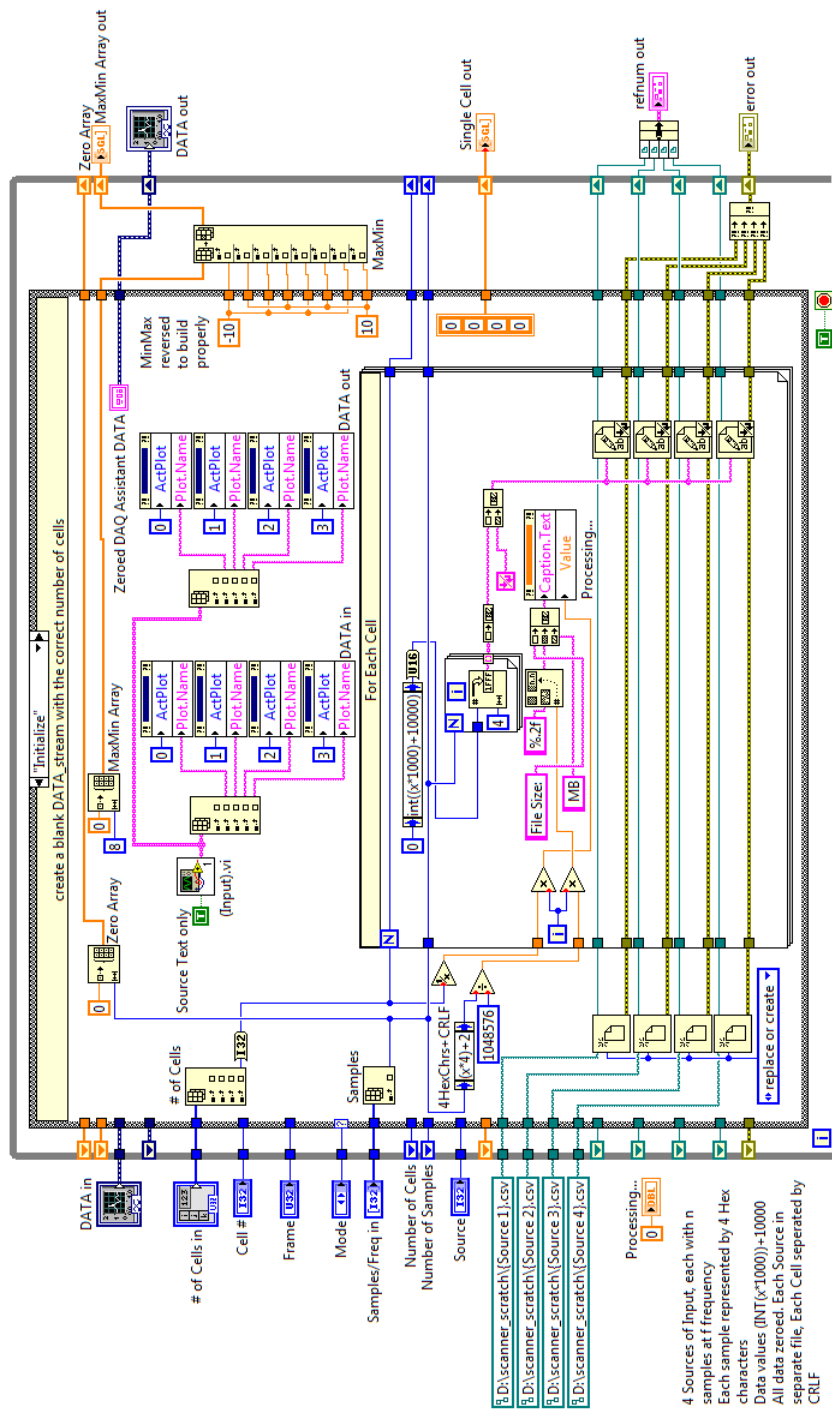


Figure 5.14: The Block Diagram of [DATA\_stream].vi, which manages the storage of the scan data in the system.

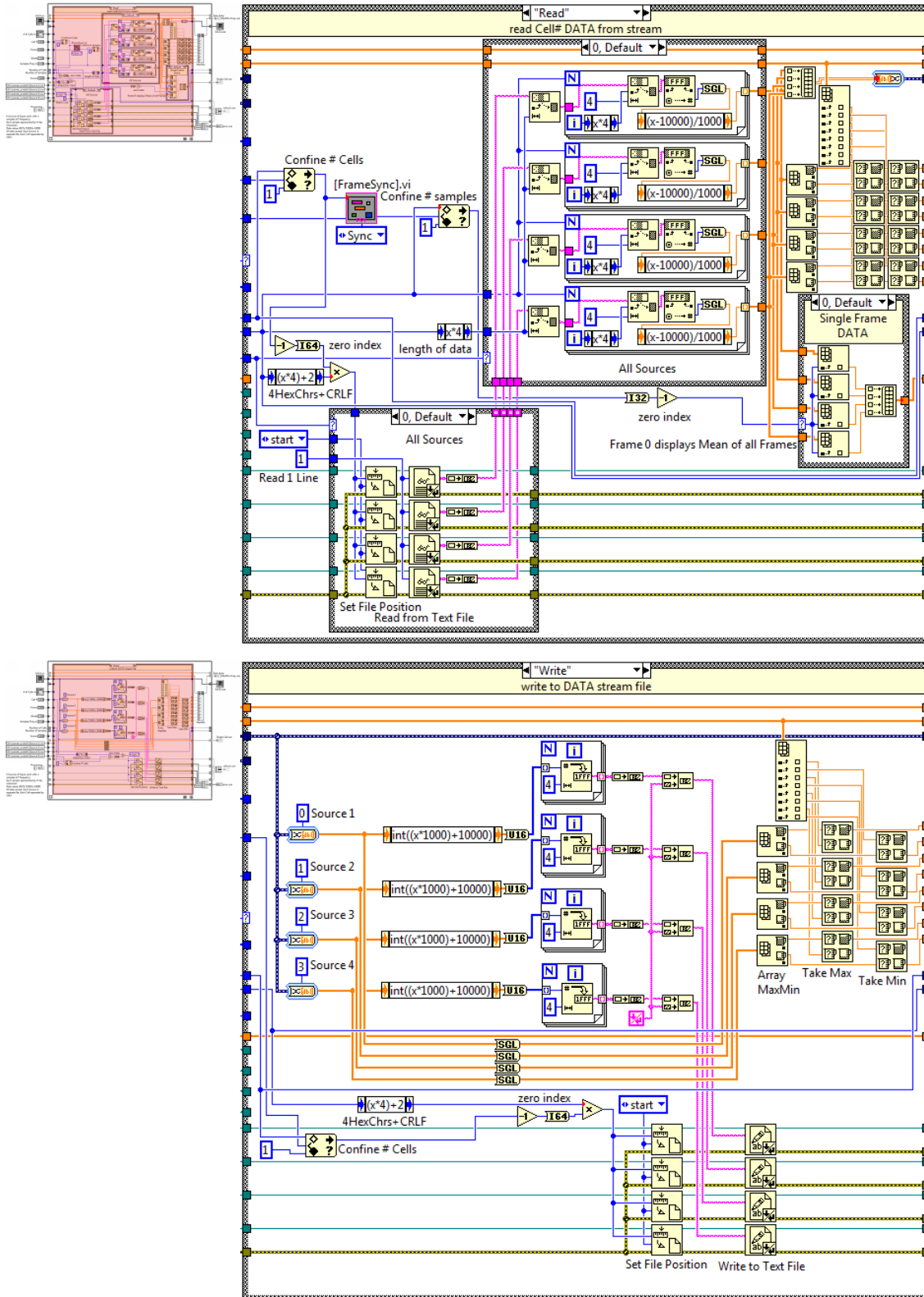


Figure 5.15: The "Read" and "Write" Cases of [DATA\_stream].vi (SC3v4c2 and SC3v4c3 in Appendix 3), which manage the scan data in the system.



As this can take time for large scans a progress bar is provided for the subVI (Figure 5.25). Using .csv files to store the data is slow, but is necessary because of the quantity of data for even a basic scan, 1000 samples of 4 sources and 200x200 cells produces 640 MB. The scanner scratch exists on the *D:* drive and contains the four files;

```
D:\scanner_scratch\{Source 1}.csv
D:\scanner_scratch\{Source 2}.csv
D:\scanner_scratch\{Source 3}.csv
D:\scanner_scratch\{Source 4}.csv
```

The *{Source}.csv* files contain the sample data for every cell in the data, one for each of the four sources. Each Sample point is stored as a 4 byte hexadecimal number so each line is a string of length four times the number of samples. Every cell in the data has its own line. To retrieve the real data value; for each 4 byte hexadecimal number convert to an integer, subtract 10000 and divide by 1000, the frame number as counted from the start of the line and cell number is equal to the line number.

Figure 5.15 presents the “Read” and “Write” cases of *[DATA\_stream].vi*. The “Read” mode retrieves all the data for the requested Cell from the four parallel .csv files. The requested Cell# is confined to the total number of cells and converted to a line number for each of the .csv files. The line required is read into memory and the string of 4 byte hexadecimal numbers is converted into single-precision arrays of data, one array for each source. The eight part “Max & Min” LabVIEW functions grid checks the Maximum and Minimum values of the currently read cell against the MaxMinArray register and replaces any appropriate values to ensure the MaxMinArray contains the maximum and minimum of the entire data. The LabVIEW “Convert to Dynamic Data” converts the arrays to graph data output for DATA output. The cell requested is first passed through *[FrameSync].vi* which stores the offsets to the actual frame for each cell as determined by the *Synchronise.vi* process described in Section 5.4.2.8 (page 118). The “Write” mode uses the “Convert from Dynamic Data” LabVIEW function to isolate each of the four channel data and convert them into single-precision arrays for the current cell. Each value in the array is multiplied by 1000, rounded to the nearest integer and

summed with 10000 to change the data from the range -10.000 to 10.000 to the range 00000 to 20000. Auto-indexed For loops are used to convert each value into a 4 byte hexadecimal number from 0000 to 4E20 and concatenate them into a single string of length four times the number of samples. The entire string overwrites the already existing line in the *{Source}.csv* file using the “Set File Position” function and “Write to Text File”. The line overwritten is defined by the Cell# input.

#### **5.4.2.5 Bitmap.vi - creating the greyscale Bitmap display**

The *Bitmap.vi* subVI handles selection of the correct portion of the overall data and the creation of a 498 x 498 greyscale image of that portion. It handles the magnification of the data if necessary and the addition of the red selected-cell rectangle to the correct cell and the green permanent “Selection” rectangle to the display. The portion of data needing displaying is defined by the “Data Display” cluster, which is an input fed by *{Data\_Display}.vi* when *Bitmap.vi* is called. *Bitmap.vi* handles whether the XY or XZ plane is being displayed and stores the entire data for the current source and layer in a shift-register for fast retrieval. The “Initialisation” case presented within [Figure 5.16](#) fills the DATA array with Zero, builds the greyscale table and stores the grey bitmap background. The “File” case ([Figure 5.17](#)) is used to retrieve a new portion of data from *{DATA\_stream}.vi* ([page 108](#)) and feed that data into the XY Array register. Whenever *Bitmap.vi* is called in “File” mode it is then called again in “Register” mode ([Figure 5.17](#) and [5.18](#)). In “Register” mode the Layer (Z), Max, Min, Mag and Cell# values are used to produce a greyscale representation of the XY Array, scaled appropriately by Mag with the selected cell highlighted by a red rectangle. The LabVIEW “Replace Array Subset” function simply overwrites as much of the 498 x 498 grey background with values from the “greyscaled DATA” array as it has available. If the array is larger than 498 in either direction, LabVIEW automatically takes only as much as will fit. If  $Mag > 1$  then a set of nested for-loops repeats the occurrence of each cell (up to 498 times) to create a new array that is “Mag” times bigger. *Bitmap\_Corner.vi* is used to define which of the cells in the XY Array register is the bottom-left-most cell displayed. *{Scan\_Region}.vi* provides the information for the permanent green “Selection

Rectangle” overlaid on the display. The added green rectangle represents the boundary of the currently defined scan region. If the scan region extends beyond the current data, then so does the green rectangle. The rectangle is permitted to exist over fractions of cells as it is based on the hardware coördinates. From *{Scan\_Region}.vi* the fractional proportion of the scan region in comparison to the DATA region is calculated. The fractional offset of the currently displayed bottom-left-most cell compared with the number of cells in the data is calculated and applied to the fractional proportion. The “display scale” (current number of pixels per cell) is calculated and applied to the fractional proportion. This produces a rectangle with edges defined as a proportional distance from the edges of the Bitmap display. The edges may extend beyond the boundary of the display and so are confined between 0 and 1 which has the effect of neatly locking the edge of the green rectangle to the edge of the bitmap if it does extend beyond. The proportional distances are converted to true pixel coördinates by multiplying by 498, and the LabVIEW *Draw Rectangle.vi* function applies the rectangle to the Bitmap. The LabVIEW *Flatten Pixmap.vi* and *Draw Flattened Pixmap.vi* functions treat the first pixel as the top-left-most element, indexed column then row, so the “Data Array” must have each row inverted and then be transposed.

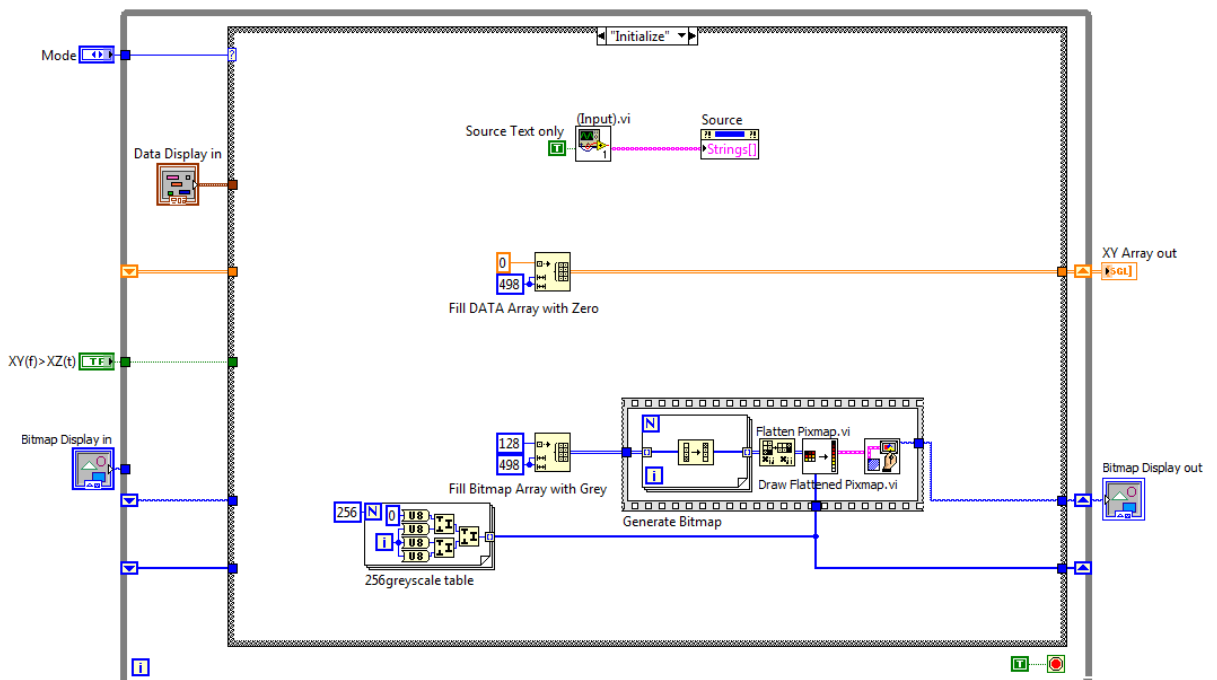


Figure 5.16: The Block Diagram of *Bitmap.vi* showing the “Initialise” case.

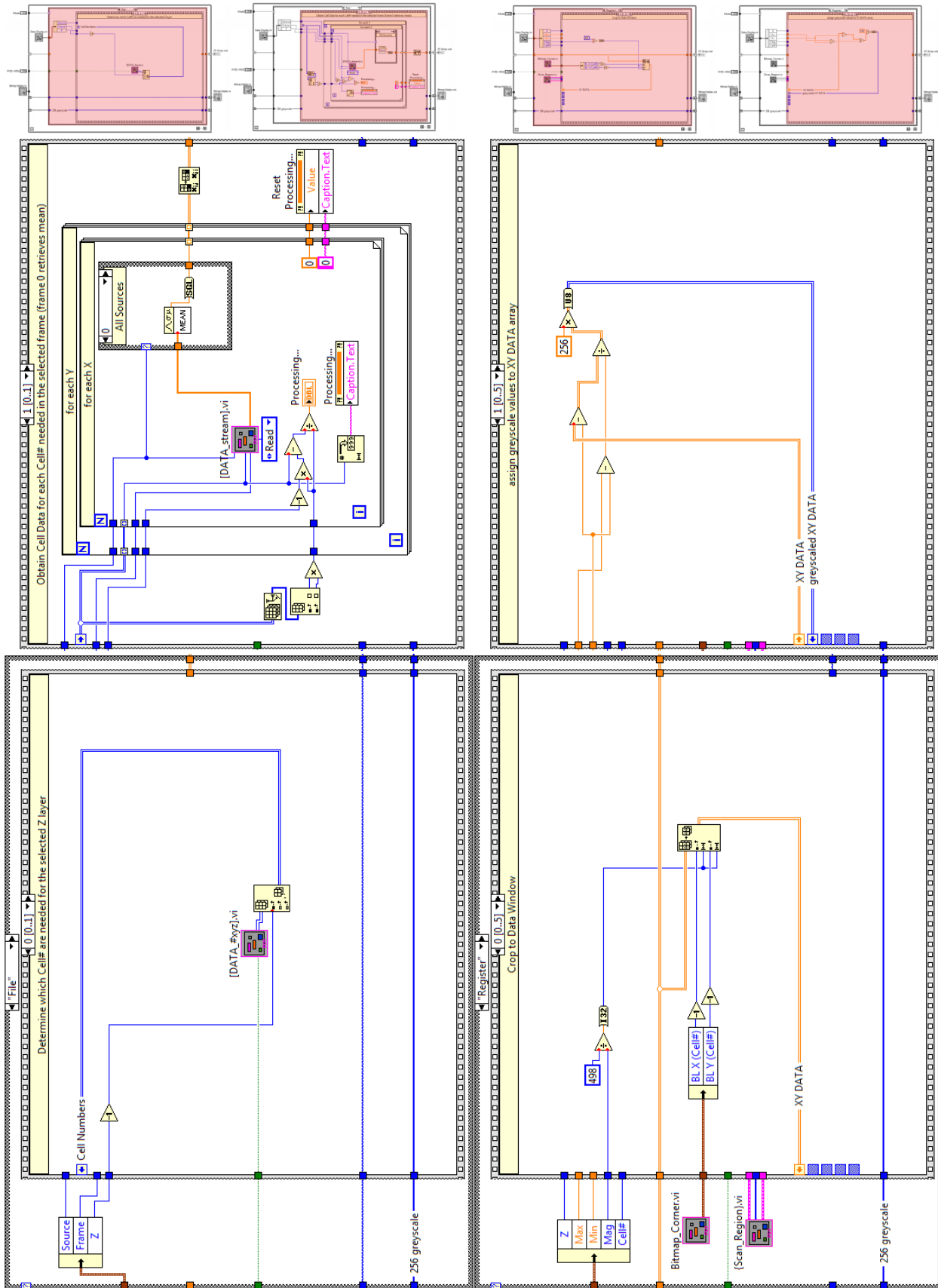


Figure 5.17: The “File” case (SC3v11c3 in Appendix 3) and “Register” case, sequence frames 0 - 1 (SC3v11c4s0 and SC3v11c4s1 in Appendix 3), of *Bitmap.vi*.



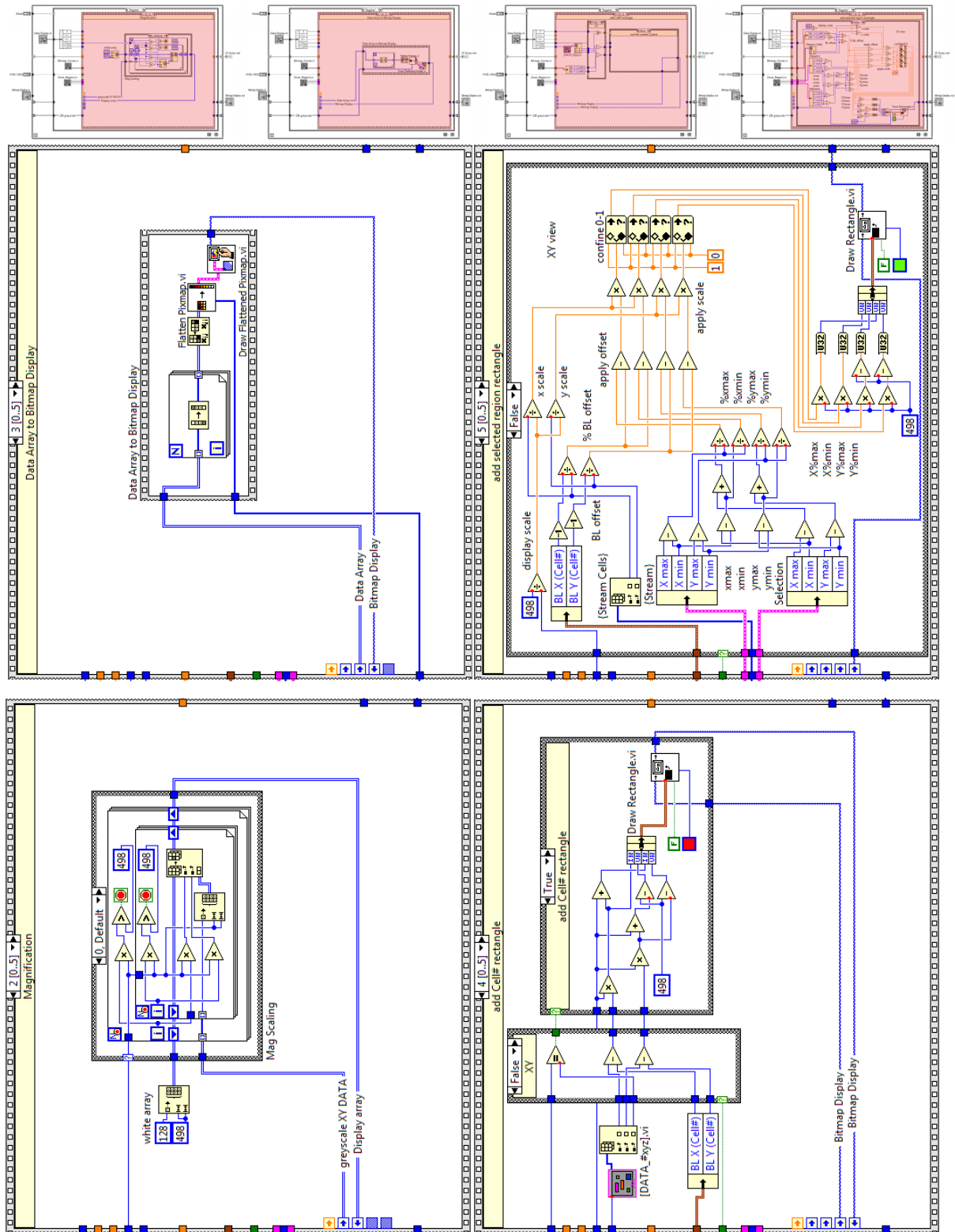


Figure 5.18: The “Register” case, sequence frames 2 - 5 (SC3v11c4s2 to SC3v11c4s5 in Appendix 3), of *Bitmap.vi*.



### 5.4.2.6 SAVE.vi - saving the scans to file

Scans can be saved as either “Static” *[S].csv* or “Dynamic” *[D].zip* files depending on whether the change between frames needs to be recorded (Section 5.5.4, page 128). Each filetype contains Header information which describes the scan which produced the data. The cluster which contains this information is produced in the initialisation sequence before being passed to the “Dynamic” or “Static” cases (Figure 5.19). The Source names are retrieved from *(Input).vi*. Examples of the structure of a Blank *[S].csv* and *[D].zip* file, produced with the initialisation data, are provided in in Chapter 5.7z of the Cardiff Portal Arxive (page ix) and through the included DVD-ROM. The Header information is structured as;

```

Filename
Creation Date:
Number of Cells [X.Y.Z.Total]:
Number of Samples.Frequency:
Xmax.Xmin.XYCellSize.Ymax.Ymin.Zmax.Zmin.ZCellSize:
Display[S1(Max.Min).S2(Max.Min).S3(Max.Min).S4(Max.Min)]:
Z Layer.Magnification.Source.Frame.Cell:
DATA[S1(Max.Min).S2(Max.Min).S3(Max.Min).S4(Max.Min)]:

```

The “File Dialog” function is used to ask for the filename with the default file name being the system date. In the “Dynamic” case the LabVIEW *New Zip File.vi* function creates and opens the specified zip file. The {Header} array is created from a combination of each element of the Header cluster, and comma delimited text array versions of the scan parameters stored in the front panel *{}.vi Functional Global Variables* (Figure 5.12), using the LabVIEW *Array to Spreadsheet String* functions. The {Header} array is written to the temporary *D:\scanner\_scratch\{Header}.csv* file which is then added to the *.zip* before being deleted. The four *scanner\_scratch\{Source}.csv* files are sequentially added to the *.zip* using the names of the sources. In the “Static” case the LabVIEW *Create File* function creates and opens a new *.csv* file. The {Header} array, created in the same way as for the “Dynamic” case, forms the first 9 rows of the *.csv*. For each Cell a minor sequence determines the Maximum, Mean and Minimum values of each Source retrieved from *[DATA\_Stream].vi* and adds a new line/row to the *.csv* file. *LOAD.vi*, described in detail in Appendix 3, effectively performs these operations in reverse to load the header information into the correct *{}.vi* subVIs, build *[DATA\_#xyz].vi* and then load the scan data into *[DATA\_stream].vi*.

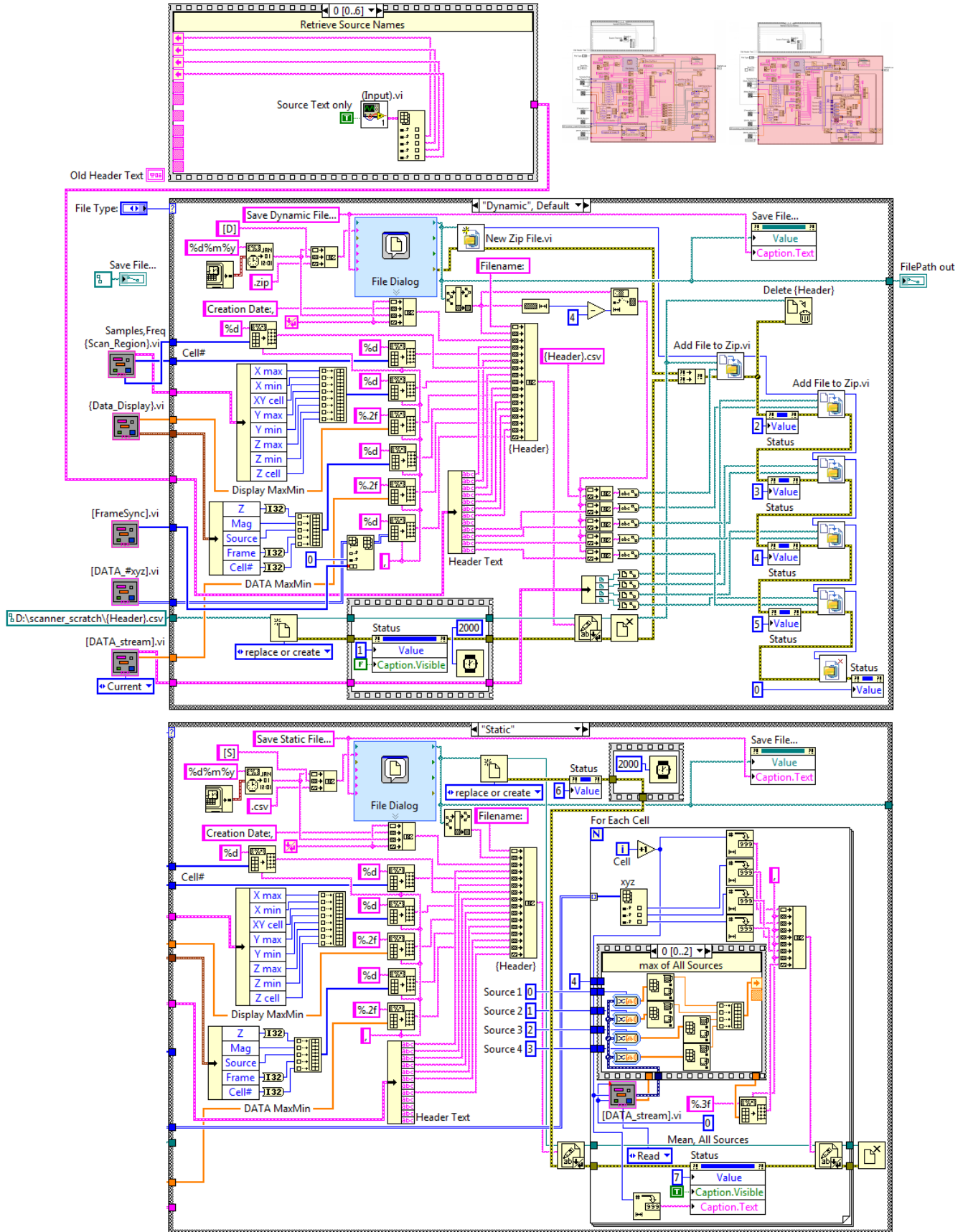


Figure 5.19: The Block Diagram of SAVE.vi showing the “Dynamic” and “Static” cases (SC3v17c1 and SC3v17c2 in Appendix 3).

### 5.4.2.7 PNG.vi - exporting PNG and Histograms of the Scans

*PNG.vi* is a state based system in its own right, though called by the 17<sup>th</sup> Event of Scanner Control 3 it executes as an independent system. The “Initialise” state (Figure 5.20) is set when *PNG.vi* is first executed. The current scan parameters are passed from the *{}.vi Global Functional Variables* to the initial front panel of *PNG.vi* (Figure 5.29(c)). A “Parameters” state provides an Event Structure controlled While loop to handle the front panel user interface and any changes to these the initial values (described in detail in Appendix 3) before one of three processing states are executed. The “Current Display” state writes the current display of Scanner Control 3 as a *.png* file. The output display includes the current green selection-rectangle and red selected-cell. The “Current Frame” state (Figure 5.21) writes a single clean *.png* file of the current Source/Layer/Frame along with an appropriate *{Histogram}.csv* and *{FrameStats}.csv* file. The *{Histogram}.csv* file provides histogram counts for each frame (or series of frames), a count of the number of pixels of each greyscale value. The *{FrameStats}.csv* file provides the Maximum, Minimum and Mean value of the entire frame, for each frame. The “PNG Stack” state (Figure 5.22) writes a *[P].zip* archive of all the *.png* files of the selected Sources, Layers, and Frames along with appropriate *{Histogram}.csv* and *{FrameStats}.csv* files. An additional *{Header}.csv* is created for *PNG.vi* by *SAVE.vi*. An example of the structure of a Blank *[P].zip* file, produced with the initialization data, is provided in in Chapter 5.7z of the Cardiff Portal Arxive (page ix). The Bitmap processing for *PNG.vi* exists within a For loop using the iteration number as a state marker for which case to execute. This architecture acts like a Stacked Sequence with the advantage of shift-registers and the ability to dynamically specify the number of iterations and conditionally terminate the sequence. This processing is developed as a compacted form of *Bitmap.vi* (page 112). The *.png* files are temporarily stored in *D:\scanner\_scratch\PNG\* before being added to the *[P].zip* archive with an internal folder structure named for the Source names in *(Input).vi*. The *{FrameStats}.csv* and *{Histogram}.csv* files are also added to the *.zip* file before it is closed when all the For loops are completed. A detailed description of the full logic of *PNG.vi* is provided in Appendix 3.



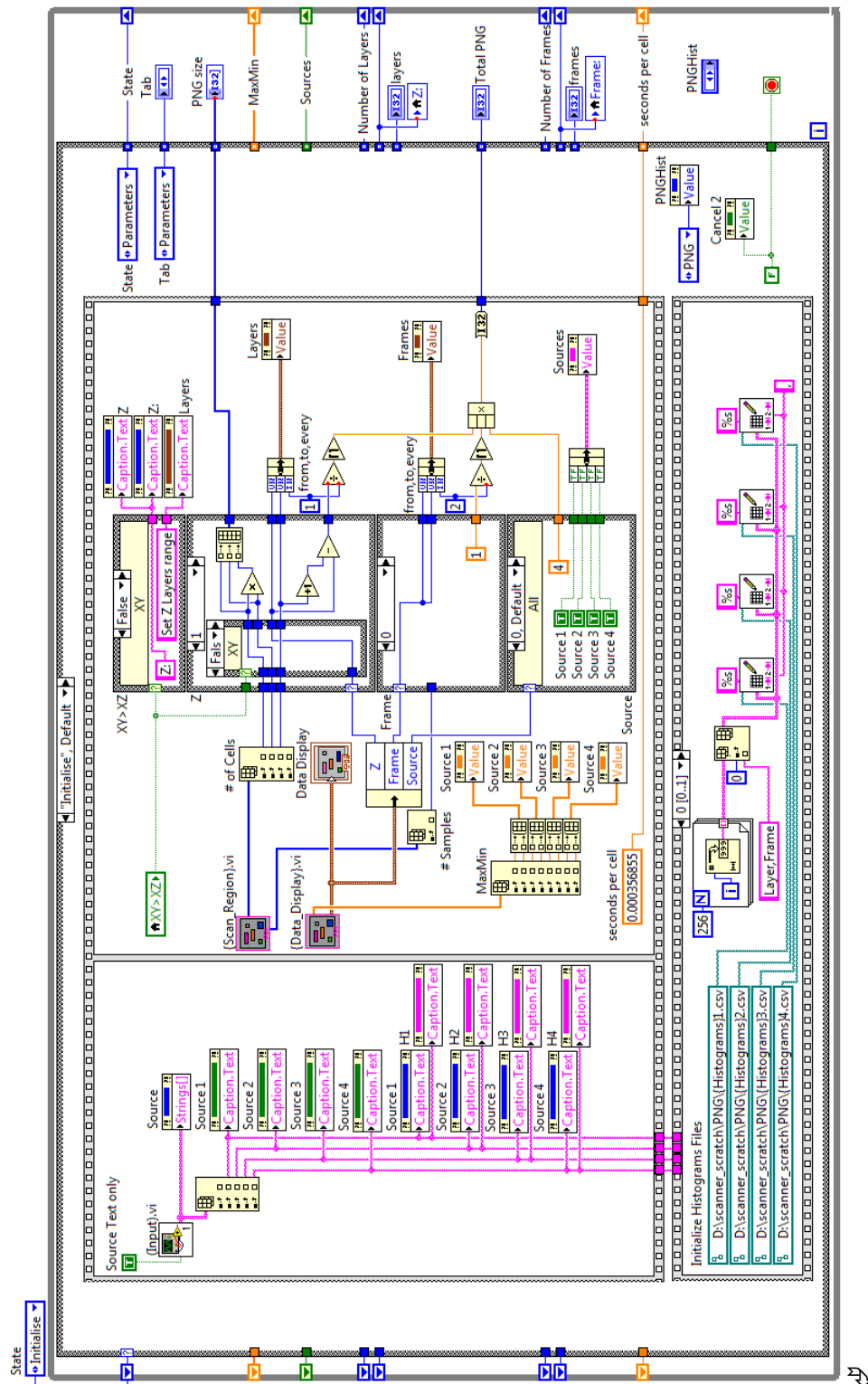


Figure 5.20: The Block Diagram of PNG.vi showing the “Initialise” case (SC3v15c1 in Appendix 3).

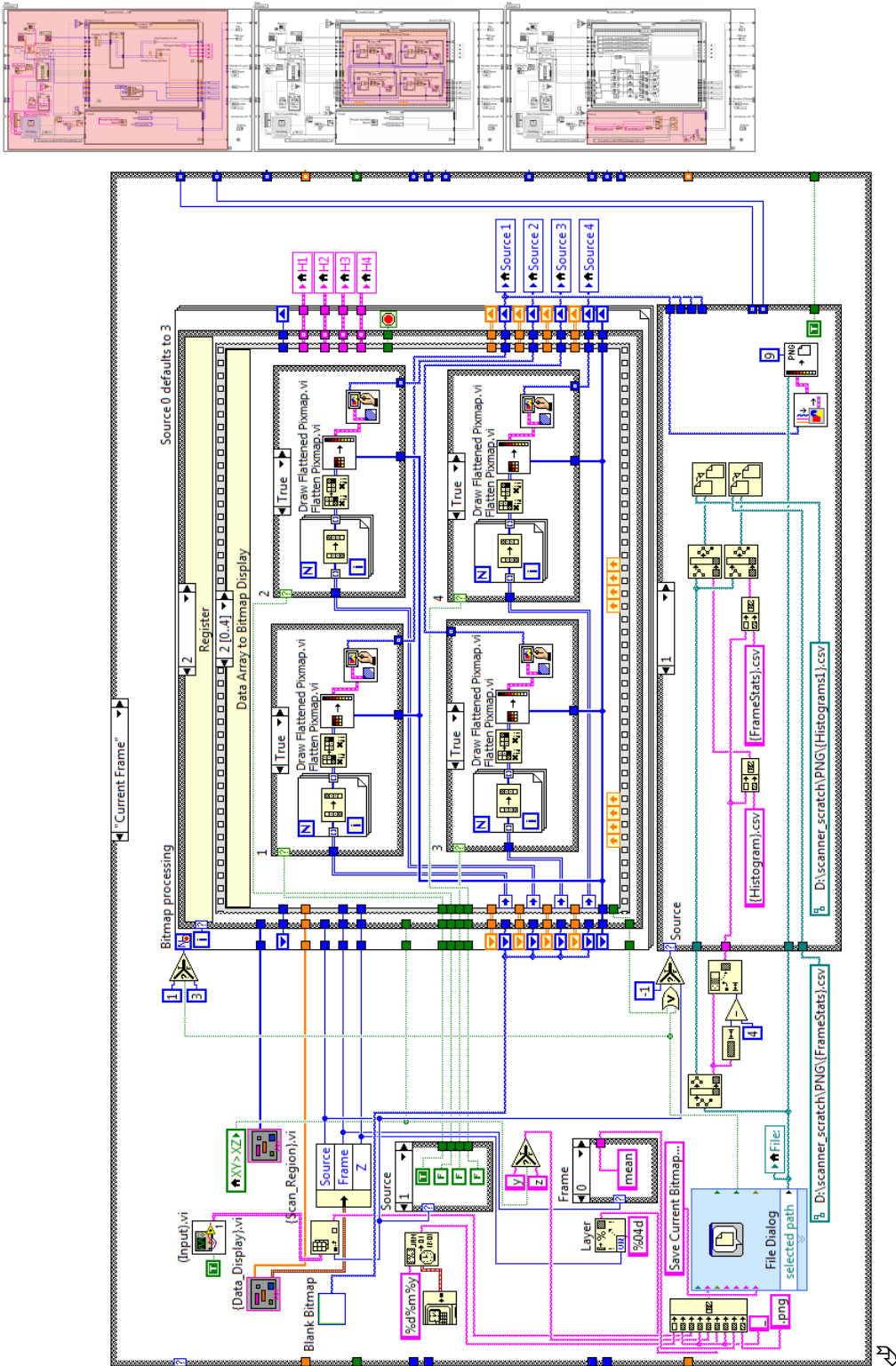


Figure 5.21: The “Current Frame” case (*SC3v15c4* in Appendix 3) of PNG.vi showing the 2nd frame of the “Register” state sequence (*SC3v15c4c(3)2s2* in Appendix 3) and the “Source 1” case of the “Write to PNG” case structure (*SC3v15c4c(4)1* in Appendix 3).

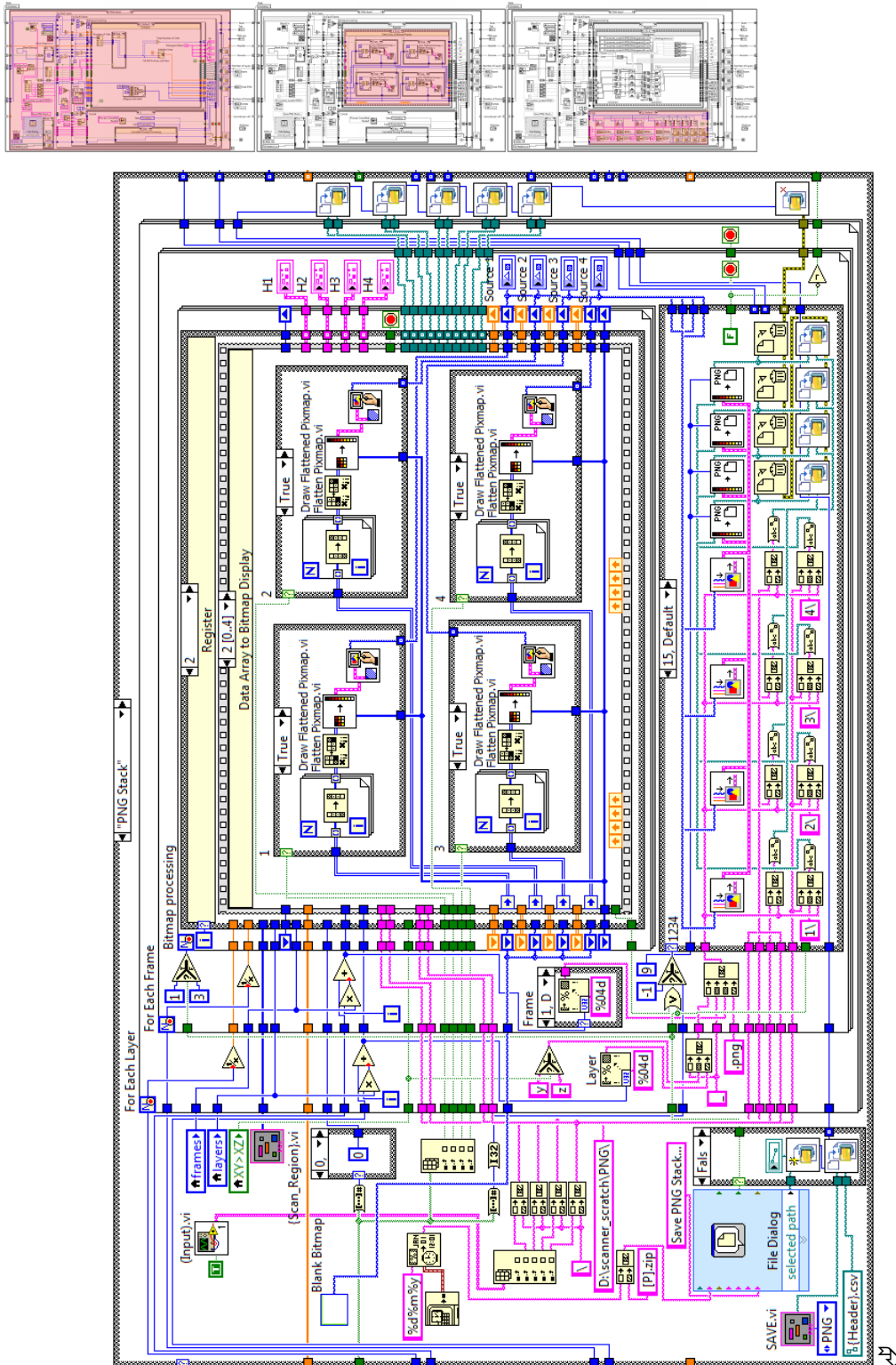


Figure 5.22: The “PNG stack” case (*SC3v15c5* in Appendix 3) of PNG.vi showing the 2nd frame of the “Register” state sequence (*SC3v15c5c(4)2s2* in Appendix 3) and the “All Sources” case of the “Write to PNG” case structure (*SC3v15c5c(5)15* in Appendix 3).

### 5.4.2.8 Synchronise.vi - processing time-series scans

A time-series “Dynamic” scan of a sample with, for example, an AC applied magnetic field does not make sense unless each cell is synchronised to the same points on the AC cycle. Synchronise.vi performs the task of finding which frame for each cell represents the first peak of the AC cycle and recording that offset in *[FrameSync].vi* so that “Frame 1” of every cell represents the maximum of the first peak. A small state based system in its own right (Figure 2.23), it is an additional data processing subVI which is stored in the ... \subVis\ (Processing)\ folder and is called from the *PROCESS.vi* shell subVI. The LabVIEW *Peak Detector.vi* function is used to identify and generate an array of all the peaks in the chosen source greater than half the maximum value of the whole data. A peak width of 10 correctly singles out the three peaks of the signal. The frame number of the first peak is extracted and recorded in *[FrameSync].vi* for each cell as an offset to be applied to the current frame in *[DATA\_stream].vi* (page 108).

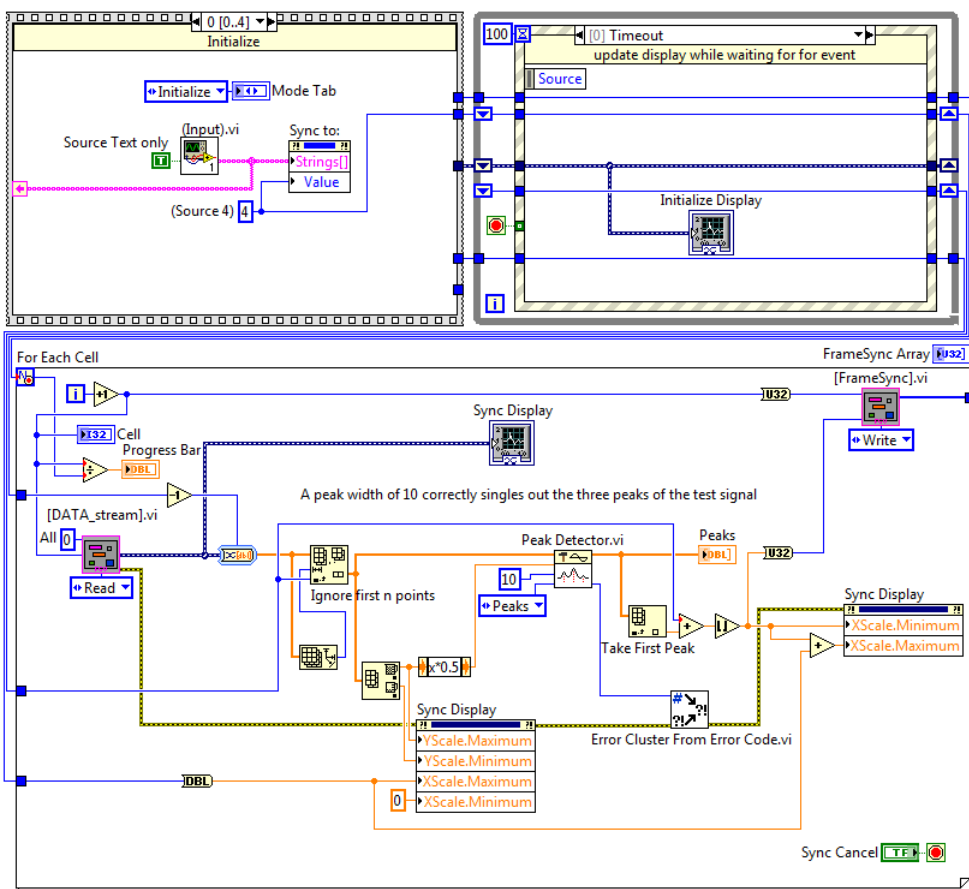




Figure 5.23: The Block Diagram of Synchronise.vi illustrating the initialisation sequence, event-controlled while loop and final processing For loop.

## 5.5 Practical Considerations when Using the Software

An Instructional Video for the use of the software is available in *Chapter 5.7z* of the Cardiff Portal Arhive (page ix) and on the accompanying DVD. Assumption is made that the Scanner Hardware and PC system have been set up correctly from the technical details provided in Chapter 4 and the Appendices, LabVIEW 15 32-bit is installed, the Scanner Control 3 folder is expanded to the desired location from the *Chapter 5.7z* archive and the *scanner\_scratch.7z* archive is expanded on the *D:\* drive.

Launching *SCANNER\_CONTROL.vi* presents the main Front Panel (Figure 5.5). *Ctrl-e* brings up the Block Diagram (Figure 5.6) where the “Offline” True/False flag can be set appropriately. It is assumed that *... \subVis\ (Input).vi* has been configured correctly for the Sensors being used by the system, in accordance with Appendix 3. Pressing “Run” initiates the user interface.

### 5.5.1 Initial User Interface

The initial User Interface is presented in Figure 5.5. The position of the scanner can be manually defined using the *Motion Control* group (Figure 5.24(a)). The arrow buttons can be used to move the scanner in either direction along each axis by a distance defined by the numerical “Step” indicator which can have the values 100000, 40000, 4000, 400, 40, 10 or 1 in units of motor steps. 4000 steps are equal to 1 mm distance. The arrow buttons are also mapped by the keyboard arrow keys with the *PageUp* and *PageDown* keys mapped to the Z+ and Z- buttons and the *Home* and *End* keys mapped to the increment and decrement of the Step indicator. An exact *Position* can also be entered numerically or the position of a particular *Cell#* by Cell Index number. If a change is made the Reset button  returns to the previous position. When initially run the Z-lock button  will be active and it will be found that the scanner head will not lower beneath  $z=0$ . This is an important safety function which prevents the scanner driving the sensors through a sample or “Floor” level. On initiation the “z-floor” is set to zero and active. In order to lower the sensor to the surface of a sample, when the time comes, it is necessary to deactivate the z-lock.

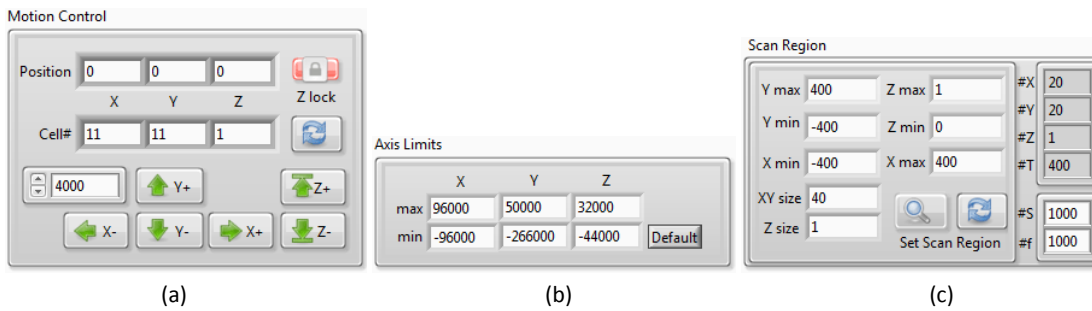


Figure 5.24: The *Motion Control* (a), *Axis Limits* (b) and *Scan Region* (c) groups of the front panel of Scanner Control 3 (presented in Figure 5.5).

**Extreme Caution** should be exercised when Z-lock is deactivated, especially when using the Z- button, *PageDown* key and the Value of the *Step Size*. In particular it is suggested the *Step Size* be low (400, 40) to avoid the sensors colliding with the sample by a mistaken button press. As soon as the sensor is the desired distance from the sample surface, as determined with help of the microscopic sight (Section 4.10.1) the Z-lock should be re-engaged. This sets the “z-floor” value to the current z-position and prevents the scanner head lowering further. Further restrictions to the position of the scanner head are provided by the *Axis Limits* group (Figure 5.24(b)). The defaults represent the edges of each axis to prevent collision with the frame, but can be set by the user if required. The origin (0,0,0) of the scanner is the current position of the scanner whenever Scanner Control 3 is run. It is advised to return the scanner to the origin (0,0,0) before Stopping the system. The origin can be reset by manually positioning the scanner head centrally and restarting the user interface.

### 5.5.2 Defining a Scan

A scan is defined by the setting of the *Scan Region* group (Figure 5.24(c)). The extent of the scan on all three axis can be entered numerically but by right-clicking on each of the numerical controls the value is set to the current position of the sensor. This is the most common way of defining the scan, by positioning the sensors to a desired location on the sample and right-clicking on the relevant controls to set the edges of the scan region. It is suggested to set the x and y corners of the scan with the sensors a safe distance from the sample and then find the lowest z position by careful incremental reduction of the z position at each of these corners, using the micrometer

levelling stage (Section 4.10.2) to adjust the horizontal level of the sample to ensure the sensor passes at a safe and even distance above the entire scan area. The corners can be easily found by middle-clicking on each of the *Scan Region* numerical controls, which moves the scanner to that position. Once a safe distance from the sample is determined the Z-lock button should be pressed to prevent any further lowering of the sensors and the *Z min* control should be right-clicked to set to the new z-floor. The *XY size* and *Z size* of each cell (in steps) can be set, the leftmost edge of each cell match the minimal edge on each axis, the maximal edges of the scan region are adjusted to be always an integer multiple of the cell size from the minimal edge. During the scan the sensors take measurements at the centre of each cell. The total number of cells on each axis, and overall, are presented. The more cells, the longer the scan. The number of samples and sampling frequency can also be set. For a “Dynamic” scan 1000 samples at 1000Hz is suggested, though better temporal resolution can be obtained with higher sampling frequency. For a non-dynamic “Static” scan it is suggested 20 samples are collected at 1000Hz, as a good compromise between noise-reduction and scan time. The estimated scan time, based on the total number of cells, the number of samples and the sampling frequency is presented in the *SCAN* group (Figure 5.26). Whilst a scan is being set up, the message “[DATA\_stream] not equal to Scan Region” is displayed beneath the *SCAN* group. This indicates that the scan data in memory, which may be a previous scan or the initial Blank data, does not correspond with the current scan settings. The reset button [↺] returns to these previous settings. To prepare for a scan the *Set Scan Region* [🔍] button must be pressed, a blank [DATA\_#xyz].vi, [DATA\_stream].vi and *Bitmap.vi* arrays are prepared (Figure 5.25). The message “[DATA\_stream] ready” is displayed when a scan is possible.

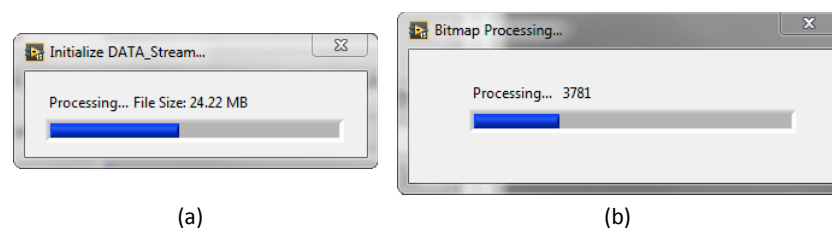


Figure 5.25: The progress bars displayed during the initialisation of the [DATA\_#xyz].vi, [DATA\_stream].vi (a) and *Bitmap.vi* (b) arrays.

### 5.5.3 Scanning

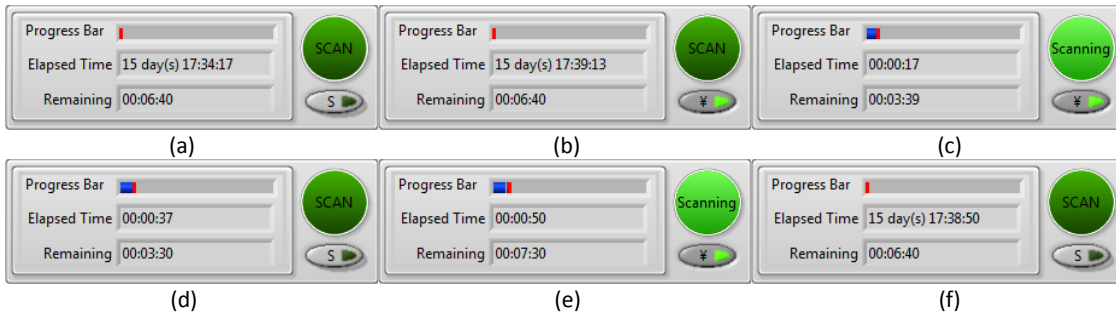





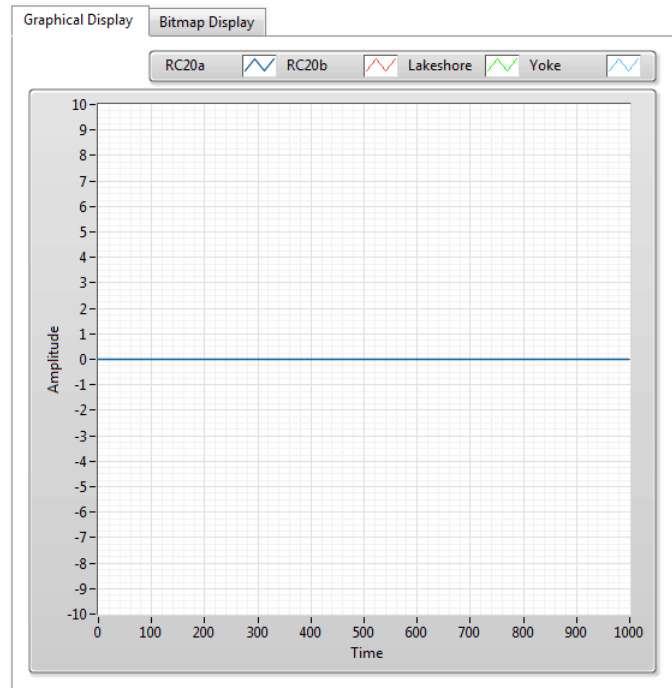


Figure 5.26: The SCAN group; (a) in preparation for a scan showing system time and estimated scan time, (b) when requesting a single sample, (c) when scanning showing elapsed and estimated time, (d) paused during a scan, (e) scanning continuing, (f) scanning complete showing system time and total scan time.

Once the *Scan Region* has been set the SCAN group (Figure 5.26) becomes active. Before beginning a scan it is advisable to use the Single-Sample button [  ] several times to test the input from the sensors (Figure 5.26(b)). To facilitate this the *Graphical Display* (Figure 5.27(b)) should be selected and the *Source:* menu on the *Data Display* group (Figure 5.27(a)) should be set to "All" to display all four sources. Right-clicking on the *Min* and *Max* controls of the *Data Display* group auto-scales the *Graphical Display* to the extents of the input data. When satisfied, the Scan can be begun by pressing the SCAN button [  ]. Scanning begins (Figure 5.26(c)). During a scan the *Bitmap Display* (Figure 5.27(c)) highlights the current cell and actively displays the build up of data as it arrives. Any *Source:*, *Layer (Z:)* or *Frame:* can be displayed during as scan and *Mag:* can be used to zoom in on the data (Figure 5.27(a)). The mouse can be used to move the data window around. The progress of the Scan can be paused at any time by pressing the active Scanning button [  ] (Figure 5.26(d)) and re-continued [  ] (Figure 5.26(e)). When paused the scan can be reset by rebuilding the scan with the *Set Scan Region* button [  ] (Figure 5.24(c)). During the scan the *Min* and *Max* controls can be actively set to adjust the contrast of the greyscale as data arrives. Right-clicking on each control sets them to the extents of the entire set of data. Middle-clicking on each control sets them to the extents of the current frame. When the scan is complete the total time is displayed in the *Remaining:* indicator (Figure 5.26(f)). The input of the sensors for each cell can also be viewed with the *Graphical Display* (Figure 5.27(b)) during a scan.

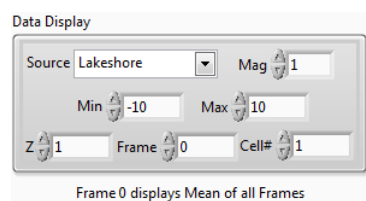




(b)



(c)



(a)

Figure 5.27: The Data Display groups (a) and the Data Display tab; the Graphical Display (b) showing a plot of Amplitude (Voltage) against Time for each of the four Sources and the Bitmap Display (c) showing a greyscale map of the scan data.

The XY>>XZ switch in the top-right corner of the front panel (Figure 5.5) controls if the Bitmap Display shows the XY layers or XZ slices of a three-dimension volume of cells.

### 5.5.4 Saving and Loading a Scan

Once a scan is complete the scan should be saved to file for future use. Pressing the “SAVE” button on the *File* group (Figure 5.28(a)) presents a dialogue box (Figure 5.28(b)) which asks if the scan should be saved as “Static” or “Dynamic”. The “Static” [S].csv format stores only the minimum, mean and maximum value of each source for each cell, losing data for individual frames, but produces a much smaller file which is easy to read interpret in an external spreadsheet program. When the scan is not of a time-series “Dynamic” nature this is the most suitable form of storing the scan. To retain all the Data from a scan the “Dynamic” [D].zip file format should be used, particularly if the scan changes over time and each frame is different. A standard Windows file dialogue window opens to ask for the name and the location of the saved file, by default the files is given a name based on the system date. Once named the *Saving File...* dialogue (Figure 5.28(c) and (d)) shows the status of the file save process. Examples of the structure of a Blank [S].csv and [D].zip file, produced with the initialization data, are provided in in *Chapter 5.7z* of the Cardiff Portal Arxive (page ix). To load a previously saved scan the “LOAD” button on the *File* group (Figure 5.28(a)) presents a dialogue box (Figure 5.28(e)) which asks which type of file is about to be loaded; a *Legacy*, *Static* or *Dynamic* file. The Scanner Control 3 system has the capacity to load “Legacy” scans saved by the Scanner Control 2 system, however the data which supports the results presented in this thesis, available in the Cardiff Portal Arxive (page ix), has been upgraded to Scanner Control 3 “Static” [S].csv files. The header information for both filetypes saves the setting for the *Data Display* group including the *Min* and *Max* values for each Source (Figure 5.27(a)), so it is useful to set these to reasonable contrast levels before saving the scan. Time-series “Dynamic” scans will initially be asynchronous, with the frames of each cell representing a different portion of the AC cycle. To make sense of these data is is necessary to synchronise the first frame of each cell so that it corresponds with the same point of the AC cycle. The synchronisation offset is saved in the “Dynamic” [D].zip {Header}.csv file. The synchronisation of the data is performed by ...\\subVIs\\(Processing)\\Synchronise.vi which is accessed by pressing the “PROCESS” button on the *File* group (Figure 5.28(a)).

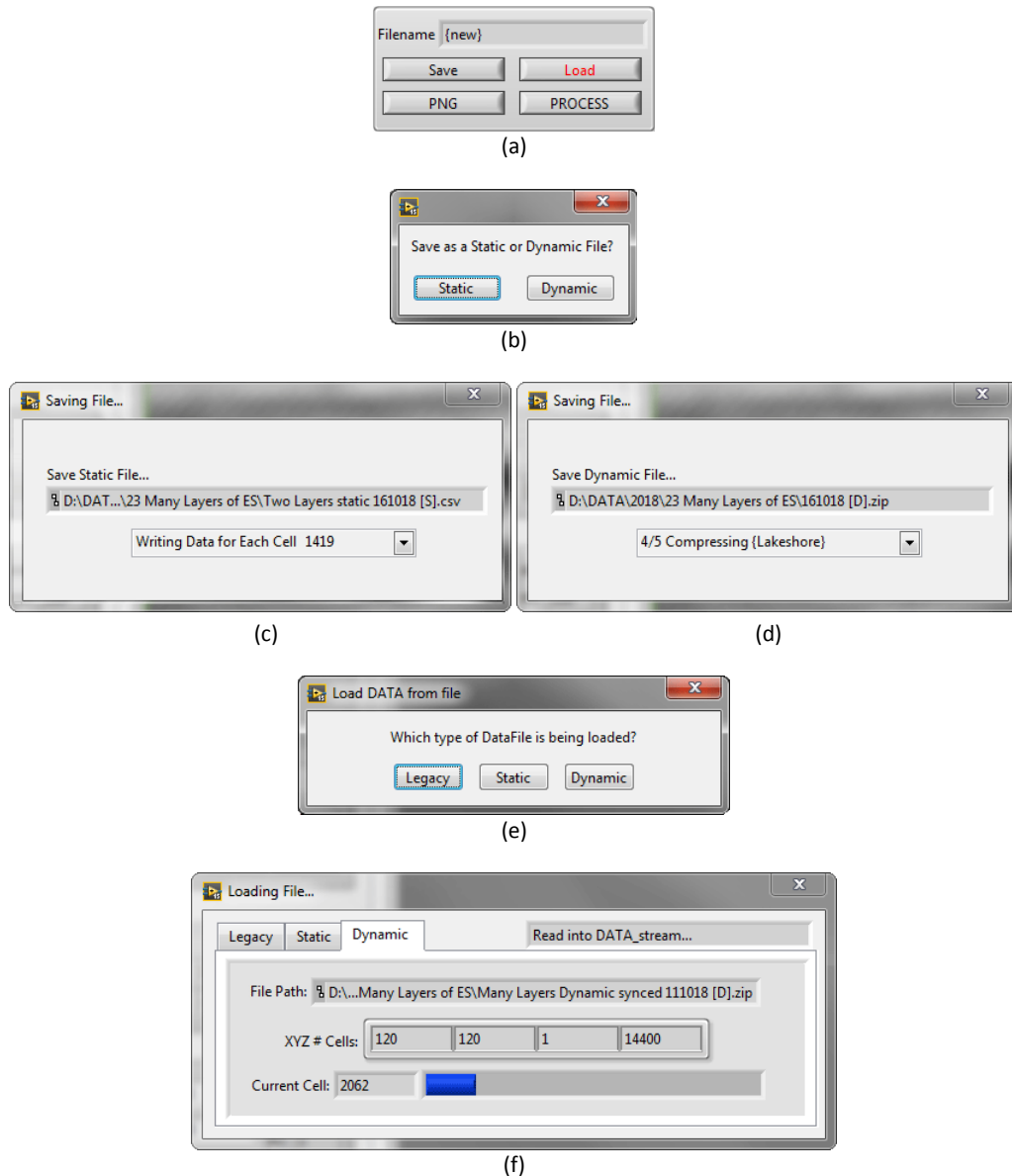


Figure 5.28: (a) The User interface *File* group, (b) the “Save as a Static or Dynamic File?” dialogue box, (c) and (d) the “Saving File...” progress display, (e) the “Which type of DataFile is being loaded?” dialogue box and (f) the “Loading File...” progress display.

### 5.5.5 Processing and Analysis of Data

Pressing the “PROCESS” button on the *File* group (Figure 5.28(a)) presents a dialogue offering a menu to choose how to process the data (Figure 5.29(a)). Future enhancements to the analysis of data can be added to this menu and to the `... \subVis\ (Processing) \` directory. The Synchronise process synchronises the first frame of each cell so that it corresponds with the same point of the AC cycle as described in

Section 5.4.2.8 (page 122). The *Synchronise.vi* User interface (Figure 5.29(a)) displays the data for the current Cell (though a different Current Cell can be selected to work from). *Synchronise.vi* finds the first peak in one of the sources and sets the first frame of each cell to the frame of that peak. By default the system looks for the first peak of the 3<sup>rd</sup> source, though any source can be selected. If desired the first n frames of data can be ignored. Pressing the *Sync* button begins the process. The resulting offsets are stored in the *[FrameSync].vi* array. Once synchronised the scan should be re-saved to retain the information, where it is stored in the *{Header}.csv* file of the “Dynamic” *[D].zip* archive. The *zxCombine* process can combine either two static scans, or two dynamic scans. The *zxCombine.vi* User interface (Figure 5.29(c)) can combine either two scans of equal clockwise and counterclockwise tilt (of any angle), or two scans one vertical, and the other at 45° counterclockwise from vertical (discussed in Chapter 7). The process defaults to combining the third source of each scan, but can be set to combine any one of the sources. The first scan and then the second scan are imported using the file-browse buttons. After the first file is selected the parameters of the scan are displayed and the Sources list populated. If the second file selected does not match the number of cells, samples and frequency parameters then a warning is given. Only if the two files correspond then the process is permitted to proceed. The output of the process is stored in the system memory using a new Source list which present the original selected source of the clockwise (or 0°) and counterclockwise (or 45° counterclockwise) scans, with the resulting calculated z-component and calculated x-component, then the results can be saved using the Save option (Figure 5.28(a)).

To produce a *.png* image of a frame of data for presentation or external study, or to produce a series or “stack” of *.png* files for a series of frames to produce an animation of a time-series scan the “PNG” button on the *File* group (Figure 5.28(a)) can be pressed, launching the *PNG.vi* (page 118) user interface (Figure 5.30). An exact replica of the Scanner Control 3 Bitmap display, including the green selection-rectangle and the red highlighted cell if present, can be exported using the “Export Current Display as PNG” button. The current Data Display group is imported into *PNG.vi* from the main user interface and informs the initial settings.

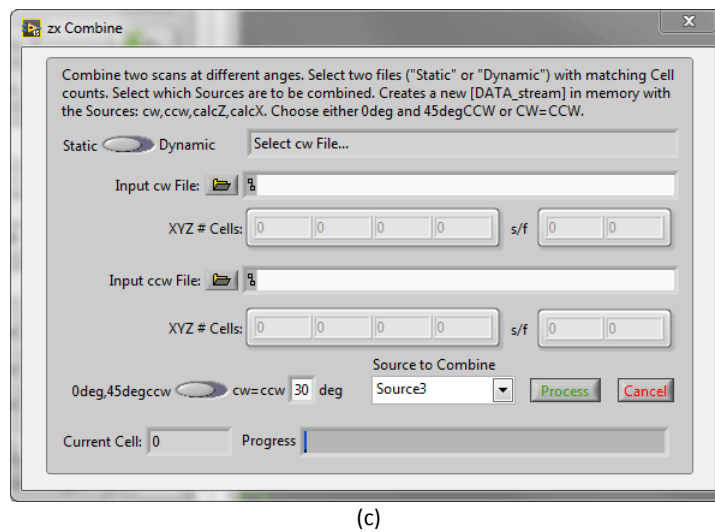
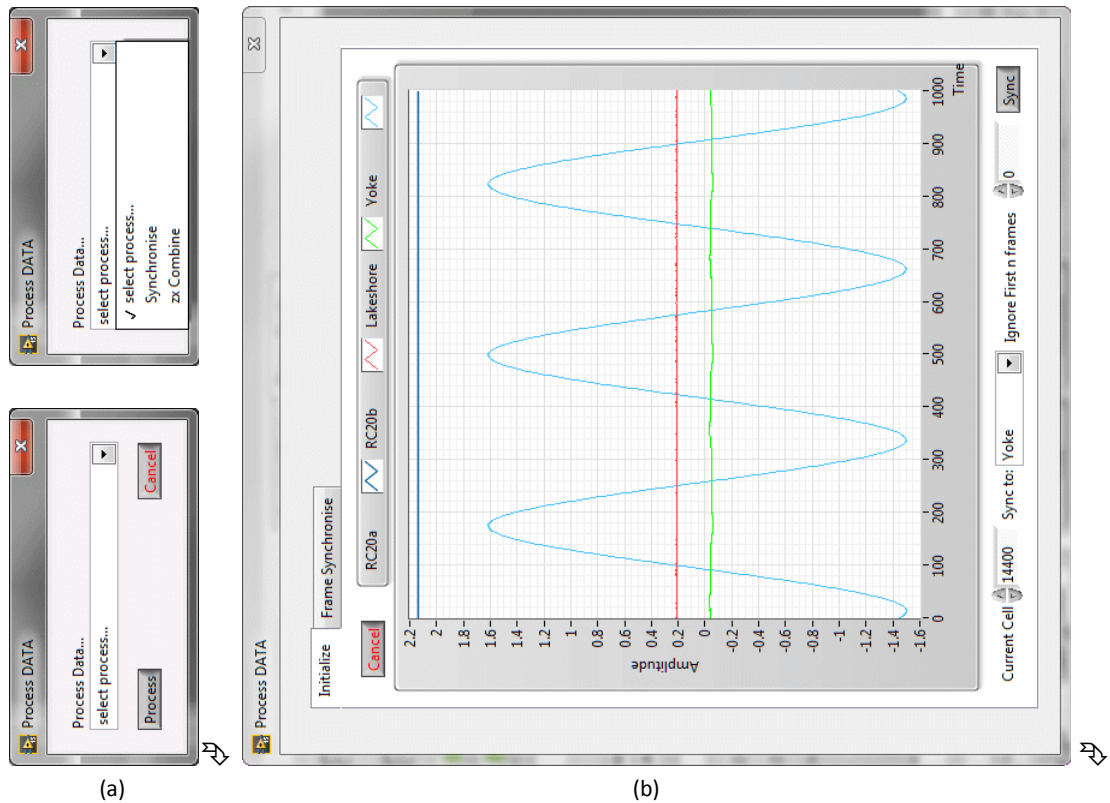


Figure 5.29: (a) The “Process DATA” menu and selection, (b) the “Process DATA” Synchronise.vi User Interface and (c) the “Process DATA” zxCombine.vi User Interface.

The “Export Current Source/Layer/Frame as PNG” button exports a single selected frame including an accompanying *{FrameStats}.csv* and *{Histogram}.csv* file. The *{Histogram}.csv* file provides histogram counts for the frame; a count of the number of pixels of each greyscale value.

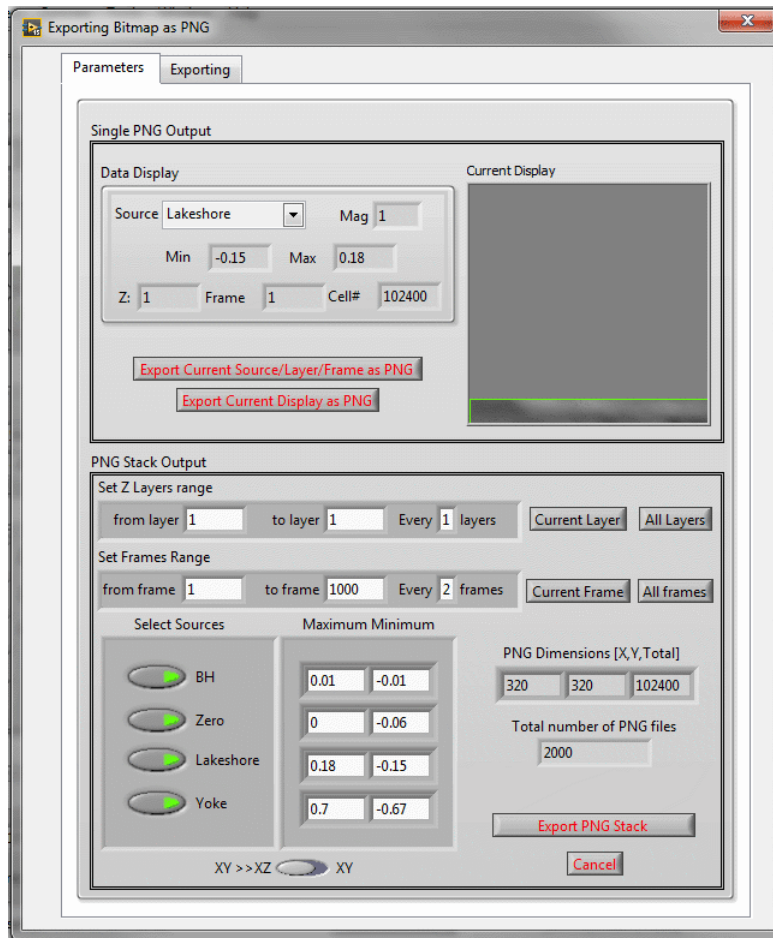


Figure 5.30: The “Exporting Bitmap as PNG” *PNG.vi* User Interface.

The *{FrameStats}.csv* file provides the Maximum, Minimum and Mean value of the entire frame. The “Export PNG Stack” exports a *[P].zip* archive which contains a series or “stack” of *.png* files for the selected range of Layers and Frames. The initial range of Layers and Frames can be adjusted. The “Current Layer”, “Current Frame”, “All Layers” and “All frames” buttons set the range appropriately. The “Every \_ layers” and “Every \_ frames” controls allow skipping. The data contrast values are initially imported from the *Data Display* group but can be changed. A boolean array allows selection of which Sources to process. The total number of *.png* files created are calculated. The *XY>>XZ* switch controls if the XY layers or XZ slices of a three-dimension volume of cells are considered. An example of the structure of a Blank *[P].zip* file, produced with the initialization data, is provided in in *Chapter 5.7z* of the Cardiff Portal Archive ([page ix](#)) and on the accompanying DVD-ROM.

## Chapter 6

# Two Dimensional Investigation of Stray Fields

The study of the domain structure in Grain Oriented Electrical Steel, Amorphous Alloy materials, *Cubex* doubly oriented Si-Fe Alloy and manufactured Planar coils by the scanning of stray fields from the sample surface has been made. Interpretation of the resulting field maps and comparison of the advantages and disadvantages of the Scanning System over other domain observation methods is given.

The scanner system has been developed to horizontally scan samples at resolutions up to 0.001 mm per cell. The scanner can scan any sample which will physically fit beneath the 3-axis arm but the default axis limits focus on a central area of 50 x 50 mm. The greater the number of cells, the longer each scan takes. A normal static scan using a mean of 20 samples per cell takes 0.02 seconds per cell, but the number of samples and sampling frequency can be altered. When scanning a sample a compromise must be made between the area of sample scanned, the resolution and the length of time the scan will take. This compromise must account for the expected size of the features present in the sample. The data produced by scans with the Scanner Control 2 software has been converted into the format for the Scanner Control 3, which contains useful header information about each scan and the supporting data for each figure presented in this chapter are provided in *Chapter 6.7z* of the Cardiff Portal Arxive ([page ix](#)) and on the accompanying DVD.

## 6.1 Domain Observation of 3% Si Grain-Oriented Electrical Steel

### 6.1.1 Comparative Scans with Different Sensors

The system has the capacity to use any sensor with an analogue voltage output for which a 3d-printed head can be designed. Three 3d-printed heads have been developed which hold the three sensors; the *Philtec* RC20 displacement sensor, the *Micromagnetics* STJ-020 TMR sensor or the *Lakeshore* 475 DSP Hall-effect probe ([Chapter 4](#)). [Figure 6.1](#) presents corresponding resulting scans from each of these sensors.

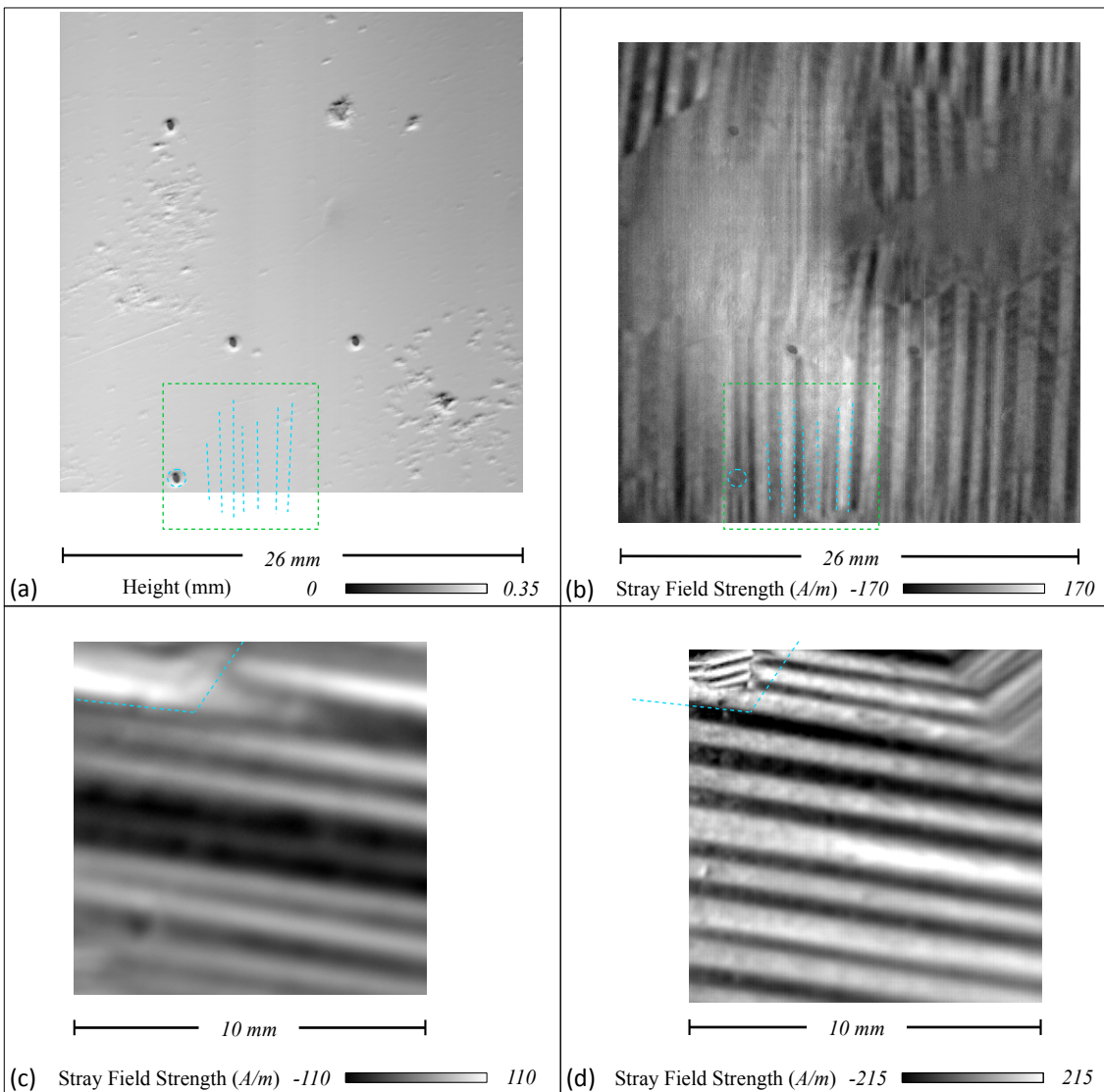


Figure 6.1: Scans of  $25 \times 25 \text{ mm}^2$  of polished 3% Si Grain Oriented Electrical Steel with; (a) *Philtec RC20* displacement sensor and (b) *Micromagnetics STJ-020* TMR sensor at  $0.05\text{mm}/\text{cell}$  resolution. A higher resolution scan of the green highlighted region and indicated domains is presented in [Figure 6.2](#). Scans of  $10 \times 10 \text{ mm}^2$  of coated 3% Si Grain Oriented Electrical Steel with; (c) *Lakeshore 475* DSP Gaussmeter Hall-effect sensor and (d) *Micromagnetics STJ-020* TMR sensor at  $0.05\text{mm}/\text{cell}$  resolution. The corresponding region of the sample is indicated. The  $H_z$  stray field strength (A/m) is indicated by a greyscale with positive field out of the page.



The topology map of a sample of polished 3% Si Grain-Oriented Electrical Steel, produced with the *Philtec* DC20 sensor, is presented in [Figure 6.1\(a\)](#). Even with a cleaned and polished sample some corrosion and micro-pitting is evident on the surface. Four pinholes are present with another two in the process of forming. These pinholes produce distinct magnetic features when the same area is scanned with the first *Micromagnetics* STJ-020 TMR sensor perpendicular to the surface ([Figure 6.1\(b\)](#)), which allows the correspondence of the two scans to be demonstrated. Both scans are at a resolution of 0.05 mm/cell. At this resolution the boundaries between different grains in the sample, of the order of 5 - 10 mm wide, are evident with the main magnetic domains largely aligned between each grain (the titular property of Grain-Oriented electrical steel). Even at this resolution, some evidence of internal structure and Lancet domains [125] within the main magnetic domains is evident. The first STJ-020 TMR sensor was not lapped to remove the corner of the silicon die and so the active area of the sample was at least 50  $\mu\text{m}$  above the surface, resulting in a stray-field strength ranging over  $\pm 170$  A/m. [Figure 6.1\(a\)](#) and [\(b\)](#) indicate the offset between the two sensors and the difficulty of concurrently scanning the same region of sample to the accuracy of the  $2 \times 4 \mu\text{m}^2$  footprint, discussed in [Chapter 4](#).

[Figure 6.1\(d\)](#) presents a 0.05 mm/cell scan of coated 3% Si Grain-Oriented Electrical Steel with the third STJ-020 TMR sensor, which has been lapped to an active area to sensor tip distance of 7  $\mu\text{m}$ . Lapping the sensor allows a closer sample surface distance which increases the measurable range of the stray field to  $\pm 215$  A/m and improves the sharpness of the image. A scan of approximately the same area of coated 3% Si Grain-Oriented Electrical Steel with the Hall-sensor based *Lakeshore* 475 DSP probe ([Figure 6.1\(c\)](#)) indicates the difference in clarity between the two magnetic sensors. The 475 DSP probe has an active area of diameter 0.51 mm, much larger than the 0.004 mm width of the STJ-020 sensor, and scans at a greater distance from the sample surface. This results in the evident blurred resolution and a stray field strength in the range  $\pm 110$  A/m.

### 6.1.2 Comparison Between Domain Observations Using the Scanner and MOKE

A higher resolution scan of the region indicated in [Figure 6.1\(b\)](#) is presented in [Figure 6.2\(a\)](#), scanned at 0.01 mm/cell; alongside a Magneto-Optical Kerr Effect (MOKE) image of the same area of sample. The Large bar domains and internal Lancet domains [125] of size 50-150  $\mu\text{m}$  are clear. The pinhole used to identify the common area and corresponding magnetic domain features are indicated with blue dotted lines.

The MOKE setup used was that developed for [126, 127] and is described and used extensively by [128]. The final result of the MOKE setup has greater resolution and clarity than the scanner system, however the production of [Figure 6.2\(b\)](#) requires a number of processing steps. [Figure 6.3](#) indicates the immediate quality of images produced by a MOKE apparatus. In reality samples have to be carefully prepared by polishing and cleaning to be able to see the Kerr effect on the sample. An uncleaned and scratched surface produces results presented in [Figure 6.3\(a\)](#). Because of the depth of field of the magnifier and the necessity of the  $\approx 60^\circ$  angle of observation, the actual region of the sample which presents in-focus domain patterns is very narrow, even when cleaned ([Figure 6.3\(b\)](#)). In order to produce the coherent image of the region presented in [Figure 6.2\(b\)](#) several tens of narrow in-focus strips, made from manually repositioning the sample, must be digitally merged ([Figure 6.2\(c\)](#)). The contrast of the image must be improved by digital level adjustment and it must be correctively distorted to adjust for the perspective. These sample requirements and post processing to produce a domain map equivalent to the region of the scan in [Figure 6.2\(a\)](#) are great disadvantages in the MOKE technique.

In contrast, though the scanning takes a long time, the results of the scanner system requires no sample preparation (and indeed can produce domain images through the coating) and, after the scan, produce an immediate, correctly planar, quantitative map of domains within the sample. Results which are also readily repeatable, and require no manual adjustments.

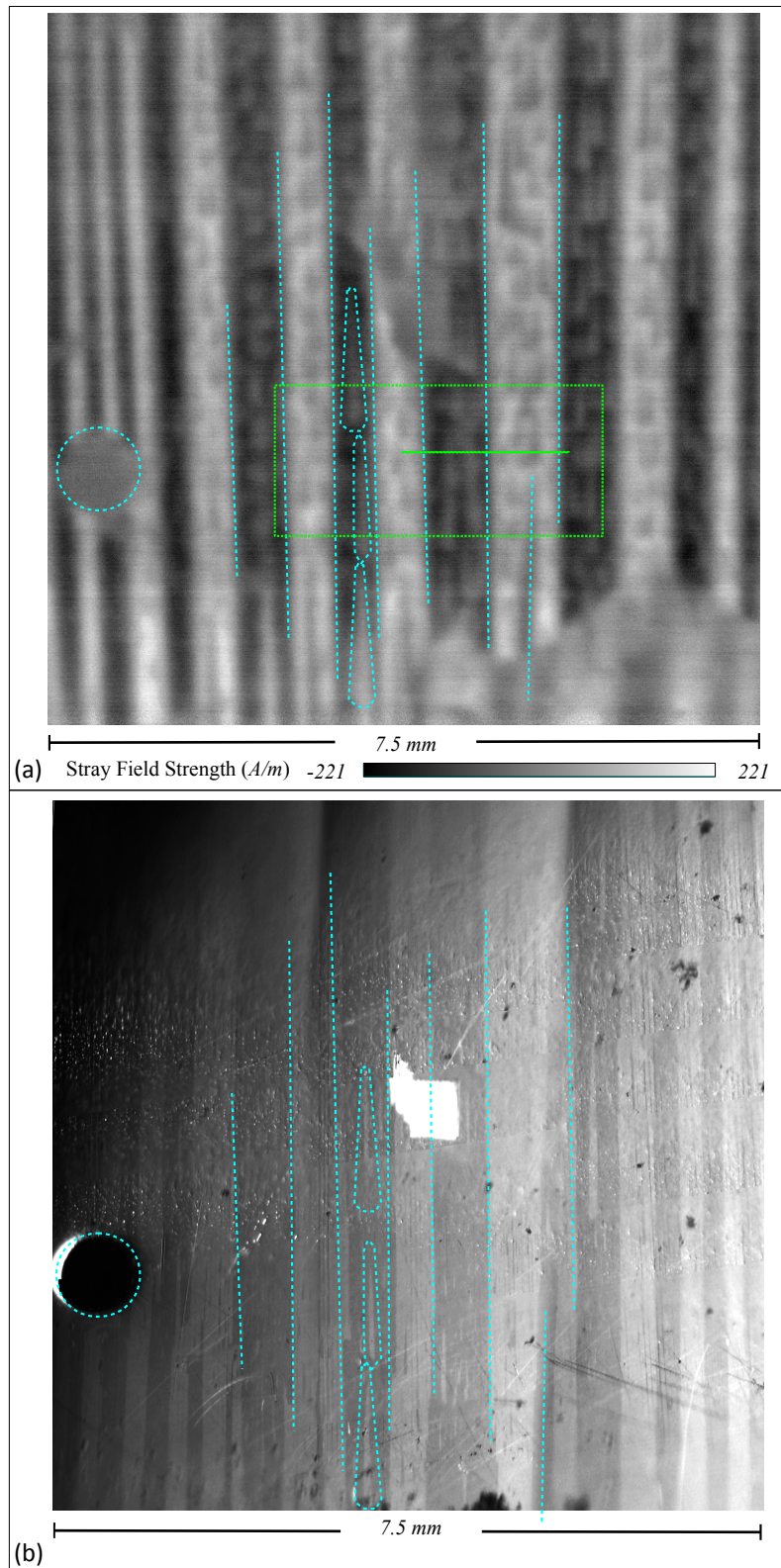


Figure 6.2: Domain observation of the 7.5 x 7.5 mm<sup>2</sup> region of polished 3% Si Grain Oriented Electrical Steel from Figure 6.1(b) produced by; (a) Scan with STJ-020 and (b) MOKE imaging of the same area of sample. The pinhole used to identify the common area and corresponding magnetic domain features are indicated with blue dotted lines. The regions of the scans of Figure 6.4 and Figure 7.5 are highlighted in green.

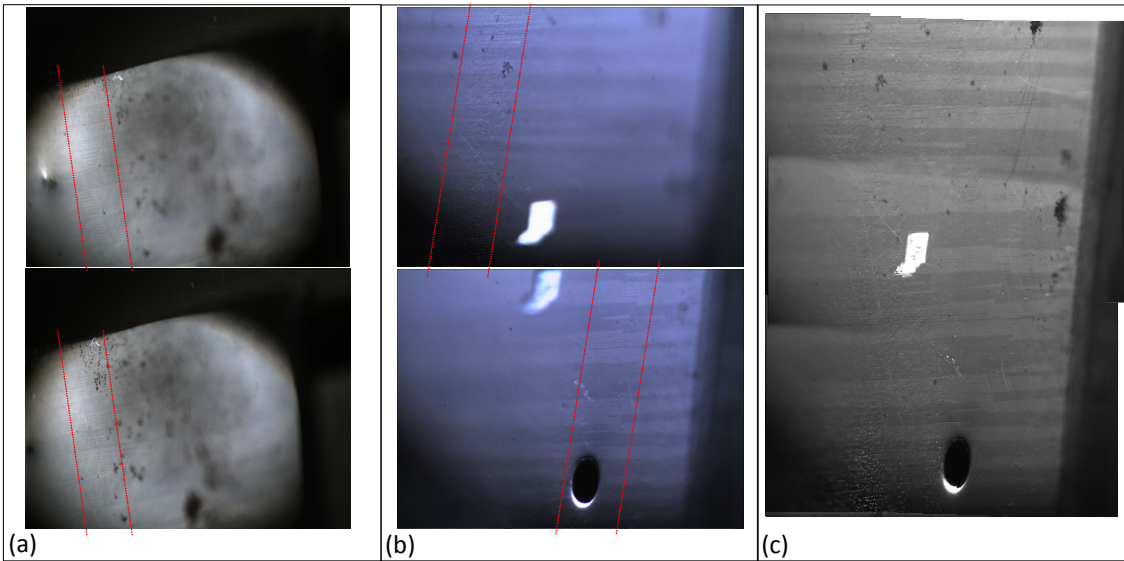


Figure 6.3: Raw Images from the MOKE system; (a) uncleaned sample, (b) cleaned sample, indicating the very narrow depth of field. The indicated narrow bands of in-focus image need to be manually combined to produce a coherent image of a large area (c), which retains perspective distortion.

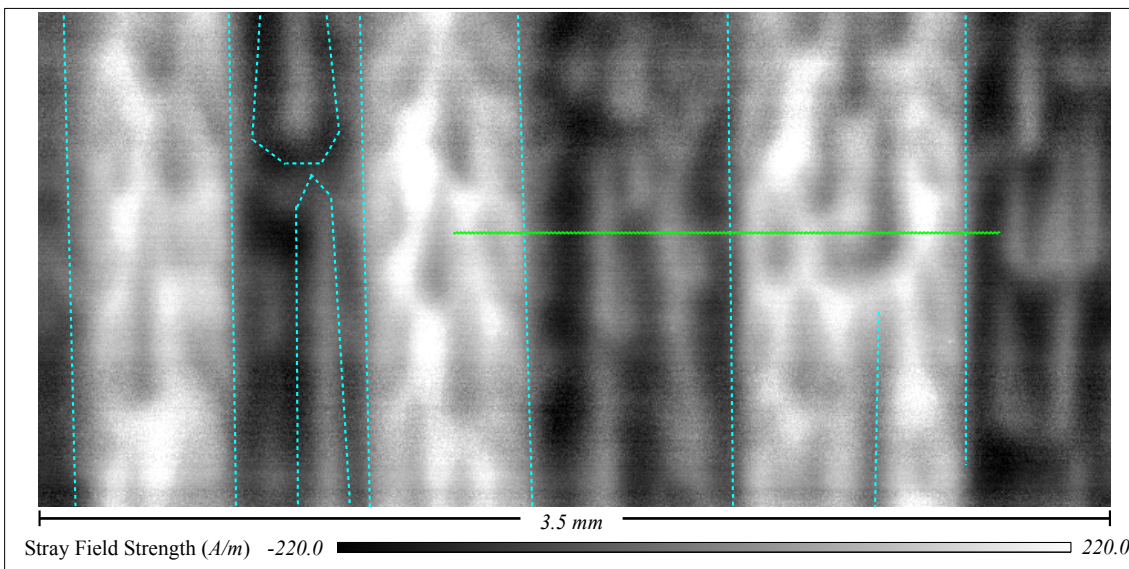


Figure 6.4: Domain observation of the 3.5 x 2.14 mm<sup>2</sup> region of polished 3% Si Grain Oriented Electrical Steel from Figure 6.2(a) produced by a scan with the STJ-020 sensor at 0.005 mm/cell. The Stray field strength ranges over  $\pm 220$  A/m. The location of the zx Transect presented in Figure 7.5 is illustrated.

[Figure 6.4](#), a further scan of the region indicated in [Figure 6.2\(a\)](#) at a resolution of 0.005 mm/cell, whilst at the limit of resolution of the  $2 \times 4 \mu\text{m}^2$  footprint of the STJ-020 TMR sensor, indicates the clarity of Lancet domains visible within the bar domains that are possible with sufficient scanning time. These results have been published in [129] presented at *23rd Soft Magnetic Materials conference Seville, 2017*.

The appearance of these initial scans of 3% Si Grain-Oriented Electrical Steel were at first unexpected, in that there is greater similarity in appearance between the scan and MOKE imaging than with domain observation with the Bitter technique [31].

Measuring the  $H_z$  stray field emanating perpendicularly from the sample surface might at first be expected to highlight the domain walls, where the rotation of the magnetization vector at a Bloch-wall theoretically causes a component of directly perpendicular field. This should be similar to the theory in which Bitter based particles are drawn to the stray field gradients from the Bloch-walls ([Chapter 3](#)). However, the results from the scanner strongly indicate the body of the domains rather than the edges, showing the difference in orientation between domains with magnetization purportedly parallel to the surface of the sample, more similar to the results of the MOKE method.

This is an incongruous result perhaps indicating that the stray fields from domains at the surface of the sample, or even the domains themselves, are not perfectly parallel to the surface but have some perpendicular component that is being measured by the sensor.

This motivated the further development of the system to the novel study of the three-dimensional structure of the stray-fields that is discussed in [Chapter 7](#).

### 6.1.3 Domains in Coated 3% Si Grain-Oriented Electrical Steel After Laser Etching the Surface

In Power transformer applications the efficiency with which the magnetization of the 3% Si Grain-Oriented Electrical Steel can switch direction at 50 or 60 Hz is important for the efficiency of the transformer as a whole [45]. One technique employed is to etch a linear defect, perpendicular to the rolling (grain-orientation) direction of the steel, during manufacture using a laser. In theory this has the effect of artificially restricting the size of bar domains, which reduces the extent of material which must undergo the energy minimisation process at each oscillation [130, 45].

A sample of coated 3% Si Grain-Oriented Electrical Steel was etched with a 10.6  $\mu\text{m}$  wide CO<sub>2</sub> laser at 14% of its 50 W total power and scanned at both 0.1 mm/cell and 0.01 mm/cell resolutions. The results of the scans are presented in Figure 6.5, with the location of the Laser etched defect lines indicated.

The restriction of the domains by the artificially created boundaries are clearly indicated. The 10.6  $\mu\text{m}$  width of the Laser line itself causes a band of fine domain closure structures with sharp discontinuities either side. Natural grain boundaries are still present and may interfere with the intended artificial boundaries.

The scans are performed with the second STJ-020 TMR sensor which is lapped to approach the surface to within 7  $\mu\text{m}$ . Even with the additional thickness of the coating the strength of the measured stray fields range over  $\pm 350$  A/m, which is approximately three-quarters greater than the field strength measured from un-etched samples, indicating that in introducing a defect to the surface of the sample the strength of fields which stray from that surface increases. This is the principle of many non-destructive testing techniques [87] but can cause undesirable effects in Power transformer applications [130, 45].

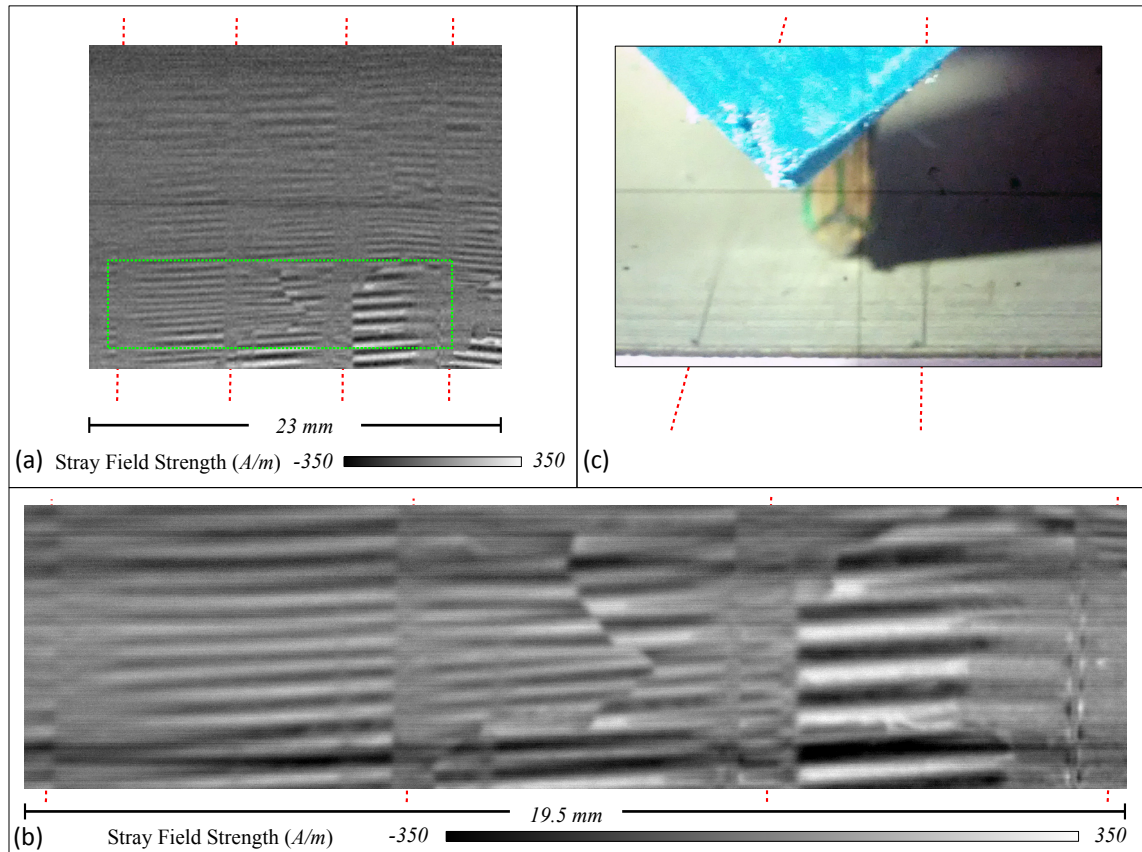


Figure 6.5: Domain observation of (a) 23 x 18 mm<sup>2</sup> region of Laser Etched Coated 3% Si Grain Oriented Electrical Steel produced by a scan with the STJ-020 sensor at 0.1 mm/cell with the 19.5 x 5 mm<sup>2</sup> region (b) indicated, scanned at 0.01 mm/cell. The Stray field strength ranges over  $\pm 350$  A/m. The coating is etched with a 10.6  $\mu\text{m}$  wide CO<sub>2</sub> laser at 14% of 50 W power along the lines indicated. (c) Photograph of the scanning through the incorporated microscopic sight.

The comparison of the stray field structure before and after laser etching of a sample is made in [Chapter 7](#) and the effects of laser etching with a dynamic AC applied magnetic field are further investigated in [Chapter 8](#).

## 6.2 Observation of Stray Fields from Amorphous Alloy Materials

### 6.2.1 Mapping Stray Fields from As-cast *Metglas* Amorphous Ribbon

To test the capacity of the system the stray fields from as-cast amorphous ribbon are investigated. [Figure 6.6](#) presents investigation of the  $H_z$  stray fields emanating from a  $19 \times 12 \text{ mm}^2$  region of as-cast 2605 Co IPF895 *Metglas* Alloy Amorphous Ribbon at progressively higher resolutions. These results have been published in [[129](#)] presented at *23rd Soft Magnetic Materials conference Seville, 2017*. Because of the lack of grains within amorphous materials it is expected that any observable domains will be of very fine-scale resolution [[131](#), [49](#), [132](#)]. Whilst stray-field features can be observed, a number of difficulties in the study of domains in this material using the scanner are apparent.

Firstly, the intrinsic domains from Amorphous materials prove themselves to be of a strength ranging over only  $\pm 88 \text{ A/m}$  which is a third of the strength from Grain-Oriented Electrical steel and just above the background Earth field of approximately  $50 \text{ A/m}$ . This leaves little scope for gaining contrast above the background noise. The common “domain viewer” method of applying a perpendicular external field to the sample to enhance the intrinsic fields [[6](#)] does not help with the scanning method; the externally applied field tends to enhance the measurement of stray fields from surface topology features more than the internal domains. This effect is used beneficially in MOKE observations [[49](#)] but causes difficulties in studying the domains within samples. Applied fields must be used when studying domain dynamics, the discussion of the difficulties encountered then are made in [Chapter 8](#).

The second difficulty in the study of as-cast amorphous ribbon is that, due to the cooling process of manufacture, the surface of the ribbon as-cast is not smooth and features undulations and ripples. The stray field features observed in [Figure 6.6](#) are more indicative of the stray fields interacting with the surface undulations of the sample than with the intrinsic domain structure.



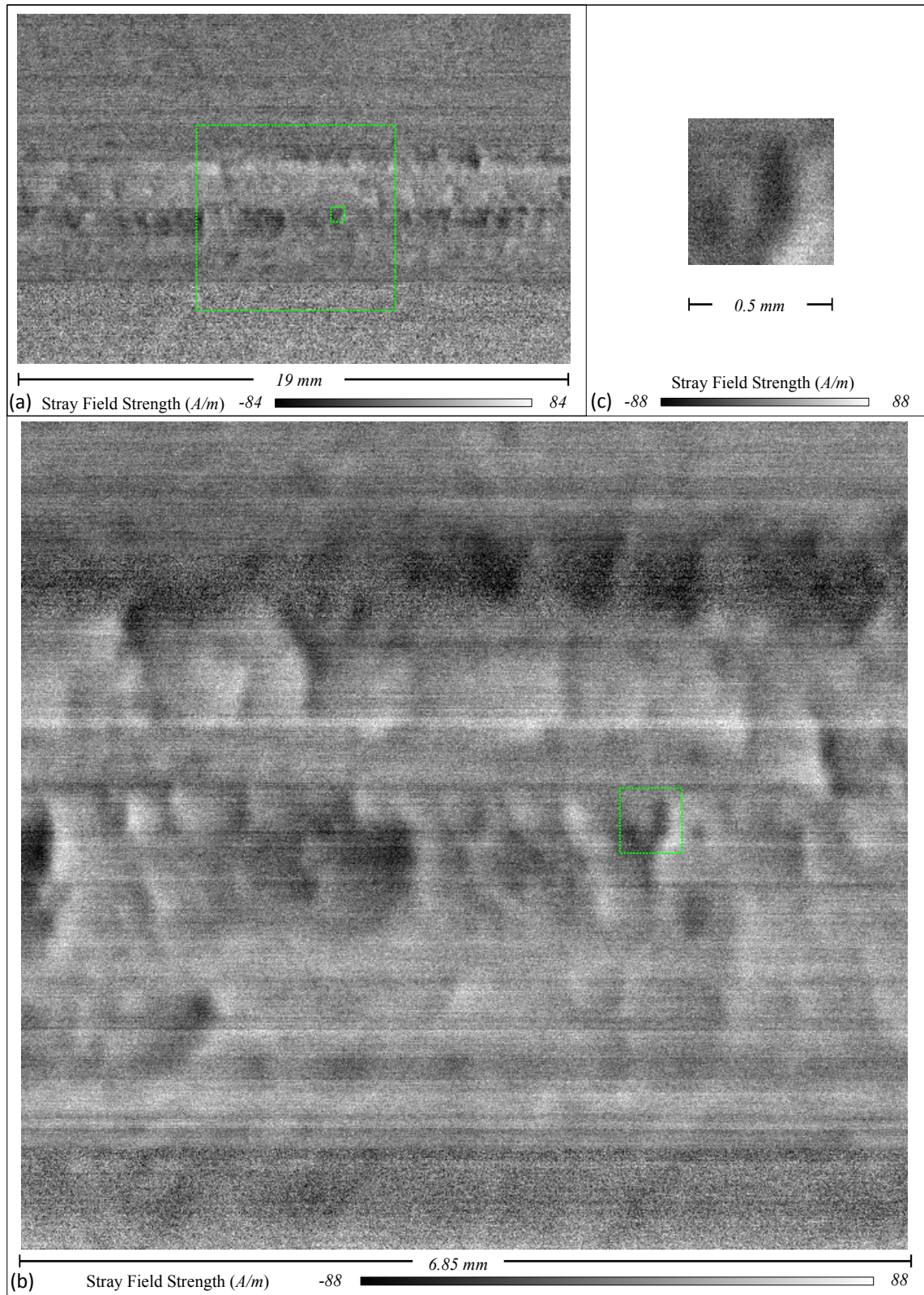


Figure 6.6: Scan of (a)  $19 \times 12 \text{ mm}^2$  region of as-cast 2605 Co IPF895 *Metglas* Alloy Amorphous Ribbon produced with the STJ-020 sensor at  $0.05 \text{ mm/cell}$ , the indicated (b)  $6.85 \times 6.4 \text{ mm}^2$  at  $0.01 \text{ mm/cell}$  and (c)  $0.5 \times 0.5 \text{ mm}^2$  at  $0.005 \text{ mm/cell}$ . The Stray field strength ranges over  $\pm 88 \text{ A/m}$ .

### 6.2.2 Mapping Stray Fields from AF10 Amorphous Wire and Comparison with the Bitter Technique

AF10 Amorphous wire is a difficult material to scan with the system because of the cylindrical topology of the sample. Nevertheless, by targeting a progressively smaller area of the very top of the wire at progressively higher resolution ([Figure 6.7\(a\)](#) and [\(b\)](#)) a scan of the top surface of AF10 Amorphous wire was achieved at a resolution of 0.001 mm/cell, presented in [Figure 6.7\(c\)](#).

As with *Metglas* Amorphous Ribbon the intrinsic stray-field strength from the wire only ranges over  $\pm 80$  A/m, close to the background Earth field of approximately 50 A/m, which makes distinguishing any features difficult. This difficulty is compounded by the size of domain features present in the material, which necessitated the 0.001 mm/cell resolution.

Three distinct lines are apparent on the 0.001 mm/cell scan which are 30  $\mu$ m apart. Two of the features indicate stray-fields into the sample and one indicated stray-fields out of the sample.

[Figure 6.8](#) presents a comparison of the same sample of AF10 material observed with a ferro-fluid Bitter technique, performed by and reproduced with permission from [6], which employed an energizing coil to also enhance the stray-fields. Helical domain boundaries can be seen, which at zero twist angle can be seen to cross the wire. The distance between each of the loops is 30  $\mu$ m with the zig-zag width of each loop concurrent with the width of the features in [Figure 6.7\(c\)](#). The difference in direction of the stray fields detected by the scan could be a selection artefact of which side of the zig-zag is contributing most to the mean strength in each cell.

It is indicative of the power of the developed scanner system that it is able to detect such weak and small features.

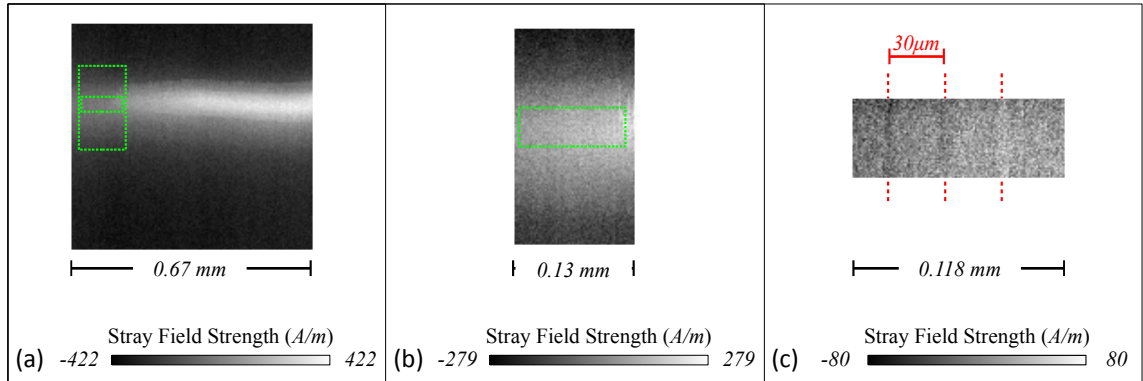


Figure 6.7: Progressively higher resolution scans of the top of AF-10 Amorphous wire (running left to right); (a) at 0.005 mm/cell, (b) at 0.002 mm/cell and (c) at 0.001 mm/cell. The Stray field strength in the final 0.001 mm/cell scan ranges over  $\pm 80$  A/m, with distinct features  $30 \mu\text{m}$  apart.

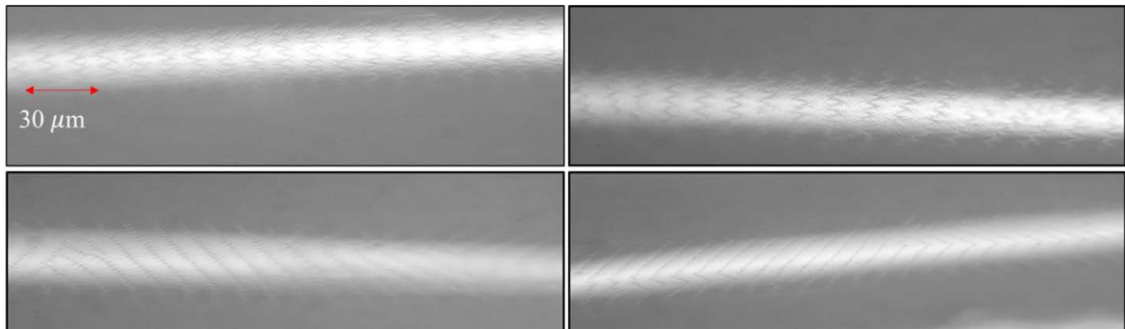


Figure 6.8: Domain structure of a 50 mm length AF-10 Amorphous wire with an applied perpendicular magnetic field of 1.1 kA/m and twist angles of (a) zero, (b)  $1/2\pi$ , (c)  $\pi$  and (d)  $2\pi$  rad. Reproduced from [6]. A red scale line indicates a distance of  $30 \mu\text{m}$  between domain lines.

## 6.3 Comparison Between the Modelled and Measured $H_z$ Fields from Different Topologies of Planar Coils

Planar coils are generally flat spirals of conductive track mounted on PCB or flexible polymer substrate. The shape, number of turns, width and thickness of track can be varied. Other classes of planar coil are the meander and mesh coils, which do not spiral but alternate direction across the substrate with varying track thickness and displacement (Figure 6.9(i)). Planar coils have found use in wireless power transfer [133], wireless communication [134] and sensing applications [135]; including non-destructive testing [136] and health monitoring [137] where their low profile and robust construction are an advantage [138].

### 6.3.1 Finite Element Modelling of Stray Fields from Planar Coils

The topologies of planar coil selected for investigation from [138] are, by convention, called Circular, Mesh, Meander and Square coils [139]. The coils were fabricated by CNC milling from a 54 mm x 30 mm FR4 PC board with 35  $\mu\text{m}$  copper thickness and a track width of 0.5 mm. The dimensions and shape of each coil have been replicated as three-dimensional models within the ANSYS® *Maxwell* 3D FEM software, given the material properties of copper and enclosed in an invisible cuboid with the material properties of vacuum; permitting the magnetic fields surrounding the coils to be calculated. Photographs of the manufactured coils and the corresponding ANSYS® models are presented in Figure 6.9(i) and (ii). Within the ANSYS finite element modelling,  $xy$ -plane slices through the vacuum cuboid are made at distances above the model consistent with the practical scanning heights used for each coil. This provides a virtual surface above the modelled coil on which can be projected the magnitude of the  $H_z$  component of the calculated fields surrounding the coil, simulating the results of a perpendicular scan at each height, and presented in Figure 6.9(iv). An automatically optimized mesh (maximum length 2 mm) is applied to the cuboid and slice which provides a resulting field resolution consistent with the measured data without excessive computing time.

### 6.3.2 Scanning of Stray Fields from Planar Coils

The four manufactured planar coils were mounted on the sample stage and energized to draw  $0.40 \text{ Amp} \pm 0.01 \text{ Amp}$  of direct current using a *Powerline Electronics* power supply. This relatively low current ensured the sensitive STJ-020 sensor was not saturated, whilst providing enough field strength to be measured. Scans of  $250 \text{ cells} \times 250 \text{ cells}$  were performed with a resolution of  $0.1 \text{ mm/cell}$  at the lowest scanning height sufficient to clear the solder points of the energizing connections. The Circular coil was scanned at a height of  $0.50 \text{ mm} \pm 0.01 \text{ mm}$ , the Mesh and Meander coils were scanned at a height of  $0.25 \text{ mm} \pm 0.01 \text{ mm}$  and the Square coil was scanned at a height of  $0.15 \text{ mm} \pm 0.01 \text{ mm}$ . The full scan of the Circular planar coil was necessarily high due to the size of the solder points and thus at a height where differences in the field from each track could not be easily distinguished, consequently an additional lower scan at  $0.15 \text{ mm} \pm 0.01 \text{ mm}$  was made of a region between the two solder points. The results of this lower scan and the corresponding ANSYS simulation are presented in [Figure 6.9\(a.iii\)](#) and [\(a.iv'\)](#). The scans of the four coils were performed with the sensor perpendicular to the sample surface. Photographs of the scan being performed above the Square planar coil are presented in [Figure 7.6](#).

The scan heights were governed by the size of the solder points, but were standardized to discrete heights to permit better comparisons to be drawn. The Circular and Square planar coils, as spiral topologies, produce much greater field strengths than the Mesh and Meander. The central loops of spiral topologies receive reinforcing field contributions from each successive concentric outer loop.

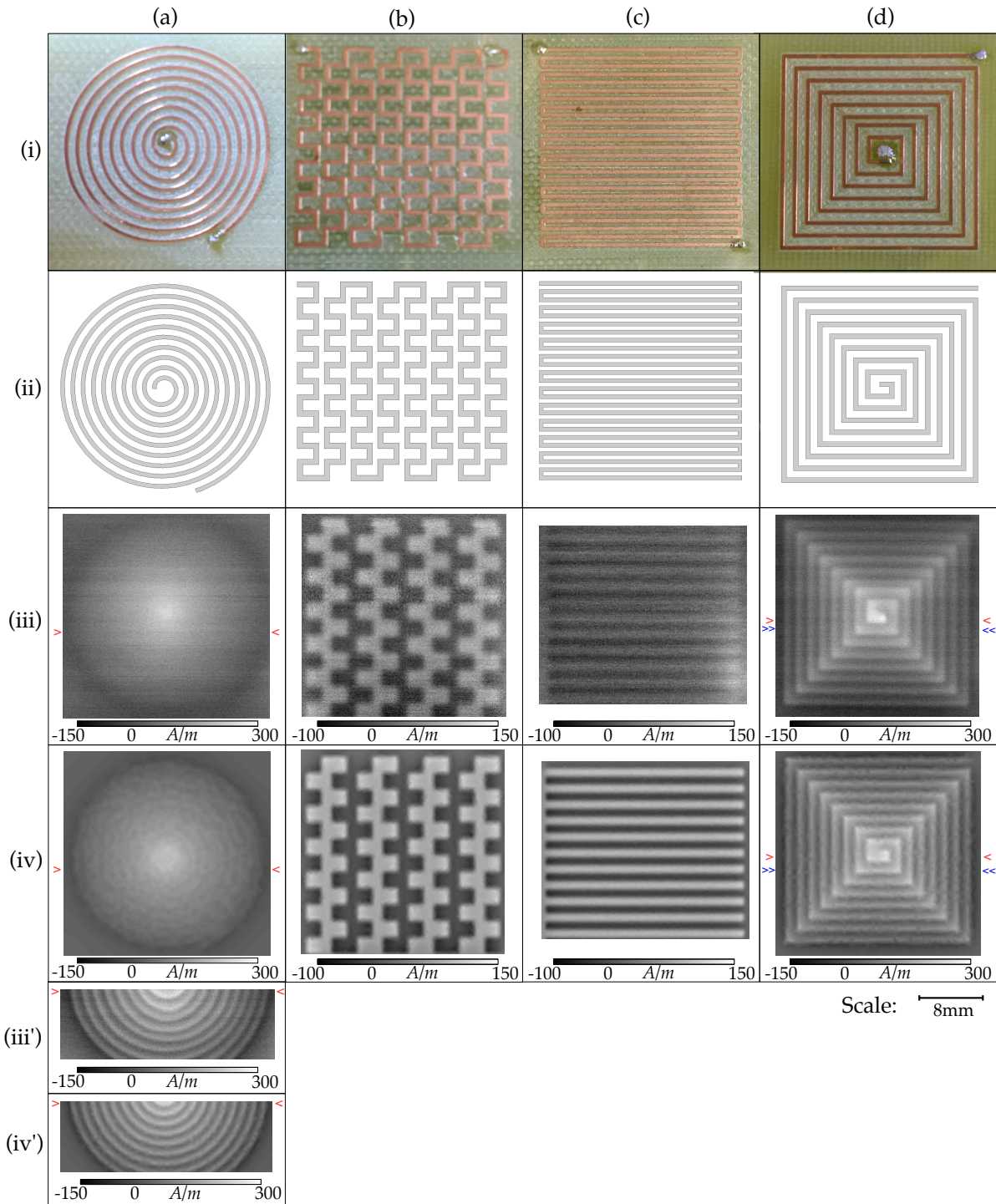


Figure 6.9: Comparison of ANSYS FEM and Scans of Planar Coils. (a) Circular, (b) Mesh, (c) Meander, (d) and Square planar coils. (i) Photographs of the manufactured coils, (ii) ANSYS models, (iii)  $H_z$  stray field scans with the TMR-020 sensor at 0.1 mm/pxl, (iv) FEM of the  $H_z$  fields above the coils. (iii') and (iv') are scans of the Circular coil at a closer scan height. The transect marked by red single-chevrons indicates the path of  $H_z$  amplitude plots (Figure 6.10). The blue double-chevrons indicate the path of the  $z_x$  Transect presented in (Figure 7.7(ii)).

In [Figure 6.9](#) the results of the scans of the Circular, Mesh, Meander and Square planar coils are presented alongside the expected results from the finite element modelling. There is a strong similarity between the measured and the modelled field shape and strength for all four topologies.

There is significant noise present in the scans, the *Micromagnetics* AL-05 power and preamplifier unit (Appendix 4) for the STJ-020 sensor is electrically noisy. This limitation has been discussed in [4] and the solution presented was to develop an alternative preamplifier. There is risk of damage to the expensive sensor if the bias voltage, if independent of the AL-05, is not governed correctly. The existing signal is judged sufficiently above the background noise not to warrant this risk. The evident variation in horizontal scan lines is a greater issue in all the scans. This is caused by slight drift in the resistance of the potentiometer used by the AL-05 to set the bias over the length of the scan, perhaps due to slight thermal variation or mechanical disturbance. The granularity within the finite element modelling maps, particularly [Figure 6.9\(a.iv\)](#), are an artefact of the mesh size. An optimized mesh size with a maximum length of 2 mm obtained this level of detail. A greater maximum mesh size led to a reduction in detail whilst a finer maximum mesh size did not improve the detail, which seemed to be a property of modelling the gradual gradients. At a scan height of  $0.5 \text{ mm} \pm 0.01 \text{ mm}$  neither the scan nor the modelling distinguish clearly the individual tracks of the Circular planar coil, leading to a conical overall field amplitude ([Figure 6.9\(a.iii\)](#) and [\(a.iv\)](#)). The closer  $0.15 \text{ mm} \pm 0.01 \text{ mm}$  scan ([\(Figure 6.9\(a.iii\)'](#) and [\(a.iv\)'](#))) illustrates how each concentric ring reinforces sequentially the fields within it. The central peak of the scan is more defined than that of the model, attributed to the central solder spike of the manufactured coil when compared with the wide flat centre of the finite-element model. The Meander and Mesh topologies produce weaker fields due to the lack of a reinforcing spiral. The checkerboard pattern of the Mesh topology is the result of some field reinforcement within each minor three-sided loop of the mesh. The Meander coil gains no reinforcement; the fields of each leg are counter to each other, resulting in a very weak overall field, only just discernible above the background noise. The increase in field strength in the lower right corner of [Figure 6.9\(c.iii\)](#) is attributed

either to an increase in current and field at the solder point in that corner, or to a difference in copper thickness or relative lifting of the copper track in the manufactured coil.

The greyscale maps represent well the shape of the  $H_z$  fields and give an approximate indication of similarity in strength. To better compare the strength of the fields for the Circular and Square planar coil, plots of  $H_z$  amplitude along a path marked by red single-chevrons in [Figure 6.9](#) are presented in [Figure 6.10](#).

A path of five cells width was used between the points marked by the red single chevrons in [Figure 6.9\(a.iii\)](#) and [\(d.iii\)](#). The measured field values plotted in [Figure 6.10](#) are the mean of each group of five cells, with the maximum and minimum values plotted as the error range. The finite element model values are taken directly from the mesh at the  $xy$ -plane height  $z_0$ , with an error range produced by also calculating the planes at  $z_0 \pm 0.1$  mm. In general, the measured field strengths are slightly lower than expected from modelling. This can be attributed to a combination of the  $\pm 0.01$  Amp error in practical current drawn and the  $\pm 0.01$  mm error in practical scan height; in addition to the statistical error from the background noise level. There is also the possibility of unaccounted power losses within the manufactured planar coils through factors [\[140\]](#) which are not adequately modelled. There is some spatial discrepancy between the modelled track positions and the milled tracks on the manufactured coils, due to the manufacturing tolerances of the CNC milling. The overall field strength is lower the greater the scan height. Though the individual tracks in the Circular coil are not easily distinguished at the greater scan height ( $z_0 = 0.5$  mm  $\pm 0.01$  mm) the plot in [Figure 6.10\(b\)](#) indicates that they are still present.

Further comparison between the different components of modelled and measured fields from Planar Coils is investigated in [Chapter 7](#).

This comparative work has been published published in [\[112\]](#), a copy of which is available in Appendix 6.



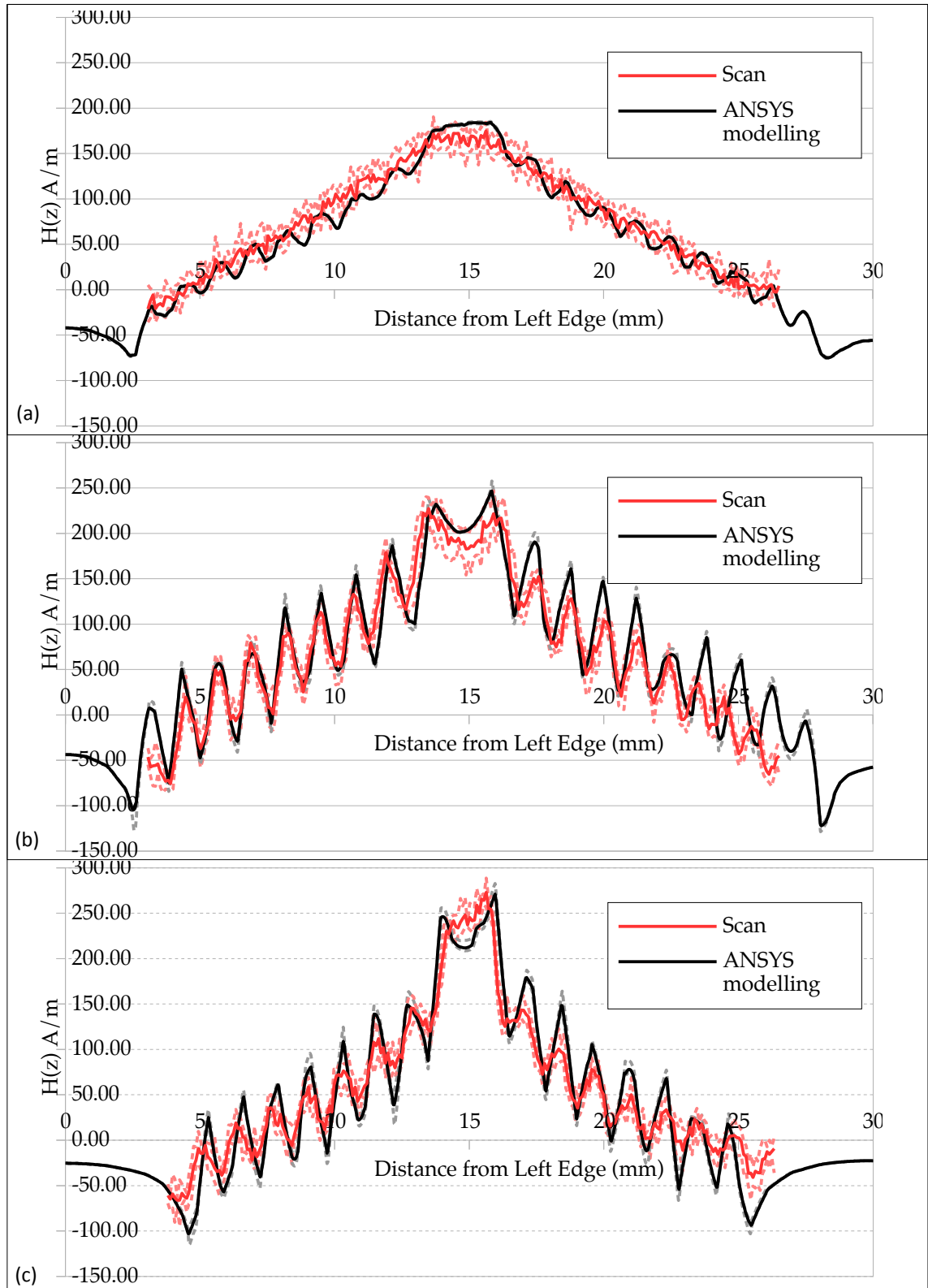


Figure 6.10:  $H_z$  amplitude plots of the (a) and (b) Circular and (c) Square planar coils along the paths indicated by red single-chevrons in Figure 6.9 at a scan height of (a)  $0.50 \text{ mm} \pm 0.01 \text{ mm}$ , (b) and (c)  $0.15 \text{ mm} \pm 0.01 \text{ mm}$ . The  $\pm$  errors are indicated by dashed lines above and below for both the Scan and ANSYS plots.

## 6.4 Observation of Stray Fields from *Cubex* Doubly Oriented Si-Fe Alloy

Doubly oriented silicon-iron is manufactured so that a proportion of the material grains have their magnetisation easy-axis in the rolling direction, as with normal 3% Si Grain-Oriented Electrical Steel, with the remaining proportion perpendicular.

The double orientation leads to unique magnetic properties which were investigated by N.A.S.A. in the 1960's for use in compact transformer cores and motor stators [141].

The manufacturing process to produce such alloys was developed by the *Cubex company, USA* [141] but later patents for similar techniques were also awarded to research by the *Nisshin Steel Co., Japan* in 1986.

The interacting stray-fields at the sample surface form interesting checkerboard domain patterns which can be used to demonstrate the scanner system.

The results of two 0.05 mm/cell and 0.01 mm/cell scans of the perpendicular  $H_z$  field from a sample of *Cubex* Doubly Oriented Si-Fe Alloy are presented in [Figure 6.11](#).

With such a complex stray-field pattern emerging from the sample it would be useful to see how the stray fields are structured in the thin three dimensional volume above the surface rather than just a planar view.

The capacity to do this is the unique advantage of the scanning system over the solely two dimensional MOKE and Bitter planar surface domain observation techniques, and motivated the development of the Scanner Control 2 system software ([Chapter 5](#)).

Investigation of the three dimensional stray field structure above the surface of a sample follows in [Chapter 7](#).

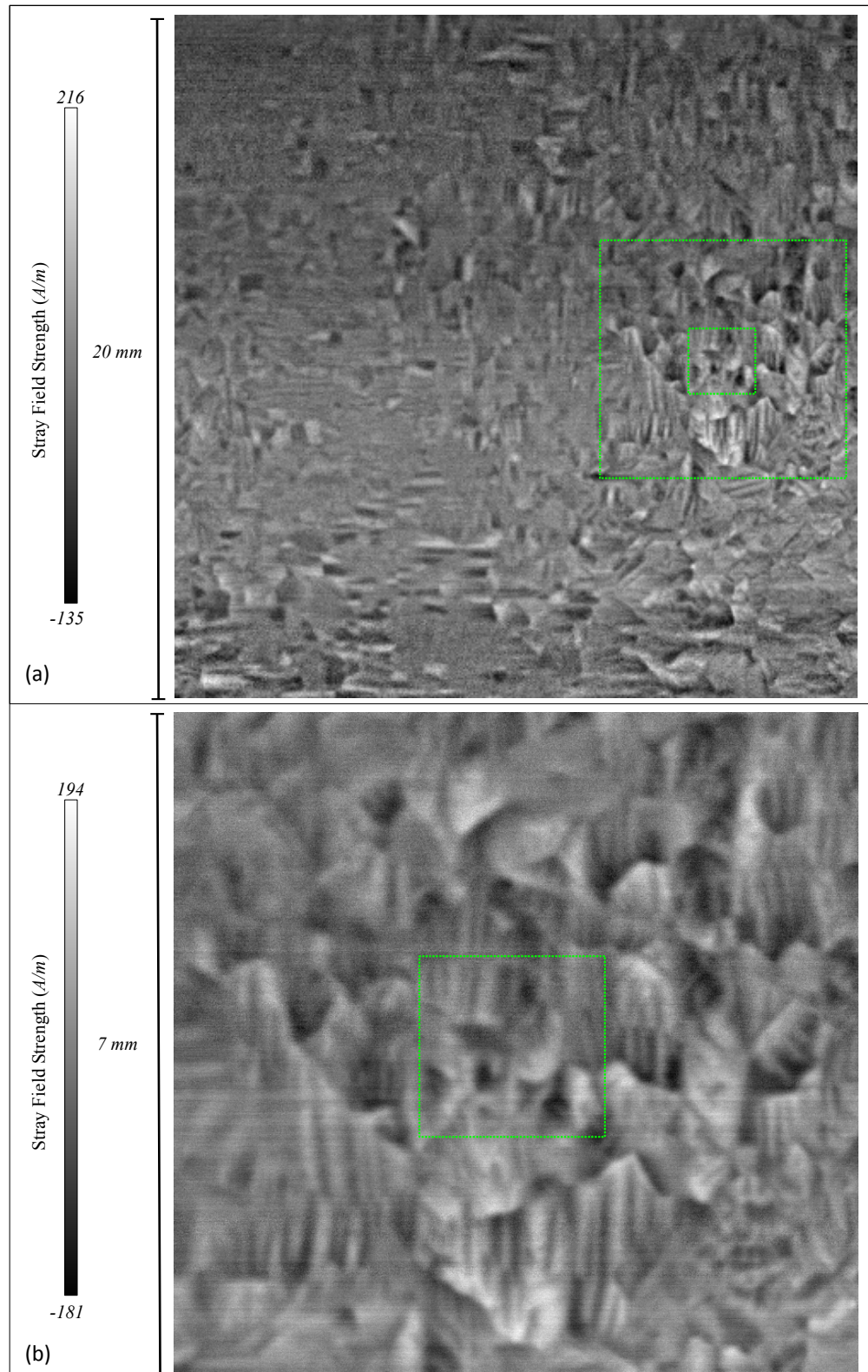


Figure 6.11: Scan of (a) 20 x 20 mm<sup>2</sup> region of *Cubex* doubly oriented Silicon-iron alloy, produced with the STJ-020 sensor at 0.05 mm/cell, with an indicated (b) 7 x 7 mm<sup>2</sup> region at 0.01 mm/cell. The Stray field strength ranges from -135 to 216 A/m. The indicated further 2 x 2 mm<sup>2</sup> region is presented in [Figure 7.1](#).



*Chapter 7***Investigation of Three Dimensional Stray Field Structure**

The ability to scan in a three dimensional volume above the surface of the sample and to derive the  $H_z$  and  $H_x$  components from only a single axis sensor is developed and demonstrated. The principles are tested against the known geometries of constructed planar coils, the expected fields from which can be determined using FEM.

**7.1 Scans of  $H_z$  Stray Fields within a Volume above a Sample Surface**

With the development of Scanner Control 2 and later Scanner Control 3 it became possible to scan not only in the  $xy$  plane, but also different layers of  $xy$  planes in steps along the  $z$  axis. Thus forming a cuboid of three dimensional cells, or a scan of the volume above the surface of a sample. With the development of the second, and then ultimately the third sensor head the TMR Sensor could additionally scan not only the field component perpendicular to the surface, but at any intermediate angle. By scanning twice, vertically and at  $45^\circ$  counterclockwise from vertical it becomes possible to calculate both the  $H_z$  and  $H_x$  components from only a single axis sensor. The purpose is to allow the novel investigation of the shape and extent of the stray fields as they extend beyond the sample surface, to permit a better understanding of the differences between domain images obtained by stray field imaging and those obtained by other techniques including the standard stray field dependent Bitter method.

### 7.1.1 $H_z$ Stray Fields Volume Scans of *Cubex* Doubly Oriented Si-Fe Alloy

The first question to ask when considering the structure and shape of stray fields in the thin volume above the surface of a sample is how far the fields extend into the air above the sample.

Figure 7.1 presents a Scan of  $H_z$  stray fields within a volume of  $2 \times 2 \times 0.2 \text{ mm}^3$  above the sample of *Cubex* doubly-oriented Silicon-iron alloy. The area over which the scans occur is highlighted in Figure 6.11. Animated sweeps through each  $xy$  Plane and each  $zx$  Slice are available in the Chapter 7.7z Cardiff Portal Arxive (page ix). The  $H_z$  Stray field strength ranges over  $\pm 200 \text{ A/m}$ .

It can be seen that even these relatively strong  $H_z$  fields reduce to levels less than the Earth's field at distances greater than 0.05 mm from the surface.

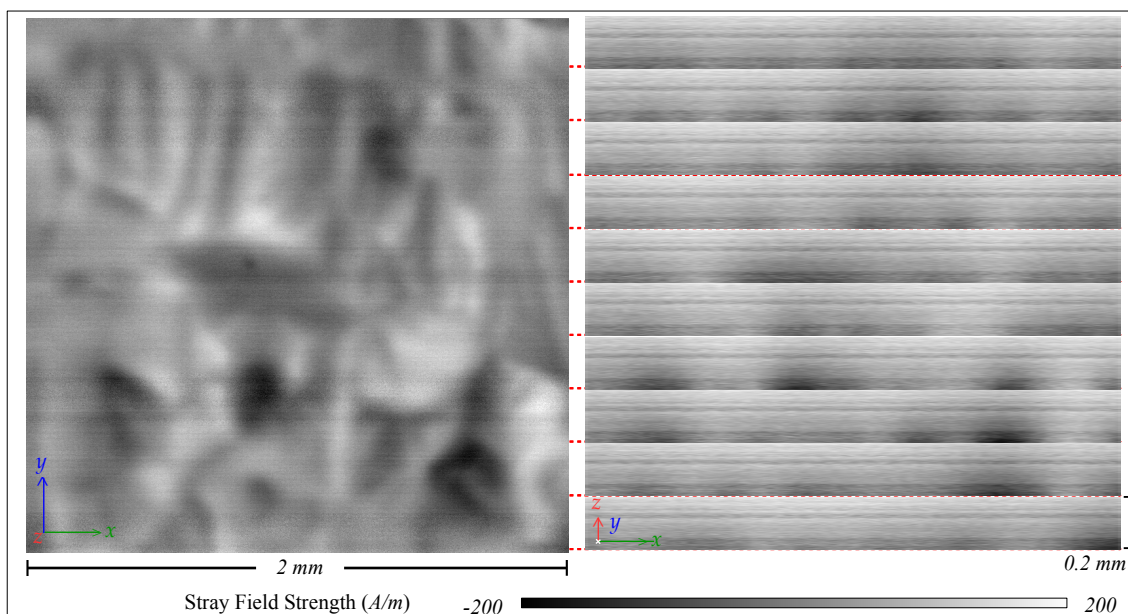


Figure 7.1: Scan of  $H_z$  stray fields within a volume of  $2 \times 2 \times 0.2 \text{ mm}^3$  above the sample of *Cubex* doubly oriented Silicon-iron alloy produced with the STJ-020 sensor at  $0.02 \times 0.02 \times 0.002 \text{ mm}/\text{cell}$  resolution. The area scanned is highlighted in Figure 6.11. The lowest  $xy$  Plane is presented along with ten different  $zx$  Slices at the indicated locations along the  $y$ -axis. Animated sweeps through each  $xy$  Plane and each  $zx$  Slice are available in the Chapter 7.7z arxive (page ix). The  $H_z$  Stray field strength ranges over  $\pm 200 \text{ A/m}$ .

### 7.1.2 H<sub>z</sub> Stray Field Volume Scans of *Metglas* Amorphous Ribbon

Figure 7.2 presents a Scan of H<sub>z</sub> stray fields within a volume of 0.5 x 0.5 x 0.1 mm<sup>3</sup> above the sample of as-cast 2605 Co IPF895 *Metglas* Alloy Amorphous Ribbon produced with the STJ-020 sensor at 0.01 x 0.01 x 0.002 mm/cell resolution. The area over which the scans occur is highlighted in Figure 6.6. Animated sweeps through each xy Plane and each zx Slice are available in the *Chapter 7.7z* Cardiff Portal Arxive (page ix). The H<sub>z</sub> Stray field strength ranges over ± 88 A/m.

It can be seen that yet again these weaker H<sub>z</sub> fields reduce to levels less than the Earth's field at distances greater than 0.05mm from the surface.

To better understand the shape of the stray field above the surface and why it does not seem to extend beyond this distance it would be advantageous to be able to resolve the **H** vector, or the individual components of the **H** vector, in each cell.

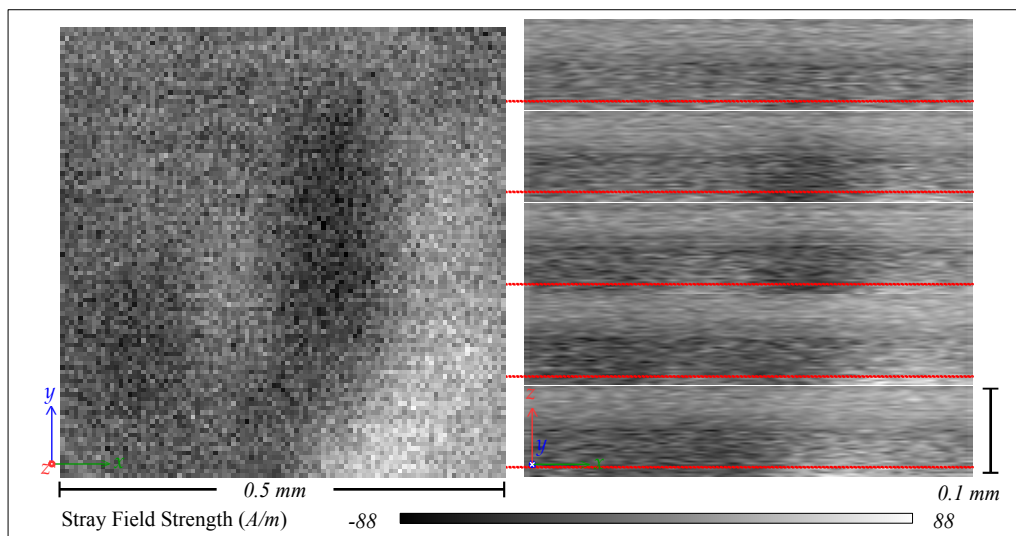


Figure 7.2: Scan of H<sub>z</sub> stray fields within a volume of 0.5 x 0.5 x 0.1 mm<sup>3</sup> above the sample of as-cast 2605 Co IPF895 *Metglas* Alloy Amorphous Ribbon produced with the STJ-020 sensor at 0.01 x 0.01 x 0.002 mm/cell resolution. The area scanned is highlighted in Figure 6.6. The lowest xy Plane is presented along with five different zx Slices at the indicated locations along the y-axis. Animated sweeps through each xy Plane and each zx Slice are available in the *Chapter 7.7z* arxive (page ix). The H<sub>z</sub> Stray field strength ranges over ± 88 A/m.

## 7.2 Resolving $H_z$ and $H_x$ Components with a Single-axis Sensor

After investigating the possibility of the use of three-axis sensors to measure all three  $H_z$ ,  $H_x$  and  $H_y$  stray-field components [142, 143, 144], most employ the same Hall-effect method as the Lakeshore 475 DSP Gaussmeter, and as such provide a low spatial resolution of  $0.1 \text{ mm}^2$  compared to the  $2 \times 4 \text{ }\mu\text{m}^2$  footprint of the STJ-020 TMR sensor (see Figure 6.1 for comparative scan results). To achieve the same resolution as the STJ-020, three-axis TMR sensor arrays are available but are prohibitively expensive. Some theoretical work has been done to mathematically derive the three individual field components from one measurement, based on assumptions about the geometry [145], but for the first time a practical solution of two consecutive scans with the sensor axis tilted is proposed to trigonometrically resolve the  $H_z$  and  $H_x$  components of the field using only the existing single-axis STJ-020 sensor. This capacity motivated the development of the second, and then ultimately the third sensor head and the concept was first presented in [118], available in Appendix 6.

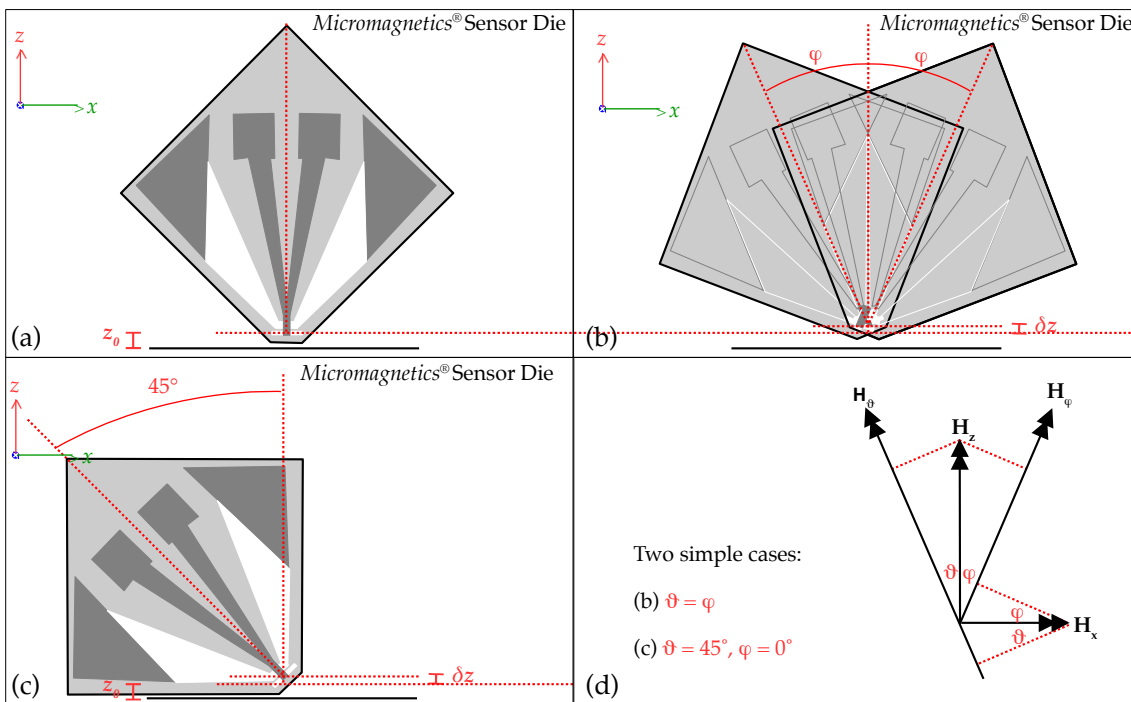


Figure 7.3: The geometry of the *Micromagnetics* STJ-020 TMR sensor die; (a) When perpendicular the minimum height of the sensor's active area  $z_0 = 12 \text{ }\mu\text{m} \pm 3 \text{ }\mu\text{m}$ . Two simple cases exist where; (b) the clockwise rotation and counterclockwise rotation are equal, or (c) the counterclockwise rotation is  $45^\circ$ , where the  $z$ -axis and  $x$ -axis components of the stray field can be easily resolved (d).



The geometry of the tilting of the STJ-020 TMR sensor is provided in [Figure 7.3\(d\)](#).

The stray-field measured at angle  $\theta$  counterclockwise to the perpendicular is formed of the  $H_z$  and  $H_x$  stray-field components by;

$$H_{\theta} = H_z \cos(\theta) - H_x \sin(\theta) \quad \text{Equation 7.1}$$

The stray-field measured at angle  $\varphi$  clockwise to the perpendicular is formed of the  $H_z$  and  $H_x$  stray-field components by;

$$H_{\varphi} = H_z \cos(\varphi) + H_x \sin(\varphi) \quad \text{Equation 7.2}$$

Two simple cases exist for determining  $H_z$  and  $H_x$  from  $H_{\theta}$  and  $H_{\varphi}$ ;

If  $\theta = \varphi$ ;

$$H_{\theta} = H_z \cos(\theta) - H_x \sin(\theta) \quad , \quad H_{\varphi} = H_z \cos(\theta) + H_x \sin(\theta)$$

$$H_{\varphi} + H_{\theta} = 2 H_z \cos(\theta) \quad , \quad H_{\varphi} - H_{\theta} = 2 H_x \sin(\theta)$$

$$H_z = \frac{H_{\varphi} + H_{\theta}}{2 \cos(\theta)} \quad , \quad H_x = \frac{H_{\varphi} - H_{\theta}}{2 \sin(\theta)} \quad \text{Equations 7.3}$$

If  $\theta = 45^\circ$ ,  $\varphi = 0^\circ$ ;

$$H_{\theta} = H_z \cos(45) - H_x \sin(45) \quad , \quad H_{\varphi} = H_z$$

remembering that  $\sin(45) = \cos(45)$  ,

$$H_{\theta} = H_z \cos(45) - H_x \cos(45)$$

$$H_{\theta} = (H_z - H_x) \cos(45)$$

$$\frac{H_{\theta}}{\cos(45)} = H_z - H_x$$

$$H_z = H_{\varphi} \quad , \quad H_x = H_z - \frac{H_{\theta}}{\cos(45)} \quad \text{Equations 7.4}$$

[Equations 7.3](#) and [7.4](#) have been incorporated into the `\Processing\` subVI `zxCombine.vi` ([Section 5.5.5](#)) to automate the combination of data from two consecutive scans.

### 7.2.1 Tilted Sensor Scanning with Sensor Head 2

Sensor Head 2, detailed in Chapter 4, was developed to enable consecutive scans of samples with the STJ-020 TMR sensor tilted either 5° clockwise or counterclockwise from the perpendicular whilst all other sensors remain perpendicular. A scan of a small 2 mm region of the polished 3% Si Grain Oriented Electrical Steel was made to test the concept of resolving the  $H_z$  and  $H_x$  components. Equations 7.3 had not at the time been incorporated into an automated process so, with each of the 4000 cells being manually combined, a small scan of only 20 x 20 x 5 cells was performed at a resolution of 0.1 mm<sup>3</sup>/cell. The manual results were originally published in [118], available in Appendix 6, but the data has since passed through the automated zxCombine.vi process of Scanner Control 3 and combined to produce the colour image presented in Figure 7.4.

The colour representation of the  $\underline{H}$  stray field vector (Figure 7.4(d)) is produced by the channel mixing of the two  $H_z$  and  $H_x$  component greyscale maps produced by zxCombine.vi. The  $H_x$  greyscale map has its Red channel removed and its Green channel inverted so Black to White is remapped as Green to Blue. The  $H_z$  greyscale map has the Green and Blue channels removed to remap from Black to Red, with the original Greyscale Overlaid to range  $H_z$  from Black through Red to White. This has the advantage of isolating and highlighting directly perpendicular positive and negative  $H_z$  fields. Figure 7.4 presents only the lowest of the  $xy$  Planes and one  $zx$  Slice of the cuboid of scan data. Animated sweeps through the  $xy$  Planes and through the  $zx$  Slices are available in Chapter 7.7z of the Cardiff Portal Arxive (page ix) and on the accompanying DVD.

The  $zx$  Slice presented in Figure 7.4 (c) is illustrated with an indication of how the  $\underline{H}$  stray field vector is rotating at the edge of the feature. This is the first indication that it may be possible to see the rotation of the magnetisation vector through the Bloch-wall using this resolving method.

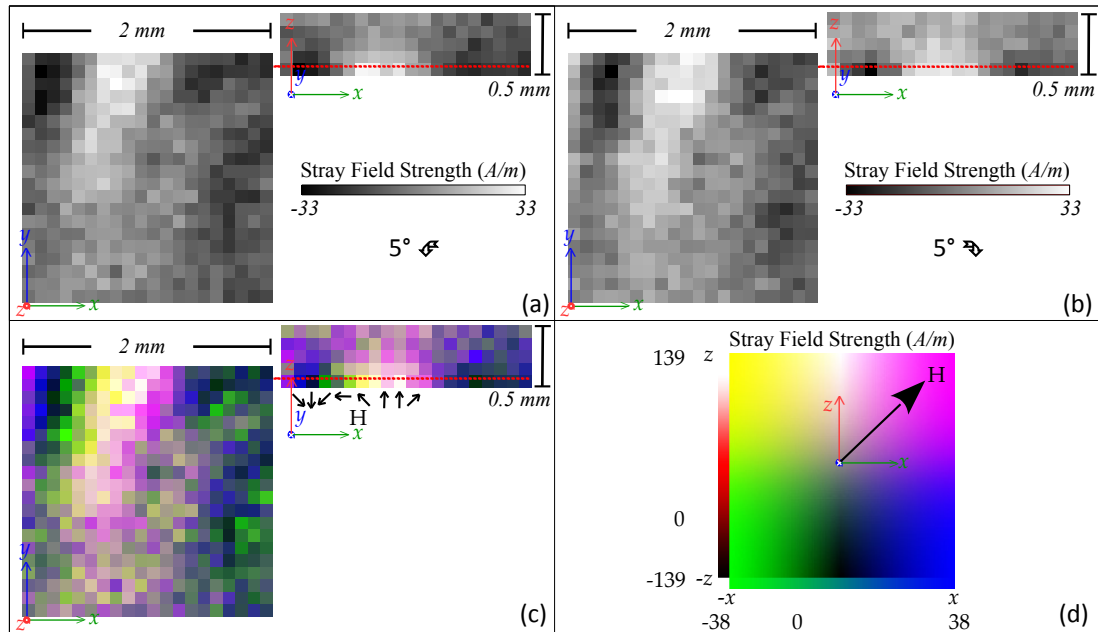


Figure 7.4: A scan of a volume of  $2 \times 2 \times 0.5 \text{ mm}^3$  above the sample of polished 3% Si Grain Oriented Electrical Steel produced with the STJ-020 sensor at  $0.1^3 \text{ mm}/\text{cell}$  resolution mounted in Sensor Head 2. Two consecutive scans with a sensor tilt of  $5^\circ$  (a) counterclockwise and (b) clockwise are combined to produce (c) colour representation of the stray field  $\mathbf{H}$  vector. Only one  $zx$  Slice is presented at the indicated location on the lowest  $xy$  Plane. (d) The colour representation of the  $\mathbf{H}$  stray field vector. The  $H_z$  stray field strength ranges over  $\pm 139 \text{ A/m}$  and the  $H_x$  stray field strength ranges over  $\pm 38 \text{ A/m}$ . Some indication of the rotation of the  $\mathbf{H}$  vector is illustrated in (c). Animated sweeps through each  $xy$  Plane and each  $zx$  Slice are available in the *Chapter 7.7z* archive (page ix).

The calculated  $H_z$  field ranges over  $\pm 139 \text{ A/m}$  whilst the calculated  $H_x$  field ranges over only  $\pm 38 \text{ A/m}$ . This unevenness indicates that, as might be expected with only a  $5^\circ$  tilt, the  $H_x$  component is being measured disproportionately less than  $H_z$ .

This, together with the inaccuracies of a 3d-printed tilting mechanism and the difficulties encountered in combining the magnetic and displacement sensors discussed in Chapter 4, motivated the development of Sensor Head 3; incorporating a ThorLabs CR1/M precision goniometer.

### 7.2.2 Variable Angle Scans with Sensor Head 3

The *ThorLabs* CR1/M precision goniometer permits a scan to be made with the sensor at any chosen angle  $\vartheta$  to the vertical, measuring the strength of stray field  $H_{\vartheta}$  at that angle. Figure 7.5 presents the results of zx Transect scan, along the transect indicated in Figure 6.4, at five different angles  $\vartheta$  to the vertical. These results were first reported in [146] and [147] and presented at the IEEE Sensors Conference 2017, Glasgow. An animated sweep through each angle is available in the *Chapter 7.7z* Cardiff Portal Arxive (page ix). These results illustrate the promise of investigating the structure of the stray-field above the surface of the sample using an angle sensor. However, because of the non-regular and unknown true structure of stray fields from the 3% Si Grain Oriented Electrical Steel sample, it is difficult to isolate if the change in the field map results from the angle tilt alone, or from the increase in minimal sample distance forced by the geometry of the sensor tip ( $\delta z$  in Figure 7.3). Hence the need for the consequent study of known planar coil geometries.

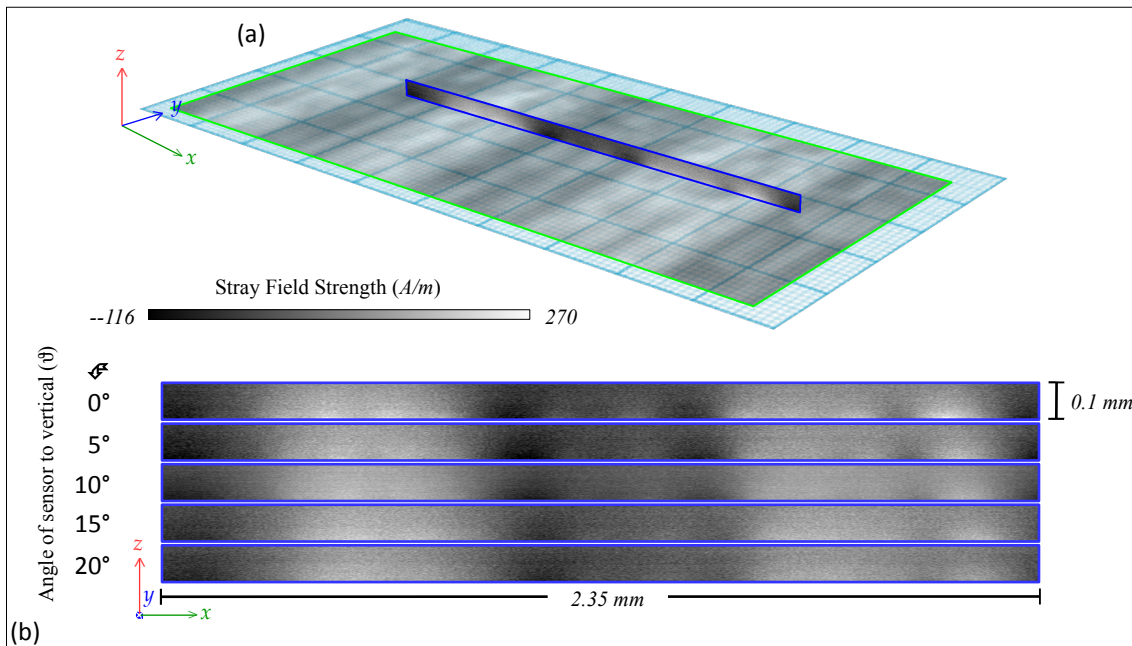


Figure 7.5: (a) Illustration of the three-dimensional relationship between zx Transect scans of polished 3% Si Grain Oriented Electrical Steel above the surface of the sample at the location indicated in Figure 6.4. (b) Scans of the stray field strength at 0°, 5°, 10°, 15°, 20° counterclockwise to perpendicular above the sample forming 2.35 x 0.1 mm zx Transects at 0.005 x 0.005 x 0.002 mm/cell resolution. The  $H_{\vartheta}$  Stray field strength ranges from -116 to 270 A/m. An animated sweep through each angle is available in the *Chapter 7.7z* arxive (page ix).

### 7.3 Comparison between the Modelled and Measured $H_z$ and $H_x$ Components of the Fields from Planar Coils

To validate and add confidence to the capacity of the system to measure the three-dimensional structure of the magnetic fields by isolating the  $H_z$  and  $H_x$  components two additional consecutive scans were made of the manufactured square planar coil discussed in [Section 6.3](#) along the transect marked by blue double-chevrons in [Figure 6.9\(d.iii\)](#). Making use of [Equations 7.4](#), one scan was made with the sensor perpendicular and a further corresponding scan made with the sensor at  $45^\circ$  counterclockwise. Only the first half of the coil was scanned to avoid possible collision of the sensor with the central solder point at the lower minimum scan height of  $z_0 = 12 \mu\text{m} \pm 3 \mu\text{m}$ . The spatial conformation between the two scans is maintained by the  $\pm 1 \mu\text{m}$  precision of the positioning arm ([Section 4.2.2](#)) and by the precision goniometer and micrometers used in the system ([Figure 4.16](#)). The axis of rotation was aligned with the centre of the active area of the STJ-020 TMR sensor using the microscope incorporated into the system ([Section 4.10.1](#)). Photographs of the vertical and angled scans underway are presented in [Figure 7.6](#).

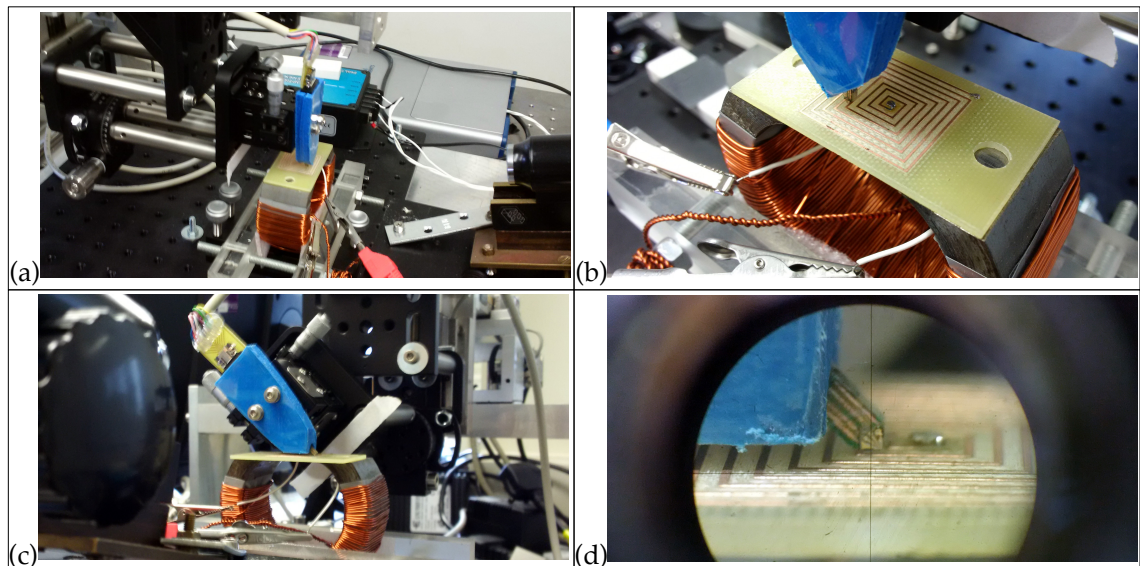


Figure 7.6: Photographs of the system scanning the square planar coil; **(a,b)** with the STJ-020 sensor perpendicular and **(c,d)** with the STJ-020 sensor at  $45^\circ$  supported by the precision goniometer of Sensor Head 3. The centre of rotation is precisely aligned to the centre of the sensor's active area.

A sensor angle of  $45^\circ$  allows for a maximum sampling of  $H_x$ , and also for the lowest active area to sample surface distance ( $z_0$ ) possible due to the shape of the sensor. There remains a difference in minimum possible sensor to surface distance between when the sensor is perpendicular and when it is tilted ( $z_0$ ). Whilst both scans shared the same maximum z-axis coordinate the minimal height ( $z_0$ ) of the  $45^\circ$  scan was necessarily  $12.5 \mu\text{m}$  above the minimal height of the perpendicular scan. Thus, allowing for a  $2.5 \mu\text{m}$  error in  $z_0$  due to surface unevenness the estimate for  $z_0$  can be determined more precisely as  $12.5 \mu\text{m} \pm 2.5 \mu\text{m}$ . The transect scan extended 10 mm above the surface of the coil. To maintain consistency with the resolution of the other scans the x-axis resolution was 0.1 mm/cell, but to gain detail to the extent of the fields above the surface the z-axis resolution was 0.01 mm/cell. The resulting  $0.1 \text{ mm} \times 0.01 \text{ mm}$  cell is presented as rectangular to maintain the correct aspect ratio between horizontal and vertical distances.

The ANSYS Maxwell 3D FEM software allows for simple determination of the magnitudes of  $H_z$  and  $H_x$  from the modelling, but to provide comparison of the measured results for the scan with the sensor at  $45^\circ$  Equation 7.1 is used with  $\vartheta = 45^\circ$  to determine  $H_{45}$ . The expected results calculated from the finite element modelling of the coil were determined by defining an xz plane slice in the modelled vacuum cuboid at a y-axis position matching the transect. Naturally, the finite element modelling is able to represent the field beneath the coil which is inaccessible to the physical sensor; but, in the case of the thin planar coils, mirrors the field above the sample.

The results of scans of the Square planar coil and the analysis to isolate the  $H_z$  and  $H_{45}$  and  $H_x$  components are presented in Figure 7.7, alongside the expected results from the finite element modelling. There is strong similarity between the measured and the modelled field shape for both the planar and the cross-section scans.

The colours used in Figure 7.7 make use of the colour representation of the  $\underline{H}$  vector described on page 160. and presented in Figure 7.7(c.v).

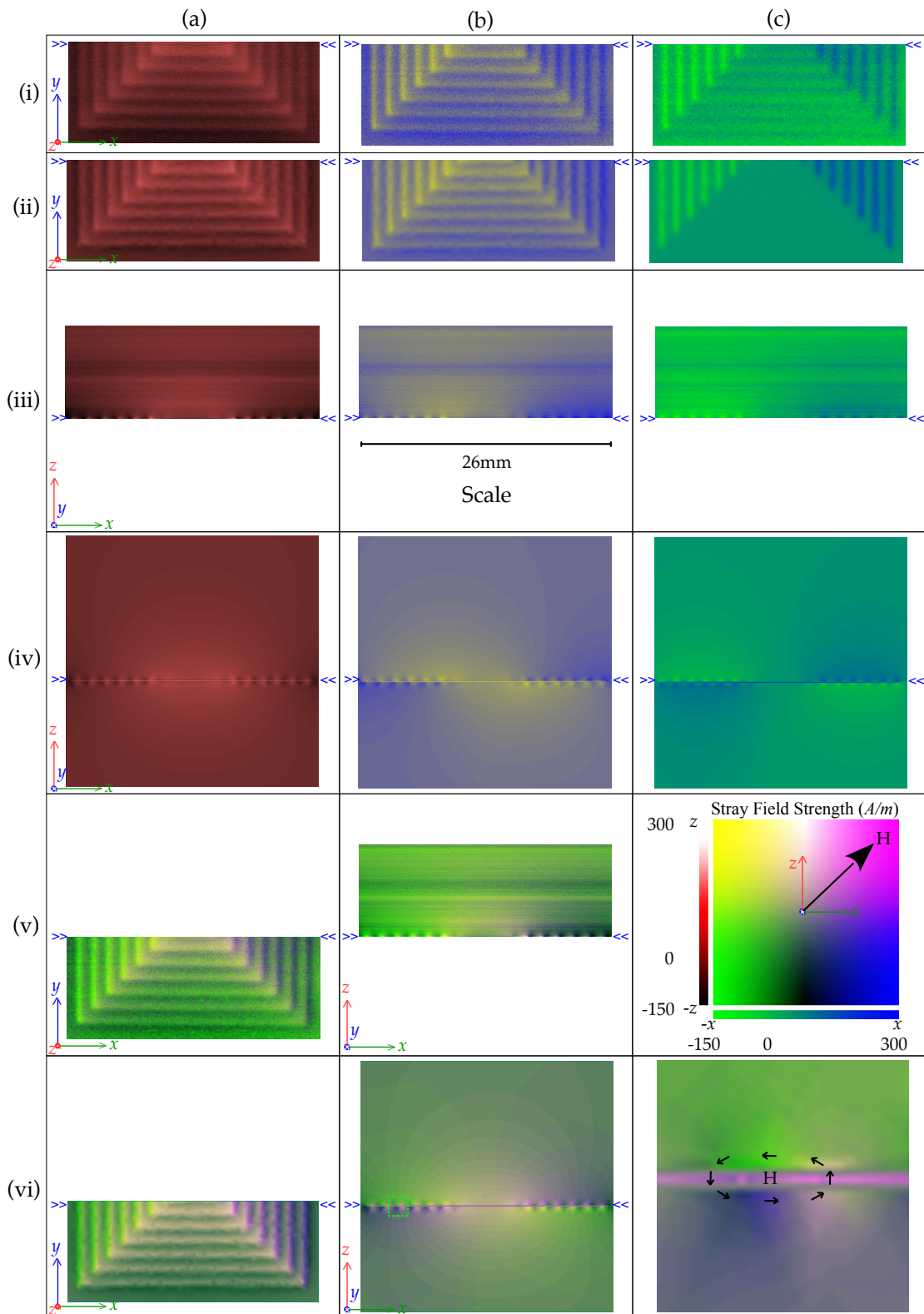


Figure 7.7: Comparison of scans of the Square planar coil with the STJ-020 sensor compared with ANSYS FEM of the corresponding topology. (i) xy Scans of the Square planar coil (ii) FEM of the fields from xy plane, (iii) zx Transect scan of the Square planar coil (iv) FEM of the fields from the zx plane; (a)  $H_z$ , (b)  $H_{45}$ , (c)  $H_x$ . Colour representation of the stray field  $\mathbf{H}$  vector are presented as scanned (a.v) and (b.v) and from FEM (a.vi) and (b.vi). (c.v) The colour representation of the  $\mathbf{H}$  stray field vector.

Again, there is significant noise in the scans, particularly in the cross-sectional scans where strong horizontal bands from background are present. Nevertheless, the field distributions expected from the finite element modelling can be seen clearly in the measured cross-sections. The curved “field boundary” lines evident in [Figure 7.7\(iv\)](#) are an artefact of the discrete shading boundaries, but serve to highlight the shape of the field distribution. The modelled fields below the coil are not accessible by practical measurement, but form a mirror of the fields above the coil. The scans of the  $H_z$  and  $H_{45}$  components have been effectively combined to calculate the  $H_x$  component, presented in [Figure 7.7\(c\)](#). The  $H_x$  component corresponds well with that expected from the ANSYS modelling. The lower tracks of the Square planar coil are not quite parallel with the scanning path and so some  $H_x$  signal is present, but a strong  $H_x$  component away from the centre of the coil on both sides is demonstrated on both the planar  $xy$  plane and the cross-sectional  $xz$  slice.

This comparison work, in combination with that in [Chapter 6](#), was originally published in [\[112\]](#), available in Appendix 6.

Full colour representations of the  $\mathbf{H}$  vector are provided in [Figure 7.7\(a.v\),\(b.v\), \(a.vi\)](#) and [\(a.vi\)](#). [Figure 7.7\(c.vi\)](#) illustrates a closeup of the fields around one of the tracks indicated on [Figure 7.7\(b.vi\)](#) which demonstrates the rotation of the  $\mathbf{H}$  vector counterclockwise and how the full colour representation process described on [page 160](#) indicates this correctly.



## 7.4 Resolved Stray Field $\underline{H}$ Vectors from Coated 3% Si Grain-Oriented Electrical Steel

With confirmation of the systems capacity to resolve the  $\underline{H}$  vector of the stray-field in the volume above the surface of a sample, investigations into the three-dimension structure, and the change in three-dimensional structure after some perturbation, can begin.

### 7.4.1 Resolved Stray Field $\underline{H}$ Vectors from Laser Etched Coated 3% Si Grain-Oriented Electrical Steel Before and After Etching

A defined region of coated 3% Si Grain-Oriented Electrical Steel, presented in [Figure 7.8\(b\)](#), was scanned both perpendicularly and at 45° counterclockwise [Figure 7.8\(c\)](#) to determine the resolved  $\underline{H}$  vector of the domains in the sample. The results of these scans are presented in [Figure 7.9\(i\)](#) and in [Figure 7.9\(a.iii\)](#) with the colour  $\underline{H}$  vector representation described on [page 160](#).

The sample was then etched diagonally across the scan region using a 10.6  $\mu\text{m}$  wide CO<sub>2</sub> laser at 14% of its 50 W total power ([Figure 7.8\(a\)](#)) and the two scans repeated. The results of the scans after laser etching are presented in [Figure 7.9\(ii\)](#) and in [Figure 7.9\(b.iii\)](#) with the colour  $\underline{H}$  vector representation.

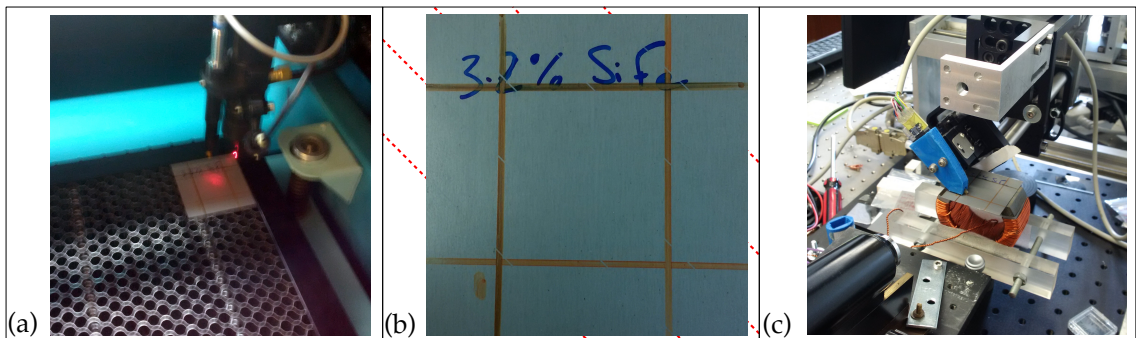


Figure 7.8: (a) Etching lines in Coated 3% Si Grain Oriented Electrical Steel with a 10.6  $\mu\text{m}$  wide CO<sub>2</sub> laser at 14% of 50 W. (b) the indicated Etched lines are present in the coating made diagonally through the central scanned region. (c) the sample is scanned perpendicularly and at 45° counterclockwise.

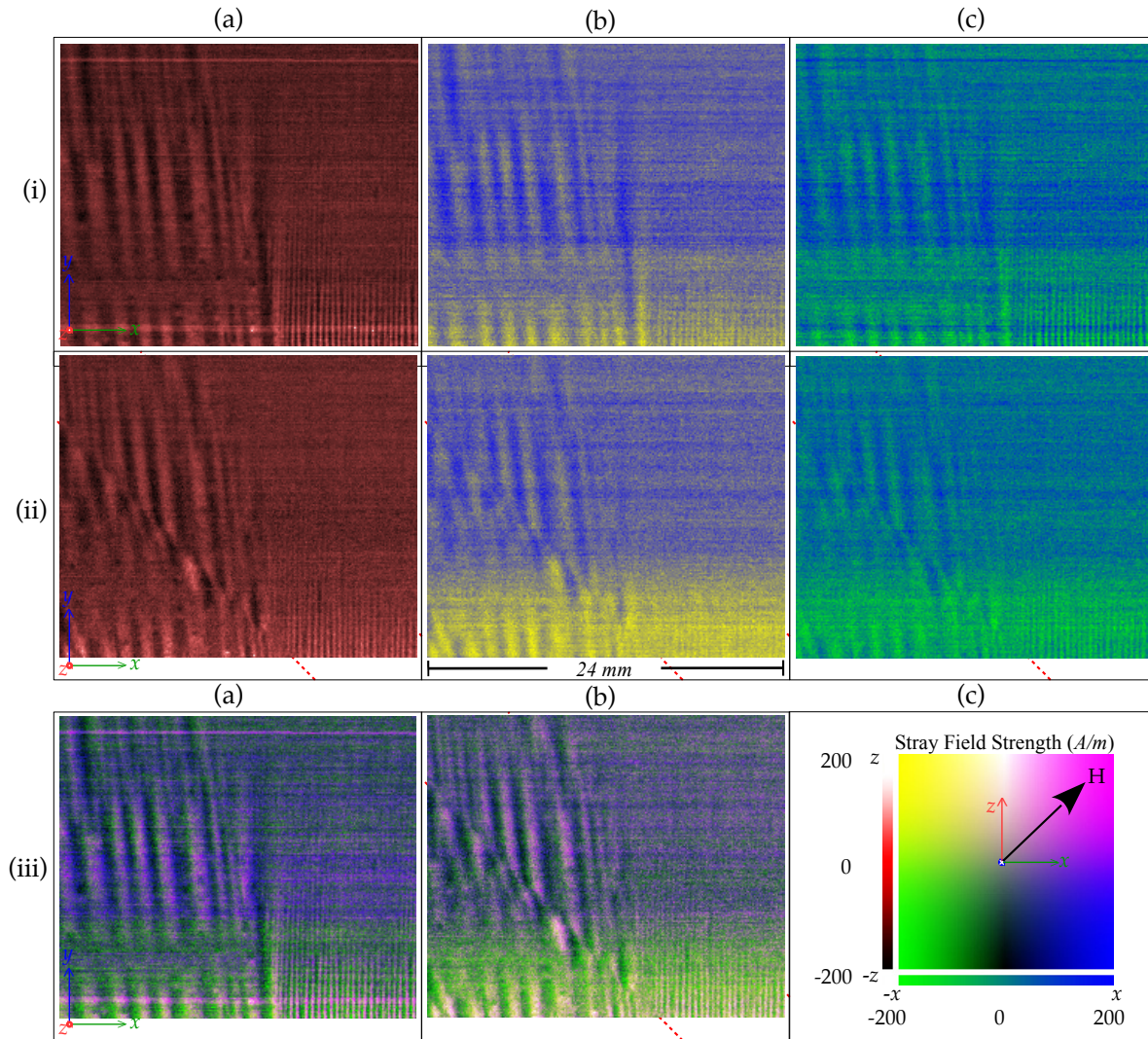


Figure 7.9: A stray field scan of 24 x 20 mm Coated 3% Si Grain Oriented Electrical Steel produced by a scan with the STJ-020 sensor at 0.1<sup>3</sup> mm/cell (i) Before and (ii) After etching the coating with a 10.6  $\mu\text{m}$  wide CO<sub>2</sub> laser at 14% of 50 W (Figure 7.8). Measured (a)  $H_z$  and (b)  $H_{45}$  fields along with calculated (c)  $H_x$  fields are presented. Colour representation of the stray field  $\underline{H}$  vector is presented before (a.iii) and after (b.iii) etching. The colour representation of the  $\underline{H}$  stray field vector is presented in (c.iii).

The laser etching causes a clear difference in the distribution of domains within the coated 3% Si Grain-Oriented Electrical Steel. The laser etching produces an artificial boundary and the domains rearrange to minimise the energy within each of the two newly defined regions [148, 149]. It can be seen from the  $\underline{H}$  vector colour representation how a narrow region of magnetisation vector rotation forms across the width of the laser etch. The stray-field orientation rotates to ensure that opposite magnetisation directions occur either side of the boundary to ensure net zero magnetisation across the boundary. Although only scanned in an  $xy$  Plane evidence of the rotation of the  $\underline{H}$  vector at the edge of each domain is indicated.

### 7.4.2 Resolved Stray field $\underline{H}$ Vector in a Volume Above Coated 3% Si Grain-Oriented Electrical Steel

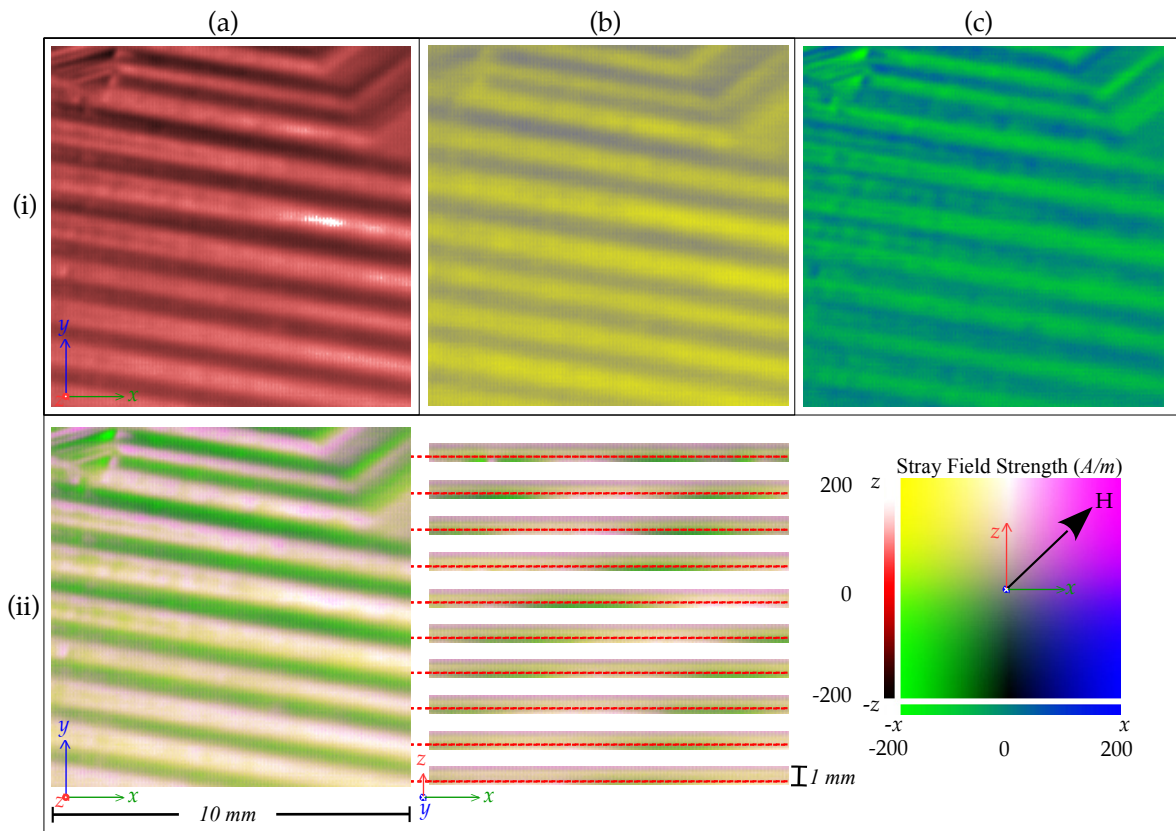


Figure 7.10: A stray field scan of fields within a volume of  $10 \times 10 \times 0.5$  mm above a sample of Coated 3% Si Grain Oriented Electrical Steel produced by a scan with the STJ-020 sensor at  $0.5 \times 0.5 \times 0.05$  mm/cell. Measured (a)  $H_z$  and (b)  $H_{45}$  fields along with calculated (c)  $H_x$  fields are presented (i). Colour representation of the stray field  $\underline{H}$  vector is presented (ii) with 10 different  $zx$  Slices at the indicated locations along the  $y$ -axis. The colour representation of the  $\underline{H}$  stray field vector is presented in (c.ii). Animated sweeps through each  $xy$  Plane and each  $zx$  Slice are available in the *Chapter 7.7z* archive ([page ix](#)).

For the first time, using the colour  $\underline{H}$  vector representation, the rotation of the  $\underline{H}$  stray field vector can be seen at the domain wall. [Figure 7.10](#) presents component resolved scans of the fields within a volume of  $10 \times 10 \times 0.5$  mm above a sample of Coated 3% Si Grain Oriented Electrical Steel. The lowest  $xy$  Plane is presented in [Figure 7.10\(ii\)](#) along with 10 different  $zx$  Slices at the indicated locations along the  $y$ -axis which demonstrate the rotation of the  $\underline{H}$  vector. Animated sweeps through each  $xy$  Plane and each  $zx$  Slice are available in the *Chapter 7.7z* Archive ([page ix](#)). The  $H_z$  Stray field strength ranges over  $\pm 200$  A/m. [Chapter 8](#) will investigate how these domain walls move in response to an alternating applied magnetic field.



*Chapter 8***Investigation of Alternating Domain Dynamics**

The Scanner Control 3 software was specifically developed with the aim of investigating the dynamics of domains as they change under the influence of an alternating externally applied field. Dynamic scans of samples are presented here as a filmstrip within the thesis, with fully animated versions of each figure available as animated GIFs in *Chapter 8.7z* of the Cardiff Portal Arxive ([page ix](#)) and on the accompanying DVD. Presentations with the animated GIFs embedded are also provided for each of the figures in the */Figures Presentations/* folder of the Arxive.

**8.1 Investigating Dynamics with the Scanner System**

Due to the damage caused to the Second STJ-020 TMR sensor described in [Chapter 4](#) and [Chapter 5](#) the first studies of dynamic systems were made with the Lakeshore DSP Gaussmeter. This had the disadvantage of much lower spatial resolution, as described in [Chapter 6](#) ([Figure 6.1](#)), but still provides meaningful results, and in particular provided the first positive observation of domain dynamics with the system.

Producing high frequency dynamic data from the slow process of procedural scanning relies principally on the assumption that the domains follow repeatable oscillatory motion. At the beginning of this phase of the investigation it was not clear if the domain wall motion within a sample would be sufficiently repeatable to produce meaningful results, and it was part of this investigation to determine what proportion of the sample surface, if any, exhibited domains with repeatable motion.

It is important to remember that, though only one cycle of excitation is presented in the results, for a 10,000 cell scan of a sample excited at 3 Hz this single cycle represents the settled repeatable motion of at least 30,000 cycles of excitation.

**8.1.1 The Process of Frame Synchronisation**

Other studies [[109](#), [11](#)] have used the “locked-in” technique of triggering the AC signal generator to pulse at the start of each set of samples. This method requires a triggerable AC signal generator. It is thought such triggering of the start of each waveform provides discontinuous excitement to the sample which may effect the dynamics of the

domains, as they are given uneven relaxation time between excitations. Rather than employing the “lock-in” method, a passive continuous sampling technique (where the oscillator runs continuously) has been developed to sample each cell at whatever the phase of a smooth continuous excitation; whilst ensuring the sample rate and frequency capture enough samples for at least two full cycles. Software post-processing (*Synchronise.vi*, [Chapter 5.4.2.8](#)) is then used to synchronise each cell to the first peak of the applied field.

### 8.1.2 Dynamic Oscillation of the Fields from the Square Planar coil

Once again the known geometry of the Square planar coil ([Figure 6.9\(d.i\)](#)) has been used to test and confirm the effectiveness of the scanning, synchronisation process and resulting output of the system.

The planar coil was energised at 3 Hz and scanned using the Lakeshore sensor at 1000 samples/cell with 1 kHz sampling rate. After synchronisation the first 333 frames provide one complete cycle. The spatial resolution of the scan was 0.1mm/pixel. An animated GIF of the complete cycle is provided in *Chapter 8.7z* of the Cardiff Portal Arxive ([page ix](#)) and on the accompanying DVD. A filmstrip of every fourth frame is presented in [Figure 8.1\(a\)](#). The pyramidal oscillation of field strength and direction from the coil is clear, with the centre of the coil the strongest, and the expected emphasis of field at the corners. Importantly these results demonstrate the effectiveness and coherence of the scanning and synchronisation systems and validate the technique that has been developed.

The PNG.vi subVi ([Section 5.4.2.7](#)) provides the capacity to calculate the mean value of the entire scan for each frame and also provides histograms counting the number of pixels of each greyscale value of each frame in the scan. The mean field produced by the entire coil ([Figure 8.1\(b.i\)](#)) corresponds directly to the voltage applied to the coil, but does not distinguish the topology of the coil in that the field is assumed even over the surface.



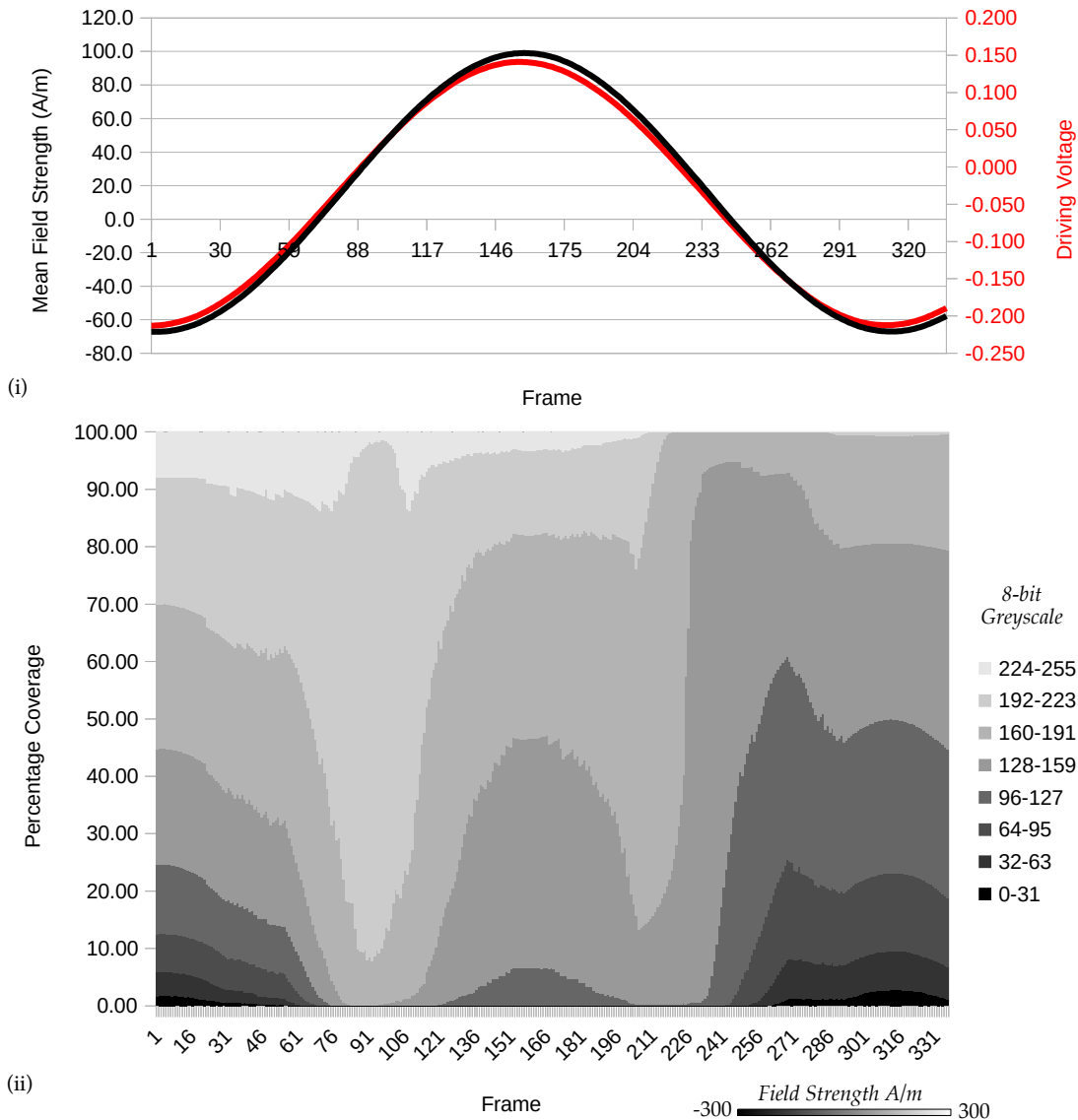


Figure 8.1(b): (i) The Mean field strength across the entire surface scanned for each of 336 frames (in black) and the voltage applied to the Square Planar Coil (in red). (ii) The percentage area coverage of each greyscale level across the entire scan for each of 336 frames. The stray field ( $H_z$ ) strength is represented in greyscale from -300 to 300 A/m.

The histogram in [Figure 8.1\(b.ii\)](#) presents the percentage coverage of each level of field. Consequently the histogram encodes some of the detail of the topology of the coil, with evidence of both the positive and negative z-axis fields in every frame. The greater prevalence of mid-grey pixels over extreme white or black indicates the concentric nature of the field reinforcement and the slight asymmetry over time is indicative of the spiral. With the square planar coil the physical position of the field sources do not move, unlike the sources of stray field from domains.



## 8.2 Investigating Stray Field and Domain Dynamics

### 8.2.1 Laser Etched Coated 3% Si Grain-Oriented Steel subjected to alternating applied field from a Yoke

The sample of Laser Etched coated 3% Si Grain-Oriented steel from [Section 6.1.3](#) has been energised with the Large C-Yoke ([Section 4.10.3](#)) at 3 Hz. This is a common method of providing an applied field to a sample [[9](#), [10](#)]. The MOKE techniques used in these studies observe the direction of magnetisation within the sample, parallel to the surface of the sample, and so are not affected by stray  $H_z$  fields from any other source.

An area of 27 mm x 25 mm of the sample has been scanned @ 0.1 mm/pixel at a sampling rate of 1 kHz. 336 frames represent one full cycle. The results, presented in [Figure 8.2\(a\)](#), indicate the extent to which stray  $H_z$  field from the Yoke itself, and from topological defects in the sample, mask any observation of the stray fields originating from the domain patterns present. Stray field from the domains in an unenergised sample of Grain-Oriented steel range over  $\pm 215$  A/m ([Figure 6.1\(d\)](#)). The Large C-Yoke has been used to help distance the tips of the Yoke from the region of scanning, nevertheless the  $H_z$  field measured by the system when energised with the Yoke ranges over  $\pm 500$  A/m ([Figure 8.2\(a\)](#)). This extra field originates not only from the Yoke itself [[36](#)], but also from stray fields from the topology of the sample and the defects in it. As the applied magnetic field oscillates the defects caused by the Laser Etching are highlighted, including an emergent spike of field between two of the Etching lines.

These effects are useful in their own right for the non-destructive testing of defects [[87](#), [111](#)] but cause great difficulty in studying the dynamics of the domains in the sample, leading to the ambiguous results of previous attempts at dynamic studies using scanner systems [[11](#)].



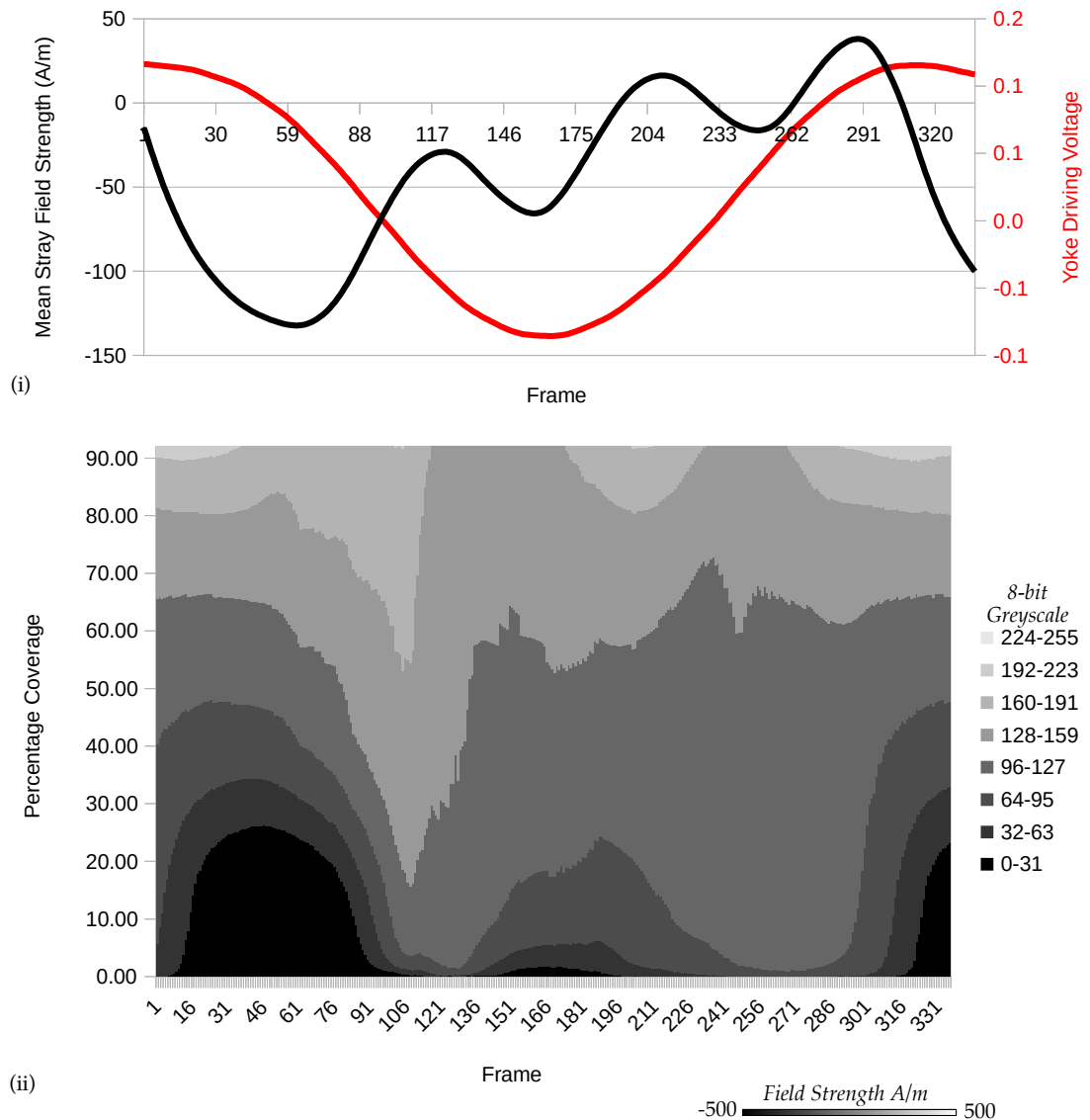


Figure 8.2(b): (i) The Mean field strength across the entire surface scanned for each of 336 frames (in black) and the voltage applied to the Large Yoke (in red). (ii) The percentage area coverage of each greyscale level across the entire scan for each of 336 frames. The stray field ( $H_z$ ) strength is represented in greyscale from -500 to 500 A/m.

Figure 8.2(b) demonstrates how the topology and defects of the Laser Etched Coated 3% Si Grain-Oriented Steel are indicated in the Mean and Histogram plots. The dominant effects are the creep of field from the Yoke at the edge of the scan and the emergent field spike between the two etchings, which results in the three peaks in Figure 8.2(b.i) and in the dominance of black pixels at frame 50 and white pixels at frame 210 in Figure 8.2(b.ii).

### 8.2.2 As-cast 2605 Co IPF895 Metglas Alloy Amorphous Ribbon subjected to alternating applied field from a Yoke

To again demonstrate the issue of the stray fields from surface topology masking any observation of domain dynamics when using a C-Yoke; the results of a scan of as-cast 2605 Co IPF895 Metglas Alloy Amorphous Ribbon, with 3 Hz oscillating applied magnetic field from the Small C-Yoke (Section 4.10.3), are presented in Figure 8.3(a).

The scan is of area 20 mm x 20 mm at a spatial resolution of 0.1 mm/pixel with a 1 kHz sampling rate. 336 frames represent one full cycle and every 4th frame is presented in the filmstrip in Figure 8.3(a) with the full animated GIF provided in Chapter 8.7z of the Cardiff Portal Arxive (page ix). The border 20 pixels of each frame presents the energising voltage ( $\pm 0.2$  V), which is provided with its own animated GIF in the arxive and in the /Figures Presentations/ folder on the DVD.

Again the stray field strength ( $H_z$ ), ranging from -500 to 500 A/m, mostly emanates from the undulating topology of the as-cast ribbon surface and the field from the Yoke at the edge of the scan. The ripples on the surface are seen to remain largely static, although careful observation of the full animated GIF (Chapter 8.7z (page ix)) indicates some rippling of the surface as the thin sample distorts slightly under the alternating applied field.

The Mean stray field plot (Figure 8.3(b.ii)) shows evidence of the effects of the two dominant bump defects in the surface of the sample. The evenness and symmetry of the Histogram plot (Figure 8.3(b.ii)), with some variation coincident with the features of the Mean field plot, indicates the general continuity and evenness of the undulations on the surface of the ribbon.

The strength of the stray fields from the surface topology of as-cast amorphous ribbon are much greater than the intrinsic strength ( $\pm 80$  A/m) of the domains previously measured in amorphous materials (Section 6.2) which again makes the observation of domain dynamics in amorphous materials [126, 150] difficult with a scanner system.

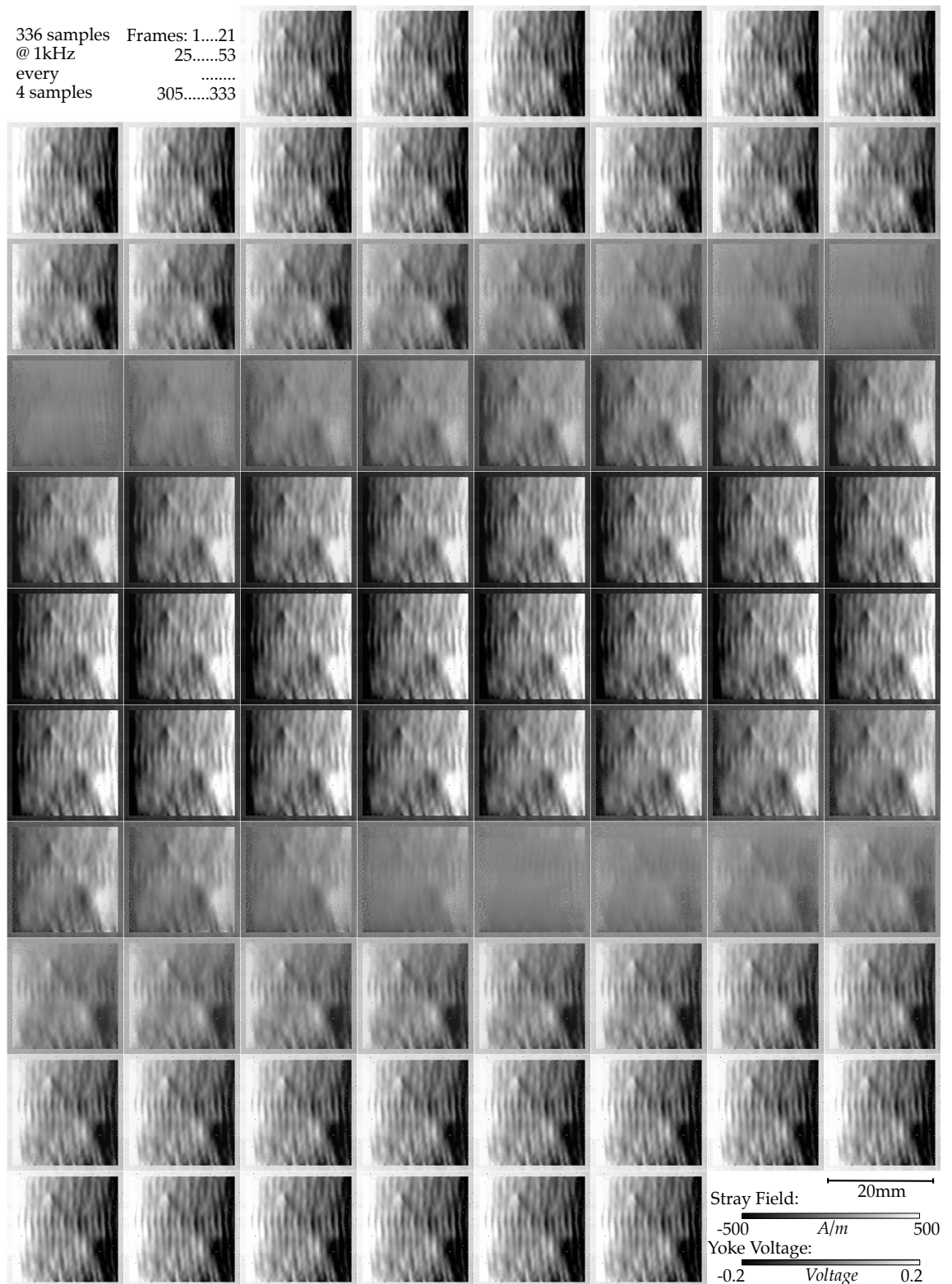


Figure 8.3(a): Filmstrip representation of a dynamic scan of As-cast 2605 Co IPF895 Metglas Alloy Amorphous Ribbon energised at 3 Hz with the Large Yoke. The full animated GIF is provided in *Chapter 8.7z* of the Cardiff Portal Arxiv ([page ix](#)). The stray field strength ( $H_z$ ) is represented in greyscale from -500 to 500 A/m. The border 20 pixels of each frame presents the oscillating voltage driving the C-Yoke ( $\pm 0.2$  V).

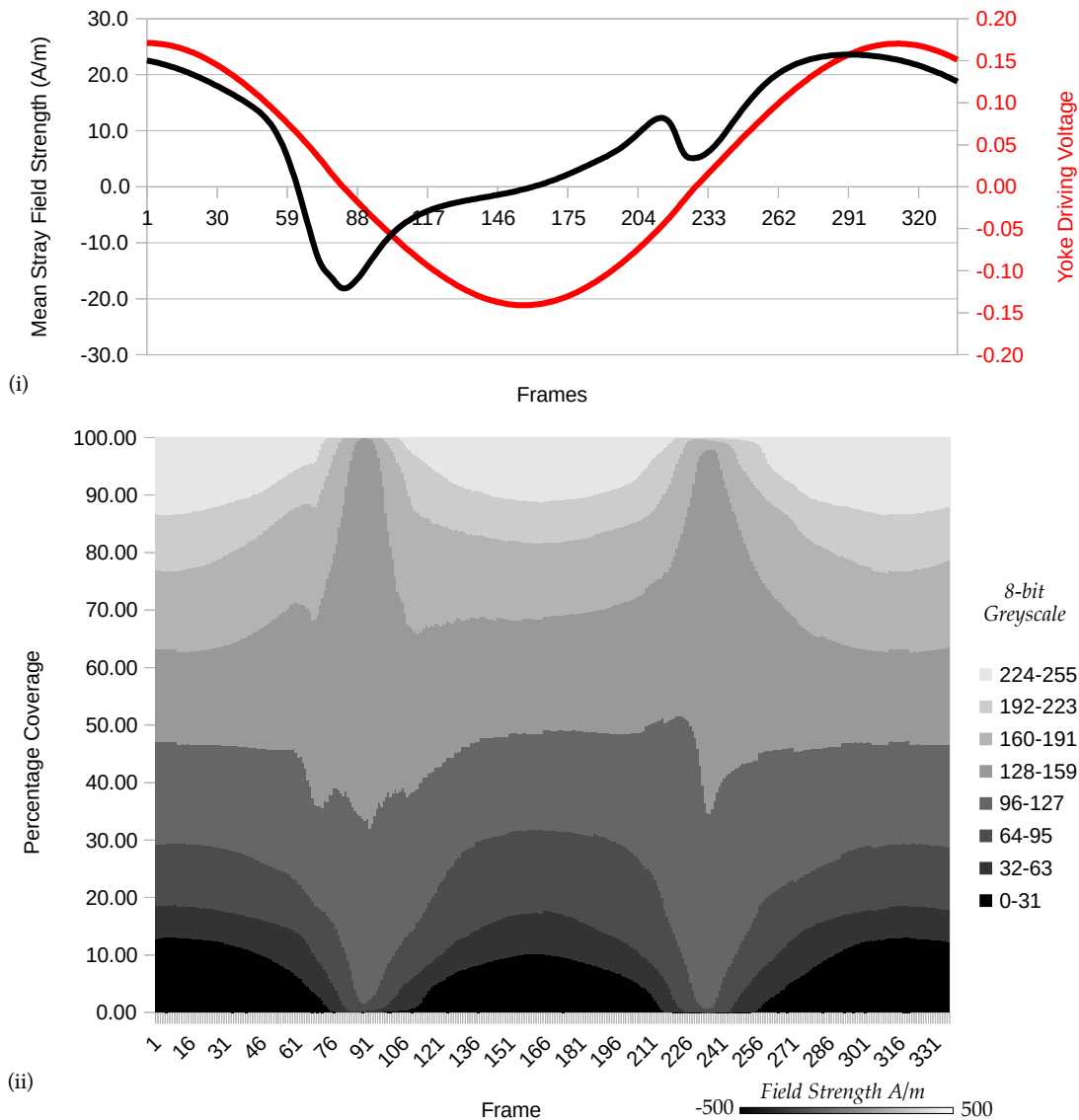


Figure 8.3(b): (i) The Mean field strength across the entire surface scanned for each of 336 frames (in black) and the voltage applied to the Large Yoke (in red). (ii) The percentage area coverage of each greyscale level across the entire scan for each of 336 frames. The stray field ( $H_z$ ) strength is represented in greyscale from -500 to 500 A/m.

To be able to investigate the domains in any samples it is necessary to remove the dominant  $H_z$  component from the C-Yoke method by applying the field parallel to the surface of the sample using coils wrapped around the sample itself. The applied field is thus directly along the x-axis rather than relying on the field from the Yoke being drawn into the sample [36].

### 8.2.3 Uncoated 3% Si Grain-Oriented Steel subjected to alternating applied field from 20 + 20 Coils

To investigate the method of applying an external field parallel to the surface of the sample (in the x-axis) using coils wrapped around the sample itself, initially 20 turns were wrapped around each end of the sample. This made a 40 turn coil with magnetisation in the x-axis of the sample of Uncoated 3% Si Grain-Oriented Steel, with an area between the two halves of the coil which could be scanned ([Figure 4.15\(e\)](#)).

Because these 20 + 20 coils were applied directly to the sample it was not possible to directly calibrate the field produced by the coils in relation to the voltage supplied to them, however it can be assumed that the 40 turns of this coil produce a field 40% the strength of the 100 turn coil calibrated in [Section 4.10.4 \(Figure 4.17\)](#), resulting in a field calibration of  $866 \text{ Am}^{-1}/\text{Volt}$ . This permits the results of the scan to be presented in A/m for both the Stray and Applied field strengths in [Figure 8.4\(a\)](#) and [Figure 8.4\(b\)](#). The sample was subjected to an oscillating applied field  $\pm 1039 \text{ A/m}$  at 3 Hz.

Due to the damage caused to the Second STJ-020 TMR sensor described in [Chapter 4](#) this scan was made with the Lakeshore DSP Gaussmeter, nevertheless this is the first time a successful observation of definitive dynamic domain motion has been observed with a two dimensional scanner system [[151](#)].

The scan of  $28 \times 20 \text{ mm}^2$  at a spatial resolution of  $0.1 \text{ mm}/\text{pixel}$  took 2000 samples per cell at a 1 kHz sampling rate. After synchronisation 336 frames represent 1 complete cycle. A filmstrip of every 5 of these frames with a 20 pixel border representing the state of the Applied field from the coils is presented in [Figure 8.4\(a\)](#). The dynamics of the domain walls are visible in the filmstrip but are best observed through the animated GIF provided in [Chapter 8.7z](#) of the Cardiff Portal Arxive ([page ix](#)) and on the accompanying DVD. Both the animated GIF of the Stray fields and Applied Field Strength are provided embedded in the [Chapter 8\[.odp/.ppt\]](#) presentation available in the [/Figures Presentations/](#) folder of the Arxive and the DVD.

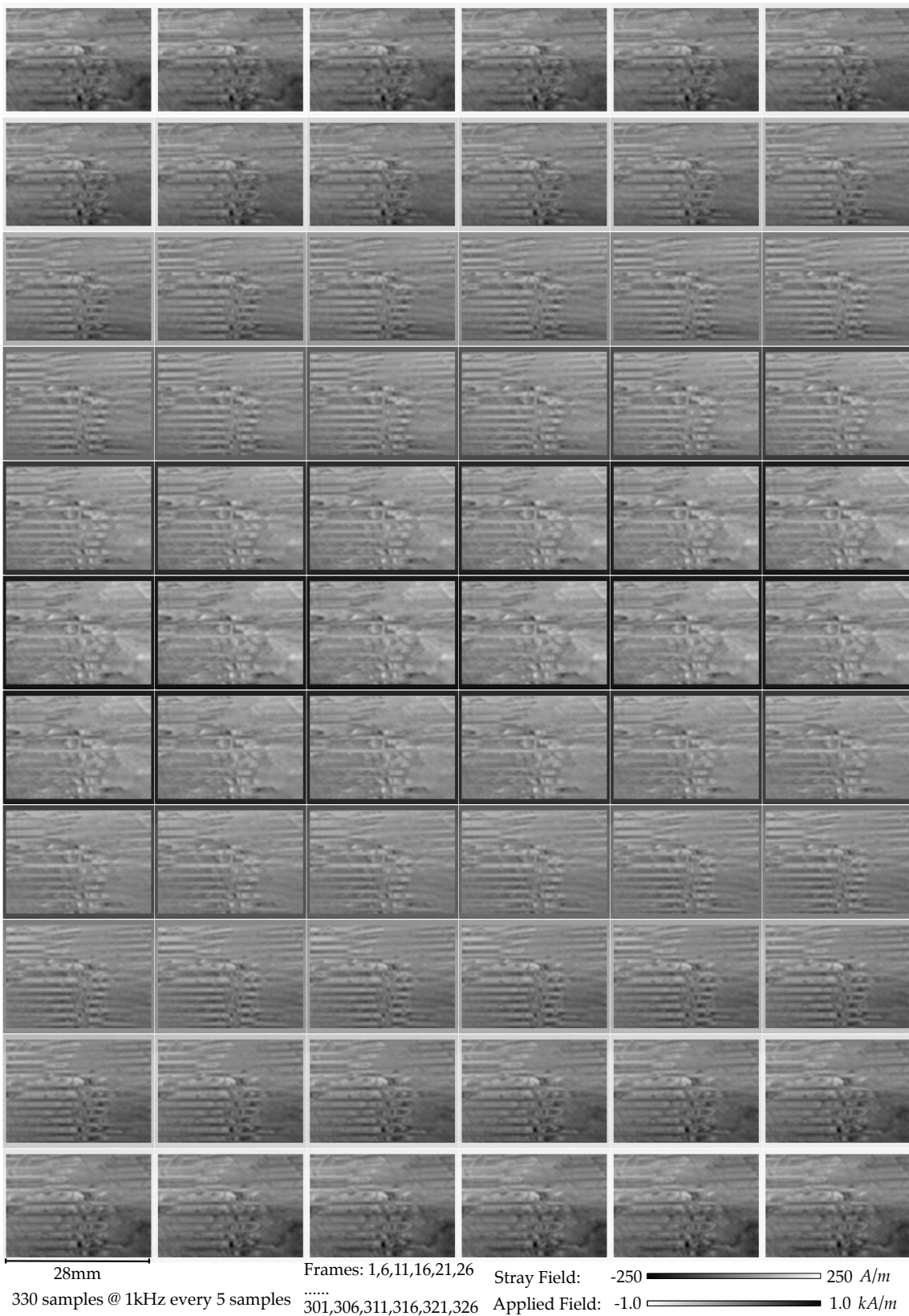


Figure 8.4(a): Filmstrip representation of a dynamic scan of Uncoated 3% Si Grain-Oriented Steel subjected to a 3 Hz oscillating x-axis field of  $\pm 1$  kA/m from the 20 + 20 coils. The full animated GIF is provided in *Chapter 8.7z* ([page ix](#)). The border 20 pixels of each frame presents the oscillating Applied field (inverted greyscale).



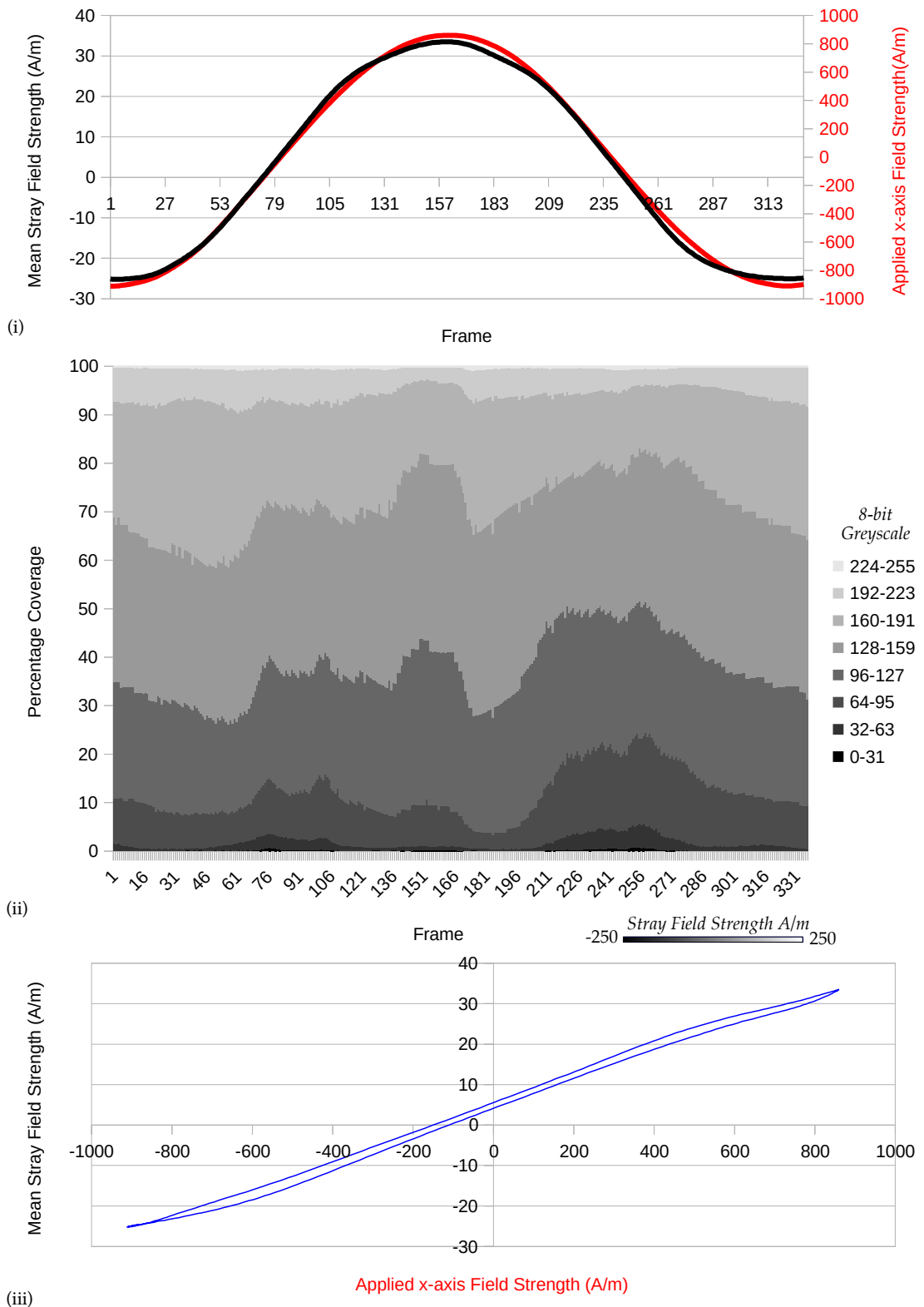


Figure 8.4(b): (i) The Mean stray field strength across the entire surface for each of 336 frames (in black) and the Applied x-axis field strength (in red). (ii) The percentage area coverage of each greyscale level across the entire scan for each of 336 frames. (iii) The Mean Stray field strength plotted against the Applied x-axis field strength.

The relative direction of the applied x-axis field produced by the coils happens to be the inverse of the polarity of the voltage applied to the coils (due to the direction of winding). This has the effect of inverting the greyscale on the Applied field scale in [Figure 8.4\(a\)](#). This has been left as it provides a better contrast for the frames, but the plots in [Figure 8.4\(b\)](#) have the positive directions of the Stray fields and the Applied field aligned.

The expansion and contraction of the domains as they respond to the oscillating applied field can be clearly seen, with slight variation dependent on the relative orientation of the grain, and grain boundary effects present. The variation in this sample is slight, even across the grain boundary, with only small variations due to some sub-surface magnetic anomalies [31]. This uniformity can be seen in the smoothness and regularity of [Figure 8.4\(b.i\)](#) and [Figure 8.4\(b.ii\)](#). The particular area of the sample scanned does not exhibit any non-uniform grain orientation.

In [Chapter 6](#) it was, unexpectedly, discovered that the images produced by the scanner system bore a closer resemblance to images from MOKE observation than from Bitter techniques. This was unexpected because MOKE analysis responds to the in-plane magnetisation vector of the domains and not, as with the Bitter technique and as expected from a z-axis sensor, the perpendicular fields straying from the domain boundaries. Consequently, it was suggested that the fields being measured by the sensor were perhaps largely composed of the perpendicular component of the domain magnetisation that is angled slightly out-of-plane.

This concept is further supported by the strong correspondence between the mean stray field measured for the sample and the applied field seen in [Figure 8.4\(b.i\)](#). The mean of stray fields from the domain walls are not necessarily expected to have any correspondence with the overall magnetisation of the sample, whilst the mean of the in-plane magnetisation vectors of the domains is very much expected to be governed by the externally applied magnetic field ([Chapter 2](#)).

There is a very slight delay between the change in applied field and the change in domain rearrangement, related to the magnetic coercivity of the sample, and plotting the Mean Stray field strength against the Applied x-axis field strength [Figure 8.4\(b.iii\)](#) permits this delay to be observed.

The Lakeshore sensor has been successful in observing the overall domain motion, but with the purchase of the third *Micromagnetics* STJ-020 sensor it became possible to observe the domain dynamics in an uncoated Coated 3% Si Grain-Oriented Steel sheet at 0.01 mm/pixel resolution and ultimately to resolve the dynamics into  $H_z$  and  $H_x$  components.

#### **8.2.4 Coated 3% Si Grain-Oriented Steel subjected to alternating applied field from 50 + 50 Coils**

To enhance the oscillating field applied to a sample the two parallel 20 turn coils were replaced by two parallel 50 turn coils which are wrapped around thin sleeves to permit them to be removed from the sample and a new sample inserted ([Section 4.10.3](#), [Figure 4.15\(b\)](#)). The resulting 100 turn coil has been calibrated ([Section 4.10.4](#), [Figure 4.17](#)) and is known to produce a field of 2.164 kA/m per Volt applied to it.

A strip of Coated 3% Si Grain-Oriented Steel was inserted into the coil, with a scan area between the coils ([Figure 4.15\(b\)](#)). Initially just the perpendicular  $H_z$  stray field component was measured with the sample subjected to a 3 Hz oscillating Applied x-axis field of  $\pm 1.95$  kA/m and scanned at a sampling rate of 1 kHz. Once synchronised 336 frames represent one full cycle.

The initial scan was of an area of  $10 \times 10$  mm<sup>2</sup> at a resolution of 0.05 mm/pixel. A filmstrip of every 4 frames with a 20 pixel border representing the state of the Applied field from the coils is presented in [Figure 8.5\(a\)](#). The dynamic expansion and contraction of the domain walls are visible in the filmstrip but are best observed through the animated GIF provided in *Chapter 8.7z* of the Cardiff Portal Arxive ([page ix](#))

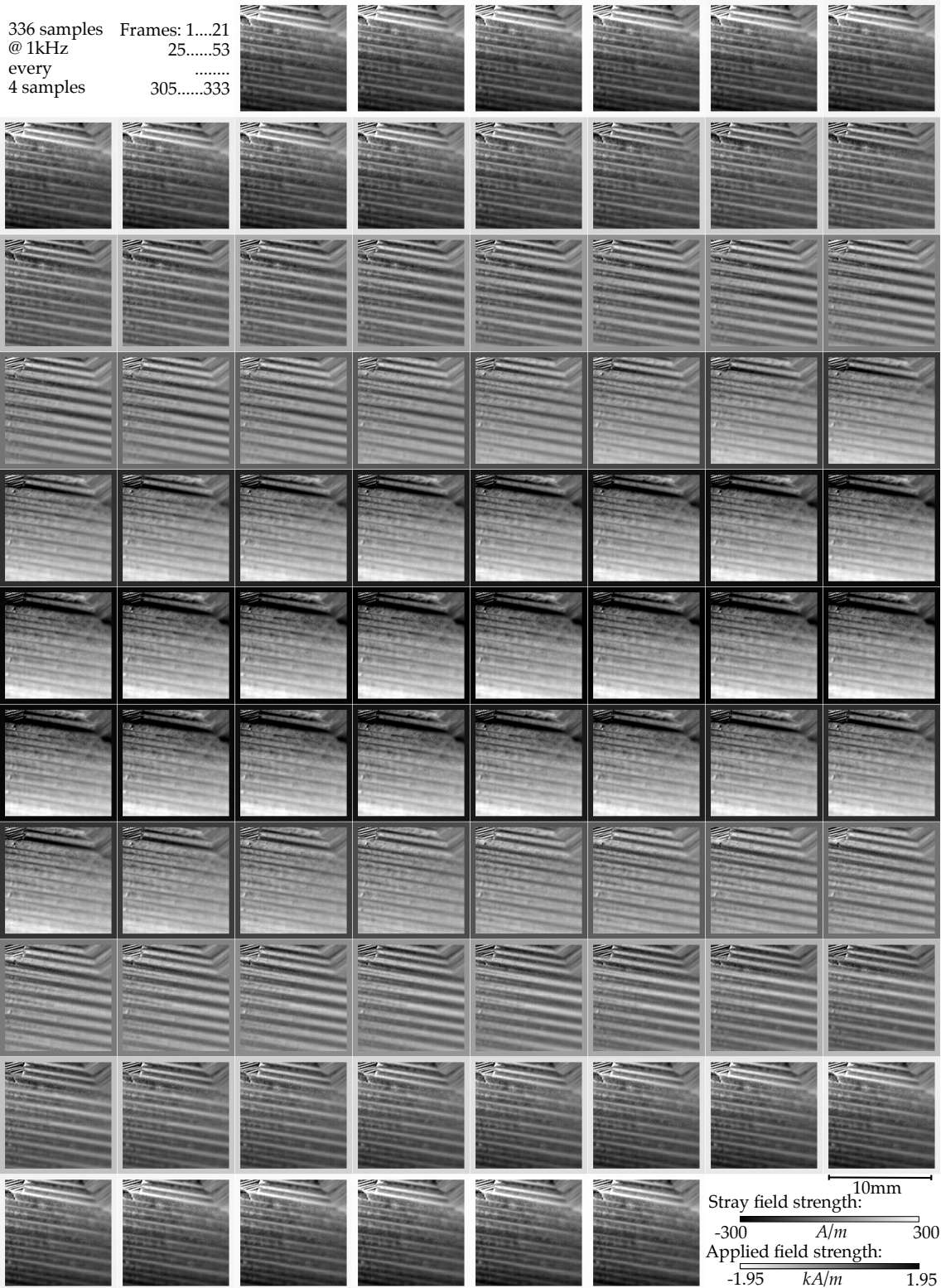


Figure 8.5(a): Filmstrip representation of a 10 x 10 mm<sup>2</sup> (@ 0.05mm/pixel) dynamic scan of Coated 3% Si Grain-Oriented Steel subjected to a 3 Hz oscillating x-axis field of  $\pm 1.95$  kA/m from the 50 + 50 coils. The stray field strength ( $H_z$ ) is represented in greyscale  $\pm 300$  A/m. The full animated GIF is provided in *Chapter 8.7z* ([page ix](#)). The border 20 pixels of each frame presents the oscillating Applied field (inverted greyscale).

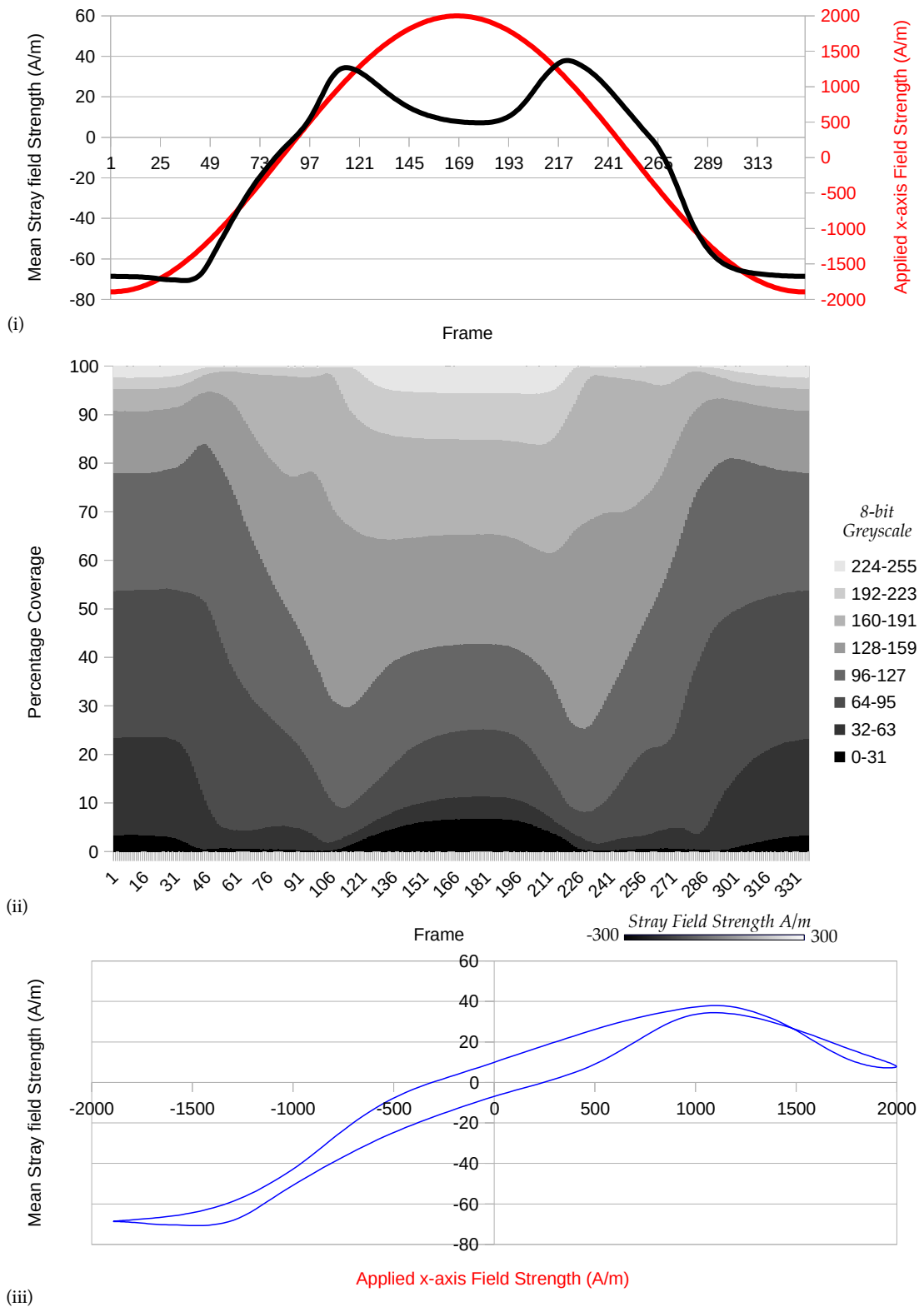


Figure 8.5(b): (i) The Mean stray field strength across the entire surface for each of 336 frames (in black) and the Applied x-axis field strength (in red). (ii) The percentage area coverage of each greyscale level across the entire scan for each of 336 frames. (iii) The Mean Stray field strength plotted against the Applied x-axis field strength.

Both the animated GIF of the Stray fields and Applied Field Strength are also provided embedded in the *Chapter 8.ppt* presentation available in the */Figures Presentations/* folder of the Cardiff Portal Arxive ([page ix](#)) and the accompanying DVD.

Importantly, the higher resolution of the STJ-020 sensor permits the dynamics of the internal Lancet domains [125] to be observed within the main bar domains. Whilst the edges of the main bar domains expand and contract, the internal Lancet domains do not appear to change physical location, but instead increase and decrease in intensity in correspondence with the polarity of the domain body around them. The relative direction of the applied x-axis field produced by the coils happens to be the inverse of the polarity of the voltage applied to the coils (due to the direction of winding). Inverting the greyscale on the Applied field scale in [Figure 8.5\(a\)](#), [Figure 8.6\(a\)](#) and [Figure 8.7\(a\)](#) provides a better contrast for the frames. The plots in [Figure 8.5\(b\)](#), [Figure 8.6\(b\)](#) and [Figure 8.7\(b\)](#) have the positive directions of the Stray fields and the Applied field aligned.

There is a grain boundary to the top of the scan, with the dominant domain direction different to the rest of the sample. The resulting non-uniformity is also apparent in the plots presenting the comparison of the Mean stray field strength against the Applied field strength, presented in [Figure 8.5\(b\)](#).

For a large part of the cycle the domains in the sample adjust to match the mean stray field strength of the sample to the externally applied field ([Figure 8.5\(b.i\)](#)), but when the positive applied field strength exceeds approximately 1.5 kA/m the grain at the top of the sample dominates and the mean stray field direction reverses. This dynamic pattern is also apparent in the Histogram plot ([Figure 8.5\(b.ii\)](#)) and causes a distortion to the tips of the Mean stray field against Applied field plot ([Figure 8.5\(b.iii\)](#)). To understand this non-uniformity better, two higher resolution scans of sub-regions within the initial scan area were made. Both these additional scans were made of 2 x 2 mm<sup>2</sup> regions at a resolution of 0.01 mm/pixel. The location of the sub-region and

the results of these two higher resolution scans are presented in [Figure 8.6](#) and [Figure 8.7](#) respectively alongside the Mean and Histogram analysis.

The 0.01 mm/pixel resolution also permits the Lancet domains to be studied in more detail and again they appear not to move as the edge of the bar domains pass through them. This re-enforces the concept of the Lancet domains as the result of magnetic features originating from internal physical structures [31]. [Figure 8.6\(a\)](#) also illustrates a clear example of a sub-surface magnetic anomaly [31] which acts in opposition to the dominant magnetisation direction. This opposing magnetic anomaly explains the flattening of the mean stray field strength at applied field strength greater than 1 kA/m illustrated in [Figure 8.6\(b.i\)](#) and visible in the histogram plot [Figure 8.6\(b.ii\)](#). The plot of stray field against applied field ([Figure 8.6\(b.ii\)](#)) is more linear but still shows distortion above 1 kA/m. The effect of the magnetic anomaly in [Figure 8.6\(a\)](#) is not itself great enough to cause the distortion in the mean applied field plot of the 10 x 10 mm<sup>2</sup> scan ([Figure 8.5\(b.i\)](#)).

The second sub-region scan is presented in [Figure 8.7\(a\)](#) demonstrates the region with dominant domain direction in opposition to the domains in the rest of the sample. Some of the domains orient with the applied field, which cause a levelling effect [Figure 8.7\(b.i\)](#) when the applied field is  $\pm 1$  kA/m, but the majority of the sub-region acts in opposition to the applied field [Figure 8.7\(b.iii\)](#). The superposition of the top region of the sample presented in [Figure 8.7\(a\)](#), and the sub-surface magnetic anomalies exemplified in [Figure 8.6\(a\)](#), result in the distortion to uniform correspondence between the mean stray field and the applied field observed in the 10 x 10 mm<sup>2</sup> scan.

The distortion of the Mean stray field plot and deformation of the Mean Stray field against Applied field plot caused by non-uniform grain orientation and sub-surface magnetic anomalies [31, 152], points to the future applications in non-destructive testing and quantifying of the quality and consistency of grain orientation during manufacture of Grain-Oriented Electrical Steel.

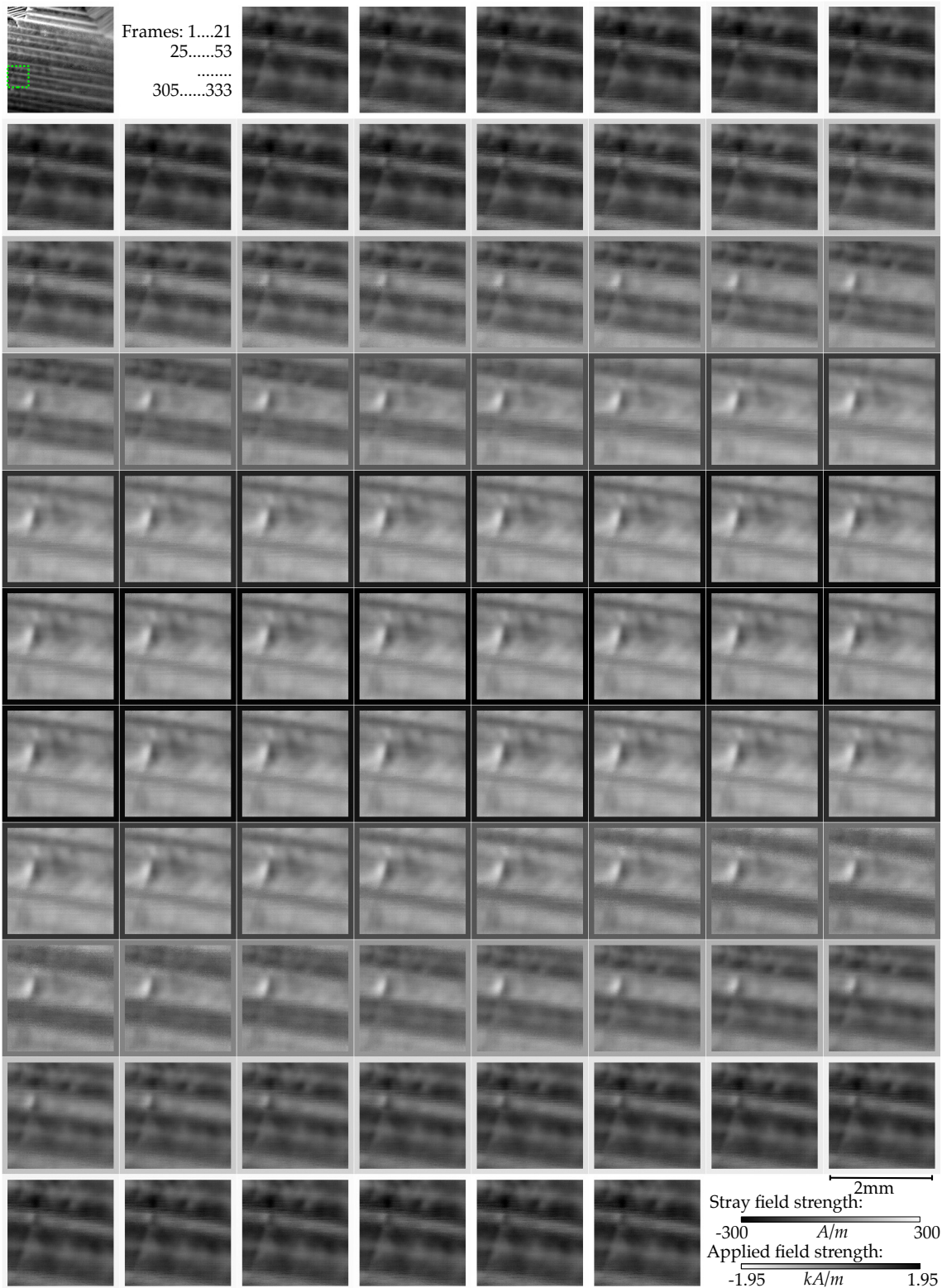


Figure 8.6(a): Filmstrip representation of a  $2 \times 2 \text{ mm}^2$  (@  $0.01\text{mm}/\text{pixel}$ ) dynamic scan of Coated 3% Si Grain-Oriented Steel, a subregion of Figure 8.5(a) as indicated in the top left frame. The stray field strength ( $H_z$ ) is represented in greyscale  $\pm 300 \text{ A/m}$ . The full animated GIF is provided in Chapter 8.7z (page ix). The border 20 pixels of each frame presents the oscillating Applied field (inverted greyscale).



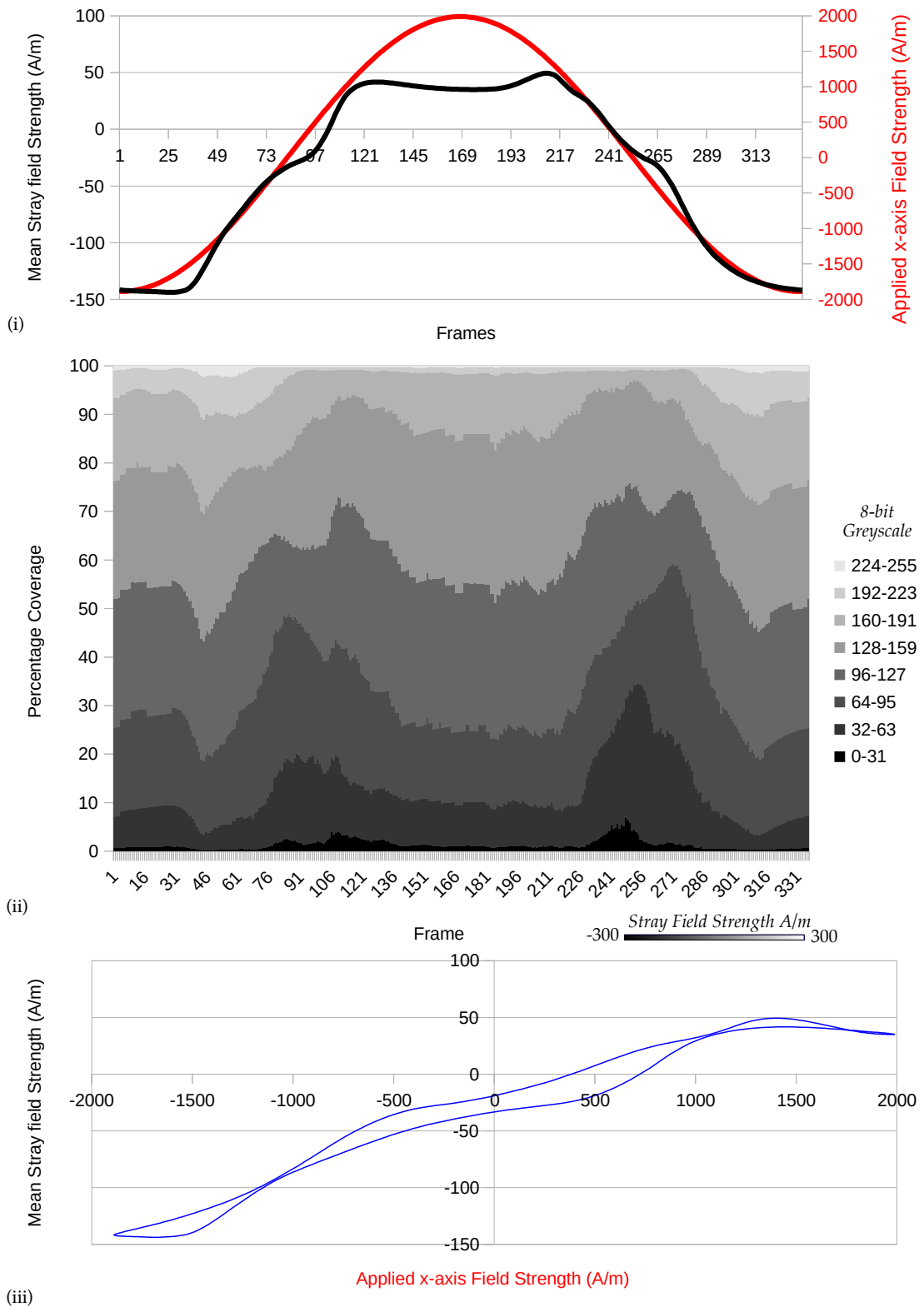


Figure 8.6(b): (i) The Mean stray field strength across the entire surface for each of 336 frames (in black) and the Applied x-axis field strength (in red). (ii) The percentage area coverage of each greyscale level across the entire scan for each of 336 frames. (iii) The Mean Stray field strength plotted against the Applied x-axis field strength.

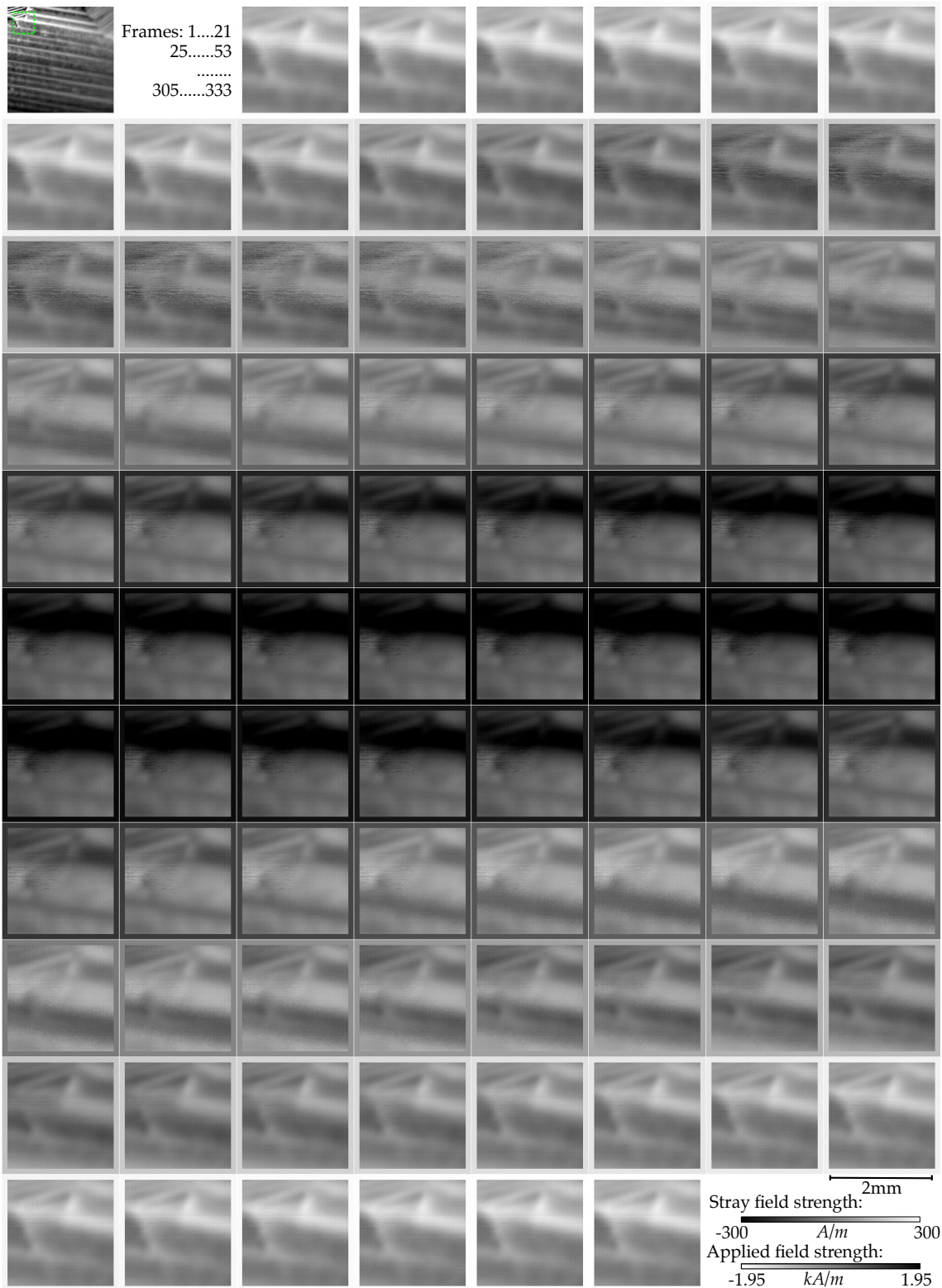


Figure 8.7(a): Filmstrip representation of a  $2 \times 2 \text{ mm}^2$  (@  $0.01\text{mm}/\text{pixel}$ ) dynamic scan of Coated 3% Si Grain-Oriented Steel, a subregion of Figure 8.5(a) as indicated in the top left frame. The stray field strength ( $H_z$ ) is represented in greyscale  $\pm 300 \text{ A/m}$ . The full animated GIF is provided in Chapter 8.7z (page ix). The border 20 pixels of each frame presents the oscillating Applied field (inverted greyscale).

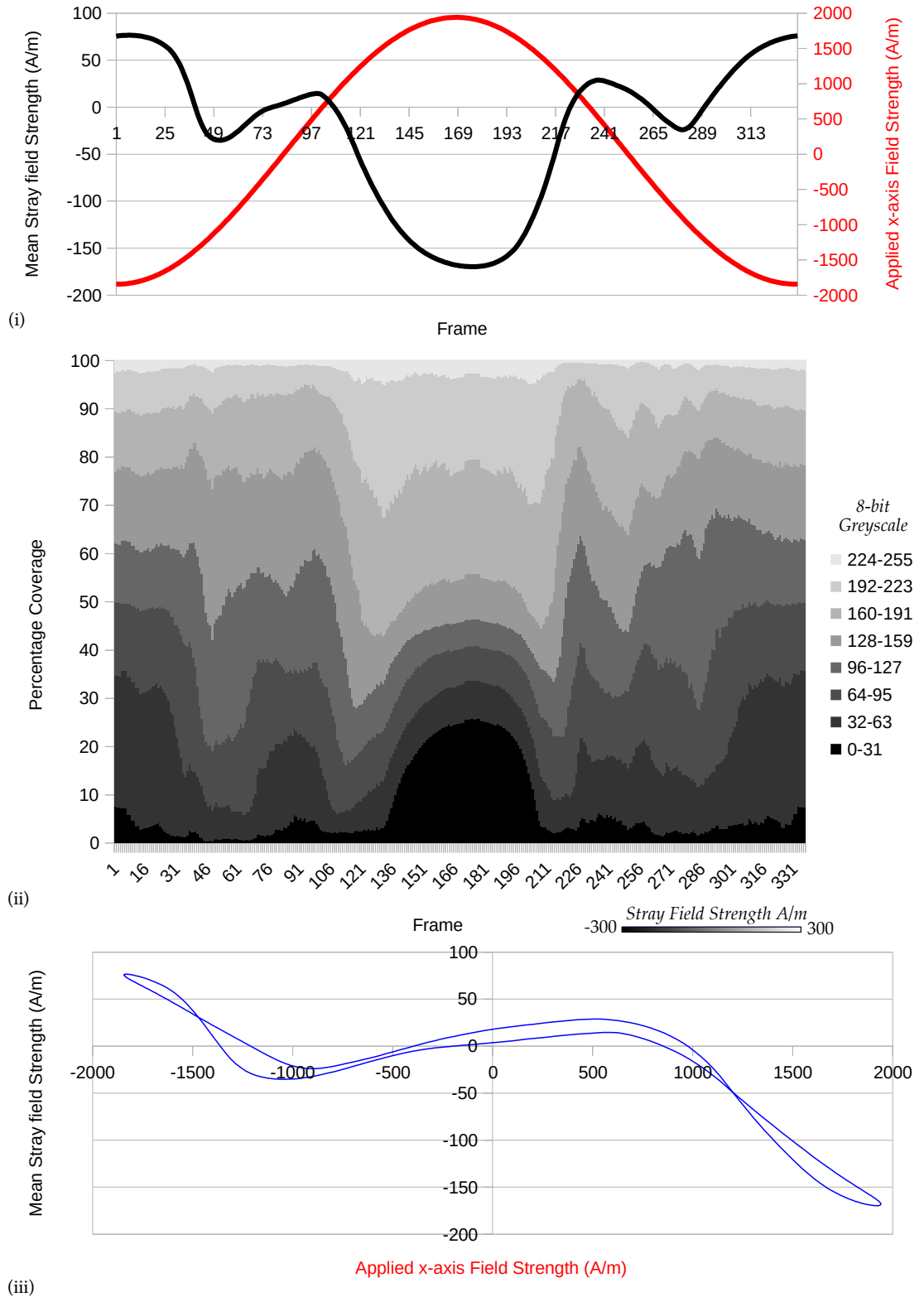


Figure 8.7(b): (i) The Mean stray field strength across the entire surface for each of 336 frames (in black) and the Applied x-axis field strength (in red). (ii) The percentage area coverage of each greyscale level across the entire scan for each of 336 frames. (iii) The Mean Stray field strength plotted against the Applied x-axis field strength.

### 8.3 Investigating Three Dimensional Stray Field Dynamics

Employing the volume scanning technique described in [Section 7.1](#) it is possible to investigate the decay of the stray fields in the thin volume just above the surface of the sample of Coated 3% Si Grain-Oriented Steel.

Employing the tilting STJ-020 TMR sensor technique described in [Section 7.2](#) it is possible to determine the  $H_z$  and  $H_x$  components of the stray fields and hence the shape of the stray fields within the thin volume just above the surface of the sample of Coated 3% Si Grain-Oriented Steel.

Combining these techniques with the development of the dynamic scanning process culminates in the investigation of the change in shape of the stray fields in the thin volume above the surface of the Coated 3% Si Grain-Oriented Steel as it is subjected to a 3 Hz oscillating Applied x-axis field of  $\pm 1.95$  kA/m using the 50 + 50 coils.

Using the same area of the sample studied in [Section 8.2.4 \(page 185\)](#) two dynamic volume scans above the sample were performed, first with the sensor perpendicular to the surface and then with the sensor at 45° counter-clockwise ([see Figure 7.6](#)).

The two scans were of a volume of  $10 \times 10 \times 0.1$  mm<sup>3</sup> at a spatial resolution of  $0.1 \times 0.1 \times 0.05$  mm<sup>3</sup> per cell with a sampling frequency of 1kHz. Both scans were synchronised independently using the *Synchronise.vi* subVI ([Section 5.4.2.8](#)), the resulting first 336 frames representing one full cycle. The *zxCombine.vi* subVI described in [Section 5.5.5](#) (and detailed in Appendix 3) is designed to handle any sized dynamic volume scan and after combination the derived  $H_z$  and  $H_x$  component greyscale PNG stacks were exported with the *PNG.vi* subVI ([Section 5.4.2.7](#)); both the xy-planes and the zx-slices. The greyscale images were then combined using the technique described in [Section 7.2.1](#) to produce the colour representation of the  $\underline{H}$  stray field vector. The 336 frames of the lowest xy-plane and 10 evenly spaced zx-slices were then combined to produce the 336 frame colour animation provided in [Chapter 8.7z \(page ix\)](#).

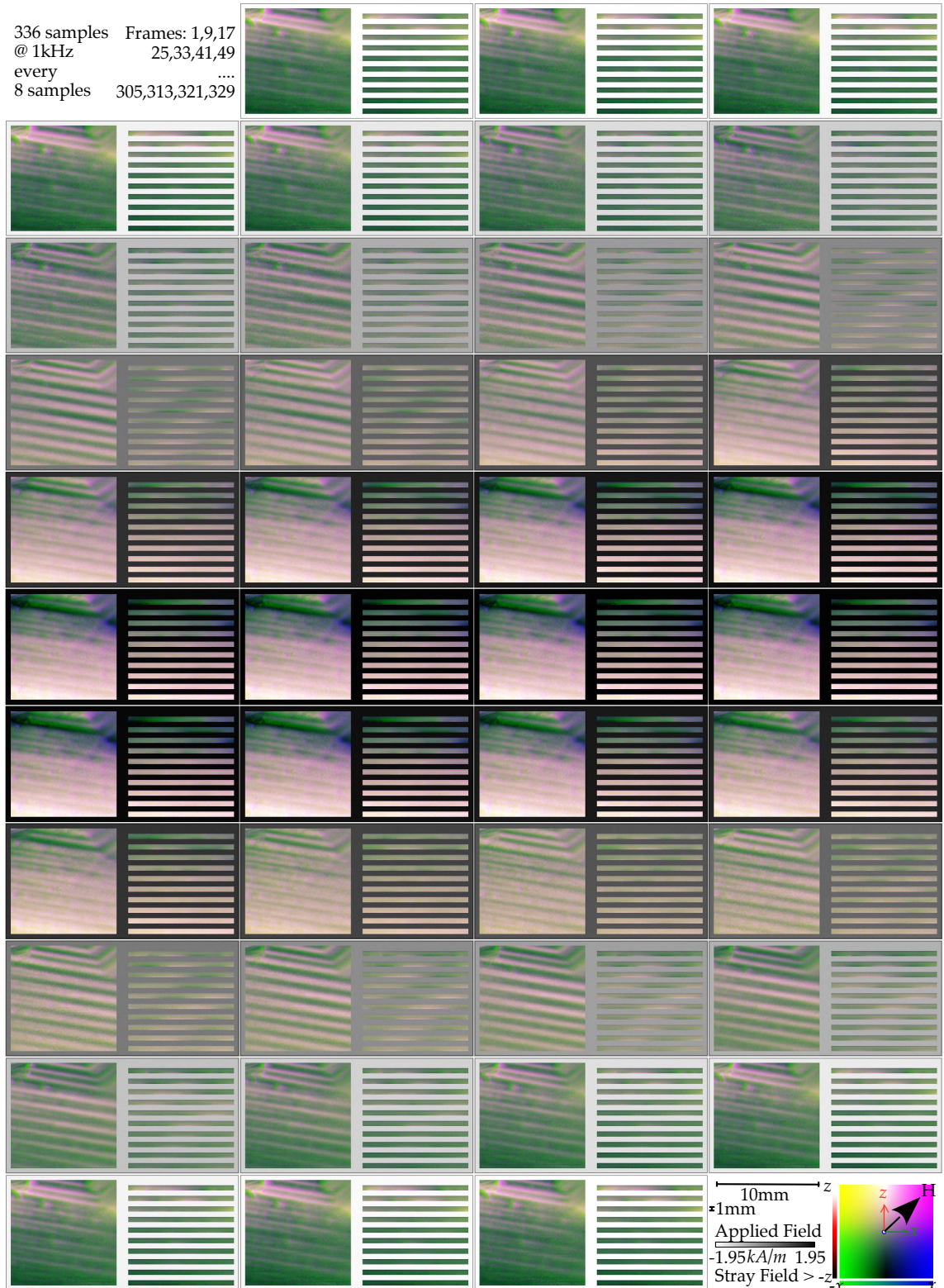


Figure 8.8: Filmstrip representation of the  $10 \times 10 \times 0.1 \text{ mm}^3$  dynamic scan of Coated 3% Si Grain-Oriented Steel subjected to a 3 Hz oscillating x-axis field (@  $0.1 \times 0.1 \times 0.05 \text{ mm}^3/\text{pixel}$ ). The full animation is provided in [Chapter 8.7z](#) ([page ix](#)). The colour representation of the  $\underline{H}$  stray field vector is provided. The  $H_z$  component ranges in magnitude  $\pm 350 \text{ A/m}$ . The  $H_x$  component ranges in magnitude  $\pm 530 \text{ A/m}$ . The background of each frame represents the Applied field ( $\pm 1.95 \text{ kA/m}$ , inverted greyscale).

The background of the animation represents the Applied field strength (inverted greyscale). A filmstrip of every 8 frames is presented in [Figure 8.8](#). The animated version is available as an animated *.gif* but also as *.mov* and *.mp4* movie files because the 256 colour palette of the animated *.gif* format limits the representation of the  $\mathbf{H}$  stray field vector. The animations are also available in the *Chapter 8.ppt* presentation available in the */Figures Presentations/* folder of the Arxive ([page ix](#)) and the DVD.

The presentation of the colourized *xy*-planes demonstrate again the expansion and contraction of the bar domains and unmoving magnetic anomalies. With the direction of the  $\mathbf{H}$  vector illustrated it is possible to see how the direction of the fields change, particularly at the edge of the domain, where the  $\mathbf{H}$  vector changes through  $180^\circ$  within a thin Bloch wall [[31](#)].

With the presentation of the *zx*-slices it is possible for the first time to watch the rotation of the  $\mathbf{H}$  vector as the edge of each domain wall passes through the slice.

The dynamic rotation of the  $\mathbf{H}$  vector from the passage of a Neél or Bloch wall at the edge of an expanding domain has been seen previously on the single axis of micro-wires [[151](#), [153](#), [154](#), [155](#)], studied for applications in Magnetostrictive delay lines [[156](#)], but has not previously been seen in two or three dimensions and this represents the culmination of all of the techniques and processing developed for this thesis.

## Chapter 9

# Conclusions

Overall conclusions of the Thesis, review of the aims achieved and the advantages and disadvantages of the Scanner System are presented. Future work is proposed including improvements to the Hardware and Software and discussion of alternative sensors and applications.

## 9.1 Review of the Original Scanner Specifications and Enhancements

From the original project specification the hardware and software had to meet a number of basic specifications. As the capabilities of the system developed and the nature of the resulting data and application of the scanner were better defined, these basic requirements evolved, with enhancements to the capacity to resolve the components of stray-fields and scan dynamic stray-fields.

### 9.1.1 Review of Scanner Hardware Specifications

The original project specification requires the scanner hardware to be able to;

- a. Make use of the existing hardware that has been provided.*

The scanner system is based on the existing 3-axis positioning arm originally inherited from a system developed by [11, 110]. The existing hardware utilises stepper motors controlled by *Parker Automation* [113] drivers without position encoders. The *Parker Automation* [113] L25i Drives receive ASCII commands through a serial RS232 connection via the legacy LabVIEW VISA libraries. Driver compatibility issues with this older hardware meant that the overall system was limited to 32-bit memory addressing rather than being able to utilise 64-bit addressing. This in turn meant the Scanner Control 3 system had to be developed with file based data storage, rather than faster RAM based storage.

The lack of functional position encoders on the system meant no PID-control positioning system could be employed. The slack/backlash compensation system (Section 4.2.2) was, successfully, developed because of this. For the cost and effort in adding functional position encoders to the existing system it would be more efficient to

replace the existing hardware with modern USB servo-motor control units such as those used in [87].

*c. Correctly position the scanner head along three independent axes.*

*d. Permit the user to confidently position a sensor in a chosen location.*

*f. Sensor positioning with a repeatable precision greater than the footprint of the sensor.*

Nevertheless, the scanner system developed, using the existing hardware, provides for  $\pm 1 \mu\text{m}$  repeatable positional precision on all three axes, smaller than the  $4 \times 2 \mu\text{m}^2$  area of the provided STJ-020 TMR sensor.

*b. Be controlled manually and automatically by an external NI LabView system.*

*e. Be adaptable, to allow any desired sensor to be physically attached.*

A modern, powerful and versatile user interface has been developed using National Instruments LabVIEW 15, through three iterations. The software architecture is modular, permitting easy adaption to future alterations in the system including different sensors and different 3-axis positioning hardware. The sensors are attached to the 3-axis arm using bespoke 3D-printed enclosures, which are quick to redesign, reprint and adapt to alternative sensor options.

*g. Operate unsupervised for periods of days at a time without fault.*

The system has successfully operated fault free continuously for over a week, performing repeated long scans. An attached USB pencil camera and use of Microsoft Remote Desktop has permitted the scanner system to be monitored and operated remotely without the need for presence of the operator once the scan is set up. Presence of the operator and caution should be taken when initially setting up a scan (Section 5.5) to avoid damage to the sensor or sample.



### 9.1.2 Review of Scanner Software Specifications

A modern, powerful and versatile user interface has been developed using National Instruments LabVIEW 15. As the capabilities of the system developed and the nature of the resulting data were better defined, these basic requirements were greatly augmented. The original project specification required the scanner software must be able to;

- a. Correctly communicate with the Parker Automation hardware to accurately control the position of the scanner head.

The Scanner Control software is based on 32-bit LabVIEW 15, which permits use of the legacy LabVIEW VISA communication libraries to send ASCII commands to the *Parker Automation* [113] L25i Drives. The L25i Drives are setup to respond to one command at a time and return status information back to the system.

- b. Guard against the scanner hardware exceeding its physical limits.

The absolute position of the sensor head is stored by the Scanner Control system, rather than the internal registers of the *Parker Automation* [113] L25i Drives; to avoid discontinuity between the hardware and software and allow the physical axis limits to be defined and guarded against directly within the *(Motion).vi* subVI (Section 5.4.2.3).

- c. Provide direct user control of the position of the scanner head.
- d. Control the actions of the scanner in a systematic automated scan.
- e. Enable the user to define the automated scan in a simple way.

Full control of the system, from manual operation through defining and executing an automated scan, is the specific purpose of the design of the Scanner Control system and such operations are detailed in Section 5.5.

f. Acquire voltage inputs from sensors attached to the scanner head and store those values alongside the corresponding sensor position.

The system is designed to sample analogue voltage levels from up to four independent sources through the *National Instruments 6351 USB mDAQ Analogue sampler* (Section 4.4.1). The acceptable voltage levels can range  $\pm 10$  V and a sampling rate of up to 1 MHz can be achieved for dynamic studies. The origin of the voltage levels (the names of the sources/sensors) can be defined modularly within the *(Input).vi* subVI (Section 5.4). At present the system has been designed to accept the analogue voltage inputs of the current suit of sensors, which aids with synchronicity between inputs, but in future the *(Input).vi* subVI could be adapted to accept inputs from sensors with digital outputs.

g. Display and permit interrogation of those data in both raw form and in the form of a greyscale map.

h. Enable the saving and loading of previous scans and the resulting data including the export of data in a form which can be understood and analysed externally.

The Scanner Control software is designed to handle the large datasets from 32-bit floating point acquisition of readings in multi-sensor, 3-axis volume, multi-component, dynamic scans and present it as a greyscale map with a specially developed mouse-based interaction that is unique to a LabVIEW system. The system can also process, save and export the data to standard comma-separated formats which can be studied with external programmes. The two main drivers for the continual development of the system were the increase in quantity of data as the system capabilities improved from being able to scan only two axes, to three axes, then to three axes over time; and the increase in understanding of the LabVIEW programming architecture [122], starting with a continuous-polling model, to an event-driven model, to a hybrid event-driven state-machine based model. The software architecture is modular permitting the software to be easily adapted to future alterations in the system, including different sensors and different 3-axis position hardware.

## 9.2 General Conclusions of the Domain Observation Studies

The system has the capacity to use any sensor with an analogue voltage output  $\pm 10$  V for which a 3D-printed head can be designed.

In contrast with MOKE and Bitter observations of domains, though the scanning takes a long time, the results of the scanner system require no particular sample preparation or post-processing enhancement. After the scan the resulting image is an immediate, correctly planar, quantitative map of domains within the sample. The results are also readily repeatable, and require no manual adjustments.

Perpendicular Stray-field Domain observations of 3% Grain Oriented Electrical Steel show an unexpected similarity with the in-plane magnetisation observations performed with MOKE techniques. This similarity is further evidenced by dynamic observations of the domain movement with the scanner by which the total mean stray field from the surface is demonstrated to closely correspond with the alternating applied field. In [Chapter 6](#) it was, unexpectedly, discovered that the images produced by the scanner system bore a closer resemblance to images from MOKE observation than from Bitter techniques. This was unexpected because MOKE analysis responds to the in-plane magnetisation vector of the domains and not, as with the Bitter technique and as expected from a z-axis sensor, the perpendicular fields straying from the domain boundaries. From this it is suggested that the fields being measured by the sensor are perhaps largely composed of the perpendicular component of the domain magnetisation that is angled slightly out-of-plane. This concept is further supported by the strong correspondence between the mean stray-field measured for the sample and the applied field seen in [Chapter 8](#). The mean of stray-fields from the domain walls are not necessarily expected to have any correspondence with the overall magnetization of the sample, whilst the mean of the in-plane magnetization vectors of the domains is very much expected to be governed by the externally applied magnetic field ([Chapter 2](#)).

When observing Amorphous materials a number of difficulties in the study of domains using the scanner are apparent. Firstly, the intrinsic domains from Amorphous

materials prove themselves to be of a strength ranging over only  $\pm 88$  A/m which is a third of the strength from Grain-Oriented Electrical steel and just above the background Earth field of approximately 50 A/m. This leaves little scope for gaining contrast above the background noise level. The common “domain viewer” method of applying a perpendicular external field to the sample to enhance the intrinsic fields [6] does not help with the scanning method; the externally applied field tends to enhance the measurement of stray-fields from surface topology features rather than the internal domains. “Domain viewer” type perpendicular field enhancement is used beneficially in MOKE observations [49] but masks the study of the domains when using a scanner. The second difficulty in the study of as-cast amorphous ribbon is that, due to the cooling process of manufacture, the surface of the ribbon as-cast is not smooth and features undulations and ripples which cause stray field effects that dominate over the domain observations. Nevertheless, some success has been achieved at the very limit of the scanner resolution in observing the annular domain boundaries present on Amorphous wire (Section 6.2.2). It is indicative of the power of the developed scanner system that it is able to detect such weak and small features.

The validity of the results from the Scanner system have been successfully tested against the known, and Finite Element Modelled, geometries of manufactured Planar coils. The results of planar, three-dimensional component-resolved and dynamic scans have all been validated against the modelled planar coils. This detailed comparative work, undertaken in Chapters 6, 7 and 8, has been successfully published in [112], a copy of which is available in Appendix 6.

The ability to scan in a three-dimensional volume above the surface of the sample and to derive the  $H_z$  and  $H_x$  components from only a single-axis sensor has been developed and demonstrated. It is found that the  $H_z$  Stray field strength from a sample of 3% Grain-Oriented Electrical Steel (which near the surface ranges over  $\pm 200$  A/m) reduces to levels less than the Earth's field at distances greater than 0.05 mm from the surface. The  $H_z$  Stray field strength from Amorphous ribbon ranges over only  $\pm 88$  A/m

but, yet again, these weaker  $H_z$  fields reduce to levels less than the Earth's field at distances greater than 0.05 mm from the surface.

Three-axis TMR sensor arrays with the high resolution of the STJ-020 sensor are available from *Micromagnetics* [85] but are prohibitively expensive. For the first time a practical solution, of two consecutive scans with the sensor axis tilted, has been developed to trigonometrically resolve the  $H_z$  and  $H_x$  components of the field using only the existing single-axis STJ-020 sensor. The concept, successfully demonstrated in [Chapter 7](#), was first presented in [118], available in Appendix 6. A sensor angle of  $45^\circ$  allows for a maximum sampling of  $H_x$  and also for the lowest active area to sample surface distance ( $z_0$ ) possible, due to the shape of the sensor.

With the component resolved study of laser-etched electrical steel a clear difference in the distribution of domains within the coated 3% Si Grain-Oriented Electrical Steel can be observed before and after etching. The laser etching produces an artificial boundary and the domains rearrange to minimise the energy within each of the two newly defined regions [148, 149]. It can be seen from the developed  $\mathbf{H}$  vector colour representation how a narrow band of magnetization-vector-rotation forms across the width of the laser etch. The stray-field orientation rotates to ensure that opposite magnetization directions occur either side of the boundary leading to net-zero magnetization across the boundary. For the first time the rotation of the  $\mathbf{H}$  stray-field vector can be seen at the domain wall. In [Chapter 8](#) it is possible to see how the  $\mathbf{H}$  vector at the domain walls rotates in response to an alternating applied magnetic field.

Producing high frequency dynamic data from the slow process of procedural scanning relies principally on the assumption that the domains follow repeatable oscillatory motion. At the beginning the investigation it was not clear if the domain wall motion within a sample would be sufficiently repeatable to produce meaningful results; but it has been shown that over a 10,000 cell scan of a sample excited at 3 Hz; the settled motion of at least 30,000 cycles of excitation is very repeatable.

It is found that if excited by a traditional C-Yoke system the perpendicular magnetic field from the Yoke itself over-saturates the sensor and prevents the stray-fields from the domains from being seen, particularly when there are strong topological features. Using parallel excitation with coils wrapped around the sample overcomes this issue.

In the observation of the dynamics of bar domains in 3% grain-oriented electrical steel it can be seen that whilst the edges of the main bar domains expand and contract, the internal Lancel domains do not appear to change physical location, but instead increase and decrease in intensity in correspondence with the polarity of the domain body around them.

The mean of all the stray-fields from the surface of the sample is very dependent on the uniformity of grain magnetization within the sample. The distortion of the Mean stray-field plot and deformation of the Mean Stray-field against Applied field plot, caused by non-uniform grain orientation and sub-surface magnetic anomalies ([Chapter 8](#)), points to future applications in non-destructive testing and quantifying of the quality and consistency of grain orientation during manufacture of Grain-Oriented Electrical Steel.

With the direction of the  $\mathbf{H}$  vector illustrated, it is possible to see how the direction of the fields change, particularly at the edge of domains, where the  $\mathbf{H}$  vector changes through  $180^\circ$  within a thin Bloch wall [31]. With the presentation of  $zx$ -slices it is possible, for the first time, to watch the rotation of the  $\mathbf{H}$  vector as the edge of each domain wall passes through the slice. The dynamic rotation of the  $\mathbf{H}$  vector from the passage of a Néel or Bloch wall at the edge of an expanding domain has been seen previously on the single axis of micro-wires studied for applications in Magnetostrictive delay lines [156], but has not previously been seen in two or three dimensions and this represents the culmination of all of the techniques and processing developed for this thesis.

### 9.3 Future Enhancements to the Scanner System

The Scanner system hardware and software have been designed to be modular and easily adapted to new application requirements.

The system can make immediate use of any analogue voltage sensor by designing and printing an appropriate Sensor-head, attaching the sensor to a free channel on the *National Instruments* 6351 USB mDAQ Analogue sampler and changing the name and channel parameters in *(Input).vi*.

Such alternative sensors could include more advanced TMR-array magnetic sensors, with multi-axis options [85] or a micro-MOKE sensor such as that developed for [82], with the prospect of producing a scanning MOKE microscope.

The disadvantage of analogue sensors are the electrical noise involved. IC Sensors with built-in calibrated analogue-to-digital converters, such as the Xtrinsic MAG3110 Three-axis digital magnetometer [144] communicate a digital output by I<sup>2</sup>C and would provide a cleaner input source. The modular nature of the software means the *(Input).vi* subVI (Section 5.4) could be modified to accept data from I<sup>2</sup>C sources without any change to the rest of the system. To maintain synchronicity between sensors it would be advisable for them all to be analogue, or all to be digital. At present there are no commercial digital magnetometers of comparable resolution to the analogue TMR sensors.

The greatest performance restriction of the system is caused by the need to store the data in temporary files on the PC hard disk, rather than in RAM. This is due to the 32-bit memory address limit imposed by the 64-bit compatibility issue with the older *Parker Automation* LabVIEW VISA drivers. If the *Parker Automation* hardware could be replaced with *Thorlabs* Servo-motor drives, such as those in use in [87, 111], then the whole system could be upgraded to 64-bit memory addressing and the

[*DATA\_stream*].vi subVI (Section 5.4.2.4) could be modified to store entirely into shift-registers rather than the scanner\_scratch files.

Again, due to the modular design of the system, only the (*Motion*).vi subVI (Section 5.4.2.3) needs to be altered to work with entirely different 3-axis positional hardware.

The dynamic studies here use an excitation frequency of 3 Hz to test that the system worked during development, and produce effective results within a reasonable timescale and data volume. With the NI 6351 mDAQ capable of a 1 MHz sampling rate, future work can look at higher excitation frequencies (including the standard 50 Hz AC power supply frequency). Consideration would have to be given to the continued use of the 10 Hz low pass filter and alternative noise reduction.

## 9.4 Final Remarks

The original project engineering design brief has been met and exceeded. A magnetic scanner has been built utilising the existing motion control hardware and 3-axis framework and an extensive, versatile, powerful and easy-to-use interface has been developed in NI LabVIEW which extends the capacity of the scanner beyond the original design brief.

The new novel capabilities of the system are the ability to scan and resolve the components of stray-fields in the three-dimensional volume above the surface of a magnetic sample, and to image the dynamics of those fields as the domains expand and contract due to an externally applied alternating magnetic field parallel to the surface.

Such scans, and resulting observations, have been performed on grain-oriented silicon iron and amorphous samples. For the first time; a dynamic three-dimensional component-resolved stray-field scan of a volume above the surface of an unprepared sample of coated 3% grain-oriented electrical steel, under alternating applied magnetic field, has been achieved.



## References

The references made throughout this work are numbered sequentially, in the order of first occurrence, and are listed here in numerical order. Wherever possible each reference includes a Digital Object Identifier which may be used to retrieve the reference from <https://www.doi.org/>.

- [1] Matesy GmbH. (2019). cmos-magview Magneto-Optical Visualization. Last Accessed: December 2019  
URL: [https://matesy.de/images/downloads/2019/CMOS\\_EN\\_201904\\_DB\\_WEB.pdf](https://matesy.de/images/downloads/2019/CMOS_EN_201904_DB_WEB.pdf)
- [2] MicroMagnetics, Inc. (2017). Magnetic tunnel junction sensor development for industrial applications. Last Accessed: December 2019  
URL: <http://www.micromagnetics.com/pdfs/mtj.pdf>
- [3] MicroMagnetics, Inc. (2017). Circuit Scan™ CS1000 Magnetic Field Imaging for Current Density Metrology. Last Accessed: December 2019  
URL: [http://www.micromagnetics.com/images/mm\\_lit.pdf](http://www.micromagnetics.com/images/mm_lit.pdf)
- [4] Lima, E., Bruno, A., Carvalho, H., & Weiss, B. (2014). Scanning magnetic tunnel junction microscope for high-resolution imaging of remanent magnetization fields. *Measurement Science And Technology*, 25(10), 105401.  
doi: [10.1088/0957-0233/25/10/105401](https://doi.org/10.1088/0957-0233/25/10/105401)
- [5] Moreton, G., Meydan, T., & Williams, P. (2016). A Novel Magnetostrictive Curvature Sensor Employing Flexible, Figure-of-Eight Sensing Coils. *IEEE Transactions On Magnetism*, 52(5), 1-4.  
doi: [10.1109/tmag.2016.2520828](https://doi.org/10.1109/tmag.2016.2520828)
- [6] Alimohammadi, S., Meydan, T., & Williams, P. (2019). Strain sensing by exploiting the Matteucci effect in amorphous wire. *International Journal Of Applied Electromagnetics And Mechanics*, 59(1), 115-121.  
doi: [10.3233/jae-171225](https://doi.org/10.3233/jae-171225)
- [7] Huber, C., Abert, C., Bruckner, F., Groenefeld, M., Muthsam, O., & Schuschnigg, S. et al. (2016). 3D print of polymer bonded rare-earth magnets, and 3D magnetic field scanning with an end-user 3D printer. *Applied Physics Letters*, 109(16), 162401.  
doi: [10.1063/1.4964856](https://doi.org/10.1063/1.4964856)
- [8] Dede, M., Akram, R., & Oral, A. (2016). 3D scanning Hall probe microscopy with 700 nm resolution. *Applied Physics Letters*, 109(18), 182407.  
doi: [10.1063/1.4966896](https://doi.org/10.1063/1.4966896)
- [9] Moses, A., Williams, P., & Hoshtanar, O. (2006). Real time dynamic domain observation in bulk materials. *Journal Of Magnetism And Magnetic Materials*, 304(2), 150-154.  
doi: [10.1016/j.jmmm.2006.02.117](https://doi.org/10.1016/j.jmmm.2006.02.117)

## References

- [10] Richert, H., Schmidt, H., Lindner, S., Lindner, M., Wenzel, B., Holzhey, R., & Schäfer, R. (2015). Dynamic Magneto-Optical Imaging of Domains in Grain-Oriented Electrical Steel. *Steel Research International*, 87(2), 232-240.  
doi: [10.1002/srin.201500013](https://doi.org/10.1002/srin.201500013)
- [11] Abdul, J., Moses, A., & Williams, P. (2009). Dynamic Studies of Magnetic Domains Using a Hall Probe Scanner. *Sensor Letters*, 7(3), 310-312.  
doi: [10.1166/sl.2009.1072](https://doi.org/10.1166/sl.2009.1072)
- [12] Coulomb, C. (1884). *Collection de mémoires relatifs à la physique*. Paris: Gauthier-Villars. pp. 414
- [13] French, A. (1968). *Special relativity* (1st ed.). London: CRC Press. pp.296  
ISBN-10: [0748764224](https://www.isbn-international.org/product/0748764224) ISBN-13: [978-0748764228](https://www.isbn-international.org/product/978-0748764228)
- [14] Thomson, J. (1897). XL. Cathode Rays. *The London, Edinburgh, And Dublin Philosophical Magazine And Journal Of Science*, 44(269), 293-316.  
doi: [10.1080/14786449708621070](https://doi.org/10.1080/14786449708621070)
- [15] Davis, E. (2007). Discovery of the electron: commentary on J. J. Thomson's classic paper of 1897. *Philosophical Magazine Letters*, 87(5), 293-301.  
doi: [10.1080/09500830701305514](https://doi.org/10.1080/09500830701305514)
- [16] Van Vleck, J. (1932). *Electric and magnetic susceptibilities*. Oxford: Clarendon Press. pp. 384  
ASIN: [B001ORBN2W](https://www.amazon.com/dp/B001ORBN2W)
- [17] Van Vleck, J. (1978). Quantum Mechanics: The Key to Understanding Magnetism. *Science*, 201(4351), 113-120.  
doi: [10.1126/science.201.4351.113](https://doi.org/10.1126/science.201.4351.113)
- [18] Tiablikov, S. (2013). *Methods in the Quantum Theory of Magnetism*. New York, NY: Springer. pp. 372  
ISBN-10: [1489971831](https://www.isbn-international.org/product/1489971831) ISBN-13: [978-1489971838](https://www.isbn-international.org/product/978-1489971838)
- [19] Coey, J. (2010). *Magnetism and Magnetic Materials* (1st ed.). Cambridge: Cambridge University Press. pp. 625  
ISBN-10: [0521816149](https://www.isbn-international.org/product/0521816149) ISBN-13: [978-0521816144](https://www.isbn-international.org/product/978-0521816144)
- [20] Yamaguchi, K., Suzuki, K., Nittono, O., & Takagi, T. (2010). Domain wall displacement simulation for deformed micro magnetic clusters. *International Journal Of Applied Electromagnetics And Mechanics*, 33(1-2), 103-110.  
doi: [10.3233/jae-2010-1102](https://doi.org/10.3233/jae-2010-1102)
- [21] Golor, M., Lang, T., & Wessel, S. (2013). Quantum Monte Carlo studies of edge magnetism in chiral graphene nanoribbons. *Physical Review B*, 87(15).  
doi: [10.1103/physrevb.87.155441](https://doi.org/10.1103/physrevb.87.155441)
- [22] Xu, L., & Zhang, S. (2013). Self-consistent Bloch equation and Landau-Lifshitz-Bloch equation of ferromagnets: A comparison. *Journal Of Applied Physics*, 113(16), 163911.  
doi: [10.1063/1.4803150](https://doi.org/10.1063/1.4803150)

- [23] Yokota, T. (2017). Three-dimensional magnetic domain structure in a model with exchange randomness. *Journal Of Magnetism And Magnetic Materials*, 432, 532-538.  
doi: [10.1016/j.jmmm.2017.02.031](https://doi.org/10.1016/j.jmmm.2017.02.031)
- [24] Efthimiadis, K., & Ntallis, N. (2018). Finite element micromagnetic simulation of the magnetic domain structures in thin films with uniaxial anisotropy. *Journal Of Magnetism And Magnetic Materials*, 446, 245-252.  
doi: [10.1016/j.jmmm.2017.09.044](https://doi.org/10.1016/j.jmmm.2017.09.044)
- [25] CGPM. (2018). Convocation of the General Conference on Weights and Measures (26th meeting). Last Accessed: December 2019  
URL: <https://www.bipm.org/utis/en/pdf/CGPM/Convocation-2018.pdf>
- [26] Foner, S. (1959). Versatile and Sensitive Vibrating-Sample Magnetometer. *Review Of Scientific Instruments*, 30(7), 548-557.  
doi: [10.1063/1.1716679](https://doi.org/10.1063/1.1716679)
- [27] Jiles, D. (2017). *Introduction to magnetism and magnetic materials* (3rd ed.). London: CRC Press. pp. 570  
ISBN-10: [113844149X](https://www.isbn-international.org/product/978-1-138-44149-X) ISBN-13: [978-1138441491](https://www.isbn-international.org/product/978-1-138-44149-X)
- [28] Moskowitz, R., & Rosensweig, R. (1967). Nonmechanical Torque-Driven Flow of a Ferromagnetic Fluid by an Electromagnetic Field. *Applied Physics Letters*, 11(10), 301-303.  
doi: [10.1063/1.1754952](https://doi.org/10.1063/1.1754952)
- [29] Stewart, D., Stevens, K., & Kaiser, A. (2004). Magnetic Barkhausen noise analysis of stress in steel. *Current Applied Physics*, 4(2-4), 308-311.  
doi: [10.1016/j.cap.2003.11.035](https://doi.org/10.1016/j.cap.2003.11.035)
- [30] Ashcroft, N., & Mermin, N. (1976). *Solid state physics* (33rd ed.). New Delhi: Cengage Learning. pp. 826  
ISBN-10: [0030839939](https://www.isbn-international.org/product/0030839939) ISBN-13: [978-0030839931](https://www.isbn-international.org/product/978-0030839931)
- [31] Hubert, A., & Schäfer, R. (2014). *Magnetic Domains: The Analysis of Magnetic Microstructures* (1st ed.). New York: Springer. pp. 724  
ISBN-10: [3662309564](https://www.isbn-international.org/product/3662309564) ISBN-13: [978-3662309568](https://www.isbn-international.org/product/978-3662309568)
- [32] Anglada-Rivera, J., Padovese, L., & Capó-Sánchez, J. (2001). Magnetic Barkhausen Noise and hysteresis loop in commercial carbon steel: influence of applied tensile stress and grain size. *Journal Of Magnetism And Magnetic Materials*, 231(2-3), 299-306.  
doi: [10.1016/s0304-8853\(01\)00066-x](https://doi.org/10.1016/s0304-8853(01)00066-x)
- [33] Gündel, A., Severino, A., Landgraf, F., & Sommer, R. (2004). Barkhausen noise and high induction losses in non-oriented electrical steel. *Journal Of Magnetism And Magnetic Materials*, 272-276, E561-E562.  
doi: [10.1016/j.jmmm.2003.11.324](https://doi.org/10.1016/j.jmmm.2003.11.324)
- [34] Yusufzai, M., & Vashista, M. (2018). On the role of magnetic field intensity for better micro-structural characterization during Barkhausen Noise analysis. *IOP Conference Series: Materials Science And Engineering*, 346, 012002.  
doi: [10.1088/1757-899x/346/1/012002](https://doi.org/10.1088/1757-899x/346/1/012002)

## References

- [35] Trout, S. (1988). Use of Helmholtz coils for magnetic measurements. *IEEE Transactions On Magnetics*, 24(4), 2108-2111.  
doi: [10.1109/20.3411](https://doi.org/10.1109/20.3411)
- [36] Tumanski, S. (2004). Analysis of magnetic field distribution in C-yoke system. *International Journal Of Applied Electromagnetics And Mechanics*, 19(1-4), 663-666.  
doi: [10.3233/jae-2004-647](https://doi.org/10.3233/jae-2004-647)
- [37] Labinac, V., Erceg, N., & Kotnik-Karuza, D. (2006). Magnetic field of a cylindrical coil. *American Journal Of Physics*, 74(7), 621-627.  
doi: [10.1119/1.2198885](https://doi.org/10.1119/1.2198885)
- [38] Stupakov, O., Perevertov, O., Stoyka, V., & Wood, R. (2010). Correlation Between Hysteresis and Barkhausen Noise Parameters of Electrical Steels. *IEEE Transactions On Magnetics*, 46(2), 517-520.  
doi: [10.1109/tmag.2009.2030415](https://doi.org/10.1109/tmag.2009.2030415)
- [39] Willcock, S., Tanner, B., & Mundell, P. (1988). The parameterization of virgin B-H curves of high strength steels. *Journal Of Magnetism And Magnetic Materials*, 72(1), 45-51.  
doi: [10.1016/0304-8853\(88\)90268-5](https://doi.org/10.1016/0304-8853(88)90268-5)
- [40] Cheng, Z., Takahashi, N., Forghani, B., Du, Y., Fan, Y., & Liu, L. et al. (2011). Effect of Variation of B-H Properties on Loss and Flux Inside Silicon Steel Lamination. *IEEE Transactions On Magnetics*, 47(5), 1346-1349.  
doi: [10.1109/tmag.2010.2086438](https://doi.org/10.1109/tmag.2010.2086438)
- [41] So, M., Nicholson, P., Meydan, T., & Moses, A. (1995). Magnetic domain imaging in coated silicon-iron using magnetoresistive sensors. *IEEE Transactions On Magnetics*, 31(6), 3370-3372.  
doi: [10.1109/20.490385](https://doi.org/10.1109/20.490385)
- [42] Lee, H., Kim, T., Kim, S., Yoon, Y., Kim, S., & Babajanyan, A. et al. (2010). Magneto-optical imaging using a garnet indicator film prepared on glass substrates. *Journal Of Magnetism And Magnetic Materials*, 322(18), 2722-2727.  
doi: [10.1016/j.jmmm.2010.04.015](https://doi.org/10.1016/j.jmmm.2010.04.015)
- [43] Xu, X., Moses, A., Hall, J., Williams, P., & Jenkins, K. (2011). A Comparison of Magnetic Domain Images Using a Modified Bitter Pattern Technique and the Kerr Method on Grain-Oriented Electrical Steel. *IEEE Transactions On Magnetics*, 47(10), 3531-3534.  
doi: [10.1109/tmag.2011.2148101](https://doi.org/10.1109/tmag.2011.2148101)
- [44] Hofmann, M., Naumoski, H., Herr, U., & Herzog, H. (2016). Magnetic Properties of Electrical Steel Sheets in Respect of Cutting: Micromagnetic Analysis and Macromagnetic Modeling. *IEEE Transactions On Magnetics*, 52(2), 1-14.  
doi: [10.1109/tmag.2015.2484280](https://doi.org/10.1109/tmag.2015.2484280)
- [45] Takajo, S., Hiratani, T., Okubo, T., & Oda, Y. (2018). Effect of Silicon Content on Iron Loss and Magnetic Domain Structure of Grain-Oriented Electrical Steel Sheet. *IEEE Transactions On Magnetics*, 54(1), 1-6.  
doi: [10.1109/tmag.2017.2759103](https://doi.org/10.1109/tmag.2017.2759103)

- [46] Kim, H., Kim, C., Seong, H., & Yoo, J. (2015). Structural Optimization of a Magnetic Actuator With Simultaneous Consideration of Thermal and Magnetic Performances. *IEEE Transactions On Magnetics*, 51(12), 1-9.  
doi: [10.1109/tmag.2015.2453422](https://doi.org/10.1109/tmag.2015.2453422)
- [47] Li, Z., Zhang, X., Gu, G., Chen, X., & Su, C. (2016). A Comprehensive Dynamic Model for Magnetostrictive Actuators Considering Different Input Frequencies With Mechanical Loads. *IEEE Transactions On Industrial Informatics*, 12(3), 980-990.  
doi: [10.1109/tii.2016.2543027](https://doi.org/10.1109/tii.2016.2543027)
- [48] Kim, Y., Yuk, H., Zhao, R., Chester, S., & Zhao, X. (2018). Printing ferromagnetic domains for untethered fast-transforming soft materials. *Nature*, 558(7709), 274-279.  
doi: [10.1038/s41586-018-0185-0](https://doi.org/10.1038/s41586-018-0185-0)
- [49] Hardcastle, M., & Meydan, T. (2000). Magnetic domain behaviour in magnetostrictive torque sensors. *Sensors And Actuators A: Physical*, 81(1-3), 121-125.  
doi: [10.1016/s0924-4247\(99\)00150-8](https://doi.org/10.1016/s0924-4247(99)00150-8)
- [50] Atalay, S., Ripka, P., & Bayri, N. (2010). Coil-less fluxgate effect in  $(\text{Co}_{0.94}\text{Fe}_{0.06})_{72.5}\text{Si}_{12.5}\text{B}_{15}$  amorphous wires. *Journal Of Magnetism And Magnetic Materials*, 322(15), 2238-2243.  
doi: [10.1016/j.jmmm.2010.02.018](https://doi.org/10.1016/j.jmmm.2010.02.018)
- [51] Atalay, S., Bayri, N., Fidan, A., Atalay, F., & Yagmur, V. (2012). Torsion sensor based on the coil-less fluxgate effect. *Sensors And Actuators A: Physical*, 178, 100-103.  
doi: [10.1016/j.sna.2012.02.049](https://doi.org/10.1016/j.sna.2012.02.049)
- [52] Borie, B., Voto, M., Lopez-Diaz, L., Grimm, H., Diegel, M., Kläui, M., & Mattheis, R. (2017). Reliable Propagation of Magnetic Domain Walls in Cross Structures for Advanced Multiturn Sensors. *Physical Review Applied*, 8(4).  
doi: [10.1103/physrevapplied.8.044004](https://doi.org/10.1103/physrevapplied.8.044004)
- [53] Bitter, F. (1931). On Inhomogeneities in the Magnetization of Ferromagnetic Materials. *Physical Review*, 38(10), 1903-1905.  
doi: [10.1103/physrev.38.1903](https://doi.org/10.1103/physrev.38.1903)
- [54] Bitter, F. (1932). Experiments on the Nature of Ferromagnetism. *Physical Review*, 41(4), 507-515.  
doi: [10.1103/physrev.41.507](https://doi.org/10.1103/physrev.41.507)
- [55] Williams, H., Bozorth, R., & Shockley, W. (1949). Magnetic Domain Patterns on Single Crystals of Silicon Iron. *Physical Review*, 75(1), 155-178.  
doi: [10.1103/physrev.75.155](https://doi.org/10.1103/physrev.75.155)
- [56] Narita, K., & Yamaguchi, T. (1975). Rotational and alternating hysteresis losses in 4% silicon-iron single crystal with the {110} surface. *IEEE Transactions On Magnetics*, 11(6), 1661-1666.  
doi: [10.1109/tmag.1975.1058979](https://doi.org/10.1109/tmag.1975.1058979)

## References

- [57] Grechishkin, R., Koledov, V., Shavrov, V., Dikshtein, I., Khovailo, V., & Takagi, T. et al. (2004). Martensitic and magnetic domain structures in polycrystalline shape memory alloys  $\text{Ni}_{2+x}\text{Mn}_{1-x}\text{Ga}$ . *International Journal Of Applied Electromagnetics And Mechanics*, 19(1-4), 175-178.  
[doi: 10.3233/jae-557-xxx](https://doi.org/10.3233/jae-557-xxx)
- [58] Faraday, M. (1846). I. Experimental researches in electricity.—Nineteenth series. *Philosophical Transactions Of The Royal Society Of London*, 136, 1-20.  
[doi: 10.1098/rstl.1846.0001](https://doi.org/10.1098/rstl.1846.0001)
- [59] Kerr, J. (1877). I. On the rotation of the plane of polarization of light by reflection from the pole of a magnet. *Proceedings Of The Royal Society Of London*, 25(171-178), 447-450.  
[doi: 10.1098/rspl.1876.0065](https://doi.org/10.1098/rspl.1876.0065)
- [60] McCord, J. (2015). Progress in magnetic domain observation by advanced magneto-optical microscopy. *Journal Of Physics D: Applied Physics*, 48(33), 333001.  
[doi: 10.1088/0022-3727/48/33/333001](https://doi.org/10.1088/0022-3727/48/33/333001)
- [61] Fowler, C., & Fryer, E. (1952). Magnetic Domains on Silicon Iron by the Longitudinal Kerr Effect. *Physical Review*, 86(3), 426-426.  
[doi: 10.1103/physrev.86.426](https://doi.org/10.1103/physrev.86.426)
- [62] Schäfer, R., & Schinnerling, S. (2000). Bulk domain analysis in FeSi-crystals. *Journal Of Magnetism And Magnetic Materials*, 215-216, 140-146.  
[doi: 10.1016/s0304-8853\(00\)00097-4](https://doi.org/10.1016/s0304-8853(00)00097-4)
- [63] Meguro, S., Akahane, K., & Saito, S. (2016). Photographic observation of magnetic domain structure with three-dimensional local magnetization direction. *Japanese Journal Of Applied Physics*, 55(7S3), 07MF04.  
[doi: 10.7567/jjap.55.07mf04](https://doi.org/10.7567/jjap.55.07mf04)
- [64] Takezawa, M., Wada, T., Morimoto, Y., & Yamasaki, J. (2007). Domain observation of amorphous wire with large diameter for micro-sensor and micro-motor application. *International Journal Of Applied Electromagnetics And Mechanics*, 25(1-4), 189-192.  
[doi: 10.3233/jae-2007-773](https://doi.org/10.3233/jae-2007-773)
- [65] Takezawa, M., Nagashima, Y., Morimoto, Y., & Yamasaki, J. (2011). Magnetic Domain Observation of Nd-Fe-B Sintered Magnets at Elevated Temperatures by Using Kerr Microscope. *IEEE Transactions On Magnetics*, 47(10), 3256-3258.  
[doi: 10.1109/tmag.2011.2154316](https://doi.org/10.1109/tmag.2011.2154316)
- [66] Životský, O., Postava, K., Kraus, L., Hrabovská, K., Hendrych, A., & Pištora, J. (2010). Surface magnetic properties and domains observation in as-quenched and annealed FeNbB ribbons. *Journal Of Magnetism And Magnetic Materials*, 322(9-12), 1523-1526.  
[doi: 10.1016/j.jmmm.2009.10.060](https://doi.org/10.1016/j.jmmm.2009.10.060)
- [67] Raghunath, G., Marana, M., Na, S., & Flatau, A. (2014). Kerr microscopy studies of the effects of bending stress on galfenol. *Journal Of Applied Physics*, 115(17), 17E310.  
[doi: 10.1063/1.4865468](https://doi.org/10.1063/1.4865468)

- [68] Naumoski, H., Maucher, A., Vandenbossche, L., Jacobs, S., Herr, U., & Chassang, X. (2014). Magneto-optical and field-metric evaluation of the punching effect on magnetic properties of electrical steels with varying alloying content and grain size. *2014 4<sup>th</sup> International Electric Drives Production Conference (EDPC)*.  
doi: [10.1109/edpc.2014.6984398](https://doi.org/10.1109/edpc.2014.6984398)
- [69] Laviano, F., Gerbaldo, R., Ghigo, G., Gozzelino, L., Przyslupski, P., & Ragusa, C. (2016). Quantitative Imaging of Magnetic Patterns in Ferromagnetic Films by Magneto-Optical Imaging With an Indicator Film. *IEEE Transactions On Magnetics*, 52(5), 1-4.  
doi: [10.1109/tmag.2015.2511726](https://doi.org/10.1109/tmag.2015.2511726)
- [70] Bennett, L., McMichael, R., Swartzendruber, L., Hua, S., Lashmore, D., & Shapiro, A. et al. (1995). Magneto-optical indicator film observation of domain structure in magnetic multilayers. *Applied Physics Letters*, 66(7), 888-890.  
doi: [10.1063/1.113421](https://doi.org/10.1063/1.113421)
- [71] Grechishkin, R., Kustov, M., Ilyashenko, S., Gasanov, O., Dumas-Bouchiat, F., & Dempsey, N. (2016). Magneto-optical imaging and analysis of magnetic field micro-distributions with the aid of biased indicator films. *Journal Of Applied Physics*, 120(17), 174502.  
doi: [10.1063/1.4966225](https://doi.org/10.1063/1.4966225)
- [72] Matesy GmbH. (2019). Magnetic Technologies & Systems. CMOS-MagView Magneto-optical visualization of magnetic fields. Last Accessed: December 2019  
URL:  
[https://www.sensor-test.de/ausstellerbereich/upload/mnpdf/en/CMV\\_en\\_201202\\_12.pdf](https://www.sensor-test.de/ausstellerbereich/upload/mnpdf/en/CMV_en_201202_12.pdf)
- [73] Ripka, P., & Janošek, M. (2010). Advances in Magnetic Field Sensors. *IEEE Sensors Journal*, 10(6), 1108-1116.  
doi: [10.1109/jsen.2010.2043429](https://doi.org/10.1109/jsen.2010.2043429)
- [74] Hall, E. (1879). On a New Action of the Magnet on Electric Currents. *American Journal Of Mathematics*, 2(3), 287.  
doi: [10.2307/2369245](https://doi.org/10.2307/2369245)
- [75] Ripka, P., Tondra, M., Stokes, J., & Beech, R. (1999). AC-driven AMR and GMR magnetoresistors. *Sensors And Actuators A: Physical*, 76(1-3), 225-230.  
doi: [10.1016/s0924-4247\(99\)00034-5](https://doi.org/10.1016/s0924-4247(99)00034-5)
- [76] Smith, C., Schneider, R., & Pohm, A. (2003). High-resolution giant magnetoresistance on-chip arrays for magnetic imaging. *Journal Of Applied Physics*, 93(10), 6864-6866.  
doi: [10.1063/1.1558248](https://doi.org/10.1063/1.1558248)
- [77] Tumanski, S.. (2013). Modern magnetic field sensors - a review. *Przegląd Elektrotechniczny*. 89. 1-12.
- [78] Tumanski, S. (2011). *Handbook of Magnetic Measurements (Series in Sensors)* (1st ed.). London: CRC Press. pp. 404  
ISBN-10: [1439829519](https://doi.org/10.1002/9781439829519) ISBN-13: [978-1439829516](https://doi.org/10.1002/9781439829516)
- [79] MicroMagnetics, Inc. (2017). STJ-020 Magnetic Microsensor Probe - Product Overview. Last Accessed: December 2019  
URL: [http://www.micromagnetics.com/docs/STJ-020\\_TMR\\_magnetic\\_microsensor.pdf](http://www.micromagnetics.com/docs/STJ-020_TMR_magnetic_microsensor.pdf)

## References

- [80] Tumanski, S., Baranowski, S. (2006). Magnetic Sensor Array for Investigations of Magnetic Field Distribution. *Journal of ELECTRICAL ENGINEERING*, 57(8/S). 185-188.
- [81] Magcam NV Impressum. (2015). Magcam MiniCube3D three-axis magnetic field camera. Last Accessed: December 2019  
URL: [http://www.360magnetics.com/wp-content/uploads/2017/03/Magcam\\_Brochure\\_MiniCube3D-1.pdf](http://www.360magnetics.com/wp-content/uploads/2017/03/Magcam_Brochure_MiniCube3D-1.pdf)
- [82] Halahovets, Y., Siffalovic, P., Jergel, M., Senderak, R., Majkova, E., & Luby, S. et al. (2011). Scanning magneto-optical Kerr microscope with auto-balanced detection scheme. *Review Of Scientific Instruments*, 82(8), 083706.  
doi: [10.1063/1.3625687](https://doi.org/10.1063/1.3625687)
- [83] Kustov, M., Laczkowski, P., Hykel, D., Hasselbach, K., Dumas-Bouchiat, F., & O'Brien, D. et al. (2010). Magnetic characterization of micropatterned Nd–Fe–B hard magnetic films using scanning Hall probe microscopy. *Journal Of Applied Physics*, 108(6), 063914.  
doi: [10.1063/1.3486513](https://doi.org/10.1063/1.3486513)
- [84] Shaw, G., Kramer, R., Dempsey, N., & Hasselbach, K. (2016). A scanning Hall probe microscope for high resolution, large area, variable height magnetic field imaging. *Review Of Scientific Instruments*, 87(11), 113702.  
doi: [10.1063/1.4967235](https://doi.org/10.1063/1.4967235)
- [85] MicroMagnetics, Inc. (2017). SpinTJ™ Magnetic Field Sensors. Last Accessed: December 2019  
URL: [https://micromagnetics.com/docs/SpinTJ\\_TMR\\_magnetic\\_sensors\\_brochure.pdf](https://micromagnetics.com/docs/SpinTJ_TMR_magnetic_sensors_brochure.pdf)
- [86] Ignatjev, V., Orlov, A., & Stankevich, D. (2018). Method of current distribution parameters measuring with using reference magnetic field source. *Measurement*, 125, 109-113.  
doi: [10.1016/j.measurement.2018.04.074](https://doi.org/10.1016/j.measurement.2018.04.074)
- [87] Okolo, Chukwunonso K. and Meydan, Turgut (2017). Axial magnetic field sensing for pulsed magnetic flux leakage hairline crack detection and quantification. *Presented at: 2017 IEEE SENSORS, Glasgow, Scotland, UK, 29 October-1 November 2017. SENSORS, 2017 IEEE.*  
doi: [10.1109/ICSENS.2017.8233983](https://doi.org/10.1109/ICSENS.2017.8233983)
- [88] Araujo, J., Reis, A., Oliveira, V., Santos, A., Luz-Lima, C., & Yokoyama, E. et al. (2019). Characterizing Complex Mineral Structures in Thin Sections of Geological Samples with a Scanning Hall Effect Microscope. *Sensors*, 19(7), 1636.  
doi: [10.3390/s19071636](https://doi.org/10.3390/s19071636)
- [89] Gontarz, S., Szulim, P., & Lei, Y. (2018). Identification of magnetomechanical phenomena in a degradation process of loaded steel elements. *Journal Of Magnetism And Magnetic Materials*, 467, 29-36.  
doi: [10.1016/j.jmmm.2018.07.045](https://doi.org/10.1016/j.jmmm.2018.07.045)
- [90] Nicholson, P. (1999). *Development of a Magnetic Domain Imaging System for Electrical Steel Using a Magnetoresistive Sensor Based Stray Field Scanning Technique* (PhD Thesis). University of Wales, Cardiff.



- [91] Jones, D., Nicholson, P., & Cox, P. (2003). APPARATUS AND METHOD OF MEASURING THE MULTI-DIMENSIONAL MAGNETIC FIELD DISTRIBUTION OF A MAGNETIC SAMPLE IN REAL-TIME. USA. Patent No.: US 6,611,142 B1
- [92] Schrag, B. D., Liu, X. Y., Carter, M. J., and Xiao, G. (2003). Scanning magnetoresistive microscopy for die-level sub-micron current density mapping. *Presented at: 29<sup>th</sup> International Symposium for Testing and Failure Analysis, Santa Clara, California, USA, 2 - 6 November 2003.*
- [93] Liu, X., Mazumdar, D., Schrag, B., Shen, W., & Xiao, G. (2004). Magnetization reversal of submicrometer Co rings with uniaxial anisotropy via scanning magnetoresistance microscopy. *Physical Review B*, 70(1).  
doi: [10.1103/physrevb.70.014407](https://doi.org/10.1103/physrevb.70.014407)
- [94] Schrag, B., & Xiao, G. (2003). Submicron electrical current density imaging of embedded microstructures. *Applied Physics Letters*, 82(19), 3272-3274.  
doi: [10.1063/1.1570499](https://doi.org/10.1063/1.1570499)
- [95] Schrag, B., Liu, X., Shen, W., & Xiao, G. (2004). Current density mapping and pinhole imaging in magnetic tunnel junctions via scanning magnetic microscopy. *Applied Physics Letters*, 84(15), 2937-2939.  
doi: [10.1063/1.1695194](https://doi.org/10.1063/1.1695194)
- [96] MicroMagnetics, Inc. (2017). Failure Analysis and Magnetic Imaging Services. Last Accessed: December 2019  
URL: [https://micromagnetics.com/products\\_m\\_f\\_imaging.html](https://micromagnetics.com/products_m_f_imaging.html)
- [97] Schrag, B. D., Carter, M. J., Liu, X., Hoftun, J. S., & Xiao, G. (2006). Magnetic Current Imaging with Magnetic Tunnel Junction Sensors-Case Study and Analysis. In *International Symposium for Testing and Failure Analysis 32*, 13. ASM International
- [98] Shen, W., Liu, X., Mazumdar, D., & Xiao, G. (2005). In situ detection of single micron-sized magnetic beads using magnetic tunnel junction sensors. *Applied Physics Letters*, 86(25), 253901.  
doi: [10.1063/1.1952582](https://doi.org/10.1063/1.1952582)
- [99] Shen, W., Schrag, B., Carter, M., & Xiao, G. (2008). Quantitative detection of DNA labeled with magnetic nanoparticles using arrays of MgO-based magnetic tunnel junction sensors. *Applied Physics Letters*, 93(3), 033903.  
doi: [10.1063/1.2963970](https://doi.org/10.1063/1.2963970)
- [100] Lei, H., Wang, K., Ji, X., & Cui, D. (2016). Contactless Measurement of Magnetic Nanoparticles on Lateral Flow Strips Using Tunneling Magnetoresistance (TMR) Sensors in Differential Configuration. *Sensors*, 16(12), 2130.  
doi: [10.3390/s16122130](https://doi.org/10.3390/s16122130)
- [101] Harti, R., Strobl, M., Schäfer, R., Kardjilov, N., Tremsin, A., & Grünzweig, C. (2018). Dynamic volume magnetic domain wall imaging in grain oriented electrical steel at power frequencies with accumulative high-frame rate neutron dark-field imaging. *Scientific Reports*, 8(1).  
doi: [10.1038/s41598-018-33835-8](https://doi.org/10.1038/s41598-018-33835-8)

## References

- [102] Freeman, M., Hiebert, W., & Stankiewicz, A. (1998). Time-resolved scanning Kerr microscopy of ferromagnetic structures (invited). *Journal Of Applied Physics*, 83(11), 6217-6222.  
[doi: 10.1063/1.367716](https://doi.org/10.1063/1.367716)
- [103] Yang, T., Gopalan, V., Swart, P., & Mohideen, U. (1999). Direct Observation of Pinning and Bowing of a Single Ferroelectric Domain Wall. *Physical Review Letters*, 82(20), 4106-4109.  
[doi: 10.1103/physrevlett.82.4106](https://doi.org/10.1103/physrevlett.82.4106)
- [104] Hoshtanar, O. (2006). *Dynamic Domain Observation in Grain-Oriented Electrical Steel Using Magneto-Optical Techniques* (PhD Thesis). University of Wales, Cardiff.
- [105] Endo, H., Hayano, S., Fujikura, M., Mogi, H., Kaido, C., & Saito, Y. (2002). Magnetic domain dynamics visualization. *International Journal Of Applied Electromagnetics And Mechanics*, 15(1-4), 409-416.  
[doi: 10.3233/jae-2002-474](https://doi.org/10.3233/jae-2002-474)
- [106] Magni, A. (2015). Stroboscopic investigation of domain wall motion at high frequencies. *International Journal Of Applied Electromagnetics And Mechanics*, 48(2,3), 295-300.  
[doi: 10.3233/jae-152001](https://doi.org/10.3233/jae-152001)
- [107] Holländer, R., Müller, C., Lohmann, M., Mozooni, B., & McCord, J. (2017). Component selection in time-resolved magneto-optical wide-field imaging for the investigation of magnetic microstructures. *Journal Of Magnetism And Magnetic Materials*, 432, 283-290.  
[doi: 10.1016/j.jmmm.2017.01.091](https://doi.org/10.1016/j.jmmm.2017.01.091)
- [108] Wells, F., Pan, A., Wilson, S., Golovchanskiy, I., Fedoseev, S., & Rozenfeld, A. (2016). Dynamic magneto-optical imaging of superconducting thin films. *Superconductor Science And Technology*, 29(3), 035014.  
[doi: 10.1088/0953-2048/29/3/035014](https://doi.org/10.1088/0953-2048/29/3/035014)
- [109] Kögel, M., Altmann, F., Tismer, S., & Brand, S. (2016). Magnetic field and current density imaging using off-line lock-in analysis. *Microelectronics Reliability*, 64, 346-351.  
[doi: 10.1016/j.microrel.2016.07.083](https://doi.org/10.1016/j.microrel.2016.07.083)
- [110] Abdul, J. (2010). *A Novel magnetic Stray Field Scanner for Imaging Static and Dynamic Magnetic Domains in Electrical Steel* (MPhil Thesis). Cardiff University.
- [111] Okolo, C., & Meydan, T. (2018). Pulsed magnetic flux leakage method for hairline crack detection and characterization. *AIP Advances*, 8(4), 047207.  
[doi: 10.1063/1.4994187](https://doi.org/10.1063/1.4994187)
- [112] Gibbs, R., Moreton, G., Meydan, T., & Williams, P. (2018). Comparison between Modelled and Measured Magnetic Field Scans of Different Planar Coil Topologies for Stress Sensor Applications. *MDPI Sensors*, 18(4), 931.  
[doi: 10.3390/s18040931](https://doi.org/10.3390/s18040931)
- [113] Parker Automation. (2001). *L25i/L50i DIN Rail Stepper Drive User Guide*. Electromechanical Division of Parker Hannifin plc. Poole, England. pp. 400

- [114] Jones, F., & Ryffel, H. (1961). *Gear design simplified*. New York, N.Y.: Industrial Press. pp. 20  
ISBN-13: [978-0-8311-1159-5](#)
- [115] Philtec, Inc. (2019). Model D6 Analog Sensor Data Sheet. Last Accessed: December 2019  
URL: <https://philtec.com/wp-content/uploads/2019/08/D6.pdf>
- [116] Philtec, Inc. (2018). Model RC20 Analog Sensor Data Sheet. Last Accessed: December 2019  
URL: <https://philtec.com/wp-content/uploads/2019/06/RC20.pdf>
- [117] LakeShore Cryotronics. (2019). Axial 400 Series Hall Probe Specifications. Last Accessed: December 2019  
URL: <https://www.lakeshore.com/products/product-detail/hall-probes/axial-specifications>
- [118] Gibbs, R., Meydan, T. and Williams, P. (2017). Investigating the three-dimensional structure of stray fields in the boundary layer at micron scale using angled volumetric scanning. Presented at: *ISEM 2017 The 18th International Symposium on Applied Electromagnetics and Mechanics, Chamonix-Mont-Blanc, France, 3-6 September 2017*.  
URL: <http://orca.cf.ac.uk/id/eprint/105469>
- [119] THORLABS. (2019). AMA027/M - Adjustable Height, Pitch and Roll Platform, Metric. Last Accessed: December 2019  
URL: <https://www.thorlabs.com/thorproduct.cfm?partnumber=AMA027/M>
- [120] National Instruments. (2016). *NI Days Event*, Queen Elizabeth II Conference Centre, London, 29<sup>th</sup> November 2016
- [121] Palmstom, A. (2018). *LabVIEW Core 1*, Cardiff School of Engineering, Cardiff University, 15<sup>th</sup> - 17<sup>th</sup> May 2018
- [122] Essick, J. (2015). *Hands-on introduction to LabVIEW for scientists and engineers*. New York, NY: Oxford University Press. pp. 688  
ISBN-10: [019021189X](#) ISBN-13: [978-0190211899](#)
- [123] LabVIEW Download - National Instruments. (2019). Last Accessed: December 2019  
URL: <http://www.ni.com/download/labview-development-system-2015/5308/en/>
- [124] Basic FGV Example, NI Community. (2019). Last Accessed: December 2019  
URL: <https://forums.ni.com/t5/Example-Programs/Basic-Functional-Global-Variable-Example/ta-p/3503982?profile.language=en>
- [125] Shin, S., Schafer, R., & De Cooman, B. (2010). Grain Boundary Penetration by Lancel Domains in Fe-3%Si Grain-Oriented Steel. *IEEE Transactions On Magnetics*, 46(9), 3574-3581.  
[doi: 10.1109/tmag.2010.2045508](#)
- [126] Meydan, T., Derebasi, N., Honda, A., & Goktepe, M. (1992). Dynamic domain motion in amorphous materials under applied tensile stress and controlled magnetisation. *Journal Of Magnetism And Magnetic Materials*, 112(1-3), 23-25.  
[doi: 10.1016/0304-8853\(92\)91101-x](#)

## References

- [127] Honda, A., Goktepe, M., Derebasi, N., Meydan, T., & Moses, A. (1992). Effect of surface roughness and tension on dynamic domain motion in grain oriented 3% silicon iron. *Journal Of Magnetism And Magnetic Materials*, 112(1-3), 20-22.  
[doi: 10.1016/0304-8853\(92\)91100-8](https://doi.org/10.1016/0304-8853(92)91100-8)
- [128] Xu, X. (2014). *Localised Variation of Magnetic Properties of Grain Oriented Electrical Steels* (PhD Thesis). Cardiff University.
- [129] Gibbs R., Meydan T. & Williams P. (2017). Investigating Stray Magnetic Field Structure in the Surface Boundary Layer. Presented at: *SMM 2017, 23rd Soft Magnetic Materials Conference, Seville, Spain 10<sup>th</sup> - 13<sup>th</sup> September 2017*.
- [130] Rauscher, P., Betz, B., Hauptmann, J., Wetzig, A., Beyer, E., & Grünzweig, C. (2016). The influence of laser scribing on magnetic domain formation in grain oriented electrical steel visualized by directional neutron dark-field imaging. *Scientific Reports*, 6(1).  
[doi: 10.1038/srep38307](https://doi.org/10.1038/srep38307)
- [131] Livingston, J., & Morris, W. (1981). SEM studies of magnetic domains in amorphous ribbons. *IEEE Transactions On Magnetics*, 17(6), 2624-2626.  
[doi: 10.1109/tmag.1981.1061525](https://doi.org/10.1109/tmag.1981.1061525)
- [132] Li, Z., Yao, K., Li, D., Ni, X., & Lu, Z. (2017). The effect of ribbon curvature on the magnetic properties of Fe-based amorphous cores. *Journal Of Materials Science: Materials In Electronics*, 28(22), 16736-16740.  
[doi: 10.1007/s10854-017-7587-x](https://doi.org/10.1007/s10854-017-7587-x)
- [133] Zhen Ning Low, Chinga, R., Tseng, R., & Jenshan Lin. (2009). Design and Test of a High-Power High-Efficiency Loosely Coupled Planar Wireless Power Transfer System. *IEEE Transactions On Industrial Electronics*, 56(5), 1801-1812.  
[doi: 10.1109/tie.2008.2010110](https://doi.org/10.1109/tie.2008.2010110)
- [134] Leung, S., & Lam, D. (2007). Performance of Printed Polymer-Based RFID Antenna on Curvilinear Surface. *IEEE Transactions On Electronics Packaging Manufacturing*, 30(3), 200-205.  
[doi: 10.1109/tepm.2007.901181](https://doi.org/10.1109/tepm.2007.901181)
- [135] Mukhopadhyay, S. (2004). A Novel Planar Mesh-Type Microelectromagnetic Sensor—Part I: Model Formulation. *IEEE Sensors Journal*, 4(3), 301-307.  
[doi: 10.1109/jsen.2004.827206](https://doi.org/10.1109/jsen.2004.827206)
- [136] Yamada, S., Katou, M., Iwahara, M., & Dawson, F. (1995). Eddy current testing probe composed of planar coils. *IEEE Transactions On Magnetics*, 31(6), 3185-3187.  
[doi: 10.1109/20.490322](https://doi.org/10.1109/20.490322)
- [137] Chen, G., Chan, I., Leung, L., & Lam, D. (2014). Soft wearable contact lens sensor for continuous intraocular pressure monitoring. *Medical Engineering & Physics*, 36(9), 1134-1139.  
[doi: 10.1016/j.medengphy.2014.06.005](https://doi.org/10.1016/j.medengphy.2014.06.005)

- [138] Moreton, G., Meydan, T., & Williams, P. (2018). Using finite element modelling and experimental methods to investigate planar coil sensor topologies for inductive measurement of displacement. *AIP Advances*, 8(4), 047503.  
doi: [10.1063/1.4994127](https://doi.org/10.1063/1.4994127)
- [139] Yamada, S., Fujiki, H., Iwahara, M., Mukhopadhyay, S., & Dawson, F. (1997). Investigation of printed wiring board testing by using planar coil type ECT probe. *IEEE Transactions On Magnetics*, 33(5), 3376-3378.  
doi: [10.1109/20.617949](https://doi.org/10.1109/20.617949)
- [140] Kuhn, W., & Ibrahim, N. (2001). Analysis of current crowding effects in multiturn spiral inductors. *IEEE Transactions On Microwave Theory And Techniques*, 49(1), 31-38.  
doi: [10.1109/22.899959](https://doi.org/10.1109/22.899959)
- [141] Mc Vay, R. E. (1964). *Improved Magnetic Components for Static Inverters and Converters*. Westinghouse Electric Corporation, Lima, Ohio: NASA-CR-54146. Last Accessed: December 2019  
URL: <https://ntrs.nasa.gov/search.jsp?R=19650003561>
- [142] Kejik, P., Schurig, E., Bergsma, F., & Popovic, R. First fully CMOS-integrated 3D hall probe. *The 13Th International Conference On Solid-State Sensors, Actuators And Microsystems, 2005. Digest Of Technical Papers. TRANSDUCERS '05*.  
doi: [10.1109/sensor.2005.1496420](https://doi.org/10.1109/sensor.2005.1496420)
- [143] Schell, J., Kammerer, J., Hebrard, L., Breton, E., Gounot, D., Cuvillon, L., & de Mathelin, M. (2012). CMOS 3D Hall probe for magnetic field measurement in MRI scanner. *10Th IEEE International NEWCAS Conference*.  
doi: [10.1109/newcas.2012.6329070](https://doi.org/10.1109/newcas.2012.6329070)
- [144] Freescale Semiconductor, Inc. (2013). Xtrinsic MAG3110 Three-Axis, Digital Magnetometer Rev:9.2 Data Sheet: Technical Data. Last Accessed: December 2019  
URL: <https://www.nxp.com/docs/en/data-sheet/MAG3110.pdf>
- [145] Lima, E., & Weiss, B. (2009). Obtaining vector magnetic field maps from single-component measurements of geological samples. *Journal Of Geophysical Research*, 114(B6).  
doi: [10.1029/2008jb006006](https://doi.org/10.1029/2008jb006006)
- [146] Gibbs, R., Meydan, T., & Williams, P. (2017). Volumetrically scanning the structure of stray-fields above grain-oriented electrical-steel using a variably angled TMR sensor. *Proceedings of IEEE Sensors 2017, IEEE Sensors Conference, SEC, Glasgow, Scotland. 30<sup>th</sup> October - 1<sup>st</sup> November 2017*.  
doi: [10.1109/icsens.2017.8234136](https://doi.org/10.1109/icsens.2017.8234136)
- [147] Gibbs R., Meydan T. & Williams P. (2017). Investigating Stray Magnetic Field Structure in the Surface Boundary Layer. Presented at: *IEEE Sensors 2017, IEEE Sensors Conference, SEC, Glasgow, Scotland. 30<sup>th</sup> October - 1<sup>st</sup> November 2017*.
- [148] Li, Y., Wilson, J., & Tian, G. (2007). Experiment and simulation study of 3D magnetic field sensing for magnetic flux leakage defect characterisation. *NDT & E International*, 40(2), 179-184.  
doi: [10.1016/j.ndteint.2006.08.002](https://doi.org/10.1016/j.ndteint.2006.08.002)

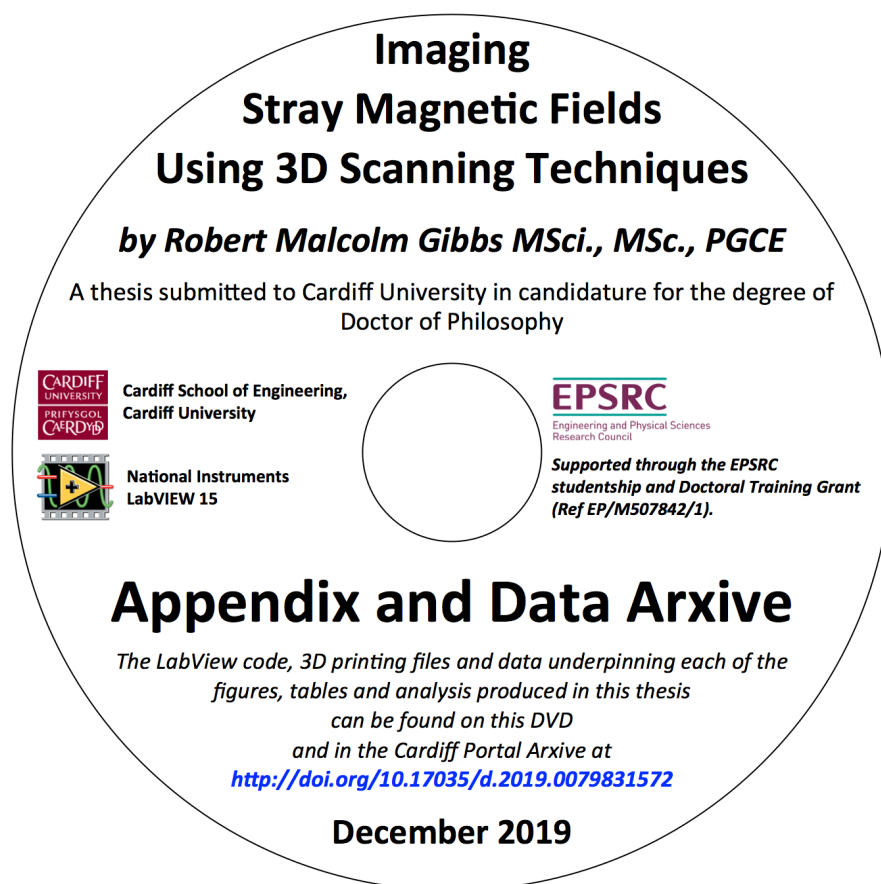
## References

- [149] Li, Y., Wilson, J., & Tian, G. (2007). Experiment and simulation study of 3D magnetic field sensing for magnetic flux leakage defect characterisation. *NDT & E International*, 40(2), 179-184.  
[doi: 10.1016/j.ndteint.2006.08.002](https://doi.org/10.1016/j.ndteint.2006.08.002)
- [150] Meydan, T., Goktepe, M., Honda, A., & Derebasi, N. (1992). Influence of bending stress on domain motion in amorphous material based magneto-elastic transducers. *Journal Of Magnetism And Magnetic Materials*, 112(1-3), 269-271.  
[doi: 10.1016/0304-8853\(92\)91170-x](https://doi.org/10.1016/0304-8853(92)91170-x)
- [151] Calle, E., Jiménez, A., Vázquez, M., & del Real, R. (2018). Time-resolved velocity of a domain wall in a magnetic microwire. *Journal Of Alloys And Compounds*, 767, 106-111.  
[doi: 10.1016/j.jallcom.2018.07.015](https://doi.org/10.1016/j.jallcom.2018.07.015)
- [152] Moses, A., & Konadu, S. (2002). Some effects of grain boundaries on the field distribution on the surface of grain oriented electrical steels. *International Journal Of Applied Electromagnetics And Mechanics*, 13(1-4), 339-342.  
[doi: 10.3233/jae-2002-489](https://doi.org/10.3233/jae-2002-489)
- [153] Finizio, S., Wintz, S., Zeissler, K., Sadovnikov, A., Mayr, S., & Nikitov, S. et al. (2018). Dynamic Imaging of the Delay- and Tilt-Free Motion of Néel Domain Walls in Perpendicularly Magnetized Superlattices. *Nano Letters*, 19(1), 375-380.  
[doi: 10.1021/acs.nanolett.8b04091](https://doi.org/10.1021/acs.nanolett.8b04091)
- [154] Yershov, K., Kravchuk, V., Sheka, D., Pylypovskyi, O., Makarov, D., & Gaididei, Y. (2018). Geometry-induced motion of magnetic domain walls in curved nanostripes. *Physical Review B*, 98(6).  
[doi: 10.1103/physrevb.98.060409](https://doi.org/10.1103/physrevb.98.060409)
- [155] O'Brien, L., Beguivin, A., Fernandez-Pacheco, A., Petit, D., Read, D., & Cowburn, R. (2012). Magnetic domain wall induced, localized nanowire reversal. *Applied Physics Letters*, 101(6), 062415.  
[doi: 10.1063/1.4742746](https://doi.org/10.1063/1.4742746)
- [156] Hristoforou, E. (2003). Magnetostrictive delay lines: engineering theory and sensing applications. *Measurement Science And Technology*, 14(2), R15-R47.  
[doi: 10.1088/0957-0233/14/2/201](https://doi.org/10.1088/0957-0233/14/2/201)









This Appendix Volume consists of six separate Appendices. Due to the number of pages and colour involved it is made available electronically through the Cardiff Portal Archive Cardiff Portal Archive at <http://doi.org/10.17035/d.2019.0079831572> and through the included DVD-ROM rather than printed. The Appendices contain the NI LabView code listings and descriptions of the three versions of the Scanner Control software, the technical design of the Scanner Hardware, a catalogue of the Data generated by this work (available under Open Access) and all published journal and conference papers. This Appendix volume is *not* intended to be read in its entirety, but as a reference source to which the text of the main Thesis links, and from which interested parties can obtain more complete detail than is pertinent to the main discussion, particularly with regard to the design and implementation of the Scanner Hardware and Software. Navigation throughout this volume can be made by hyperlink, by the page numbers provided in the Content and Elements Structure Index pages and also by the unique Element codes printed on the top right of each page.





